

# Statistical Methods for Attenuation Correction in Time of Flight Positron Emission Tomography (TOF-PET)

Ahmadreza Rezaei

**Promoters:**

Prof. Johan Nuyts  
Prof. Michel Defrise

**Jury Members:**

Prof. Uwe Himmelreich  
Prof. Jinyi Qi  
Prof. Paul Suetens  
Prof. Stefaan Vandenberghe

**Session Chairs:**

Prof. Koen Van Laere  
Prof. Uwe Himmelreich

Dissertation presented in partial  
fulfillment of the requirements  
for the degree of Doctor in  
Biomedical Sciences

© Copyright KU Leuven

Without written permission of the promoters and the author it is forbidden to reproduce or adapt in any form or by any means any part of this publication. Requests for obtaining the right to reproduce or utilize parts of this publication should be addressed to KU Leuven, Faculty of Medicine, Department of Imaging and Pathology, Division of Nuclear Medicine, Herestraat 49 - bus 7003, B-3000 Leuven, tel. +32-16-343715.

A written permission of the author is also required to use the methods, products, schematics and programs described in this work for industrial or commercial use, and for submitting this publication in scientific contests.

---

## Acknowledgements

First and foremost, I would like to express my sincere gratitude to my promoters Prof. Johan Nuyts and Prof. Michel Defrise for their guidance and support throughout this journey of mine. Dear Johan, thank you for leaving no walls between us, having the door always open and welcoming me with a friendly face every time that I approached you. I have learnt a lot from you academically and otherwise. Dear Michel, your mathematical views and reasoning have always pointed me in the right direction and consequently have expanded my critical thinking. In our meetings with Johan and Michel, I was exposed to their intuitive and mathematical ways of thinking and this experience I will always cherish. I also want to give a special thanks to the jury members for spending their valuable time reading and evaluating this work.

I would like to thank Christian Michel, Michael Casey, Charles Watson, Vladimir Panin, Maurizio Conti and Judson Jones from the Molecular Imaging devision of Siemens Medical Solutions in Knoxville for the fruitful discussions we have had over the years, for providing data and for supplying us with code and software which helped reduce our data processing efforts. Special thanks also goes to Christian and Anne for their warm hospitality and the wonderful time I spent at their place.

The contribution of Sigrid Stroobants, Steven Staelens and Michel Lambrechts from Universiteit Antwerpen helped improve our study since they provided time of flight emission data which we did not have access to at the time. Furthermore, finding data for our quantitative analysis of the different methods introduced in the course of this PhD would not have been possible if it weren't for the help of Fernando Boada and Thomas Koesters from NYU. I would like to express my gratitude to all these people for paving the way for the future application of this research in clinical practice.

I was fortunate to spend time on research in Australia. This and it's valuable outcomes would not have been possible if it weren't for the support of Prof. Roger Fulton from the University of Sydney. I should not forget to acknowledge the group members of the Brain and Mind Research Institute, Jung-Ha Kim, Georgios Angelis, John Gillam and Will Ryder for not only the scientific discussions but also for the very interesting friendly talks at lunch and for helping Maryam and I see some of the beauties of Sydney and Australia in the short period that we were there.

---

We learnt from each other, we traveled and we have lots of unforgettable memories together. I have to give a special thanks to my colleagues and lab members for creating a warm and sharing work environment which we have all benefited from. So thank you Kathleen, Lin, Katrien, Koen, Selmin, Matthew, Anna, Tao, Esmaeel and Georg. I would also like to acknowledge Marlein from the molecular Small Animal Imaging Centre for all the small talks we had during the animal study scans. Although we were not members of the same lab, I have always enjoyed the long distance discussions and sharing of ideas with Koen Salvo and Didier Benoit.

I'd like to thank my dear Iranian friends in Belgium, Ali & Elham, Hamed & Sima and Keyvan & Lisa for their support and love and for all the friendly gatherings which helped us avoid getting home sick. Also thanks to Mojtaba, Ali and Farhad for all the fun we had together during the first couple of years of my PhD, and to Pouyan and Mehdi for all the long distance chats and the moral support.

A special thanks to my beloved parents for their unconditional love and support. To my parents-in-law for supporting and facilitating Maryam's trip to Belgium in my absence. My warmest thanks and sincerest gratitude goes to the love of my life, Maryam. I would not be here if it weren't for your love and support, your patience and understanding, and the strength you give me each day.

Ahmad.

---

## Summary

The re-introduction of time of flight (TOF) in positron emission tomography (PET) has been made possible due to the recent developments in detector technology. Previous studies have demonstrated some of the benefits gained by using TOF information during reconstruction. In this study we investigate the added value of the TOF information for the problem of attenuation correction from PET emission data only.

We demonstrate numerically and mathematically in chapter 2 that the attenuation sinogram can be estimated from the TOF-PET emission data. However, we find that the TOF-PET emission data determine the attenuation sinogram only up to a constant, and therefore also the emission image up to a related scale. Therefore, some constraining is still required to obtain a quantitative PET reconstruction.

The joint estimation problem is later studied with an iterative approach, building on previous work for non-TOF emission tomography. In chapter 3 the TOF extension of the maximum likelihood activity and attenuation reconstruction (MLAA) algorithm is presented, jointly reconstructing an activity and attenuation image pair from the TOF-PET emission measurements. In chapters 4 and 5 an algorithm is developed called MLACF which avoids the reconstruction of the attenuation image and jointly estimates a sinogram of the attenuation correction factors together with a reconstruction of the activity image. In chapter 4, the problem is studied for the ideal case where there is no scatter or randoms contribution, the general case where scatter and/or randoms are present is studied in chapter 5. In an attempt to make use of the computed tomography (CT-) derived attenuation images in the joint estimation framework, a maximum likelihood algorithm was developed which estimates the activity image together with a deformation of the available attenuation map. This algorithm is called MLRR, its derivation and first validation are presented in chapter 6. The MLRR algorithm reconstructs an activity image while deforming the CT-based attenuation image in order to correct for possible misalignments between the PET emission and CT transmission measurements.

An attempt is made to validate the joint reconstruction of MLAA to the gold-standard reconstructions of MLEM with the CT-based attenuation image on a set of whole-body patient scans in chapter 7. We show that inconsistencies in the emission data can very differently influence the activity reconstructions of the MLEM and MLAA. We find that when the CT and PET data are well aligned, MLAA and MLEM agree well, the deviations seem acceptable for clinical purposes. When there is a mismatch between PET and CT, attenuation correction by MLAA is superior. The guaranteed alignment produced by the joint estimation methods makes them a powerful tool for mitigating the problem of incorrect attenuation correction of the PET emission data in gated PET studies. Chapter 8 presents a modified version of the MLACF algorithm, which improves the visual quality and quantitative accuracy of the activity reconstruction in respiratory gated TOF-PET.



---

## Samenvatting

De herintroductie van “time-of-flight” (TOF) positron emissie tomografie (PET) is mogelijk gemaakt door recente ontwikkelingen in detectortechnologie. Verschillende studies hebben aangetoond dat TOF nuttige bijkomende informatie levert die gebruikt kan worden om de beeldkwaliteit te verbeteren. In dit werk wordt onderzocht hoe met behulp van TOF gecorrigeerd kan worden voor attenuatie, enkel op basis van de TOF-PET emissie data.

In hoofdstuk 2 tonen we met simulaties en met een wiskundige afleiding aan dat het sinogram van de attenuatielijnen geschat kan worden uit de TOF-PET emissiedata zelf. Het blijkt echter dat de TOF-PET data het attenuatiesinogram (en daardoor ook het gecorrigereerde activiteitsbeeld) maar bepalen op een constante na. Daardoor zijn er bijkomende beperkingen nodig om te kunnen garanderen dat de gereconstrueerde beelden kwantitatief correct zijn.

Geïnspireerd door eerder onderzoek op non-TOF PET, bestuderen we diverse iteratieve algoritmes voor de gelijktijdige berekening van de activiteit en de attenuatie uit TOF-PET data. In hoofdstuk 3 wordt een uitbreiding van het zogenaamde MLAA algoritme voorgesteld (Maximum Likelihood reconstruction of Activity and Attenuation) voor de gelijktijdige berekening van een activiteitsbeeld en een attenuatiebeeld uit TOF-PET data. In de hoofdstukken 4 en 5 wordt een algoritme voorgesteld dat samen met het activiteitsbeeld een attenuatiesinogram berekent in plaats van een attenuatiebeeld. In hoofdstuk 4 wordt dit probleem bestudeerd voor het ideale geval waarin er geen bijdrage is van Compton verstrooiing of van toevallige coïncidenties. Het algemene geval, waarbij wel rekening gehouden wordt met Compton verstrooiing en/of toevallige coïncidenties, wordt besproken in hoofdstuk 5. Om ook gebruik te kunnen maken van een beschikbare attenuatiemap (typisch verkregen op basis van CT in PET/CT scanners), werd een nieuw ML algoritme ontwikkeld. Dit algoritme berekent gelijktijdig het activiteitsbeeld en een vervorming van de attenuatiemap. Dit algoritme kreeg de naam MLRR, de afleiding en een eerste validatie worden besproken in hoofdstuk 6. MLRR reconstrueert het activiteitsbeeld en berekent tegelijk de vervorming van de gegeven attenuatiemap die nodig is om te corrigeren voor mogelijke fouten in de alignering van de PET met die attenuatiemap.

Hoofdstuk 7 bespreekt een eerste validatiestudie waarbij reconstructies van een reeks klinische “whole body” TOF-PET scans met MLAA vergeleken worden met de huidige gouden standaard, nl de reconstructies met MLEM en de attenuatiemap afgeleid van het CT-beeld. We tonen dat inconsistenties in de emissiedata een sterk verschillend effect kunnen hebben op de reconstructies met MLAA en MLEM. We stellen vast dat wanneer de CT en PET data goed gealigneerd zijn, MLAA en MLEM gelijkaardige beelden produceren, de verschillen zijn aanvaardbaar voor klinische toepassingen. Wanneer er een mismatch is tussen CT en PET zijn de reconstructies van MLAA superieur. De gegarandeerde alignering van de activiteit en de attenuatie maakt deze algoritmes ook bijzonder nuttig bij de attenuatiecorrectie van een reeks PET-beelden met triggering op de ademhaling. In hoofdstuk 8 wordt een aangepaste versie van het MLACF algoritme voorgesteld, dat de visuele kwaliteit en de kwantitatieve nauwkeurigheid van de reconstructie in TOF-PET met

---

ademhalingstriggering duidelijk verbetert.

# Contents

<b>1</b>	<b>Introduction</b>	<b>1</b>
1.1	Positron Emission Tomography . . . . .	1
1.2	Attenuation Correction in PET . . . . .	4
1.3	Research Objectives . . . . .	12
<b>2</b>	<b>Time-of-flight PET data determine the attenuation sinogram up to a constant</b>	<b>17</b>
2.1	Introduction . . . . .	18
2.2	Time-of-flight 2D PET data . . . . .	19
2.3	Proofs . . . . .	20
2.4	Analytic inversion . . . . .	24
2.5	Approximate error analysis . . . . .	25
2.6	Numerical example . . . . .	26
2.7	Conclusion . . . . .	32
<b>3</b>	<b>Simultaneous Reconstruction of Activity and Attenuation in Time-of-Flight PET</b>	<b>35</b>
3.1	Introduction . . . . .	36
3.2	Theory and methods . . . . .	37
3.3	Experiments . . . . .	42
3.4	Discussion . . . . .	52
3.5	Conclusion . . . . .	54
3.6	Appendix . . . . .	54
<b>4</b>	<b>Transmission-less attenuation correction in time-of-flight PET: analysis of a discrete iterative algorithm.</b>	<b>57</b>
4.1	Introduction . . . . .	58
4.2	The MLACF algorithm . . . . .	60
4.3	Numerical results . . . . .	68
4.4	Conclusion . . . . .	74
4.5	Appendix: convergence of the MLACF algorithm. . . . .	76
<b>5</b>	<b>ML-reconstruction for TOF-PET with Simultaneous Estimation of the Attenuation Factors</b>	<b>81</b>
5.1	Introduction . . . . .	82
5.2	Methods . . . . .	83
5.3	Experiment Design . . . . .	87

## CONTENTS

---

5.4 Results . . . . .	91
5.5 Discussion . . . . .	98
5.6 Conclusion . . . . .	100
<b>6 Simultaneous Reconstruction of the Activity Image and Registration of the CT Image in TOF-PET</b>	<b>103</b>
6.1 Introduction . . . . .	104
6.2 Method/Theory . . . . .	105
6.3 Experiment Design . . . . .	110
6.4 Results . . . . .	115
6.5 Discussion . . . . .	122
6.6 Conclusion . . . . .	124
6.7 Appendix A . . . . .	125
6.8 Appendix B . . . . .	126
<b>7 Joint reconstruction of activity and attenuation in Time-of-Flight PET: A Quantitative Analysis</b>	<b>129</b>
7.1 Introduction . . . . .	130
7.2 Materials and Methods . . . . .	132
7.3 Results . . . . .	135
7.4 Discussion . . . . .	142
7.5 Conclusion . . . . .	143
7.6 Acknowledgments . . . . .	144
7.7 Appendix . . . . .	144
<b>8 Reconstruction of a Motion and Attenuation Corrected Activity Distribution in Gated TOF-PET</b>	<b>147</b>
8.1 Introduction . . . . .	148
8.2 Methods . . . . .	148
8.3 Simulation Design . . . . .	149
8.4 Results . . . . .	151
8.5 Conclusion . . . . .	153
<b>9 Discussion</b>	<b>155</b>
9.1 Future Perspectives . . . . .	160
<b>Bibliography</b>	<b>161</b>

# Chapter 1

## Introduction

### 1.1 Positron Emission Tomography

Emission tomography (positron emission tomography (PET) and single photon emission computed tomography (SPECT)) systems are functional imaging modalities which aim at imaging the human body at a metabolic level by tracing local concentrations of a particular molecule within the body. For that purpose, many different radiopharmaceuticals (or tracers) have been designed by labeling particular molecules with a particular radio-isotope. A wide variety of radiopharmaceuticals exist which are most extensively being used in brain function and cancer research studies [1]. In PET, the most commonly used tracer is fluorodeoxyglucose ( $^{18}\text{F}$ -FDG). FDG is a glucose analog and when labeled with the  $^{18}\text{F}$  radio-isotope, a PET system can measure the radio-isotope concentrations and in dynamic PET scans the glucose metabolism within a local region of the body can be deduced. After injecting a patient with  $^{18}\text{F}$ -FDG, the molecule is circulated through the cardiovascular system and distributed within the body. The isotope which the pharmaceutical is labeled with decays by emitting a positron which is subsequently annihilated (i.e. the mass of the electron-positron pair is converted to the energy of a photon-pair travelling at almost opposite directions). In PET, the detection of both of the emitted photons produces an output signal (an event is detected), whereas a SPECT system would generate an output signal when either of the two photon-pairs are detected. However, SPECT systems are designed and optimized for imaging with single photon emitting tracers and are typically not used for the detection of high (511 keV) energy  $\gamma$ -rays.

The emitted  $\gamma$ -ray photons are detected in PET/SPECT detectors which are composed of scintillator crystals and photo-detectors. Interactions of these  $\gamma$ -ray photons with electrons in the scintillator crystal structure are mostly via the photo-electric effect and to a smaller extent through Compton scattering. Upon absorption of the high energy photons in the scintillator medium, a high amount of energy is deposited in the crystal structure. The high energy deposit of an absorbed  $\gamma$ -ray excites electrons in the crystal structure of the scintillator which subsequently emits secondary lower energy photons in the optical wavelengths to return to a lower energy

## 1. INTRODUCTION

---

state. Photo-detectors such as photo-multiplier tubes (PMTs), avalanche photo-diodes (APDs) or silicon photo-multipliers (SiPMs) which are optically coupled to the scintillator crystals are typically used to detect these secondary emitted photons. In the case of the PMTs, the secondary emitted photons are yet again absorbed through the photo-electric effect in the photo-cathode of the PMT. This photo-electron is initially guided toward and then through cascades of dynodes which emit electrons upon an electron impact (increasing the number of electrons emitted at each stage). The electrons are then subsequently collected and an output signal is generated in the anode of the PMT. Traditionally, PMTs have been the choice for photo-detectors in PET and SPECT. However since they are relatively bulky and more importantly they are highly influenced by magnetic fields (limiting their use in hybrid PET/MR scanners) they are currently being replaced by APDs and SiPMs. For more detail on the physics of scintillation and photon detection please refer to [1].

Some scintillation properties of typical PET scintillators are summarized in table 1.1 [2]. Among other key characteristics of scintillators used in PET systems are the attenuation length of the scintillator, its light output, and the scintillation decay time. A small attenuation length would insure that the high energy  $\gamma$ -ray is absorbed in less amount of the scintillator medium, an increased light output would increase the photon detectability and therefore energy resolution and position discrimination, and a small scintillation rise-time and decay-time provide a better spatial resolution associated with the time of flight (TOF) measurements as well as narrowing the coincidence timing window.

Table 1.1: Typical PET scintillator characteristics

	BGO	GSO	LuAP	LaBr <sub>3</sub>	LSO	LYSO
Attenuation length @ 511 keV (cm)	1.04	1.42	1.05	2.13	1.15	1.12
Scintillation decay time (ns)	300	60	18	35	42	48
Light output (photons/keV)	9	8	10	61	25	32
Peak wavelength (nm)	480	440	365	358	420	420

Typical PET scanners are constructed by arranging the detectors (scintillator material and the photo-detectors) on the curved surface of a cylinder. The length and radius of this cylinder would then determine the axial field of view (FOV) and the radial FOV of the PET scanner, respectively. As opposed to SPECT where a physical collimator is placed on top of the detectors to filter the arriving photons based on their direction of emission, the collimation in PET is achieved electronically. A pair of detected photons would register as an output event when the photon-pair are detected within a given coincidence time interval. This coincidence timing is set based on the time required for a photon to travel the maximum distance between all detector pairs in addition to the uncertainties brought about by the scintillator

## 1.1. Positron Emission Tomography

---

decay time and the electronics. The coincidence time window is typically in the range of 4 ns. Figure 1.1 shows a detector ring schematic of a PET scanner where an annihilation event has been detected at detector pairs  $D_1$  and  $D_2$ . The line connecting the two detector pairs is commonly referred to as a line of response (LOR), which is indexed by a radial offset index  $s$  and an angular index  $\phi$ .

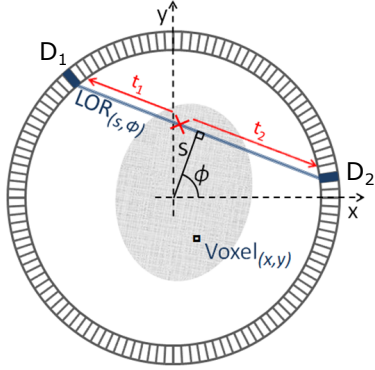


Figure 1.1: Schematic of a PET detector ring.

Although when acquiring the emission data, coincident events from all possible LORs could be considered, events from certain detector pairs are often ignored, e.g. detector pairs within a certain transaxial vicinity. This is to restrict the measured events to the LORs which cross the scanner bore and also to limit some degradation effects when estimating the tracer activity distribution. Furthermore, coincidence events measured by the PET system fall into three sub categories; 1- true, 2- scatter and 3- random coincidence events. Figure 1.1 depicts a true coincident event where the photon annihilation has occurred along the measured LOR. In the case of a scatter event, the emitted photons undergo at least one Compton scattering prior to detection, hence the measured LOR no longer represents the photon's point of annihilation, and random coincidence events arise when the detected photons originate from different annihilation events. The two latter types of coincidence events are undesired events which upon other factors depend on the length of the coincidence timing window, the energy resolution of the PET system, the total amount of activity and attenuating medium within the scanner and if not appropriately corrected for, can influence the quantification of the tracer activity distribution.

During acquisition, the emission data are either stored in a listmode format where different attributes of an event (e.g. index of the detector pair, energy deposit in each detector, etc) are stored as they are observed, or in a sinogram format where the events are histogrammed in a vector of dimension equal to the total number of possible LORs. The task of image reconstruction is then to estimate the distribution (indexed by  $x$  and  $y$  in figure 1.1) of the radioactivity in the FOV of the scanner from the emission measurements.

## 1. INTRODUCTION

---

### 1.1.1 Time of Flight in PET

Among the different attributes of a detected PET event, current state-of-the-art PET scanners also provide an estimate of the difference in the photon arrival times at each end of the LOR. If for each measured event a perfect photon arrival time could be measured at both ends of all the measured LORs (this would correspond to a perfect TOF-resolution), the emission reconstruction problem would be reduced to assigning the event to the voxel which is at a distance  $c\Delta t/2$  from the center of the LOR, where  $c$  is the speed of light and  $\Delta t = t_2 - t_1$  is the difference in the photon-pair arrival times. Unfortunately (and most importantly), due to the intrinsic scintillation decay time of scintillators, there are limits to the achievable accuracy of the TOF-measurement. Current state-of-art PET scanners (LSO based scintillators) can measure the difference in the photon arrival times with a TOF accuracy of 400-600 ps, and it is expected that the next generation of TOF-PET system will achieve a TOF-resolution of 200 ps.

Furthermore, the TOF information is usually discretized and stored in a predefined number of TOF-bins. This resampling of the emission data could in practice produce artifacts if the TOF-bin size becomes comparable to the TOF-resolution of the PET system. However, if the TOF-bin size is set roughly to half the TOF-resolution or less, little degradation should be expected as this rebinning of the TOF-data would result in a negligible (less than 1%) aliasing in its power spectrum [3].

The reconstruction of the tracer distribution with the added TOF information has been shown to significantly improve the emission reconstructions [4]–[8]. For a uniform cylinder of activity, the gains obtained using TOF information was shown to be proportional to the diameter of the cylindrical phantom [4], [9]. This was enough to show gains in TOF-PET brain studies for systems with a TOF-resolution exceeding 1.3 ns [10]. Furthermore, the localization provided by the TOF information accelerates the convergence of the iterative reconstruction algorithms [11] as well as providing an improved contrast-to-noise ratio of the TOF activity reconstructions compared the corresponding non-TOF reconstructions [10], [12]. Moreover, recent studies have shown that in TOF PET, the artifacts induced by attenuation correction errors as well as inaccuracies in detector sensitivities are less severe than in non-TOF PET [13].

## 1.2 Attenuation Correction in PET

It is well known that the attenuation of  $\gamma$ -ray photons follow the Beer-Lambert law, i.e. the photons are attenuated proportional to the product of the linear attenuation coefficient which describes the fraction of the  $\gamma$ -rays that are absorbed of scattered per unit thickness of the attenuating medium and the total length travelled within the attenuating medium. Regardless of the annihilation point of photon-pairs along a measured LOR, the two photons travel the entire LOR length to be detected. Hence in PET, emission measurements along an LOR are attenuated by a ratio exponentially proportional to the projection of the attenuation image  $\mu$  along that

LOR as:

$$B_1/B_0 = e^{-T(s,\phi)} = \exp \left\{ - \int_{-\infty}^{+\infty} dl \mu(s\hat{u}^\perp + l\hat{u}) \right\} \quad (1.1)$$

where  $B_1$  and  $B_0$  are the number of photons measured with and without the effect of the attenuation medium  $\mu$ ,  $T(s,\phi)$  is the radon transform of the attenuation image  $\mu$ , and  $\hat{u}$  and  $\hat{u}^\perp$  are unit vectors along and perpendicular to the LOR and can be explicitly defined as:

$$\hat{u}^\perp = (\cos \phi, \sin \phi), \quad \hat{u} = (-\sin \phi, \cos \phi)$$

The linear attenuation coefficient of a material depends primarily on the energy of the traversing  $\gamma$ -ray. For the 511 keV  $\gamma$ -rays in PET, typical attenuation values for tissue and bone are 0.096 and 0.172 cm<sup>-1</sup> [14], respectively. A quantitative reconstruction of the tracer uptake distribution requires appropriate correction for the attenuation affecting the emission measurements.

Traditionally, a separate low dose transmission measurement with a radioactive isotope (positron or single photon emitter) was acquired pre-injection. The transmission data were then reconstructed to give the attenuating medium and were subsequently projected and used to correct the emission measurements with. The benefit of correcting for attenuation using a positron emitter transmission source is that the transmission measurements and hence the reconstructed attenuation medium are both at the same 511 keV photon energy of the emission data. However, the correction technique required an additional acquisition which can become very time consuming. Although methods have been proposed that reduce the transmission scan time and use the emission measurements as well as transmission measurements to reconstruct the attenuation image [15], attenuation correction using transmission scans are no longer being used in standard clinical practice.

With the advent of state-of-the-art hybrid PET/CT systems [16], the attenuation correction methods with transmission measurement acquired with a radioactive isotope were replaced by attenuation correction using the CT transmission data [17]. The method benefits by the fast data acquisition of the CT. However, the 511 keV attenuation correction of the emission data becomes less trivial. Since the CT transmission data are typically acquired in a range of 80-140 kVp (kVp or kilovoltage peak is the peak voltage applied to the CT X-ray tube), they are not representative of the attenuation affecting the emission measurements, unless the attenuation correction values are corrected for the difference in the photon energies. In commercial scanners, after the reconstruction of CT data a bilinear interpolation technique is used to extrapolate the attenuation values to 511 keV attenuation values, and the extrapolated image is then used to correct the emission measurements [14]. Even then the attenuation reconstruction might suffer from degradations affecting the CT attenuation reconstructions e.g. beam hardening effects [18]. In addition to this extrapolation, differences between the PET and CT resolutions also need to be taken into account. More importantly, since the CT and PET scans are acquired sequentially and that the CT data are acquired almost instantaneously whereas

## 1. INTRODUCTION

---

the PET data are acquired over a relatively long time interval, artifacts due to possible misalignment of PET and CT data as well as artifacts due to patient and/or breathing motion can be expected.

In the case of hybrid PET/MR scanners, the attenuation problem is even more challenging [19], [20]. As MR images provide information on the proton densities of different organs as opposed to their electron density (which the attenuating properties of different material are closely related to), the MR images provide no direct measurement of how the emission measurements are affected by attenuation. In addition to the aforementioned problem, typical MR images provide a low-signal in regions with very different attenuating properties, namely bone structures, the lungs and air (e.g. sinus, stomach..). Although different MR sequences have been developed that better differentiate these regions, the topic is an open research problem. Typical MR attenuation correction techniques either use a pre-defined atlas of attenuation images which is first registered to the reconstructed MR image and then is used for attenuation correction or assign different tissue attenuation values to different segmented regions of the standard sequence MR images. More recently, the use of the newly developed ultrashort-echo-time (UTE) and zero-echo-time (ZTE) sequences which provide better MR signals for bone tissue have been studied for attenuation correction in brain imaging [21]. The benefit of attenuation correction with the MR compared to the CT is that no extra dose is delivered to the patient. However, the presence of patient abnormalities and the use of predefined tissue attenuation values in addition to the problem of the heavy-attenuating MR coils has limited the success of the MR-based attenuation correction methods. Furthermore, time-wise the MR acquisition is relatively longer (and even more so for the newly developed sequences) than the time required to obtain CT transmission data. In the new simultaneous PET/MR scanners [22], [23] however, this time burden is minimized as the MR data and the PET emission measurements are being acquired simultaneously.

The aforementioned approaches to attenuation correction all have their limitations. This is why several groups have attempted to jointly estimate the activity and attenuation images from the emission data only. In the following, we classify the techniques that have been developed to reconstruct an attenuation corrected activity reconstruction from the emission data only and briefly discuss some of these available methods.

### 1.2.1 Emission-based Attenuation Correction

The emission-based attenuation correction methods could be classified in two broad categories: 1- methods which explicitly make use of the consistency conditions of the radon transform, and 2- iterative methods which implicitly use the consistency of the reconstructions and refine an initial guess of the activity and attenuation images. These two categories are discussed in more detail in the following.

### Consistency Condition Methods

It is known, that the attenuated radon transform (PET emission measurements) of a smooth function (tracer distribution) with compact support satisfies [24]:

$$\forall \{k, m | 0 \leq m < k\} \in \mathbb{N} : \int_0^{2\pi} \int_{-\infty}^{+\infty} s^m e^{ik\phi} e^{T(s,\phi)} E(s, \phi) ds d\phi = 0 \quad (1.2)$$

where  $E$  is the PET emission measurements, and  $s$  and  $\phi$  are the radial and angular coordinates, respectively. Equation (1.2) is also commonly referred to as the Helgason-Ludwig consistency conditions and are powerful tools used in emission reconstruction. The Helgason-Ludwig consistency conditions of an emission data set could be better understood if we consider its Fourier transform. The conditions state that, after taking the Fourier transform of the  $m$ -th moment of the attenuation corrected emission data all the Fourier coefficients of index greater than  $m$  should be zero [25]. Although attenuation correction methods using the consistency conditions (1.2) exist, it is believed that these equations are not enough to exactly determine the attenuation image  $\mu$ . Furthermore, with noise in the emission measurements the higher order conditions become less reliable and are of limited use, hence constraining of the estimated attenuation image or correction factors is deemed to be necessary. In the following we will discuss methods proposed for both SPECT and PET. However, it should be noted that for SPECT imaging the expression for the consistency conditions are slightly different to (1.2) as the SPECT emission data are affected differently compared to PET. The general formulation of SPECT consistency conditions can be found in [26].

In the pioneering work of [27] the attenuation image was modelled by a motion affected attenuation image which was otherwise known. The work demonstrates that a set of affine motion parameters could be obtained by utilizing similar consistency equations during reconstruction for SPECT imaging. Furthermore, the Helgason-Ludwig consistency conditions have been used in more recent studies [24], [28] to solve the attenuation correction problem by computing the elliptical parameters of a uniformly attenuating medium for both SPECT and PET, respectively. The results of the proposed method were tested in simulations as well as on experimental data, and thought to mitigate the attenuation alignment problem in clinical patient data. In [29] the SPECT consistency conditions were used to estimate a spline representation of the attenuating medium support. The results were then compared to the simpler ellipsoid model of the attenuation medium computed from the consistency conditions, where a similar accuracy was reported for the two methods. The stability of these methods to the optimization method of choice [30] as well as to different initializations [31] has also been investigated in the literature. Although different accuracies were reported for the different optimization methods studied, the optimization methods were found to be stable enough to estimate the elliptical parameters even in case of noisy measurements.

Similarly in [32], a constant attenuating elliptical medium was estimated using a different type of consistency condition for SPECT imaging. The consistency conditions used in [32] closely resemble the Fourier slice theorem, which establishes

## 1. INTRODUCTION

---

a set of equations between the Fourier transforms of the emission data and of the activity image.

Moreover, the availability of CT-based attenuation images has minimized the need for estimating the shape of the attenuating medium, and the focus shifted to solving possible alignment problems between PET/SPECT and CT data. The previous work on estimating the motion parameters of a template using the consistency conditions of (1.2) was extended to a 3D attenuation template for 3D PET and SPECT data [33], [34], respectively. In [35], [36], the CT-based attenuation volume was used as the 3D matching template, and although with limited success, the method showed improvements in the case of PET and CT misalignments.

The majority of the works on attenuation correction have been focused on estimating the attenuation image or on refining an available atlas using consistency conditions (e.g. (1.2)) to compute the attenuation correction factors from the estimated attenuating image (and therefore enable attenuation correction of the emission data). However, there are also methods that avoid the intermediate step of the attenuation estimation and attempt to directly estimate the attenuation correction factors from SPECT emission data [37]. It was found however, that these consistency equations were not rich enough to estimate the exact attenuation correction factors in a simulated SPECT myocardial perfusion study.

Another set of conditions that are commonly used are the set of discrete consistency conditions. When applied to the emission measurements  $E$ , the direct consistency conditions state that the projection of a consistent reconstruction is required to be identical to the emission measurements. This is a consistency constraint that the iterative methods (which will be discussed next) also intrinsically rely on. The direct consistency condition could be expressed as:

$$\mathcal{P}[\mathcal{R}[E(s, \phi)]] = E(s, \phi) \quad (1.3)$$

where  $\mathcal{P}$  is the forward projection operator and  $\mathcal{R}$  is some reconstruction operator. Note that here, the attenuation correction factors are absorbed in the operators  $\mathcal{P}$  and  $\mathcal{R}$ .

The projection operator  $\mathcal{P}$  is a linear operator. Therefore, if an image and its projection are represented by column matrices, then the projection operator can be represented as a multiplication of the image with a matrix, often referred to as the system matrix. Similarly the reconstruction operator could be replaced by the pseudo-inverse of the system matrix  $\mathcal{R} = \mathcal{P}^+$ . In [38], [39], a matrix representation of (1.3) is formulated and a reconstruction algorithm is proposed for SPECT imaging which relies on a QR decomposition of the system matrix at each iteration of the algorithm, and later extended for PET imaging in [25]. Similarly in [40] an inversion algorithm was proposed after adding a Tikhonov regularization term to the discrete consistency conditions (1.3). The feasibility of joint activity and attenuation estimation was demonstrated on a 2D simulation of SPECT data. However, the results reported in [40] are strongly affected by cross-talk artifacts, where a local under/over estimation of the activity reconstruction is accounted for by an under/over estimation of the attenuation coefficient values of the same region in the attenuation reconstruction.

In [41], the direct consistency conditions (1.3) were used in a simulated annealing framework, which was initialized with an attenuation image with the same topology as, but different from, the actual attenuation. The algorithm then managed to jointly estimate the activity and attenuation images from the emission data. In 2D SPECT simulations, more accurate results were obtained when using the discrete consistency conditions (1.3) as opposed to the Helgason-Ludwig consistency conditions (1.2). In a more recent study and with a similar approach to [41], a method was proposed which limited the attenuation reconstruction to determining the attenuation coefficients of previously segmented regions to typically known tissue attenuation values [42]. The algorithm uses the expectation maximization algorithm to alternately update both activity and attenuation images. This is subsequently followed by a segmentation of the attenuation reconstruction, and an estimation and assignment of the attenuation coefficient values to each segmented region. The attenuation values were estimated using the Helgason-Ludwig consistency conditions (1.2) and from a subset of typical tissue attenuation values. The method was shown to effectively estimate non-uniform attenuators when accurate detection of image boundaries was possible.

### Iterative Methods

In this section methods are introduced which intrinsically use the data consistency conditions and recursively decrease residual errors between the emission data and the projection of the current reconstruction (equation 1.3, LHS). Based on the noise assumption (Gaussian or Poisson), the methods could be classified in two sub-categories;

1. methods which attempt to jointly estimate activity  $\lambda$  and attenuation  $\mu$  by minimizing a quadratic cost function of the emission data  $E$  and a data acquisition model  $\bar{Y}$  [43]–[46]:

$$[\lambda, \mu]^{LS} = \arg \min_{\lambda, \mu} Q(E, \lambda, \mu) \quad (1.4)$$

$$Q(E, \lambda, \mu) = \sum_i \left\| \bar{Y}_i(\lambda, \mu) - E_i \right\|^2 \quad (1.5)$$

where  $i$  denotes the LOR index (only a single index is needed because the discrete data can be represented as a column matrix). Methods in this class of algorithms find a relatively simple formulation and the available optimization tools are very appealing. However, this formulation of the problem does not take the Poisson nature of the measurements into account. Although this drawback has been occasionally remedied by weighting the quadratic cost function by the emission data, a second class of algorithms has been developed with the assumption that the emission data are generated randomly through a Poisson distributed process.

2. methods which aim at solving the joint estimation problem by maximizing the

## 1. INTRODUCTION

---

emission likelihood function [25], [46]–[49]:

$$[\lambda, \mu]^{ML} = \arg \max_{\lambda, \mu} L(E, \lambda, \mu) \quad (1.6)$$

$$L(E, \lambda, \mu) = \sum_i E_i \ln \bar{Y}_i(\lambda, \mu) - \bar{Y}_i(\lambda, \mu) \quad (1.7)$$

This formulation of the problem is more appealing among researchers, as it takes the Poisson nature of the emission measurements into account.

The data  $\bar{Y}$  is commonly modelled as the sum of the projection of the activity image  $\lambda$  attenuated by the attenuation image  $\mu$  and of an additive contribution of randoms and/or scatter  $S$ . For PET, this can be written as:

$$\forall i : \bar{Y}_i(\lambda, \mu) = P_i[\lambda] e^{-P_i[\mu]} + S_i \quad (1.8)$$

where  $i$  is the index of the LOR. The corresponding expression for SPECT is somewhat more complicated because in SPECT, the attenuation depends on the position of the activity along the LOR.

In a pioneering work on the topic [43], the joint activity and attenuation problem for SPECT imaging was reduced to a mixed convex-concave feasibility problem and was solved with a previously developed convex optimization method (i.e. Cyclic Subgradient Projections method). However, it should be noted that although the problem of activity reconstruction with known attenuation and the problem of attenuation reconstruction with known activity are known to be convex, the joint activity and attenuation reconstruction problem is not jointly convex. In [44], the multiplicative algebraic reconstruction technique (MART) which has been shown to converge [50] was modified to allow an alternating update of the activity and attenuation images, respectively. Although some promising results were obtained in a simple 2D simulation when additional constraints were applied to the attenuation reconstruction, the method was found to be quantitatively inaccurate due to cross-talk between the activity and attenuation reconstructions.

In [47] the likelihood formulation (1.7) of the joint estimation problem was used instead of its quadratic formulation (1.5). In the proposed maximum likelihood activity and attenuation reconstruction (MLAA) method, the activity and attenuation reconstructions were updated sequentially. The activity image was updated by the maximum likelihood expectation maximization (MLEM) algorithm while keeping the attenuation image fixed, and the attenuation image was update by the maximum likelihood transmission reconstruction (MLTR) algorithm keeping the activity image fixed. Although promising results were reported in simulated as well as clinical PET and SPECT data, prior information in the form of a bi-modal intensity prior and a smoothing prior (respectively enforcing expected tissue attenuation values and the local smoothness of the reconstructed attenuation values) was needed to limit the cross-talk between the activity and attenuation reconstructions.

The attenuation image is updated in [47] using a gradient ascent algorithm, and the attenuation update was obtained after replacing the log-likelihood function by a quadratic surrogate. In [48], with a similar approach an EM algorithm is proposed

for the attenuation image reconstruction in SPECT. However even with an EM estimate of the attenuation image, similar results were reported as the preceding works on simultaneous activity and attenuation reconstructions, as the final activity and attenuation images were not free of the cross-talk artifacts.

In order to minimize the artifacts induced by cross-talk between the activity and attenuation reconstructions, a method was proposed which reduced the attenuation reconstruction problem to the estimation of the attenuation image from a selection of basis functions [45], [51] in SPECT. In their formulation, the attenuation image was represented as a weighted sum of previously computed basis functions from a population of transmission scan reconstructions. Similar to the previous methods, the activity and attenuation reconstructions were updated alternately. The activity image was updated using the MLEM algorithm in early iterations and the reconstruction algorithm was then changed to the conjugate gradient (CG) method for a better convergence. The attenuation image was updated using the CG method. Although the strong constraints applied to the attenuation image (i.e. the use of basis functions) were found to eliminate the cross talk problem, the reconstructions did not seem artifact-free.

In a comparative study [46], the Poisson model and the Gaussian model of the SPECT emission data were used for joint estimation of activity and attenuation with different regularizations applied to the attenuation reconstruction. In this work, the conventional reconstruction algorithms as well as the alternating updating procedures were avoided, and instead the limited-memory Broyden-Fletcher-Goldfarb-Shanno (l-bfgs) optimization algorithm was used to simultaneously update the activity and attenuation images. Although no significant differences were reported between the Poisson model and the Gaussian model reconstructions, strong dependence on the final reconstruction to initialization was reported. Similar results were also reported in [49] for PET where the activity and attenuation estimates were sequentially updated by incorporating a Gauss-Newton update rule. Among the regularizers used in [46], the L<sub>1</sub> regularizer which favours piecewise linear attenuation coefficients were thought to outperform the others.

With an approach similar to the one of [47], a joint reconstruction algorithm was developed in [25], [52], [53] which used the alternating updating scheme for activity and attenuation reconstructions. In the joint reconstruction algorithm, the activity reconstruction was updated using the MLEM algorithm and the Newton Raphson method was used to update the attenuation reconstruction by maximizing a quadratic surrogate to the emission likelihood (1.7). Similar to previous findings, cross-talk artifacts were reported after applying the reconstruction algorithm to SPECT emission data as described. However, after incorporating an iterative data refinement technique into the algorithm the cross-talk artifacts were eliminated from the joint reconstructions.

Similar to the works by [41] and [45], a new algorithm was proposed in [54] focusing on SPECT cardiac imaging. The proposed algorithm uses a patient-dependent attenuation template which is iteratively registered to the activity reconstruction. The method represents the body and the different organs by 3D active contours, and refines the predefined contours iteratively by registering them to the activity

## 1. INTRODUCTION

---

reconstruction. Typical tissue attenuation coefficient values are then assigned to each of the regions/organs modelled by the active contours, and the method is iterated until convergence. As these organs/contours are being modified in each iteration, the method can adapt to inter-patient anatomical differences, whereas the method proposed in [45] does not have this added flexibility.

The advent of the state-of-the-art PET/MR systems allows the use of patient-specific 3D anatomical templates to be used in the joint estimation framework without the additional dose burden of a CT acquisition. In [55], [56] a joint reconstruction algorithm was proposed which reduced the reconstruction problem to estimating the attenuation coefficient values of different regions of interest (ROIs) previously segmented from the 3D MR image. In contrast to a previous work [54], the attenuation coefficient values were directly estimated from the TOF-PET emission data and were not limited to a subset of expected tissue attenuation. The latter study demonstrated that when an accurate segmentation of the MR prior image is available, quantitative results similar to the gold-standard PET/CT reconstructions could be obtained.

The limited application and use of the emission-based attenuation correction methods in the clinical practice has mainly been due to the longstanding problem of attenuation and activity cross-talk and also in part due to the limitations of the aforementioned methods. Fortunately, it appears that with improving time-of-flight information the crosstalk problem for emission-based attenuation correction is substantially reduced as demonstrated in [13] where the TOF activity reconstructions become more robust to attenuation correction artefacts as the TOF-resolution improves. These new findings motivate the study of the joint estimation of activity and attenuation problem with TOF-PET data, in hope for the design of more general reconstruction algorithms which could eliminate the major limiting factors for the implementation of emission-based attenuation correction methods in clinical practice.

### 1.3 Research Objectives

The aim of this project was to investigate the value of the added TOF information in PET measurements for attenuation correction, and to improve the attenuation correction of PET emission data. We have been able to demonstrate numerically and mathematically that the attenuation can be estimated from TOF-PET emission data, provided that the extent over which the activity is distributed is large compared to the TOF-resolution. However, the TOF-PET data determine the attenuation factors (and therefore also the corrected emission image) only up to a constant scale. Consequently, for quantitative PET, some constraining is still required to impose the correct scale factor. We have proposed several methods, each exploiting this TOF-based attenuation information in a different way, to make effective use of the available information in different settings. These contributions are briefly described in the next paragraphs.

In [57], we were able to show that when TOF information is available, it is possible to estimate the activity image up to a scale and the attenuation sinogram up to a related additive constant. Soon after, a mathematical proof of our claim was

derived and a new analytical algorithm was developed for attenuation estimation in TOF PET [58]. The proof was obtained by exploiting the consistency condition for the TOF Radon transform [3], [59], and was later extended to the case of 3D TOF-PET emission measurements [60]. Details of this will be discussed in chapter 2.

Moreover, in [61], we analyzed the effect of time-of-flight on the joint estimation problem with an iterative approach, building on previous work for non-TOF emission tomography [47], [62]. While the analytical method is able to formulate the problem in a closed-form and directly compute the attenuation image from it, the iterative maximum likelihood activity and attenuation reconstruction (MLAA) provides a means to incorporate prior knowledge (i.e. smoothness of the attenuation image, negligible attenuation values outside the object medium, etc.) and is able to model the Poisson nature of the emission data, hence resulting in more robust reconstructions compared to the analytical method. Details of this work are presented in chapter 3.

Alternatively, we demonstrated that the activity image can also be jointly estimated together with the attenuation correction factors [63]–[66] (i.e. a sinogram of attenuation correction factors is estimated instead of an image of the attenuation coefficients). This newly developed maximum likelihood attenuation corrections factor (MLACF) algorithm makes alternating updates of the activity image and the attenuation correction factors. If there is no scatter or randoms contribution, this two step MLACF algorithm reduces to a single step MLEM-like algorithm. Although MLACF does not impose consistency to the estimated attenuation factors, the activity reconstructions possess similar noise characteristics as activity reconstructions of MLAA for considerable amounts of noise in the emission data. In addition, the method also proved to be robust to possible errors in the detector pair sensitivities. In chapter 4 the MLACF algorithm without additive randoms/scatter contribution will be presented, and a convergence analysis of the algorithm will be provided. The case of an additive contribution will be discussed in chapter 5.

In current PET/CT scanners, the CT and PET scans are acquired sequentially, and furthermore the PET data are acquired over a relatively long time interval whereas CT attenuation values are acquired almost instantaneously. Thus, artifacts due to patient and/or breathing motion are expected in emission reconstructions together with artifacts due to possible misalignment of PET and CT data. In an attempt to make use of the CT-derived attenuation image in the joint estimation framework, the maximum likelihood reconstruction of activity and registration of attenuation (MLRR) algorithm was developed [67], [68]. The MLRR algorithm aims at combining the high signal to noise ratio of the CT image with the optimal (i.e. the maximum likelihood) alignment produced by the joint estimation. The algorithm jointly estimates an activity image together with deformation parameters by maximizing the likelihood associated with the reconstructed activity image and deformed CT-based attenuation image. It was found that the activity reconstructions of MLRR were comparable to the ones produced by MLAA in terms of bias and variance, and that the method was able to correct for the discrepancies between the CT attenuation image and the attenuation image which has affected the data. Details and results of this method will be presented in chapter 6.

Figure 1.2 shows the MLEM, MLAA, MLACF and MLRR activity reconstructions

## 1. INTRODUCTION

---

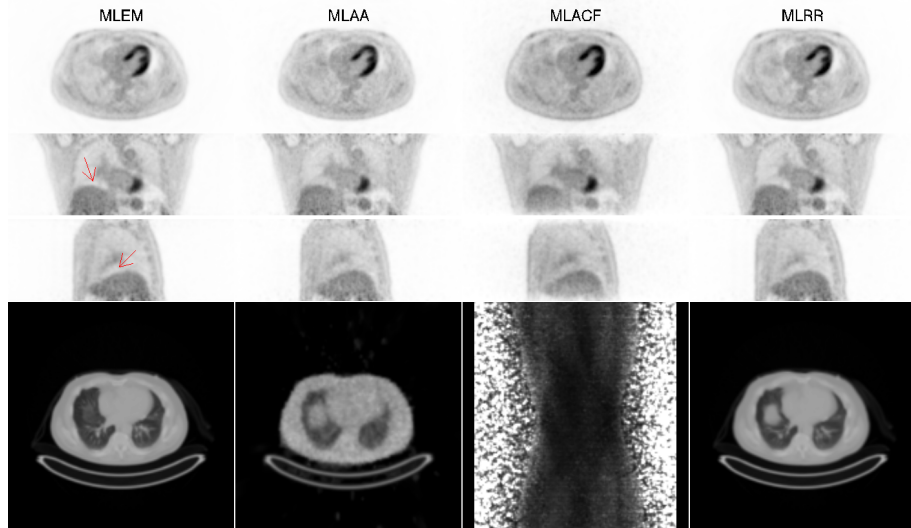


Figure 1.2: Activity (top) and attenuation/ACF (bottom) reconstructions of MLAA (second column), MLACF (third column), and MLRR (fourth column) compared to the reference MLEM reconstruction with the CT attenuation image (first column). The reconstructions are from a 4 minute  $^{18}\text{F}$ -FDG patient scan injected with 296 MBq of the tracer.

of a patient scan. The reconstructions are from a 4 minute  $^{18}\text{F}$ -FDG scan of a patient injected with 296 MBq of the tracer. Comparison between the CT (used for the attenuation correction of the MLEM activity reconstruction) and the joint attenuation estimates of MLAA and MLRR suggests a mismatch between the CT and the PET data, which in turn leads to inaccuracies in the reconstructed activity image (most obvious in the sagittal and coronal views). The patient data was collected from the Siemens Biograph mCT PET/CT scanner with a TOF-resolution of  $527.5 \pm 4.9$  ps FWHM for clinical emission count rates, which corresponds to  $79.125 \pm 0.735$  mm FWHM. We would like to thank S. Stroobants, S. Staelens and M. Lambrechts of the Universiteit Antwerpen for providing the TOF-PET emission data.

In chapter 7 we attempt to validate the joint reconstruction of MLAA to the gold-standard reconstructions of MLEM with the CT-based attenuation image on a set of whole-body patient scans. Since the MLEM and the joint reconstructions have different degrees of freedom (while MLEM reconstructs the activity, MLAA is reconstructing a pair of activity and attenuation images), the activity reconstructions can be differently influenced by inconsistencies in the emission data. A possible cause of such an inconsistency is slight over/under estimation of the expected additive contribution of the randoms and/or scatter in the emission data. We have reason to believe that this is the case from preliminary results on the comparison of the MLEM and MLAA activity reconstructions. Therefore, we have proposed a method that could better model the expected additive contribution of the emission data [69], compared to conventional methods. We find that with an accurate estimate of the additive scatter contribution the reconstructions of MLAA and MLEM are within

the clinically acceptable range of  $\pm 10\%$ . The validation results of this study are presented and discussed in chapter 7.

The guaranteed alignment produced by the joint estimation methods provides a powerful tool in mitigating the problem of incorrect attenuation correction of the PET emission data in gated PET studies. With simple 2D experiments we tried to get more insight in how motion affects the joint reconstructions of activity and attenuation [70]. We later demonstrated that the availability of a well aligned pair of activity and attenuation image for each frame of gated TOF-PET data helps in the estimation of between-frame motion parameters [70]. This is because both attenuation and activity reconstructions must comply with a single deformation field, and this in turn also avoids the problem of noise registration since the activity and attenuation reconstructions have a different noise structure.

Building on the registration methodology in MLRR, in chapter 8 we present a method that jointly estimates an activity image together with transformation parameters that deform the activity image to a corresponding frame of the gated TOF-PET data. By using a modified version (for gated TOF-PET data) of the MLACF algorithm, we obtain an activity image which is corrected for attenuation. In the proposed algorithm, the activity and motion estimates are then updated sequentially. In our framework, the activity image can be reconstructed in either a specific reference frame (chosen among the frames) or a virtual reference frame. Our simulations indicate that the use of all (frames) TOF-PET emission data significantly improves the quantification and that the choice of the reference frame which is used for the activity reconstruction does also influence the properties of the final tracer distribution reconstruction.

The chapters of this PhD manuscript have been either published or are in preparation for submission. In chapter 2 where I am the second author, in addition to the fruitful discussions with my promoters, I have been involved in providing the numerical proof-of-principle simulations presented in the chapter. Also, during one of our discussions we decided to submit our results on the MLACF reconstruction algorithm in separate papers. In one, the case of no additive randoms or scatter case (chapter 4) was analyzed, and in the other the general case (chapter 5) was studied. In chapter 4 where I am the second author, I have been involved in discussions as well as some simulations which did not end up in the published manuscript.



## Chapter 2

# Time-of-flight PET data determine the attenuation sinogram up to a constant

M. Defrise, A. Rezaei, and J. Nuyts, “Time-of-flight PET data determine the attenuation sinogram up to a constant”, *Physics in Medicine and Biology*, vol. 57, no. 4, pp. 885–899, Feb. 2012

### Abstract

In positron emission tomography (PET), a quantitative reconstruction of the tracer distribution requires accurate attenuation correction. We consider situations where a direct measurement of the attenuation coefficient of the tissues is not available or unreliable, and where one attempts to estimate the attenuation sinogram directly from the emission data by exploiting the consistency conditions that must be satisfied by the non-attenuated data. We show that in time-of-flight (TOF) PET, the attenuation sinogram is determined by the emission data except for a constant and that it can be estimated efficiently using a simple analytic algorithm. The stability of the method is illustrated numerically by means of a 2D simulation.

## 2.1 Introduction

In positron emission tomography (PET), an accurate quantitative reconstruction of the tracer distribution requires taking into account the attenuation of the photons by the tissues. The spatial distribution of the attenuation coefficient (the *attenuation image*) is usually estimated by means of a CT scan, extrapolated to the required photon energy of 511 keV, and forward projected to obtain the attenuation sinogram [17]. There are situations however where this external information about the attenuation is unavailable, incomplete, or potentially inaccurate due for instance to patient motion between the transmission scan and the emission scan or to the utilization of radiological contrast agents [71]. Despite recent progresses [72]–[74], estimating the attenuation from MR data in PET-MR scanners remains complex and more prone to errors than with PET-CT scanners. In all these cases, any additional information should be exploited to improve the stability and accuracy of the reconstruction. Potential sources of additional information include known values of the attenuation coefficients in various types of tissues [75] and also the emission data themselves, which have long been known to contain significant information about the attenuation. An interesting illustration of the latter is given for two-dimensional (2D) PET by theorem 2.1 in [76]: *if the tracer distribution consists of finitely many point sources, one of which is outside the convex hull of the attenuating medium, then the attenuation factors are determined in a unique way for all lines of response containing a source, i.e. for all lines of response for which the attenuation factors are needed for image reconstruction.* This theorem and similar properties explain the success of statistical iterative algorithms that simultaneously estimate the tracer distribution and the attenuation image from the combined emission and transmission data. The goal of these algorithms is to supplement the poor signal-to-noise ratio in the transmission data measured with external rotating positron sources in PET scanners of the previous generations [15], [43], [77], [78].

The question then naturally arises: is it possible to estimate the attenuation correction factors using only the emission PET data? The answer is negative: emission data do not determine the attenuation correction factors [76]. The simplest examples of non-uniqueness involve problems where the tracer distribution and the attenuating medium are both radially symmetrical. Nevertheless, there have been attempts to solve this problem. Natterer *et al* [24], [79] use the Helgason-Ludwig consistency conditions to estimate the coefficients of a simple parametric model of the attenuation image, such as a uniform ellipse mimicking the abdomen. Iterative methods have also been described, see e.g. [25], [47], [48], as well as methods based on discrete consistency conditions [39]. Despite some encouraging results, the problem is poorly determined and in most cases the estimated attenuation image contains artefacts, which mirror structures of the activity image (these errors are referred to as *cross-talk artefacts*). The poor stability of this problem also explains why PET images reconstructed without attenuation correction are not only quantitatively inaccurate, but also structurally inaccurate, missing for instance lung tumors where the increased attenuation almost exactly compensates the increased tracer uptake [80].

This paper deals with attenuation correction in time-of-flight (TOF) PET. Recent studies [13], [56], [81], [82] have shown that time-of-flight (TOF) reconstruction is more robust than non-TOF reconstruction when the attenuation image is not known accurately. We provide new insight into this issue, with the following results. First, by exploiting the consistency condition for the TOF Radon transform, we prove in section 2.3 that under fairly general assumptions the emission 2D TOF data determine the attenuation sinogram up to an additive constant. Secondly, section 2.4 presents an analytical algorithm to solve this problem, and an approximate analysis of noise propagation is given in section 2.5. Numerical results with simulated 2D TOF data in section 2.6 illustrate the performance of this algorithm.

## 2.2 Time-of-flight 2D PET data

We parametrize the 2D TOF data of a tracer distribution  $f(\vec{x} = (x, y))$  as

$$p(\phi, s, t) = \int_{-\infty}^{\infty} dl f(s\hat{u}^\perp + l\hat{u}) w(t - l) \quad (2.1)$$

where  $s$  and  $\phi$  are the usual transaxial sinogram coordinates and  $w(t)$  is the TOF profile. The unit vectors

$$\hat{u}^\perp = (\cos \phi, \sin \phi) \quad \hat{u} = (-\sin \phi, \cos \phi) \quad (2.2)$$

are respectively orthogonal and parallel to the line of response. The TOF bin  $t = 0$  corresponds to the mid-point of the line of response (LOR). The attenuation coefficient is denoted by  $\mu(\vec{x})$  and the attenuation factors are

$$a(\phi, s) = \exp\left\{-\int_{-\infty}^{\infty} dl \mu(s\hat{u}^\perp + l\hat{u})\right\} = \exp\{-(\mathcal{R}\mu)(\phi, s)\} \quad (2.3)$$

with  $\mathcal{R}$  denoting the 2D Radon transform. The *attenuation sinogram*  $(\mathcal{R}\mu)(\phi, s)$  is the Radon transform of the *attenuation image*  $\mu(\vec{x})$ . The measured data are  $m(\phi, s, t) = p(\phi, s, t)a(\phi, s)$ .

We make the following assumptions:

1. The TOF profile is a Gaussian with standard deviation  $\sigma < \infty$ ,

$$w(t) = e^{-t^2/2\sigma^2} / \sqrt{2\pi}\sigma. \quad (2.4)$$

2. For each measured line of response  $(\phi, s)$ , the TOF data are measured for all  $t \in \mathbb{R}$ .
3. The tracer distribution  $f(\vec{x})$  and the attenuation coefficient  $\mu(\vec{x})$  are non-negative functions with continuous first derivatives and bounded supports.
4. No line of response is totally attenuated, so that  $a(\phi, s) > 0$  for all  $\phi, s$ .

---

## 2. TIME-OF-FLIGHT PET DATA DETERMINE THE ATTENUATION SINOGRAM UP TO A CONSTANT

---

Define the sinogram region  $\Omega$  as the set of lines of response that contain activity,

$$\Omega = \{(\phi, s) \in [0, \pi) \times \mathbb{R} \mid m(\phi, s, t) > 0\} \quad (2.5)$$

With these assumptions, the following results hold true:

- Theorem 1: The emission data determine the  $\phi$  and the  $s$  derivatives of the Radon transform  $\mathcal{R}\mu$  of the attenuation image for all  $(\phi, s) \in \Omega$ .
- Corollary 2: The emission data determine the Radon transform  $\mathcal{R}\mu$  of the attenuation image up to an additive constant within the region  $\Omega$ .
- Corollary 3: If the attenuation factor  $a(\phi, s)$  is known for some line of response  $(\phi, s) \in \Omega$ , then the emission data determine in a unique way all attenuation factors within  $\Omega$ .

### 2.3 Proofs

#### 2.3.1 Proof of Theorem 1

Consider some line of response  $(\phi, s) \in \Omega$ . Let  $f_1(\vec{x})$  and  $f_2(\vec{x})$  be two tracer distributions and  $\mu_1(\vec{x})$  and  $\mu_2(\vec{x})$  two attenuation images which satisfy

$$m(\phi', s', t) = p_1(\phi', s', t)a_1(\phi', s') = p_2(\phi', s', t)a_2(\phi', s') \quad (2.6)$$

for  $(\phi', s')$  in a neighborhood of  $(\phi, s)$  and  $t \in \mathbb{R}$ . Here  $p_j$  and  $a_j$ ,  $j = 1, 2$  are defined by equations (2.1) and (2.3) with  $f$  and  $\mu$  replaced by  $f_j$  and  $\mu_j$ . To prove theorem 1, we must show that

$$\frac{\partial(\mathcal{R}\mu_2 - \mathcal{R}\mu_1)}{\partial\phi} = \frac{\partial(\mathcal{R}\mu_2 - \mathcal{R}\mu_1)}{\partial s} = 0. \quad (2.7)$$

The noise-free, attenuation corrected, 2D TOF data (2.1) satisfy a range condition defined by the partial differential equation ([59], see [3] for the extension to 3D TOF PET):

$$\mathcal{D}p = t \frac{\partial p}{\partial s} + \frac{\partial p}{\partial \phi} - s \frac{\partial p}{\partial t} + \sigma^2 \frac{\partial^2 p}{\partial s \partial t} = 0. \quad (2.8)$$

For completeness the proof of this property is given in appendix 2.7. Applying the differential operator  $\mathcal{D}$  to  $m$ , and using the fact that (2.8) is satisfied by  $p_1$  and  $p_2$  and that  $a_1$  and  $a_2$  are independent of the TOF variable  $t$ , one obtains the following identity:

$$\mathcal{D}m = p_1(t a_{1,s} + a_{1,\phi}) + \sigma^2 a_{1,s} p_{1,t} = p_2(t a_{2,s} + a_{2,\phi}) + \sigma^2 a_{2,s} p_{2,t} \quad (2.9)$$

where we omit the variables  $(\phi, s, t)$  and the subscript “ $\xi$ ” denotes the partial derivative w.r.t. a variable  $\xi$ , thus,

$$a_{j,s} = \frac{\partial a_j(\phi, s)}{\partial s} \quad a_{j,\phi} = \frac{\partial a_j(\phi, s)}{\partial \phi} \quad p_{j,t} = \frac{\partial p_j(\phi, s, t)}{\partial t} \quad j = 1, 2. \quad (2.10)$$

Defining the functions

$$q_j(\phi, s, t) = p_j(\phi, s, t) \exp(t^2/2\sigma^2) \quad j = 1, 2 \quad (2.11)$$

and their partial derivatives  $q_{j,t} = \partial q_j / \partial t$ , equation (2.9) can be rewritten after multiplication by  $a_2 \exp(t^2/2\sigma^2) > 0$  as,

$$a_2 a_{1,\phi} q_1 + \sigma^2 a_2 a_{1,s} q_{1,t} = a_{2,\phi} a_2 q_2 + \sigma^2 a_{2,s} a_2 q_{2,t}. \quad (2.12)$$

From equation (2.6),  $a_2 q_2 = a_1 q_1$  and  $a_2 q_{2,t} = a_1 q_{1,t}$  (because the functions  $a_j(\phi, s)$  are independent of  $t$ ), and therefore equation (2.12) becomes

$$(a_2 a_{1,\phi} - a_1 a_{2,\phi}) q_1 + \sigma^2 (a_2 a_{1,s} - a_1 a_{2,s}) q_{1,t} = 0 \quad (2.13)$$

or, using  $a_j > 0$  and dividing by  $a_1 a_2$ ,

$$\alpha q_1 + \sigma^2 \beta q_{1,t} = 0 \quad (2.14)$$

with

$$\begin{aligned} \alpha &= \frac{\partial \log(a_1)}{\partial \phi} - \frac{\partial \log(a_2)}{\partial \phi} = \frac{\partial(\mathcal{R}\mu_2 - \mathcal{R}\mu_1)}{\partial \phi}, \\ \beta &= \frac{\partial \log(a_1)}{\partial s} - \frac{\partial \log(a_2)}{\partial s} = \frac{\partial(\mathcal{R}\mu_2 - \mathcal{R}\mu_1)}{\partial s}. \end{aligned} \quad (2.15)$$

For the fixed line of response  $(\phi, s)$  that we are considering, equation (2.14) is an ordinary differential equation (ODE) in  $t$ , which must be satisfied for all  $t \in \mathbb{R}$ .

We first show that  $\beta = 0$ . For, suppose  $\beta \neq 0$ , then the solution of the ODE (2.14) is

$$p_1 = \exp(-t^2/2\sigma^2) q_1 = C \exp\left(-\frac{(t + \alpha/\beta)^2}{2\sigma^2}\right) \quad (2.16)$$

with  $C > 0$  because  $m(\phi, s, t) > 0$ . But comparison with equation (2.1) shows that  $p_1$  defined by equation (2.16) corresponds to a tracer distribution which, along the line  $(\phi, s)$ , is a point source at  $t = -\alpha/\beta$ . This can be verified by noting that the unique solution of the equation

$$C \exp\left(-\frac{(t + \alpha/\beta)^2}{2\sigma^2}\right) = \int_{-\infty}^{\infty} dl f_1(s\hat{u}^\perp + l\hat{u}) \frac{1}{\sqrt{2\pi}\sigma} e^{-(l-t)^2/2\sigma^2} \quad (2.17)$$

is  $f_1(s\hat{u}^\perp + l\hat{u}) = \sqrt{2\pi}\sigma C \delta(l + \alpha/\beta)$ <sup>1</sup>. A point source is contradictory with the assumption that  $f \in C^1$ , and therefore we conclude that  $\beta = 0$ . Equation (2.14) then reduces to  $\alpha q_1 = 0$ , which implies  $\alpha = 0$  because  $q_1 > 0$ . This concludes the proof of theorem 1.

---

<sup>1</sup>This can be seen by taking the 1D Fourier transform w.r.t.  $t$ . Note that since  $\alpha$  and  $\beta$  both change sign when swapping the indices 1 and 2,  $f_2$  is also a point source along that line, at the same location but possibly with another intensity  $C$ .

### 2.3.2 Proof of Corollary 2

From theorem 1, the  $\phi$  and  $s$  derivatives of  $\mathcal{R}\mu$  are determined by the emission data for all LORs within the domain  $\Omega$  defined by equation (2.5). Consider two arbitrary lines of responses  $A = (\phi_a, s_a) \in \Omega$  and  $B = (\phi_b, s_b) \in \Omega$ . From the Lemma in Appendix 2.7, these two lines of response can always be linked by a continuous piece-wise smooth curve  $\mathcal{L}_{AB}$  in the sinogram, defined parametrically by  $(\phi(u), s(u))$ ,  $u \in [0, 1]$  with  $(\phi(0), s(0)) = (\phi_a, s_a)$  and  $(\phi(1), s(1)) = (\phi_b, s_b)$ , and such that  $(\phi(u), s(u)) \in \Omega$  for  $0 \leq u \leq 1$ . Integrating equation (2.7) along  $\mathcal{L}_{AB}$  yields

$$\mathcal{R}\mu_2(\phi, s) - \mathcal{R}\mu_1(\phi, s) = K \quad (2.18)$$

for  $(\phi, s) \in \Omega$  and for some constant  $K$ , or equivalently  $a_2(\phi, s) = e^{-K}a_1(\phi, s)$ . This concludes the proof of Corollary 2. Corollary 3 immediately follows.

### 2.3.3 Remarks

1. Theorem 1 and the two corollaries allow estimating the attenuation factors  $a(\phi, s)$  only within  $\Omega$ , the interior of the support of the emission sinogram, but this is all that is needed to reconstruct the tracer distribution  $f(\vec{x})$ . On the other hand, when the support of the attenuating medium is larger than the support of  $f(\vec{x})$ , reconstructing the attenuation image  $\mu(\vec{x})$  is impossible unless additional information is available.
2. The third hypothesis for theorem 1 limits its applicability to functions  $f$  and  $\mu$  with continuous first derivatives. This condition is not satisfied in general but the PET detectors act as low-pass filters and the data are, therefore, samples of a smoothed function  $p$ . This low-pass filtering is shift variant and it is unlikely that it would preserve the consistency condition. However, the major limitation to the practical accuracy of the method is probably related to the discrete data sampling and to the noise rather than to this differentiability condition.
3. The condition  $m(\phi, s, t) > 0$  defining the region  $\Omega$  where the sinogram gradient can be recovered becomes in practice  $m(\phi, s, t) > \epsilon$ , with  $\epsilon$  some lower bound on the activity along a LOR. Therefore, stability problems are expected for LORs close to the boundary of the support of the sinogram. This problem will be illustrated in section 2.6.
4. According to Corollary 2, the attenuation sinogram is determined by the emission data only up to an additive constant  $K$ . Note, however, that if the support of both the tracer distribution and the attenuation image is the disk of radius  $R$ , the constant sinogram

$$(\mathcal{R}\mu_K)(\phi, s) = \begin{cases} \log(K) & |s| \leq R \\ 0 & |s| > R \end{cases} \quad (2.19)$$

corresponds to an attenuation image

$$\mu_K(\vec{x}) = \begin{cases} \frac{\log(K)}{\pi\sqrt{R^2 - |\vec{x}|^2}} & |\vec{x}| \leq R \\ 0 & |\vec{x}| > R \end{cases} \quad (2.20)$$

This attenuation image is singular at the boundary of the disk and hence does not satisfy assumption 3 in section 2.3. It is likely that an iterative algorithm including a smoothness constraint or an upper bound on the attenuation coefficient would not reach this solution.

5. One way to apply corollary 3 is to add outside the convex hull of the scanned object a small reference object with a known attenuation and activity [83]. The attenuation  $a(s, \phi)$  is then known for any LOR that crosses this reference but does not cross the scanned object, and corollary 3 then allows recovering  $a(s, \phi)$  for all LORs in  $\Omega$ .
6. The proof of theorem 1 can be extended to the case of 3D TOF-PET with a cylindrical scanner. Only a sketch of this extension is given here. Consider a cylindrical scanner of length  $L$  with axis along the vertical axis  $z$ , and two LORs  $A$  and  $B$  which have activity. The LOR  $A$  intersects the detector area (the lateral surface of the cylinder) in two detector points with coordinates  $(x_A^1, y_A^1, z_A^1)$  and  $(x_A^2, y_A^2, z_A^2)$  with  $|z_A^1| \leq L/2$ ,  $|z_A^2| \leq L/2$ . Similarly for  $B$ . The two LORs can be related continuously as follows.
  - a) Applying Theorem 1 within the vertical plane (i.e. parallel to the  $z$ -axis) containing  $A$ , move continuously from  $A$  to its projection  $A_p$  onto the transaxial plane  $z = 0$ .  $A_p$  is the LOR linking the two detector points  $(x_A^1, y_A^1, 0)$  and  $(x_A^2, y_A^2, 0)$ .
  - b) Applying Theorem 1 within the transaxial plane  $z = 0$ , move continuously from  $A_p$  to the projection  $B_p$  of LOR  $B$  onto the transaxial plane  $z = 0$ .  $B_p$  links the two detector points  $(x_B^1, y_B^1, 0)$  and  $(x_B^2, y_B^2, 0)$ . See the lemma in appendix 2.7.
  - c) Applying Theorem 1 within the vertical plane containing  $B$ , move continuously from  $B_p$  to  $B$ .

One easily checks that each step can be achieved involving only intermediate LORs that connect detectors with  $|z| \leq L/2$ , thus belonging to the active area of the cylindrical scanner. For most realistic configurations, all these intermediate LORs have activity and therefore one concludes that the 3D TOF-PET emission data determine, up to a single global constant, the integral of the attenuation image  $\mu$  along all LORs which have activity. Due to the axial truncation of the scanner, the lemma of appendix 2.7 cannot be extended to 3D, and for some non simply connected activity images, several constants may be needed.

## 2.4 Analytic inversion

This section describes an analytic algorithm to estimate the attenuation sinogram from 2D emission TOF data, following essentially the logic of the proof of theorem 1. Using the same notations, consider some line of response  $(\phi, s) \in \Omega$ . The attenuation-corrected data  $m/a$  are consistent and must therefore satisfy equation (2.8). Noting that  $a(\phi, s) \neq 0$  and replacing  $p$  by  $m/a$ , equation (2.8) becomes

$$\begin{aligned} 0 = \mathcal{D} \left( \frac{m(\phi, s, t)}{a(s, \phi)} \right) &= \frac{1}{a(s, \phi)} \mathcal{D}m(\phi, s, t) - \frac{m(\phi, s, t)}{a(s, \phi)^2} \left( t \frac{\partial a(s, \phi)}{\partial s} + \frac{a(s, \phi)}{\partial \phi} \right) \\ &- \frac{\sigma^2}{a(s, \phi)^2} \frac{\partial m(\phi, s, t)}{\partial t} \frac{\partial a(s, \phi)}{\partial s}. \end{aligned} \quad (2.21)$$

Multiplying this equation by  $a(s, \phi)$ , we obtain

$$\begin{aligned} t \frac{\partial m(\phi, s, t)}{\partial s} + \frac{\partial m(\phi, s, t)}{\partial \phi} - s \frac{\partial m(\phi, s, t)}{\partial t} + \sigma^2 \frac{\partial^2 m(\phi, s, t)}{\partial s \partial t} \\ = m(\phi, s, t) \left\{ t \frac{\partial \log a(\phi, s)}{\partial s} + \frac{\partial \log a(\phi, s)}{\partial \phi} \right\} + \sigma^2 \frac{\partial m(\phi, s, t)}{\partial t} \frac{\partial \log a(\phi, s)}{\partial s}. \end{aligned} \quad (2.22)$$

All factors related to  $m$  can be obtained from the data, and therefore we can estimate the two quantities  $\partial \log a(\phi, s)/\partial s = -\partial(\mathcal{R}\mu)(\phi, s)/\partial s$  and  $\partial \log a(\phi, s)/\partial \phi = -\partial(\mathcal{R}\mu)(\phi, s)/\partial \phi$  (see equation (2.3)) by means of a least-square fitting in  $t$ . In practice, this fit is done using the measured TOF interval  $\tau = [t_1, t_2]$ , which should be large enough relative to the object diameter to ensure good stability. Define (the variables  $\phi, s$  are omitted)

$$\begin{aligned} H_{ss} &= \int_{\tau} dt (m t + \sigma^2 m_{,t})^2, \quad H_{s\phi} = \int_{\tau} dt m (m t + \sigma^2 m_{,t}), \quad H_{\phi\phi} = \int_{\tau} dt m^2, \\ J_s &= \int_{\tau} dt (\mathcal{D}m) (m t + \sigma^2 m_{,t}), \quad J_{\phi} = \int_{\tau} dt (\mathcal{D}m) m. \end{aligned} \quad (2.23)$$

Then the unweighted least-square estimate of the derivatives are

$$\frac{\partial(\mathcal{R}\mu)(\phi, s)}{\partial s} = -\frac{J_s H_{\phi\phi} - J_{\phi} H_{s\phi}}{H_{ss} H_{\phi\phi} - H_{s\phi}^2}, \quad \frac{\partial(\mathcal{R}\mu)(\phi, s)}{\partial \phi} = -\frac{J_{\phi} H_{ss} - J_s H_{s\phi}}{H_{ss} H_{\phi\phi} - H_{s\phi}^2}. \quad (2.24)$$

By the Schwarz inequality, the denominator  $H_{ss} H_{\phi\phi} - H_{s\phi}^2$  is non-negative and is zero only if  $m = C(m t + \sigma^2 m_{,t})$  for some constant  $C$  independent of  $t$  (but possibly depending on  $\phi$  and  $s$ ). When this happens, one easily checks from equation (2.23) that the numerators in (2.24) also vanish. This 0/0 undeterminacy only occurs if  $f$  is a point source along this line<sup>2</sup>. Therefore, equation (2.24) can always be calculated except if the LORs only contains a point source.

---

<sup>2</sup>This can be seen from equation (2.17) in the previous section. Note also that in the limit  $\sigma \rightarrow \infty$ , any distribution is essentially a point source relative to the TOF resolution, and in this case undeterminacy also results.

Using equation (2.24) for all LORs  $(\phi, s) \in \Omega$ , we obtain the  $s$  and the  $\phi$  derivatives of the attenuation sinogram  $\mathcal{R}\mu(\phi, s)$ . We are then left with the problem of estimating a function  $\mathcal{R}\mu(\phi, s)$  from a noisy measurement of its gradient  $(\nabla\mathcal{R}\mu)(\phi, s)$  over a domain  $(\phi, s) \in \Omega$ , up to an additive constant. In section 2.6, we use a straightforward discretization of this problem with a two-point finite difference approximation of each component of the gradient. This leads to a set of linear equations with a band-diagonal matrix, which is solved with a simple linear iterative algorithm. Alternative methods exist, see e.g. [84].

Some insight into the meaning of equation (2.22) can be gained by noting that the whole problem is invariant for translation; hence, we can consider the central time bin of a LOR through the origin of the coordinate system, thus setting  $t = s = 0$ . The equation reduces then to

$$\frac{\partial m(\phi, 0, 0)}{\partial \phi} = m(\phi, 0, 0) \frac{\partial \log a(\phi, 0)}{\partial \phi} + \mathcal{O}(\sigma^2) \quad (2.25)$$

This equation reflects the fact that, in the limit of a small time resolution  $\sigma \rightarrow 0$ , the data are simply equal to  $m(\phi, 0, 0) = f(0, 0)a(\phi, 0)$ , and therefore, in this limit the angular variation of the data is equal to the angular variation of the attenuation. The terms in  $\sigma^2$  in equation (2.22) provide the correction that takes into account the finite width of the TOF profile.

## 2.5 Approximate error analysis

Expressions (2.24) for the radial and azimuthal derivatives of the attenuation sinogram are nonlinear functions of the TOF data  $m(\phi, s, t)$ , and an exact analysis of the stability is impractical. We derive an approximate variance estimate by assuming that the major contribution to the variance is due to the error on  $\mathcal{D}m(\phi, s, t)$ . This approximation is justified by the fact that  $\mathcal{D}m(\phi, s, t)$  depends on a second derivative of the data, whereas  $H_{ss}$ ,  $H_{s\phi}$  and  $H_{\phi\phi}$  in equation (2.23) only involve first derivatives of  $m$ . With this approximation, we only need to consider the variance on  $J_s$  and  $J_\phi$ . Assuming that the samples of  $\mathcal{D}m(\phi, s, t)$  are independent random variables with variance  $\epsilon^2$  and that the integrals over  $t$  are discretized with a TOF sampling step  $\Delta_t$ , one has:

$$\begin{aligned} \text{Var} \left( \frac{\partial(\mathcal{R}\mu)(\phi, s)}{\partial s} \right) &\simeq \frac{\Delta_t}{(H_{ss}H_{\phi\phi} - H_{s\phi}^2)^2} \int_{\tau} dt \epsilon^2 \left( (m t + \sigma^2 m_{,t}) H_{\phi\phi} - m H_{s\phi} \right)^2 \\ &\simeq \frac{\Delta_t \epsilon^2}{(H_{ss}H_{\phi\phi} - H_{s\phi}^2)^2} \left( H_{ss}H_{\phi\phi}^2 - 2H_{s\phi}H_{\phi\phi}H_{s\phi} + H_{s\phi}^2H_{\phi\phi} \right) \\ &\simeq \frac{\Delta_t \epsilon^2 H_{\phi\phi}}{H_{ss}H_{\phi\phi} - H_{s\phi}^2} \end{aligned} \quad (2.26)$$

and similarly

$$\text{Var} \left( \frac{\partial(\mathcal{R}\mu)(\phi, s)}{\partial \phi} \right) \simeq \frac{\Delta_t \epsilon^2 H_{ss}}{H_{ss}H_{\phi\phi} - H_{s\phi}^2} \quad (2.27)$$

## 2. TIME-OF-FLIGHT PET DATA DETERMINE THE ATTENUATION SINOGRAM UP TO A CONSTANT

---

Recall that  $\epsilon$  represents the noise on  $\mathcal{D}m(\phi, s, t)$ , which is expected to be larger than the noise on the measured data  $m$  since  $\mathcal{D}$  involves derivatives. Nevertheless, equations (2.26) and (2.27) suggest that the derivatives of the attenuation sinogram can be recovered from the emission TOF data with a good stability for LORs such that  $H_{ss}H_{\phi\phi} - H_{s\phi}^2$  is not too small.

To gain additional insight, consider a LOR along which the activity distribution is a centred Gaussian with standard deviation  $\sigma_f$  and total activity equal to 1. Using equation (2.1) and (2.4) the data is (we omit the  $\phi$  and  $s$  variables):

$$m(t) = \frac{\exp(-t^2/(2(\sigma^2 + \sigma_f^2)))}{\sqrt{2\pi} \sqrt{\sigma_f^2 + \sigma^2}} a \quad (2.28)$$

where  $a = a(\phi, s) = \exp\{-(\mathcal{R}\mu)(\phi, s)\}$ , and hence

$$m(t) t + \sigma^2 m_{,t}(t) = \frac{t \sigma_f^2 \exp(-t^2/(2(\sigma^2 + \sigma_f^2)))}{\sqrt{2\pi} (\sigma_f^2 + \sigma^2)^{3/2}} a. \quad (2.29)$$

Inserting this into (2.23) and integrating over  $\tau = (-\infty, +\infty)$  yields

$$H_{ss} = \frac{\sigma_f^4}{4\sqrt{\pi} (\sigma_f^2 + \sigma^2)^{3/2}} a^2, \quad H_{s\phi} = 0, \quad H_{\phi\phi} = \frac{1}{2\sqrt{\pi} (\sigma_f^2 + \sigma^2)^{1/2}} a^2 \quad (2.30)$$

and from (2.26),

$$\text{Var}\left(\frac{\partial(\mathcal{R}\mu)(\phi, s)}{\partial s}\right) \simeq \frac{4\Delta_t \epsilon^2 \sqrt{\pi} (\sigma_f^2 + \sigma^2)^{3/2}}{\sigma_f^4} a^{-2}. \quad (2.31)$$

For this simple example, the variance on the radial derivative of the attenuation sinogram increases as  $\sigma^3$ , when the TOF resolution is larger than the object size ( $\sigma \gg \sigma_f$ ), and decreases down to a constant when  $\sigma \ll \sigma_f$ . In the limit of a point like object  $\sigma_f \rightarrow 0$ , the variance becomes infinite as expected from the proof in section 2.3.

## 2.6 Numerical example

A 2D TOF simulation experiment was performed to illustrate the method and to obtain a first assessment of its stability to noise. In this experiment, the gradient of the attenuation sinogram  $\mathcal{R}\mu$  is estimated from the TOF emission data using equation (2.24). Several methods could be used to estimate the attenuation sinogram from its gradient. In this study, we have used the iterative Landweber algorithm. Finally, to determine the additive constant (see equation (2.18)), we assume that the image can be segmented to impose the known attenuation coefficient to a region containing (mostly) tissue.

### 2.6.1 The software phantom

Figure 2.1 shows the true activity and attenuation distributions. The diameter of the field of view was 40 cm. The TOF-resolution profile was Gaussian with a full-width at half maximum (FWHM) of 500 ps, corresponding to a spatial FWHM of 7.5 cm. The attenuation coefficients were 0.095/cm for tissue, 0.0317/cm for lung,



Figure 2.1: Activity  $f$  (left) and attenuation  $\mu$  (right) images of the simulated phantom. The image size is 40 cm  $\times$  40 cm, the simulated TOF resolution was 7.5 cm FWHM.

0.142/cm for bone and 0/cm for air. To generate the data, the activity and the attenuation images were sampled on a  $384 \times 384$  grid (pixel size of 0.104 cm), and forward projected to obtain sinograms of 128 angular samples over  $180^\circ$ , 384 uniform radial samples and 128 TOF-bins. The attenuation image was forward-projected using Joseph's method. The activity image was forward-projected with a TOF-PET projector implemented by rotating the image for each angle  $\phi$  such that the LORs are parallel to the columns, and then convolving the image with the 1D Gaussian TOF-kernel.

Prior to estimation of the attenuation sinogram, the simulated TOF data were rebinned to  $128 \times 128 \times 128$  bins with pixel size  $\Delta_\phi = 1.4^\circ$  along  $\phi$ ,  $\Delta_s = 0.3125$  cm along  $s$  and  $\Delta_t = 0.3125$  cm along  $t$ . The attenuation sinogram was reconstructed into a  $128 \times 128$  image grid with pixel size of 0.3125 cm.

### 2.6.2 Estimating the gradient of the attenuation sinogram

We observed that noise propagation can be strongly reduced by a moderate smoothing of the attenuated emission sinogram in three dimensions. The noise-free and the noisy data were all smoothed with a Gaussian kernel of 2 pixels FWHM along  $s$  (0.625 cm) and along  $\phi$  ( $2.8^\circ$ ) and 0.7 times the TOF-FWHM along  $t$  (5.25 cm). The latter smoothing was taken into account by increasing the value of  $\sigma$  accordingly in the subsequent calculations, as  $\sigma^2 = \sigma_{TOF}^2 + (0.7 \times \sigma_{TOF})^2$ . The derivatives along  $\phi$ ,  $s$  and  $t$  were approximated as finite differences, and the integrals over  $t$  in equation (2.23) were approximated as a Riemann sum. Straightforward implementation of (2.24) then yields estimates of the derivatives of the attenuation sinogram. Results for a simulation without and with noise are shown in figures 2.2 and 2.3, respectively. For the simulation with noise, the highest expected count (Poisson mean) was 3.7 photons in the attenuated TOF-sinogram, and in the corresponding TOF-integrated

## 2. TIME-OF-FLIGHT PET DATA DETERMINE THE ATTENUATION SINOGRAM UP TO A CONSTANT

---

sinogram (i.e. the non-TOF sinogram shown in figure 2.3) the maximum expected count was 132 photons.

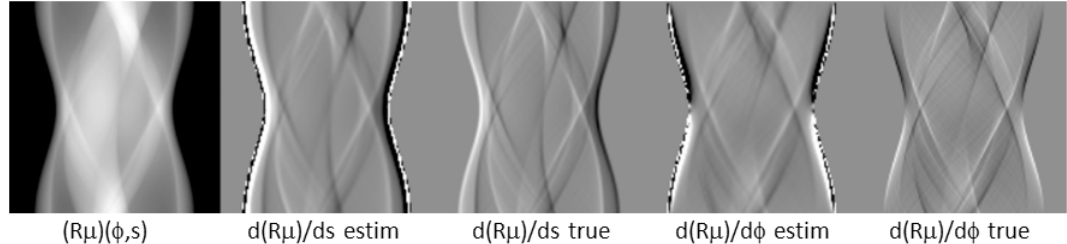


Figure 2.2: Reconstruction from noise free TOF emission data. The attenuation sinogram  $\mathcal{R}\mu$  is shown at the left. The subsequent images show the estimated and true radial and angular derivatives of  $\mathcal{R}\mu$ .

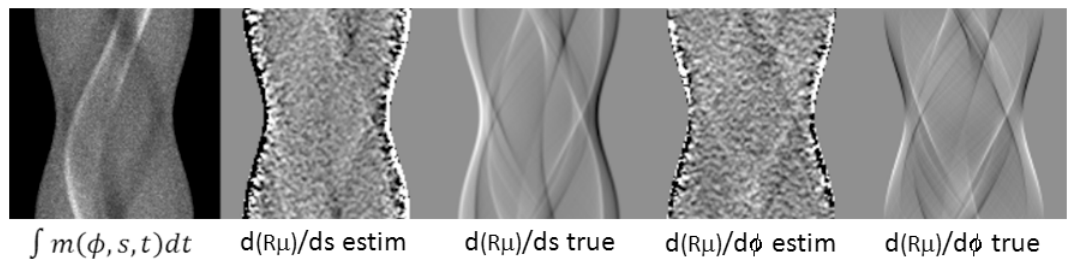


Figure 2.3: Reconstruction from noisy TOF emission data. The TOF-integrated noisy emission sinogram is shown at the left. The subsequent images show the estimated and true radial and angular derivatives of  $\mathcal{R}\mu$ .

### 2.6.3 Estimating the attenuation sinogram from its gradient

As illustrated in figure 2.2 and 2.3, the estimates of the derivatives are inaccurate near the boundaries of the object, even in the absence of noise. This is expected from the discussion in the previous sections because these LORs have vanishing activity as one approaches the boundary. To identify these unreliable estimates, the maximum of the absolute values is computed in a central region of the derivative sinograms. All pixels with an absolute value exceeding this maximum are excluded from the subsequent calculations, together with their four nearest neighbors along the same row  $\phi$ . This heuristic approach eliminated most of the unreliable values from contributing to the final estimate. For the example in figures 2.2 and 2.3 (second and fourth columns), the excluded pixels correspond to the totally white and black pixels, which are all located close to the boundaries of the sinogram.

An iterative Landweber algorithm is applied to estimate the attenuation sinogram  $\mathcal{R}\mu$  from its derivatives. We denote by  $R_s$  and  $R_\phi$  the sampled  $128 \times 128$  derivative sinograms estimated previously based on (2.24), and rescaled by the corresponding sampling intervals so that  $R_s \simeq \Delta_s \partial \mathcal{R}\mu / \partial s$  and  $R_\phi \simeq \Delta_\phi \partial \mathcal{R}\mu / \partial \phi$ . We denote by

$S^k$  the estimate of the attenuation sinogram  $\mathcal{R}\mu$  at the  $k^{th}$  iteration. The algorithm updates the estimate as

$$S^0 = 0 \quad (2.32)$$

$$S^{k+1} = S^k + \omega\alpha_s M_s D_s^*(R_s - D_s S^k) + \omega\alpha_\phi M_\phi D_\phi^*(R_\phi - D_\phi S^k) \quad (2.33)$$

where  $D_\xi$  is the discrete approximation of the derivative with respect to  $\xi = s, \phi$ . We implemented  $D_\xi$  as a convolution with  $[-1/2, 0, 1/2]$  along  $\xi = s, \phi$ . The adjoint operator  $D_\xi^*$  is the convolution with  $[1/2, 0, -1/2]$  along  $\xi$ . The diagonal matrix  $M_s$  selects the reliable pixels from  $R_s$  as described above, and similar for  $M_\phi$ . Finally, the parameters  $\alpha_s > 0$  and  $\alpha_\phi > 0$  define the relative weight given to the radial and azimuthal derivatives, and  $\omega$  is a relaxation factor. To ensure convergence of the Landweber iteration [85], the relaxation factor should be in the interval  $(0, 2/L)$ , where  $L$  is the largest eigenvalue of the matrix  $A = \alpha_s D_s^* D_s + \alpha_\phi D_\phi^* D_\phi$ . Ignoring subtleties near the image boundary, this matrix is circulant and corresponds to a 2D convolution with the kernel

$$\begin{pmatrix} \dots & 0 & 0 & 0 & 0 & 0 & 0 & 0 & \dots \\ \dots & 0 & 0 & 0 & -\alpha_\phi/4 & 0 & 0 & 0 & \dots \\ \dots & 0 & 0 & 0 & 0 & 0 & 0 & 0 & \dots \\ \dots & 0 & -\alpha_s/4 & 0 & \alpha_s/2 + \alpha_\phi/2 & 0 & -\alpha_s/4 & 0 & \dots \\ \dots & 0 & 0 & 0 & 0 & 0 & 0 & 0 & \dots \\ \dots & 0 & 0 & 0 & -\alpha_\phi/4 & 0 & 0 & 0 & \dots \\ \dots & 0 & 0 & 0 & 0 & 0 & 0 & 0 & \dots \end{pmatrix} \quad (2.34)$$

The eigenvalues of a circulant  $n \times n$  matrix with elements  $c_k$  are given by [86]:

$$\text{eigenvalue}_m = \sum_k c_k e^{-2\pi i m k / n}, \quad \text{with } i = \sqrt{-1}, \quad m = 0, \dots, n-1 \quad (2.35)$$

It follows that the magnitude of the largest eigenvalue of  $D_s^* D_s$  and of  $D_\phi^* D_\phi$  does not exceed 1; therefore, the largest eigenvalue of  $A$  does not exceed  $\alpha_s + \alpha_\phi$ . The results shown in this paper were obtained with 5000 iterations,  $\alpha_s = \alpha_\phi = 1$  and  $\omega = 1/2$ .

The estimated sinogram  $S$  has an arbitrary offset  $K$ , which can only be estimated if prior knowledge is available. We assume here that a first reconstruction  $F_S^0$  is made, that  $F_S^0$  can be segmented, and that one has some prior knowledge about the attenuation coefficient(s) in some of the segmented regions. The value of  $K$  can then be estimated by imposing the known attenuation coefficient(s) (for instance in a least squares sense). Here this was done by using a unit non-TOF sinogram  $S_1$  (which is set to 1 for all LORs that have some activity in the original sinogram and zero elsewhere) and its reconstruction  $F_1$ . The offset  $K$  is then obtained by requiring that the image  $F_S^0 + KF_1$  satisfies the prior knowledge about the attenuation.

In this experiment, we used as prior knowledge the attenuation coefficient of tissue and used simple thresholding to obtain a region containing mostly tissue and bone. We forced the median value of that region to the attenuation of tissue. The reconstructions were made with filtered backprojection (FBP). These reconstructions

## 2. TIME-OF-FLIGHT PET DATA DETERMINE THE ATTENUATION SINOGRAM UP TO A CONSTANT

---

are less accurate closer to the object boundary, because of the increasing contribution of the unreliable boundary values during application of the ramp filter. Attenuation sinograms estimated with this approach are shown in figure 2.4 for simulations with no, moderate, and high noise. The first two correspond to the results shown in figures 2.2 and 2.3, respectively. In the last simulation, the maximum noise-free count in the TOF-sinogram was 1.23 photons. The maximum in the corresponding non-TOF sinogram was 44.1 photons. Figure 2.5 shows a horizontal profile through the four sinograms of figure 2.4. Note that estimating  $K$  from the reconstructions created some bias in the sinograms, because of the reconstruction errors near the boundary of the object.

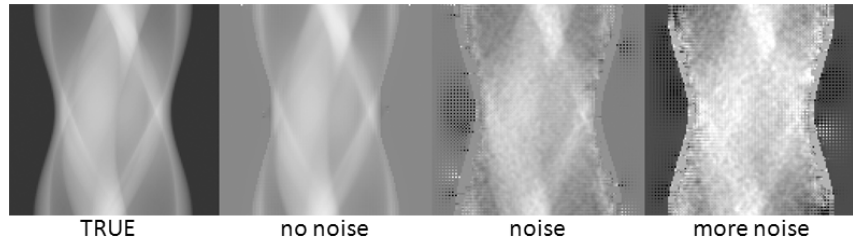


Figure 2.4: The true and estimated attenuation sinograms for the cases with no, moderate and high noise.

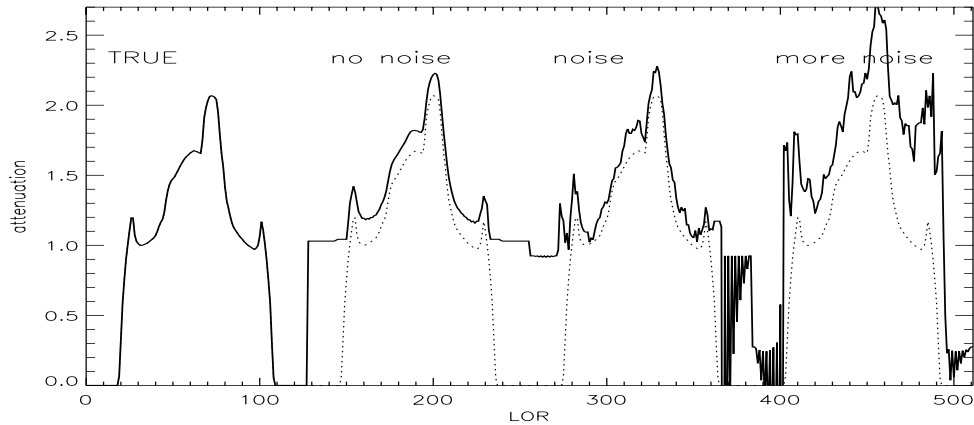


Figure 2.5: Horizontal profiles through the sinograms shown in figure 2.4 (mean of 6 rows around row 25 (of 128)). The dashed curve is the true profile, the solid curves show the true profile and the profiles through the noise-free and two noisy sinograms.

We also present in figure 2.6 the reconstructions of the attenuation image to illustrate the performance of the method. However, as mentioned before, no reconstruction of the attenuation image is needed for PET attenuation correction. For comparison, reference images are shown as well, which were obtained from the attenuated emission sinogram by assuming that the true activity distribution (figure 2.1)

was known. In that case, the reconstruction problem reduces to that in transmission tomography. These reference CT reconstructions were made with FBP, and with a maximum-likelihood algorithm [75] dedicated to transmission tomography. We have applied smoothing to the two FBP and MLTR reference images to obtain a resolution similar to that obtained with the new algorithm.

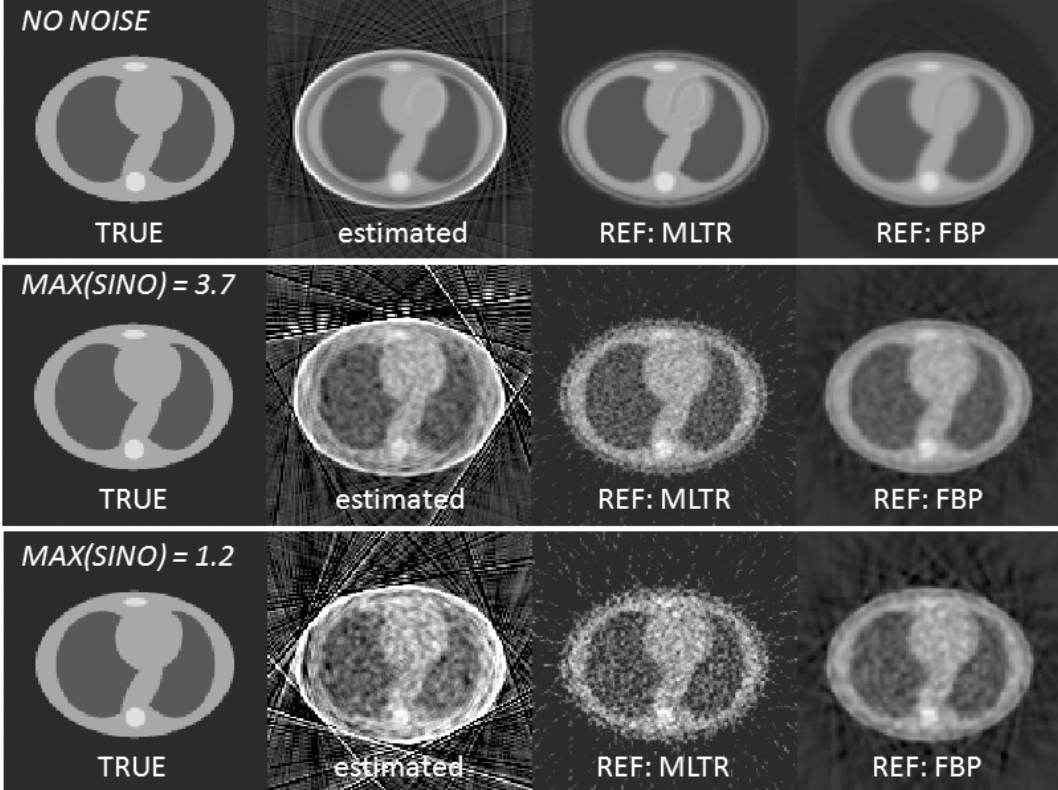


Figure 2.6: Reconstructions of the attenuation image from simulated data without noise (top row), with noise (middle row), and with more noise (bottom row). From left to right: the true attenuation image, the image estimated by the analytical method of section IV, and the references images reconstructed with the maximum-likelihood MLTR algorithm [75] and with FBP. These reference images were computed from the TOF-integrated attenuated emission sinogram, assuming that the true activity distribution was known.

Small residual cross-talk from the activity in the heart is visible in the three noise-free reconstructions of the attenuation image in figure 2.6; this is tentatively attributed to the use of different projectors for simulation and reconstruction. Figure 2.6 also shows that the accuracy of the reconstructions is lower in the neighbourhood of the phantom external boundary. This is true even for the two reference CT reconstructions because they use as “blank” scan the (assumed known) unattenuated emission sinogram, which has low values in the LORs tangent to the phantom boundary.

## 2.7 Conclusion

The main contribution of this paper is to show that when time-of-flight information is available, the joint estimation of attenuation and activity from a PET emission sinogram has a unique solution, except for a constant. The proof of this property suggested an analytical method to estimate the attenuation sinogram, which is local in the sense that the derivatives of the attenuation sinogram for a given line of response are calculated using only neighboring lines of response. The implementation of the analytic method for simulated data demonstrates that theorem 1 is not only a theoretical result but has a practical impact.

As expected, equation (2.31) shows that the variance on the estimated derivative sinograms reaches its asymptotic minimal value for perfect TOF resolution. However, at least for a Gaussian object, the variance is only 10% higher than this asymptotic value when the width of the object is four times larger than the width of the TOF kernel. That indicates that with current state-of-the-art TOF systems, good results are expected for clinical applications.

How to optimally extract the information from the time-of-flight data is still an open question. The analytic method was applied here for illustration and validation, but it is likely that iterative algorithms will lead to significantly superior results, on the one hand by modeling the Poisson nature of the noise, and on the other hand by exploiting any available additional information on the attenuation image. It remains to be seen whether the analytic method might be useful to provide an initial estimate and thereby reduce the required number of iterations. In [57] a method based on a maximum-likelihood approach is proposed and evaluated with 2D simulations. The results of that study also indicate that TOF stabilizes the joint estimation problem, even in the presence of noise.

This paper deals with 2D PET data. At the end of section 2.2, we showed how the proof of uniqueness can be extended to 3D TOF PET by applying theorem 1 separately within a sequence of axial and transaxial planes. However, a direct analytical implementation of this approach is unlikely to be optimal, and future work is ongoing to derive a 3D algorithm to efficiently estimating the 4D gradient of the attenuation sinogram.

## Acknowledgements

This work is supported by the grant G.0569.08 of the Fonds voor Wetenschappelijk Onderzoek Vlaanderen (F.W.O), and by a GOA-project from KU Leuven. The authors thank Girish Bal, Mike Casey, Maurizio Conti, Christian Michel, Vladimir Panin and Charles Watson (Siemens Healthcare, Molecular Imaging, Knoxville, TN) for useful discussions.

## Appendix 1

To prove (2.8), use  $dw(t)/dt = -tw(t)/\sigma^2$ ,  $d\hat{u}^\perp/d\phi = \hat{u}$  and  $d\hat{u}/d\phi = -\hat{u}^\perp$  to rewrite the LHS as

$$\begin{aligned} & \int_{-\infty}^{\infty} dl w(t-l) \left\{ t\hat{u}^\perp \cdot \nabla f + s\hat{u} \cdot \nabla f - l\hat{u}^\perp \cdot \nabla f + s\frac{(t-l)}{\sigma^2}f - \sigma^2\frac{(t-l)}{\sigma^2}\hat{u}^\perp \cdot \nabla f \right\} \\ &= \int_{-\infty}^{\infty} dl w(t-l) \left\{ s\hat{u} \cdot \nabla f + s\frac{(t-l)}{\sigma^2}f \right\} = s \int_{-\infty}^{\infty} dl \frac{d}{dl}(w(t-l)f) = 0 \end{aligned} \quad (2.36)$$

where the argument of  $f$  is everywhere as in equation (2.1).

## Appendix 2

*Lemma.* Consider the 2D Radon transform  $p(\phi, s)$  of some non-negative smooth function  $f(\vec{x})$ , and two lines of response  $A$  and  $B$  such that  $p(A) \neq 0$  and  $p(B) \neq 0$ . Then  $A$  and  $B$  can be linked by a continuous piece-wise smooth curve  $(\phi(u), s(u))$  in the sinogram, parametrized by a real parameter  $u \in [0, 1]$  and such that  $(\phi(0), s(0)) = A$  and  $(\phi(1), s(1)) = B$ , and such that  $p(\phi(u), s(u)) > 0$  for  $0 \leq u \leq 1$ .

*Proof.* Since  $p(A) \neq 0$ , there is at least one point  $a \in A$  such that  $f(a) > 0$ . Similarly, take some point  $b \in B$  such that  $f(b) > 0$ . The curve is defined as follows: first rotate line of response  $A$  around point  $a$  until it contains both  $a$  and  $b$ . Since all these lines contain  $a$ , and  $f(a) > 0$  and  $f$  is smooth, one has that  $p > 0$  for all these lines. Next, rotate the line of response around  $b$  until it coincides with  $B$ . Again,  $p$  remains strictly positive during this rotation because  $f(b) > 0$ .



## Chapter 3

# Simultaneous Reconstruction of Activity and Attenuation in Time-of-Flight PET

A. Rezaei, M. Defrise, G. Bal, C. Michel, M. Conti, C. Watson, and J. Nuyts,  
“Simultaneous Reconstruction of Activity and Attenuation in Time-of-Flight PET”,  
*IEEE Transactions on Medical Imaging*, vol. 31, no. 12, pp. 2224–2233, Dec. 2012

## Abstract

In positron emission tomography (PET) and single photon emission tomography (SPECT), attenuation correction is necessary for quantitative reconstruction of the tracer distribution. Previously, several attempts have been undertaken to estimate the attenuation coefficients from emission data only. These attempts had limited success, because the problem does not have a unique solution, and severe and persistent “cross-talk” between the estimated activity and attenuation distributions was observed. In this paper, we show that the availability of TOF information eliminates the cross-talk problem by destroying symmetries in the associated Fisher information matrix. We propose a maximum-a-posteriori reconstruction algorithm for jointly estimating the attenuation and activity distributions from TOF PET data. The performance of the algorithm is studied with 2D simulations, and further illustrated with phantom experiments and with a patient scan. The estimated attenuation image is robust to noise, and does not suffer from the cross-talk that was observed in non-TOF PET. However, some constraining is still mandatory, because the TOF data determine the attenuation sinogram only up to a constant offset.

### 3. SIMULTANEOUS RECONSTRUCTION OF ACTIVITY AND ATTENUATION IN TIME-OF-FLIGHT PET

---

#### 3.1 Introduction

In nuclear medicine tomographic imaging (positron emission tomography (PET) and single photon emission tomography (SPECT)), a quantitative and artifact-free reconstruction of the tracer distribution can only be obtained if an accurate correction for the photon attenuation in the body of the patient is applied. The attenuation correction factors can be obtained from transmission measurements with radioactive sources, or be derived from well-aligned CT images [2], [17], [87]. Since both approaches have their limitations, several groups have attempted to jointly estimate the activity and attenuation images from the emission data only [25], [27], [28], [39], [41], [43], [45], [47], [48]. These attempts were based on the use of analytical consistency conditions, discrete consistency conditions and (penalized) maximum likelihood methods. Although some useful results have been obtained, the results have generally been disappointing. Nearly all studies report the so-called cross-talk problem, where localized errors in the activity image are compensated by localized errors in the attenuation image. This seems to be a fundamental problem. In the maximum-likelihood approach, the problem is manifested as the presence of local maxima in the likelihood function. However, in cases where incomplete information about the attenuation coefficients is available, these methods can be used to estimate the missing information, which is a less ill-posed problem than estimating the entire attenuation image [56], [88], [89].

Time-of-flight (TOF) Positron Emission Tomography (PET) was studied in the 1980's, but its implementation as a clinical instrument was too challenging at the time. Thanks to recent advances in electronics and in scintillation research, TOF PET has now been introduced in commercial systems [10], [13], [90]–[92]. The use of TOF information results in faster convergence of iterative reconstruction algorithms [11] and in an improved contrast-to-noise ratio [10], [12]. Moreover, recent studies have shown that in TOF PET, the artifacts induced by attenuation correction errors are less severe than in non-TOF PET [13]. This finding indicates that TOF PET data contain information about attenuation factors, that is not present in non-TOF PET data, justifying a study of the joint estimation problem in TOF PET.

In this paper, the simultaneous reconstruction of the activity and attenuation from TOF PET projections is studied as a maximum-likelihood problem, building on previous work for non-TOF emission computed tomography [47], [89]. In the following section this algorithm, Maximum Likelihood Activity and Attenuation estimation (MLAA), is briefly described. An analysis of the Fisher information matrix gives an intuitive explanation why local maxima in the form of cross-talk are a problem in non-TOF systems and why the use of TOF information eliminates this problem. However, the possible presence of other local maxima in the TOF likelihood needs further investigation. It is found that even with TOF PET the problem is still under-determined, i.e., TOF PET data determine the activity image up to a constant factor and the attenuation sinogram up to a (related) constant term. In the following section, some 2D simulation experiments are described and the results are presented. A 2D small scale simulation experiment was done to study the features of the Fisher matrix. 2D TOF PET simulations of a thorax phantom were done

to study MLAA reconstructions with respect to the visual quality as a function of the TOF resolution, the constant factor/term and noise propagation. The stability of TOF-MLAA is studied numerically by starting the algorithms from a series of different initial images, including images containing cross-talk from the non-TOF MLAA reconstructions. The thorax phantom is also used to study bias and variance properties in a tissue region for MLEM and MLAA reconstructed emission images for multiple noise realizations. The method was applied to fully 3D TOF PET phantom scans and a patient scan, acquired on a commercial TOF PET system. Finally, the results of these 2D and 3D experiments are discussed in section IV.

## 3.2 Theory and methods

### 3.2.1 MLAA

In TOF PET, the expected count  $\bar{y}_{it}$  for line of response (LOR)  $i$  and time difference  $t$  can be expressed as follows:

$$\bar{y}_{it} = \sum_{j=1}^J c_{ijt} \lambda_j e^{-\sum_k l_{ik} \mu_k} + s_{it} \quad (3.1)$$

where  $\lambda_j$  and  $\mu_k$  are the activity and attenuation coefficient at voxel  $j$  and  $k$  respectively,  $J$  is the total number of voxels,  $c_{ijt}$  is the sensitivity of the detector at  $(i, t)$  for activity in  $j$  in absence of attenuation,  $l_{ik}$  is the intersection length of LOR  $i$  with voxel  $k$ , and  $s_{it}$  is the expected contribution of scatter and/or randoms. Assuming that the data are Poisson distributed, the log-likelihood function can be written as

$$L(\theta, y_{it}) = \sum_{it} y_{it} \ln \bar{y}_{it} - \bar{y}_{it} \quad (3.2)$$

where  $y_{it}$  is the measured count at  $(i, t)$  and  $\theta = [\lambda^T, \mu^T]^T$  is the set of  $2J$  parameters that has to be estimated. Note that summation over the TOF index ( $t$ ) yields the corresponding non-TOF values, which are denoted by omitting the index  $t$ :  $\sum_t c_{ijt} = c_{ij}$ ,  $\sum_t y_{it} = y_i$  and  $\sum_t s_{it} = s_i$ .

The MLAA algorithm uses an interleaved updating: in every iteration first the activity is updated keeping the attenuation coefficients constant, and then vice versa. This can be written as follows:

$$\forall i : a_i^h = e^{-\sum_j l_{ij} \mu_j^h} \quad (3.3)$$

$$\forall j : \lambda_j^{h+1} = \frac{\lambda_j^h}{\sum_{it} a_i^h c_{ijt}} \sum_{it} a_i^h c_{ijt} \frac{y_{it}}{\sum_\xi a_i^h c_{i\xi t} \lambda_\xi^h + s_{it}} \quad (3.4)$$

$$\forall i : \psi_i^h = a_i^h \sum_{jt} c_{ijt} \lambda_j^{h+1} \quad (3.5)$$

### 3. SIMULTANEOUS RECONSTRUCTION OF ACTIVITY AND ATTENUATION IN TIME-OF-FLIGHT PET

---

$$\forall j : \mu_j^{h+1} = \mu_j^h + \frac{\sum_i l_{ij} \frac{\psi_i^h}{\psi_i^h + s_i} (\psi_i^h + s_i - y_i)}{\sum_i l_{ij} \frac{(\psi_i^h)^2}{\psi_i^h + s_i} \sum_\xi l_{i\xi}} \quad (3.6)$$

where the superscript  $h$  denotes the iteration number. The non-TOF sinogram  $a^h$  represents the attenuation computed from the current estimate  $\mu^h$ , and the non-TOF sinogram elements  $\psi_i^h$  represent the expected TOF-integrated count for LOR  $i$ , but without the additive contribution  $s_i$ . Expression (3.4) is a standard Maximum Likelihood Expectation Maximization (MLEM) iteration [93], which makes explicit use of the TOF PET data. Expression (3.6) is the Maximum Likelihood for Transmission tomography (MLTR) update [94], [95], which only uses the TOF-integrated data. Note that the sinogram with elements  $\sum_{jt} c_{jxt} \lambda_j^{h+1}$  plays the role of the blank scan, while the TOF integrated data  $y_i$  are treated as the transmission scan.

Both MLEM and MLTR can be accelerated with ordered subsets. Furthermore, because the TOF information improves convergence of MLEM but not that of MLTR, we typically cycle through the subsets faster for the MLTR updates (using the same subsets definition for both). Thus, for every MLEM update  $N \geq 1$  MLTR updates are done, and when all projections have contributed once to the activity updates, they have contributed  $N$  times to the attenuation updates. This decreases the processing time considerably, also because the MLTR updates only involve non-TOF projections and backprojections. Unless otherwise stated,  $N = 5$ .

#### 3.2.2 The curvature of the likelihood

In [58] it has been shown that for TOF PET, the joint estimation problem has a unique solution, except for a constant scale factor. However, this result does not exclude the existence of local maxima in the TOF likelihood function. Convergence to a global maximum would be guaranteed provided that the matrix of second derivatives of the TOF likelihood with respect to the complete parameter space,  $\theta$ , were negative definite. Although the log-likelihood function is known to be concave with respect to  $\lambda$  or  $\mu$ , so far we have not been able to prove concavity with respect to  $\theta$ .

If the algorithm is started with initial images sufficiently close to the true solution, then any gradient ascent algorithm should converge to the global maximum of the likelihood, even in the presence of (distant) local maxima. Therefore, it is meaningful to study the stability of the ML-algorithm close to the true solution. This stability is determined by the curvature of the likelihood. In the following, we study that curvature for both TOF and non-TOF systems. It is shown that close to the true solution, other possible solutions still exist for the non-TOF case (commonly referred to as cross-talk) whereas these solutions are eliminated with the introduction of TOF information.

In our analysis we ignore the non-negativity constraint and the scatter/randoms contributions, assume the likelihood has been maximized and then look for a small

change  $\Delta\theta$  that does not change the gradient of the likelihood. If such a  $\Delta\theta$  can be found, then both  $\theta$  and  $\theta + \Delta\theta$  maximize the likelihood, implying that the problem is under-determined. A small  $\Delta\theta$  does not change the gradient of the likelihood if it satisfies the following equation:

$$\sum_k \frac{\partial^2 L}{\partial \theta_j \partial \theta_k} \Delta\theta_k = 0, \quad j = 0, \dots, 2J \quad (3.7)$$

Since we are at the likelihood maximum, we make the approximation that the second derivative of the likelihood can be replaced by its expectation, equal to minus the Fisher information matrix (FIM) [96], [97]. Equation 3.7 then becomes:

$$F\Delta\theta = 0 \quad (3.8)$$

where,  $F$  is the  $2J \times 2J$  FIM and  $\Delta\theta$  is the  $2J \times 1$  matrix representing the change in the parameter space.

Replacing  $\theta$  with  $[\lambda^T, \mu^T]^T$ , the Fisher information matrix can be rewritten in a quadrant form as follows

$$\begin{aligned} F &= -E\left[\frac{\partial^2 L}{\partial \theta \partial \theta}\right] \\ &= \begin{pmatrix} -E\left[\frac{\partial^2 L}{\partial \lambda \partial \lambda}\right] & -E\left[\frac{\partial^2 L}{\partial \lambda \partial \mu}\right] \\ -E\left[\frac{\partial^2 L}{\partial \mu \partial \lambda}\right] & -E\left[\frac{\partial^2 L}{\partial \mu \partial \mu}\right] \end{pmatrix} = \begin{pmatrix} F_{\lambda\lambda} & F_{\lambda\mu} \\ F_{\lambda\mu}^T & F_{\mu\mu} \end{pmatrix} \end{aligned} \quad (3.9)$$

where  $E$  is the expectation operator and for all  $j, k = 1, \dots, J$  combinations,

$$-E\left[\frac{\partial^2 L}{\partial \lambda_j \partial \lambda_k}\right] = \sum_{i,t} \frac{c_{ijt} c_{ikt}}{\bar{y}_{it}} e^{-2 \sum_\xi l_{i\xi} \mu_\xi} \quad (3.10)$$

$$-E\left[\frac{\partial^2 L}{\partial \mu_j \partial \mu_k}\right] = \sum_{i,t} l_{ij} \bar{y}_{it} l_{ik} = \sum_i l_{ij} \bar{y}_i l_{ik}, \quad (3.11)$$

$$\begin{aligned} -E\left[\frac{\partial^2 L}{\partial \lambda_j \partial \mu_k}\right] &= -\sum_{i,t} c_{ijt} l_{ik} e^{-\sum_\xi l_{i\xi} \mu_\xi} \\ &= -\sum_i c_{ij} l_{ik} e^{-\sum_\xi l_{i\xi} \mu_\xi}. \end{aligned} \quad (3.12)$$

Replacing  $\Delta\theta$  with  $[\Delta\lambda^T, \Delta\mu^T]^T$ , (3.8) becomes

$$\begin{pmatrix} F_{\lambda\lambda} & F_{\lambda\mu} \\ F_{\lambda\mu}^T & F_{\mu\mu} \end{pmatrix} \begin{pmatrix} \Delta\lambda \\ \Delta\mu \end{pmatrix} = 0 \quad (3.13)$$

$F_{\lambda\lambda}$  is expected to be invertible, because the reconstruction of the activity is fairly stable when the attenuation is fixed. If  $F_{\lambda\lambda}$  is indeed invertible, then  $\Delta\lambda$  can be eliminated, yielding

$$(F_{\mu\mu} - F_{\lambda\mu}^T F_{\lambda\lambda}^{-1} F_{\lambda\mu}) \Delta\mu = 0. \quad (3.14)$$

### 3. SIMULTANEOUS RECONSTRUCTION OF ACTIVITY AND ATTENUATION IN TIME-OF-FLIGHT PET

---

In the following, we show that for non-TOF systems, and in particular near the center of uniform objects, the operators  $F_{\mu\mu}$ ,  $F_{\lambda\mu}$  and  $F_{\lambda\lambda}$  are all very similar, such that the equation is expected to be (almost) satisfied for many possible local changes  $\Delta\mu$ . The corresponding  $\Delta\lambda$  that results in cross-talk can be computed from (3.13). The incorporation of TOF information changes the operator  $F_{\lambda\lambda}$ , such that (3.14) no longer has solutions for local changes  $\Delta\mu$ .

Inserting (3.10)-(3.12) into (3.13) yields

$$\begin{aligned} \sum_{kit} \frac{c_{ijt}c_{ikt}}{\bar{y}_{it}} e^{-2\sum_{\xi} l_{i\xi}\mu_{\xi}} \Delta\lambda_k &= \sum_{ki} c_{ij}l_{ik} e^{-\sum_{\xi} l_{i\xi}\mu_{\xi}} \Delta\mu_k \\ \sum_{ki} l_{ij}c_{ik} e^{-\sum_{\xi} l_{i\xi}\mu_{\xi}} \Delta\lambda_k &= \sum_{ki} \bar{y}_i l_{ij}l_{ik} \Delta\mu_k \end{aligned} \quad (3.15)$$

For the non-TOF case, the TOF index  $t$  must be dropped, and the first equation in (3.15) becomes:

$$\sum_{ki} \frac{c_{ij}c_{ik}}{\bar{y}_i} e^{-2\sum_{\xi} l_{i\xi}\mu_{\xi}} \Delta\lambda_k = \sum_{ki} c_{ij}l_{ik} e^{-\sum_{\xi} l_{i\xi}\mu_{\xi}} \Delta\mu_k$$

The coefficients  $c_{ij}$  and  $l_{ij}$  both represent the contribution of pixel  $j$  to the acquisition along LOR  $i$  and should have very similar values. Assuming they are identical except for a factor (which can be absorbed in  $\lambda$  or  $\mu$  by changing the units), the non-TOF equations become:

$$\begin{aligned} \sum_i l_{ij} \frac{e^{-\sum_{\xi} l_{i\xi}\mu_{\xi}}}{\bar{y}_i} \sum_k l_{ik} (e^{-\sum_{\xi} l_{i\xi}\mu_{\xi}} \Delta\lambda_k - \bar{y}_i \Delta\mu_k) &= 0 \\ \sum_i l_{ij} \sum_k l_{ik} (e^{-\sum_{\xi} l_{i\xi}\mu_{\xi}} \Delta\lambda_k - \bar{y}_i \Delta\mu_k) &= 0 \end{aligned} \quad (3.16)$$

An extreme case is obtained when the attenuation corrected counts  $\bar{y}_i e^{\sum_{\xi} l_{i\xi}\mu_{\xi}}$  are constant for all LORs  $i$  that intersect the region where  $\Delta\lambda$  is non-zero. In that case, the two sets of equations in (3.16) become identical and will have non-zero solutions. For example, if one considers a small change at a single pixel  $k$ , the solution equals

$$\frac{\Delta\lambda_k}{\Delta\mu_k} = \bar{y}_i e^{\sum_{\xi} l_{i\xi}\mu_{\xi}}. \quad (3.17)$$

The use of time-of-flight changes the elements of the submatrix  $F_{\lambda\lambda}$  in the Fisher information matrix, destroying the similarity between the two equations. As a result, pixel-by-pixel cross-talk becomes impossible. However, the existence of other possible local maxima of the likelihood still needs to be thoroughly analyzed.

#### 3.2.3 Uniqueness of the solution

The analysis above indicates that TOF information eliminates high-frequency cross-talk between the emission and attenuation reconstructions in the joint estimation.

However, it does not exclude low-frequency cross-talk. In our experiments, we observed that MLAA produces images that are visually free of artifacts, but differ from the true images by a scale factor. Here we attempt to gain some insight in this scaling effect, by deriving a scaled solution from the true image. Suppose the images  $[\lambda, \mu]$  maximize the likelihood. If we multiply  $\lambda$  with a constant, the computed sinogram  $\bar{y}$  eq. (3.1) is multiplied with the same constant. We show that we can always increase the attenuation image  $\mu$  to compensate for that change, such that we obtain an alternative solution that produces the same  $\bar{y}$  and therefore the same (maximum) likelihood.

Assume that the true tracer distribution is  $\lambda^o$  and the true attenuation image is  $\mu^o$ . The sinogram attenuation factors due to the attenuation image  $\mu^o$  equal  $\exp(-P\mu^o)$ , where  $P$  is the non-TOF projection operator. Consequently, the attenuated emission sinogram (without the scatter/randoms contributions) equals  $\bar{y} = (P_t\lambda^o) * \exp(-P\mu^o)$ , where  $P_t$  is the TOF projector operator. We also assume that  $\lambda^o$  and  $\mu^o$  have a finite support  $S$ , meaning  $\lambda_j^o = 0$  and  $\mu_j^o = 0$ ,  $\forall j \notin S$ , where  $j$  is the voxel index.

Define a sinogram region  $\Omega$  as the set of lines of response that contain activity (the projection of  $S$  produces this sinogram region). Now consider a non-TOF sinogram  $U$  which is uniform within the sinogram region  $\Omega$ :

$$U_i = \ln(\alpha), \quad \forall i \in \Omega$$

where  $i$  is the sinogram index,  $\alpha > 0$  and sinogram  $U$  is allowed to have any values outside  $\Omega$ . Consistent sinograms satisfying the above condition can be found so there exists an image  $\mu^\alpha$  such that inside  $\Omega$  we have  $U = P\mu^\alpha = \ln(\alpha)$  and hence  $\exp(-P\mu^\alpha) = 1/\alpha$ . Thus, the attenuation created by the modified attenuation image  $(\mu^o + \mu^\alpha)$  equals  $P\mu^o/\alpha$ . It follows that sinogram  $\bar{y}$  can also be obtained with activity image  $\alpha\lambda^o$  and attenuation image  $\mu^o + \mu^\alpha$ , for any  $\alpha$  where  $\mu^o + \mu^\alpha \geq 0$ . Note that with this construction, the activity is globally scaled while the attenuation undergoes a position dependent scaling.

Interestingly, when the sinogram region  $\Omega$  is known exactly and the attenuation values are set to zero outside this region:

$$U_i = \begin{cases} \ln(\alpha), & \forall i \in \Omega \\ 0, & \forall i \notin \Omega \end{cases}$$

sinogram  $U$  can no longer be expressed by a projection of a bounded attenuation image  $\mu^\alpha$ . This is due to the singularities in  $\mu^\alpha$  present at the boundaries of  $S$  making it unlikely for any joint estimation reconstruction to reach a scaled solution of the true images. This would imply that the solution of joint estimation is truly unique with a known object boundary. However, our first experiments indicate that the practical value of this argument is questionable, because small errors in the object's boundary seem to be enough to reintroduce the scaling problem.

In [58], this problem is studied based on a consistency condition for 2D TOF PET data. It was shown there that the set of scaled solutions  $\{\alpha\lambda^o, \mu^o + \mu^\alpha : \alpha > 0\}$  described above are the only solutions to the joint estimation problem from TOF PET emission data. Thus, it will still be necessary to use some a-priori knowledge

### 3. SIMULTANEOUS RECONSTRUCTION OF ACTIVITY AND ATTENUATION IN TIME-OF-FLIGHT PET

---



Figure 3.1: Activity and attenuation images of the simulated phantoms: left: the 16x16 pixels phantom to study the Fisher information matrix, right: the 2D thorax phantom.

about the expected intensities of the activity and/or the attenuation images. In most cases, the most convenient will be to use a-priori values for the attenuation in tissue.

## 3.3 Experiments

In the following figures, the activity images will be shown in a white-to-black color map whereas a black-to-white color map will be used to show the attenuation images.

### 3.3.1 2D Simulations

Figure 3.1 shows the two phantoms used in our 2D phantom studies. We use a Field-of-View (FOV) of 40 cm for the study of the features of the FIM and the study of visual quality of the reconstructions as a function of time resolution and iterations. For the study of the influence of different initializations on the induced constant factor/term, noise propagation and bias and variance in emission reconstructions more realistic TOF specifications adjusted to commercially available TOF PET systems will be used.

#### The Fisher information matrix

In this study, the  $16 \times 16$  circular phantom shown in figure 3.1 with uniform activity and uniform tissue attenuation was used. For this toy problem, the Fisher information matrix can be computed explicitly because its size is only  $512 \times 512$ . Non-TOF submatrices of the Fisher information matrix were compared to a TOF system with a spatial resolution of 2.5 cm FWHM corresponding to a pixel resolution. These submatrices,  $F_{\lambda\lambda}$ ,  $F_{\lambda\mu}$  and  $F_{\mu\mu}$ , are considered as operators and their impulse response is computed for the pixel located near the center of the FOV.

Figure 3.2 shows the central row of each of the FIM submatrices defined in (3.9) reshaped into the size of the emission and attenuation images. It should be noted that since only the first term of the FIM incorporates both TOF projection and TOF

backprojection operators, the elements of this first term,  $F_{\lambda\lambda}$ , change for a TOF system while the other three terms remain unchanged.

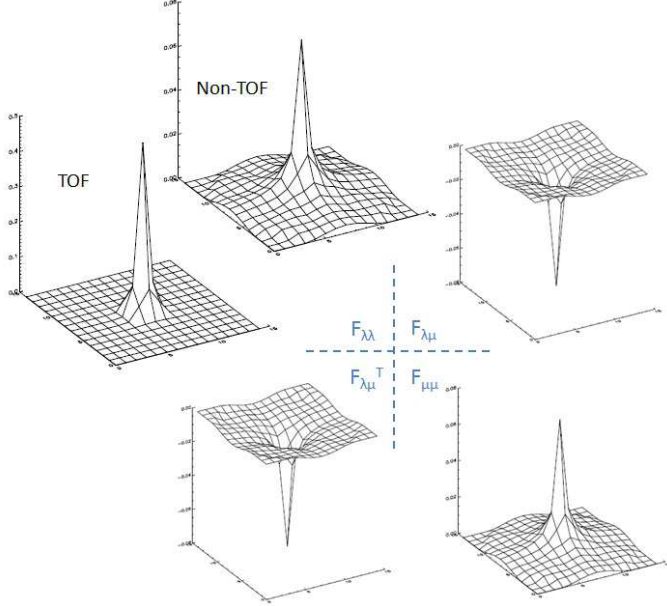


Figure 3.2: The four Fisher Information PSFs for a change in the emission/attenuation of the pixel located near the center of the FOV. Top-left: the effect of emission change in the emission image for a TOF and a non-TOF system, top-right: the effect of attenuation change seen in the emission image, bottom-left: the effect of emission change seen in the attenuation image and vice versa, bottom-right: the effect of attenuation change seen in the attenuation image.

The top left figures show the FIM response in the emission image for a small change of the activity in the pixel located close to the center of the FOV, for both TOF and non-TOF systems. The top right and bottom left figures show the influence of a small change in the attenuation and activity of the central pixel seen in the emission and attenuation images respectively. The bottom right figure shows the effect of a change in the attenuation image for a change of attenuation for the same pixel. Using the term Point Spread Function (PSF) with caution<sup>1</sup>, figure 3.2 shows the four PSFs for the pixel in the center of the FOV.

It can be seen from figure 3.2 that the four PSFs of a non-TOF system are very similar. Comparing this to the system of equations (3.13), it can be seen that for some simultaneous change in the emission and attenuation values of the central pixel, these changes can potentially cancel each other out (as long as they don't violate the non-negativity constraint). Hence, these changes can not be identified from the measurements because they do not modify the value of the likelihood, which remains at its maximum. On the other hand, for a TOF system the four PSFs are no longer similar. Thus, a change in the activity of a pixel can no longer be compensated by a

<sup>1</sup>position dependant PSF in the FIM

### 3. SIMULTANEOUS RECONSTRUCTION OF ACTIVITY AND ATTENUATION IN TIME-OF-FLIGHT PET

---

change in the attenuation of the same pixel, which makes high-frequency activity and attenuation cross-talk impossible.

#### Thorax Phantom

For the 2D thorax phantom shown in fig 3.1, 2D sinograms with 128 detectors (bin size 3.125 mm), 128 projection angles over 180 degrees and a TOF sampling density of at least  $4/\text{FWHM}_{\text{TOF}}$  were generated. An oversampling of 3 was used during simulation (i.e. 3 rays per LOR, 9 subpixels per image pixel) to account for slight mismatch between the simulation and reconstruction projectors and the reconstructed images had  $128 \times 128$  pixels. The emission data provide no attenuation information about LORs that do not intersect the activity distribution. Therefore, MLAA was applied with a penalty that is active only for the voxels located outside the body contour and inside the body contour, no priors were applied. In that external region, we use a penalty that favors zero attenuation values outside that body contour. We find an estimate of the object boundary by thresholding either the sinogram or the initial reconstruction and outside this boundary the intensity prior was set to have a negative derivative for any pixel value, except for zero and tissue attenuation (in which case the derivative was zero). The addition of this prior, modifies the MLTR update step of eq. (3.6) by the addition of the prior gradient and its second derivative to the numerator and the denominator, respectively. Details of the prior are provided in the appendix.

To study the effect of TOF resolution on image quality, simulations were conducted for multiple TOF resolutions varying from 40 cm (approximately non-TOF) to 2.5 cm corresponding to time resolutions of 2667 ps to 167 ps. Simultaneous activity and attenuation images were reconstructed varying the number of iterations to study the convergence properties. For these experiments the attenuation image was initialized by filling the correct body contour uniformly with tissue attenuation and a uniform activity within the FOV was used as the initial activity image.

Figure 3.3 shows the resulting activity and attenuation reconstructions of the noiseless thorax phantom after 5, 15 and 50 iterations of MLAA for varying TOF resolutions. In this study the attenuation images were updated only once for each update of the activity ( $N=1$ ).

It can be seen from figure 3.3 that, after 50 iterations of MLAA the estimated activity and attenuation images for a TOF resolution of 40 cm FWHM still suffer from cross-talk and have not visually converged to the true images. When the TOF resolution is improved to 20 cm FWHM, the reconstructions after 50 iterations improve significantly, but they still differ from the true images. For TOF resolutions below 20cm FWHM the reconstructions visually converge to the true image. However, the reconstructions differ from the true images by a scaling factor which can not be seen here. It can also be seen that as the TOF resolution increases the speed of convergence increases as well.

Next, the simulation specifications were adjusted according to the Siemens Biograph scanner specifications [92]. For the 2D thorax phantom shown in fig 3.1, 2D sinograms with 200 detectors (bin size 4.01 mm) and 168 projection angles over 180

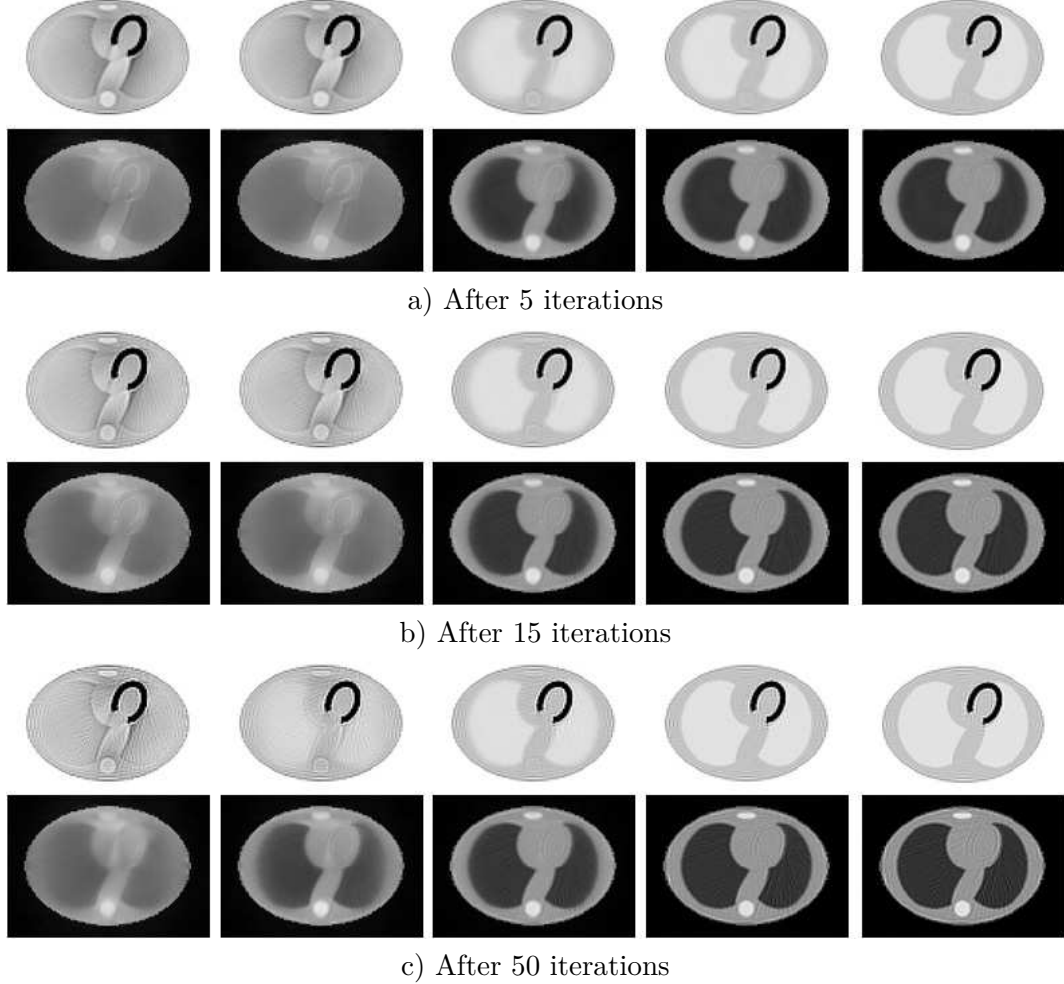


Figure 3.3: Activity and attenuation reconstructions after 5, 15 and 50 iterations and 32 subsets of MLAA for TOF resolutions of 40 cm (approximately non-TOF), 20 cm, 10 cm, 5 cm and 2.5 cm.

degrees were generated. An effective TOF resolution of 580 ps (= 8.7 cm) FWHM and a time-bin width of 312 ps were used to generate the sinograms. This time-bin width of 312 ps is sufficient to avoid aliasing artifacts in the reconstructed image [3]. However, it results in an effective broadening of the TOF FWHM, which can have an impact on the speed of convergence. Our simulations indicate that this effect is negligible. We used an oversampling of 3 during simulations, the reconstructed images had  $200 \times 200$  pixels and as before MLAA with a penalty that is only active outside the body contour was used. The following MLAA reconstructions are after 3 iterations of 42 subsets with  $N=5$ .

To study the effect of different initializations on the final MLAA reconstructions, initial attenuation images with the correct body contour were filled with 0.5, 1 and 2 times tissue attenuation. A zero image, a smooth image with attenuation

### 3. SIMULTANEOUS RECONSTRUCTION OF ACTIVITY AND ATTENUATION IN TIME-OF-FLIGHT PET

---

concentrated at the center, an image with random noise and an image designed to encourage cross-talk near the heart were also used for this purpose. We found that the MLAA reconstructions converged to very similar images that differed from the true image just by a scale factor. Each of these initialization images produced a different scale factor in the final reconstruction image but apart from this the reconstructions were cross-talk free and comparable to the true activity and attenuation images.

Figure 3.4 shows a few of the initial images used in this study together with their final TOF-MLAA reconstructions. The final reconstructions shown in figure 3.4 show no sign of activity and attenuation cross-talk. However the final activity reconstructions appear in different shades which is due to the scale factor which the activity reconstructions differ by from the true activity distribution. The right most initializations used in figure 3.4 was produced by a non-TOF MLAA reconstruction to encourage cross-talk in the activity and attenuation images. As with all other initial images used, after sufficient iterations of the algorithm, the reconstructions visually converged to the true image, but differed by a scale factor. This indicates that TOF-MLAA is able to get rid of any cross-talk which might be already present in the initial images.

Poisson noise was then added to the sinogram of the 2D thorax phantom to analyze the behaviour of MLAA under noisy conditions. The maximum count in the sinogram was chosen to be less than 10. The activity and attenuation images were reconstructed from this noisy sinogram starting from uniform initial images. As reference images, we used the MLEM reconstruction of the activity using the true attenuation coefficients and the MLTR reconstruction of the attenuation using the true activity distribution. The same experiment was repeated for a noise-free sinogram. We assume that the resulting noise-free reconstruction is a good estimate of the mean over many noise realizations. From these images, noise correlation coefficients (NCC) were computed between the MLAA reconstructions ( $\mathcal{M}$ ) and the reference reconstructions ( $\mathcal{R}$ ) as,

$$NCC = \frac{\sum_j (\mathcal{M}_j^n - \mathcal{M}_j^f)(\mathcal{R}_j^n - \mathcal{R}_j^f)}{\sqrt{\sum_j (\mathcal{M}_j^n - \mathcal{M}_j^f)^2 \sum_j (\mathcal{R}_j^n - \mathcal{R}_j^f)^2}}, j = 1, \dots, J \quad (3.18)$$

where subscript  $j$  determines the pixel index and superscripts  $n$  and  $f$  determine the noisy and the noise-free reconstructions respectively.

Figure 3.5 compares the MLAA reconstructions from a noisy sinogram to the reference images computed from MLEM and MLTR reconstructions, revealing strong noise correlations. A noise correlation coefficients of 0.86 was computed for the MLAA reconstructed activity image starting from uniform initial images with respect to the MLEM reconstructed activity image with known attenuation. The same measure was computed to be 0.92 for the MLAA reconstructed attenuation image with respect to the MLTR reconstructed attenuation image with known activity. This high noise correlation suggests that TOF simultaneous reconstruction handles noise just as reconstructions from known activity or attenuation images. Apparently, the noise in the sinogram does not propagate to make simultaneous reconstructions unstable.

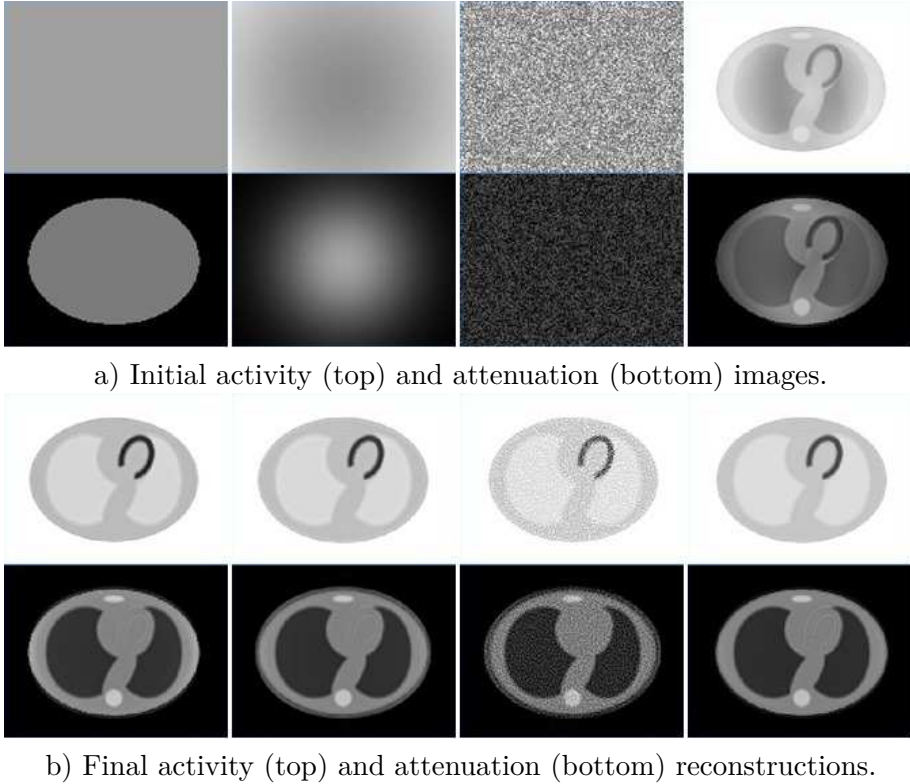


Figure 3.4: Initial activity and attenuation (top) images and their respective TOF-MLAA activity and attenuation reconstructions (bottom). Initial images from left to right: uniform attenuation within the body contour filled with tissue attenuation, smooth attenuation image with attenuation concentrated at the center, initial images filled with random noise and a non-TOF MLAA reconstruction image designed to encourage cross-talk.

With more realistic noise in the emission data, we study bias and variance in the MLEM and MLAA emission reconstructions as a function of reconstruction updates. We presume that an estimate of the scale in the attenuation-corrected emission sinogram is available and we plot the bias and variance curves for a 4.5 cm diameter region-of-interest (ROI) in a tissue region of the thorax phantom shown in figure 3.6. The bias is then computed in each reconstruction update for 100 different noise realizations as the relative difference of the ROI values to the true ROI values of the thorax phantom. Figure 3.6 shows the bias and variance curves in the ROI for 200 MLEM and MLAA updates of the emission image. The marked points on the curves correspond to bias and variance values after 20 emission updates, i.e. updates 20, 40, 60, ..., 200. We do not use subsets in this study and as before N=5.

Figure 3.6 shows that the MLEM reconstructions outperform the MLAA reconstructions, yielding a lower bias at the same variance level. This observation is expected since MLEM uses a known attenuation, whereas MLAA estimates both the emission and the attenuation. Comparison between the marked points on the

### 3. SIMULTANEOUS RECONSTRUCTION OF ACTIVITY AND ATTENUATION IN TIME-OF-FLIGHT PET

---

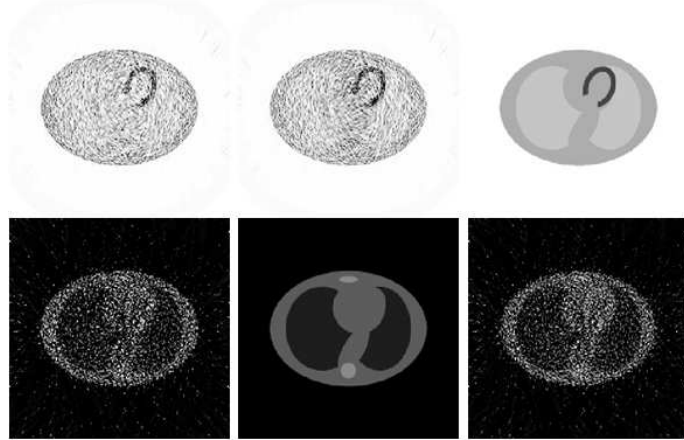


Figure 3.5: Activity (top) and attenuation (bottom) images reconstructed from a noisy sinogram. The reconstructed results of MLAA initialized by uniform images (left) are compared to that of an MLEM (center) and MLTR (right) with known attenuation and activity images respectively.

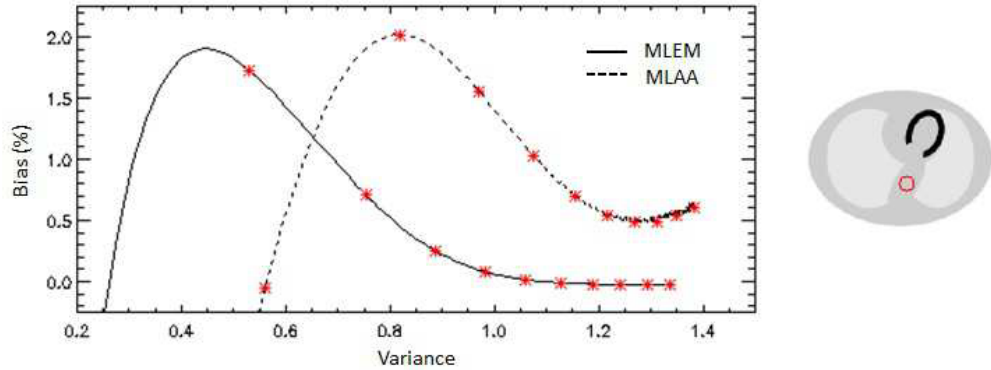


Figure 3.6: Bias and variance curves (left) in the MLEM and MLAA reconstructed emission images as a function of reconstruction updates for a 4.5 cm diameter ROI shown in red (right). The marked points on the curves show bias and variance values for 20 updates of the emission image which are computed from 100 different noise realizations.

two curves (at every 20 iterations) indicates that MLEM also converges faster than MLAA. The left end of the curves correspond to unreliable transient values of bias and variance at the first few updates of the reconstructed emission image.

#### 3.3.2 Phantom scans and patient study

A fully 3D implementation of MLAA has been applied to two phantom scans and a clinical patient study. The scans have been acquired on a Siemens Biograph mCT system [92]. The TOF PET data are organized as 5D sinograms, consisting of 400

radial bins, 168 azimuthal angles, 9 co-polar angles, up to 109 planes (depending on the co-polar angle) [98], and 13 time bins of 312 ps width, with an effective TOF resolution of 580 ps. The patient bore of the scanner is 78 cm with a PET field-of-view of 69 cm, which makes truncation an issue for big phantoms or patients.

By simple thresholding and backprojection operations, a reasonable estimate of the body contour can be obtained [47]. In order to deal with the scale problem in the MLAA reconstructions, we impose the known value of tissue attenuation to the 75<sup>th</sup> percentile of the attenuation value within this (initial) body contour. This value is imposed by scaling the entire attenuation image. The scale factor required to insure tissue attenuation rapidly converges to 1. For the images considered here, the 75<sup>th</sup> percentile corresponded to tissue, but of course, more sophisticated segmentation algorithms could be used for this purpose. Outside the body contour however, the same background prior as described above and in the appendix was used to encourage background attenuation values to become zero. In both 3D studies, the smoothing relative difference prior of [99] was also used to encourage smoothness in the attenuation images.

### 3D Phantom Study

The NEMA IEC body phantom [100] was used to evaluate the simultaneous activity and attenuation reconstructions in 3D. The measurements corresponded to a 5 minute scan of 229 MBq injection scanned 2 hours post-injection. The phantom was located close to the center of the FOV. In this study, the contributions of scatter were not taken into account and we did not try to enforce bed attenuation in the attenuation image.

Results from 3D reconstructions of activity and attenuation of the NEMA IEC body phantom located near the FOV center of the mCT are shown in figures 3.7 and 3.8. The reconstructions are shown for two different transaxial planes: one having more details in the activity image, figure 3.7, and one with more details in the attenuation image, figure 3.8. The MLAA reconstructions are compared to the CT-based attenuation image and the OSEM reconstructions of the activity with CT-based attenuation correction. The reconstructions shown here are from 3 MLAA iterations of 42 subsets.

The TOF-MLAA reconstructions do not suffer from activity and attenuation cross-talk. However because we did not correct for scatter, slight activity is present within the cavity of the NEMA phantom and some excess attenuation around the object of interest. It can also be seen in figure 3.8 that the algorithm has tried to compensate for bed attenuation by putting attenuation values outside the boundary of the object. Using the CT-based scatter estimate [101] and bed attenuation during MLAA reconstructions, activity and attenuation images were reconstructed free of these artifacts, however, the results are not shown here. Similar results were also obtained for the phantom in the off-center position.

### 3. SIMULTANEOUS RECONSTRUCTION OF ACTIVITY AND ATTENUATION IN TIME-OF-FLIGHT PET

---

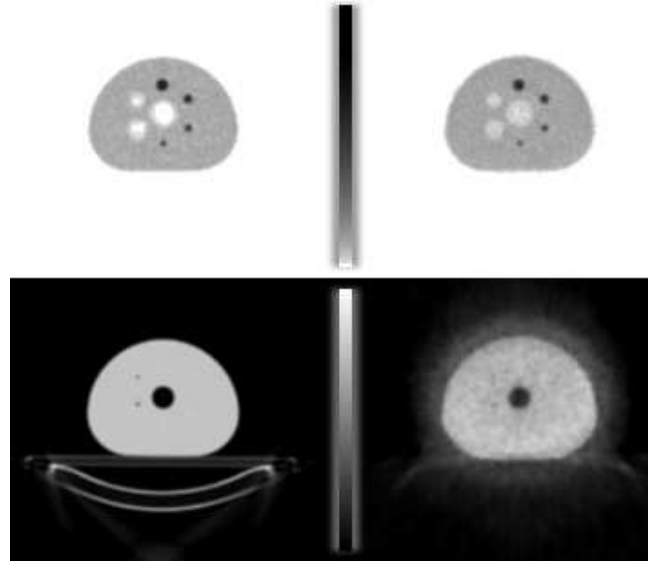


Figure 3.7: CT attenuation corrected MLEM reconstructions (top-left), FBP attenuation reconstruction of the CT (bottom-left), MLAA reconstructed emission (top-right) and attenuation (bottom-right) images of the 3D NEMA phantom located near the center of the FOV. The vertical bars represent the gray level lookup table for activity and attenuation.

#### Clinical study

A clinical five minute scan of the thorax of a patient injected with 570 MBq  $^{18}\text{F}$ -FDG was used to reconstruct the activity and attenuation images. Due to the patient size, the TOF PET measurements suffer from truncation near the edge of the FOV of the system. As shown below, the truncation affected the reconstruction of the arms in the PET and CT images, as well as in the MLAA images. Two different MLAA reconstructions were computed. For the first reconstruction, we used the precomputed CT scatter estimate and imposed the CT-based bed attenuation in the attenuation image. This reconstruction illustrates the effectiveness of TOF data for joint activity and attenuation estimation in ideal situations. In the second reconstruction, no scatter correction was done and no information about the bed was used.

Figures 3.9 and 3.10 show the activity and attenuation reconstructions from the clinical data, respectively. In this study we used the CT-based scatter and bed attenuation values during MLAA reconstructions. The activity reconstructed from OSEM with CT-based attenuation correction and the one of MLAA are shown in figure 3.9 and the CT attenuation image and the reconstructed MLAA attenuation image are shown in figure 3.10.

The two activity reconstructions shown in figure 3.9 look visually very similar and do not show obvious signs of cross-talk. For a quantitative analysis of MLAA and MLEM activity reconstructions please refer to chapter 7. Looking at the attenuation

### 3.3. Experiments

---

reconstruction of MLAA in figure 3.10, a good lung-tissue discrimination is observed. The algorithm has also been able to produce a fairly good estimate of the patient body contour making use of the tracer uptake in the entire body. However, the attenuation values are slightly elevated near the heart. This is probably due to significantly higher activity uptake in the heart, but further analysis is needed.

Figure 3.10 also shows that the MLAA attenuation reconstructions suffer less from truncation artifacts. This is partly because the CT scanner uses a slightly smaller FOV compared to the PET scanner of the mCT, and because iterative algorithms handle truncation better than analytic reconstructions. In this comparison, the portion of the liver visible in the lung of the patient is slightly different, which we attribute to the breathing motion during acquisition.

Figure 3.11 shows the activity and attenuation reconstructions from the clinical data without any CT-based compensation for scatter or attenuation values outside the patient boundary. As before, the reconstructions seem to be free of activity and attenuation cross-talk. However, in this MLAA reconstruction the activity is overestimated. This is associated to the excess attenuation in the attenuation image due to the over-estimation of the patient boundary.

The attenuation reconstruction of figure 3.11 shows that MLAA has been able to make a useful reconstruction of the attenuation medium but with less lung-tissue contrast than before. It has also been able to reconstruct the portion of the bed which lies inside the convex hull of the region containing activity. However, the

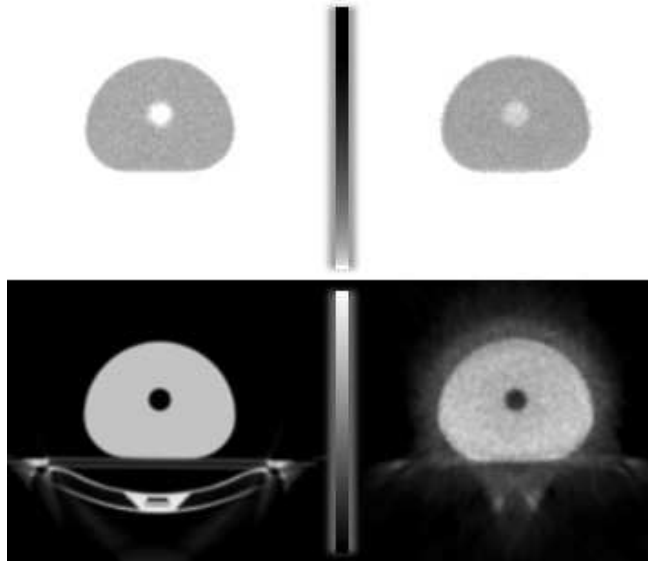


Figure 3.8: CT attenuation corrected MLEM reconstructions (top-left), FBP attenuation reconstruction of the CT (bottom-left), MLAA reconstructed emission (top-right) and attenuation (bottom-right) images of the 3D NEMA phantom located near the center of the FOV. The vertical bars represent the gray level lookup table for activity and attenuation.

### 3. SIMULTANEOUS RECONSTRUCTION OF ACTIVITY AND ATTENUATION IN TIME-OF-FLIGHT PET

---

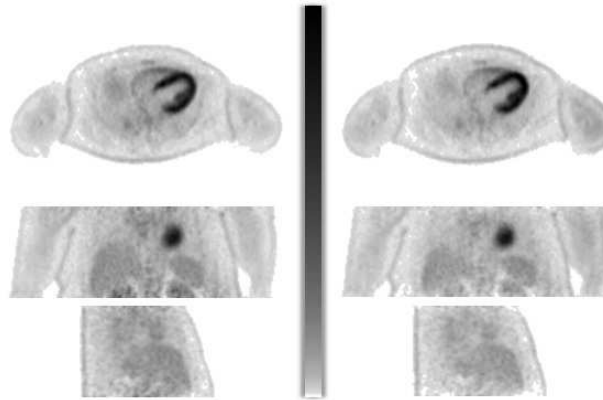


Figure 3.9: Transaxial (top), coronal (center) and sagittal (bottom) view of the activity corrected with CT-based attenuation (left) and the activity reconstructed with MLAA (right) and CT-based scatter and bed correction. The MLAA image was smoothed with a 3D Gaussian with 6 mm FWHM to match approximately the resolution of the standard reconstruction. The vertical bar represents the gray level lookup table.

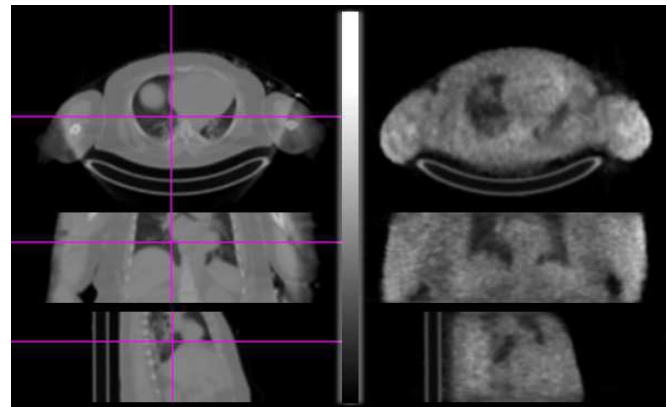


Figure 3.10: Transaxial (top), coronal (center) and sagittal (bottom) view of the CT-based attenuation image (left) and attenuation image reconstructed with MLAA (right) from the emission data and CT-based scatter and bed correction. The MLAA image was smoothed with a 3D Gaussian with 6 mm FWHM. The vertical bar represents the gray level lookup table.

boundary of the patient has been slightly over-estimated (region above the patient) which is mainly due to scatter.

## 3.4 Discussion

Simultaneous reconstruction of attenuation and activity in SPECT and non-TOF PET has been investigated by many groups, and was found to be a very ill-posed

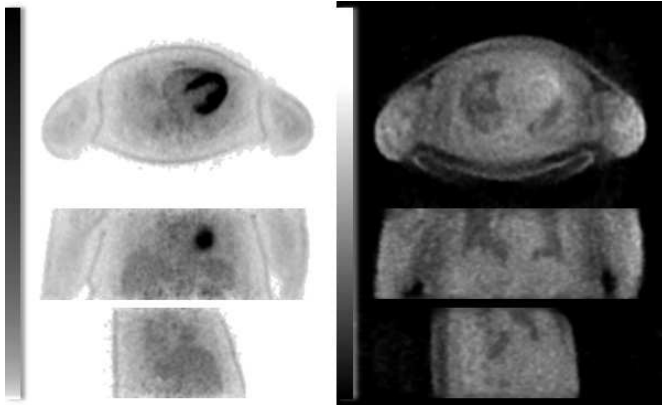


Figure 3.11: Transaxial (top), coronal (center) and sagittal (bottom) view of activity (left) and attenuation (right) reconstructed with MLAA without any CT-based scatter and bed correction. The MLAA images were smoothed with a 3D Gaussian with 6 mm FWHM. The vertical bars represent the gray level lookup table for activity and attenuation.

problem. Previous studies have shown that the use of time-of-flight reduces the sensitivity of the PET reconstruction to attenuation correction errors. The study presented here reveals that time-of-flight information has the ability to stabilize the joint estimation problem, and may therefore enable quantitative PET imaging without relying on transmission scans or other anatomical imaging procedures. Estimating the attenuation from the emission data has the advantage that it ensures a correct match with respect to photon energy and patient position, and probably a good match in the presence of motion blurring (e.g. heart beat, breathing). In practice, the method could prove useful in mitigating the problem of PET - CT registration when misalignment is an issue. When the PET data are compensated for attenuation based on the CT, the boundaries of a misaligned CT propagate into the PET image, affecting the subsequent registration. Attenuation correction independent of the CT may help to solve this problem.

As suggested by our experiments, and as proven by the theoretical analysis in [58], the TOF PET data enable the estimation of the attenuation sinogram up to a constant term, and therefore the estimation of the activity up to a constant factor. It is anticipated that in most applications, this constant can be determined in a fairly straightforward way by imposing the known attenuation value of tissue to a segmented portion of the attenuation image. An alternative way would be to combine the method with full or partial transmission information, which could e.g. be obtained by adding transmission source(s) in the field of view [83].

The PET emission data provide no (or at least incomplete) information about attenuation along LORs that do not intersect a region containing a significant amount of radioactive tracer. Many tracers, including  $^{18}\text{F}$ -FDG, show uptake in the entire body. For such tracers, it is valid to assume that the attenuation along LORs without activity is zero everywhere. In our experiments, we have applied a prior

### 3. SIMULTANEOUS RECONSTRUCTION OF ACTIVITY AND ATTENUATION IN TIME-OF-FLIGHT PET

---

encouraging the assignment of zero attenuation to such regions. It should be noted that reconstruction of the attenuation image outside the activity region has a slower convergence rate than the reconstruction of the attenuation image inside the activity region, even in the absence of the background prior. For these reasons, adding the effect of additional attenuating medium, specifically the bed, to the attenuation reconstruction instead of reconstructing the bed along with the unknown attenuation medium would be a more reasonable and practical approach.

The PET emission data are always noisy so in addition to the background prior, we use a smoothing Markov prior [99] in the attenuation image and a small amount of post-smoothing in the activity image. Many other priors have been proposed for emission and transmission tomography. Evaluation of such priors for regularization of this joint estimation problem is a topic for further research.

In both the 3D phantom study and the clinical study, we do not compensate for any scatter in the measurements and still are able to achieve reasonable reconstructions. We believe that given these scatter un-compensated reconstructions, it is possible to make an estimate of the scatter and refine the final activity and attenuation reconstructions in an additional step. In the clinical patient study, the patient was injected with a non-specific tracer that has a detectable accumulation in all tissues. This made attenuation reconstruction with roughly the true boundary possible. For more specific tracers that do not dissipate to the entire body, reconstruction of the attenuation image with the correct boundary might prove to be more difficult. The use of external sources [83] can help in these situations.

## 3.5 Conclusion

In this paper, the feasibility of simultaneous activity and attenuation reconstruction from the measurement data was investigated for a time-of-flight system. The MLAA algorithm, which makes alternated updates to the activity and attenuation images by means of the existing MLEM and MLTR algorithms, was used for this purpose.

The feasibility of this approach was verified for 2D and 3D phantom studies as well as for a clinical study. It was found that the utilization of time-of-flight information in simultaneous reconstructions eliminates the problem of activity and attenuation cross-talk. However, to ensure quantitative accuracy, limited prior knowledge is still required, because the solution is only determined up to a constant.

It was shown that as the time resolution of the TOF system improves, the convergence improves as well. The joint ML reconstruction was found to be robust to noise in the emission sinogram.

## 3.6 Appendix

The background prior we use is an absolute intensity prior favoring zero attenuation in the background. Since in each iteration the gradient of the prior is added to the one of the likelihood, here we only express the gradient of this background prior.

Defining  $\partial\mathcal{BG}/\partial\mu_j$  as the gradient of the prior we set this value to be,

$$\frac{\partial\mathcal{BG}}{\partial\mu_j} = \frac{-W_{\mathcal{BG}}}{\sigma^2} \frac{|\mu_j(\mu_j - \mu_T)|}{\mu_j + c\mu_T}, \quad j = 1, \dots, J \quad (3.19)$$

where  $\mu_j$  is the attenuation value at voxel  $j$ ,  $W_{\mathcal{BG}}$  defines the prior strength,  $\mu_T$  is our expected tissue attenuation,  $\sigma$  is a standard deviation measure of tissue which was set to  $\mu_T$  and parameter  $c$  is a skewness parameter. It can be seen that the prior has no effect for voxels with zero or tissue attenuation values. Parameter  $c$  is used to adjust the prior strength to have a greater effect for attenuation values near zero than attenuation values close to  $\mu_T$ . In the simulations we used  $c = 0.05$  and replaced  $\partial^2\mathcal{BG}/\partial\mu_j^2$  by its upper limit  $-W_{\mathcal{BG}}/c\sigma^2$ .



## Chapter 4

# Transmission-less attenuation correction in time-of-flight PET: analysis of a discrete iterative algorithm.

M. Defrise, A. Rezaei, and J. Nuyts, “Transmission-less attenuation correction in time-of-flight PET: Analysis of a discrete iterative algorithm”, *Physics in Medicine and Biology*, vol. 59, no. 4, pp. 1073–1095, Feb. 2014

### Abstract

The Maximum Likelihood Attenuation Correction Factors (MLACF) algorithm has been developed to calculate the maximum-likelihood estimate of the activity image and the attenuation sinogram in time-of-flight PET, using only emission data without prior information on the attenuation. We consider the case of a Poisson model of the data, in the absence of scatter or random background. In this case the maximization with respect to the attenuation factors can be achieved in a closed form and the MLACF algorithm works by updating the activity. Despite promising numerical results, the convergence of this algorithm has not been analysed. In this paper we derive the algorithm and demonstrate that the MLACF algorithm monotonically increases the likelihood, is asymptotically regular, and that the limit points of the iteration are stationary points of the likelihood. Because the problem is not convex, however, the limit points might be saddle points or local maxima. To obtain some empirical insight into the latter question, we present data obtained by applying MLACF to 2D simulated TOF data, using a large number of iterations and different initializations.

---

## 4. TRANSMISSION-LESS ATTENUATION CORRECTION IN TIME-OF-FLIGHT PET: ANALYSIS OF A DISCRETE ITERATIVE ALGORITHM.

---

### 4.1 Introduction

Positron emission tomography (PET) aims at estimating the spatial distribution of a tracer molecule labelled with a positron emitting isotope. This distribution, called the *activity image*, is reconstructed from the *emission data*, which consist of pairs of 511 keV photons detected in coincidence by detectors surrounding the patient. An accurate reconstruction requires in addition information on the spatial distribution of the attenuation coefficient for the 511 keV photons (the *attenuation image*), which is needed to compensate for the absorption or scattering of the photons by the tissues. Failure to correct for attenuation prevents accurate quantification of the tracer uptake and can also affect the qualitative interpretation of the images. This happens for instance when the increased tracer uptake in a localized lesion is almost exactly compensated by the increased attenuation caused by this lesion [80]. This paper deals with attenuation correction in time-of-flight (TOF) PET.

Various methods have been implemented to measure the attenuation image [102]. The state-of-the-art method uses a hybrid PET/CT scanner and obtains the attenuation image as a by-product of the diagnostic CT scan. The CT scan measures the attenuation coefficient at an average photon energy between 50 keV and 100 keV, these data are then extrapolated to the required energy of 511 keV to yield the attenuation image used for PET [17]. A benefit of this method is the good spatial resolution and signal-to-noise ratio (SNR) of the CT measurements compared to the PET emission data. However there are situations where the CT information is incomplete or inaccurate. In clinical practice, the most common source of bias is the geometrical mismatch between the emission data and the attenuation image, caused by patient motion or by different respiratory patterns in the CT and PET scans. This mismatch can be reduced by synchronizing the PET and CT scans with the respiratory motion (*gated scans*) but this increases the CT radiation exposure unless ultra-low dose protocols are applied [103]. Additional difficulties with CT-based attenuation correction arise when using radiological contrast agents [71], or when the axial field-of-view covered by the CT scan is limited to reduce the radiation dose [104].

An alternative solution for attenuation correction recently emerged with the hybrid PET/MR scanners. These scanners also provide anatomical images with good resolution and SNR but avoid radiation exposure and allow simultaneous acquisition of the PET and MR data. However, the relationship between the physical parameters measured in MR and the 511 keV attenuation coefficient is complex, and despite recent progresses [20], [72]–[74], [105] estimating the attenuation from MR data remains more prone to errors than with PET-CT scanners.

While the CT or MR data do not contain direct information about the activity image, the opposite is not true: the PET emission data do contain information about the attenuation image. This motivated the development of iterative algorithms, which simultaneously estimate the tracer distribution and the attenuation image from the combined emission and transmission data measured with external rotating positron sources [15], [77], [78]. A more ambitious approach is to dispose altogether with transmission data by estimating the attenuation image using only the emission

data. Various algorithms have been proposed to that effect [24], [25], [39], [43], [47], [48], [79], but they meet limited success unless strong prior knowledge is available, such as the assumption that the attenuation is uniform, which is an acceptable approximation for some applications such as brain imaging. This limited success is not surprising since it is known [76] that the solution to the simultaneous estimation is not unique in the absence of prior information.

The measurement of the time-of-flight in modern PET scanners increases the amount of information by a factor roughly equal to the ratio between the patient diameter and the width of the TOF profile, which is of the order of 8 cm in current scanners [91], [92], [106]. This additional information can be exploited to compress the data by reducing the number of angular [3], [107] or TOF [108] samples, and was also shown to improve the robustness of image reconstruction to errors in the attenuation image [13], [81]. Successful simultaneous reconstructions of attenuation and emission from combined PET and MR data [56], [82], [109] have also demonstrated the useful informative content of TOF-PET data.

This paper explores attenuation correction in TOF-PET using only the emission data. The study of an analytical model with continuous sampling and noise free data has shown [58] that the solution of the simultaneous estimation is unique in the sense that

- the activity image is uniquely determined up to a global multiplicative constant and,
- the *attenuation factors* (the exponential of minus the line integral of the attenuation image) are uniquely determined for all lines of response (LORs) which have activity, up to the reciprocal of the same multiplicative constant.

We consider here a discrete model of the problem and apply maximum likelihood (ML) estimation, which is expected to yield better results than an analytical model, owing to the high noise level in typical PET data. Two discrete ML approaches are possible.

- The first one maximizes the data likelihood with respect to the activity and attenuation images. This can be done by alternatively updating the activity and the attenuation images using the MLAA algorithm originally introduced for non-TOF PET [47]. The analysis of this algorithm for TOF-PET and its evaluation with simulated and measured data [61] opens promising perspectives for clinical applications. A similar approach is proposed in [110].
- The second ML approach maximizes the data likelihood with respect to the activity image and the *attenuation sinogram*, which is the set of attenuation factors for all LORs. Maximization can be achieved with the MLACF algorithm presented at the 2012 IEEE Medical Imaging Conference [63].

We investigate here this second approach. Both MLAA and MLACF aim at maximizing the data likelihood, but the two approaches are based on different parameterizations of the unknown quantities and are therefore not equivalent. A first

---

## 4. TRANSMISSION-LESS ATTENUATION CORRECTION IN TIME-OF-FLIGHT PET: ANALYSIS OF A DISCRETE ITERATIVE ALGORITHM.

---

difference is that the number of parameters to be estimated can be very different in 3D TOF-PET where the number of LORs in the attenuation sinogram is much larger than the number of voxels in the attenuation image. A second difference is the impossibility with MLACF to add regularizing penalties based on prior knowledge of the attenuation coefficients in some classes of tissues [75]. This is because MLACF only estimates attenuation factors, the attenuation image is only calculated after reconstruction as an optional byproduct required to estimate the scatter background or the geometric alignment with CT data.

This paper presents the derivation of the MLACF algorithm for the case where the background due to scatter and randoms events is negligible or has been pre-corrected. As will be shown in section 4.2 this assumption allows a closed form optimization with respect to the attenuation factors and leads to a simple iterative algorithm, which only involves updating the activity image and is similar to the standard ML-EM algorithm. Sections 4.2 and 4.3 present a mathematical and a numerical study of the convergence of the algorithm. The extension to the case with background is analysed in [66], the algorithm involves in that case alternately updating the attenuation sinogram and the activity image.

## 4.2 The MLACF algorithm

### 4.2.1 The joint likelihood for simultaneous estimation of the activity image and attenuation sinogram

Consider a scanner which histograms the coincidence data in  $N$  LORs, with  $T$  time-of-flight bins for each LOR. We denote the measured data as  $\mathbf{y} = \{y_{i,t} \in \mathbb{N}_0, i = 1, \dots, N, t = 1, \dots, T\}$ , where  $y_{i,t}$  is the number of events detected for LOR  $i$  and time bin  $t$ , and  $\mathbb{N}_0$  is the set of non-negative natural numbers. The activity image is parameterized as a vector  $\lambda = \{\lambda_j \geq 0, j = 1, \dots, M\}$ . Any discrete parameterization can be used but one typically takes  $M$  voxel basis functions, and  $\lambda_j$  is then the tracer concentration in voxel  $j$ . The goal of PET is to estimate  $\lambda$  from the data  $\mathbf{y}$ .

The expectation value of the non-attenuated data is denoted  $p_{i,t}$  and is related to the activity image by

$$p_{i,t} = \sum_{j=1}^M c_{i,j,t} \lambda_j \quad i = 1, \dots, N \quad t = 1, \dots, T \quad (4.1)$$

where the system matrix elements  $c_{i,j,t} \geq 0$  model the physics of the scanner, and we assume throughout the paper that there is no background due to scatter or random coincidences (or that the data have been pre-corrected). Quantities summed over the TOF index are denoted by omitting the  $t$  index, in particular we define  $y_i = \sum_{t=1}^T y_{i,t}$ ,  $c_{i,j} = \sum_{t=1}^T c_{i,j,t}$  and  $p_i = \sum_{t=1}^T p_{i,t}$ .

The attenuation factors, denoted  $a_i$ , are independent of the TOF bin. This is the key property that ultimately allows solving the simultaneous estimation. The

attenuation factors are related to the attenuation image  $\mu$  by

$$a_i = \exp\left\{-\sum_{j=1}^M l_{i,j} \mu_j\right\} \quad i = 1, \dots, N \quad (4.2)$$

where the system matrix elements  $l_{i,j} \geq 0$  correspond to the parameterization used for  $\mu$ , which is not necessarily the same as for  $\lambda$ . Equation (4.2) and the constraint  $\mu_j \geq 0$  imply the natural constraint  $0 < a_i \leq 1$  on the attenuation factors.

In this paper we seek to estimate  $\lambda$  and  $a$  from the emission data  $\mathbf{y}$ , and equation (4.2) will not be used. With this approach the attenuation factors are seen as nuisance parameters of the estimation problem since the objective of PET is the visualization of the tracer distribution, while CT or MR data provide anatomical details and are used for localizing the activity. The attenuation image may nevertheless be needed for some applications, such as the geometric alignment of the anatomical data with PET. Although  $\mu$  can in principle be reconstructed from the attenuation factors  $a_i$ , such a reconstruction may be difficult in practice because the  $a_i$  can be estimated only for LORs containing activity. This issue will not be discussed here.

The expectation value of the measured attenuated data is  $\langle y_{i,t} \rangle = a_i p_{i,t}$  and the logarithm of the likelihood is

$$L(y, \lambda, a) = \sum_{i=1}^N \sum_{t=1}^T \{-a_i p_{i,t} + y_{i,t} \log(a_i p_{i,t})\} \quad (4.3)$$

with  $p_{i,t}$  given by equation (4.1) and terms independent of  $\lambda$  and  $a$  have been omitted. The goal of ML estimation is to calculate a maximizer of the likelihood,

$$(\lambda^*, a^*) \in \arg \max_{0 < a_i \leq 1, \lambda_j \geq 0} L(y, \lambda, a) \quad (4.4)$$

The notation  $\in$  indicates that the maximizer is not unique. First there is the scale invariance  $L(y, \lambda, a) = L(y, \alpha\lambda, a/\alpha)$  for any  $\alpha > 0$ , which has an obvious physical interpretation and also holds for the continuous model [58]. In addition, local maxima cannot be excluded because the log-likelihood (4.3) is not jointly concave in  $(a, \lambda)$  even though it is concave in  $a$  and in  $\lambda$  separately<sup>1</sup>. The possibility of local maxima of the likelihood will be investigated numerically in section 4.3.

In the next section, the likelihood will be maximized with respect to  $a$  at fixed activity image  $\lambda$ , allowing to eliminate the attenuation factors from the set of parameters that must be estimated.

### 4.2.2 Maximizing the likelihood at fixed $\lambda$

Consider a fixed activity image  $\lambda$ . The log-likelihood (4.3) is the sum of  $N$  functions depending each on a single attenuation factor  $a_i$ , with first and second derivatives given by

$$\frac{\partial L(y, \lambda, a)}{\partial a_i} = \sum_{t=1}^T \left\{ -p_{i,t} + \frac{1}{a_i} y_{i,t} \right\}, \quad \frac{\partial^2 L(y, \lambda, a)}{\partial a_i^2} = \sum_{t=1}^T \frac{-1}{a_i^2} y_{i,t} \leq 0. \quad (4.5)$$

<sup>1</sup>the same holds when the likelihood is parametrized using  $\lambda$  and  $\mu$  as with the MLAA approach.

---

4. TRANSMISSION-LESS ATTENUATION CORRECTION IN TIME-OF-FLIGHT PET:  
ANALYSIS OF A DISCRETE ITERATIVE ALGORITHM.

---

For each LOR with activity, i.e. such that  $y_i = \sum_t y_{i,t} > 0$ , the log-likelihood has a unique maximizer

$$a_i^* = \frac{\sum_{t=1}^T y_{i,t}}{\sum_{t=1}^T p_{i,t}} = \frac{y_i}{p_i} \quad (4.6)$$

If in addition we impose the constraint  $a_i \leq 1$ , the maximizer becomes

$$\begin{aligned} a_i^* &= \frac{y_i}{p_i} && \text{if } \frac{y_i}{p_i} \leq 1 \\ &= 1 && \text{otherwise,} \end{aligned} \quad (4.7)$$

as can be verified by noting that  $\partial L(y, \lambda, a)/\partial a_i|_{a_i^*=1} \geq 0$  at the upper edge of the allowed domain  $a_i \leq 1$  when  $y_i \geq p_i$ .

In this paper, we ignore the constraint  $a_i \leq 1$  and always use  $a_i^* = y_i/p_i$ . The following lemma shows that this can be done provided  $L(y, \lambda, a)$  has an unconstrained optimizer.

*Lemma 1.* Let

$$(a_c, \lambda_c) \in \arg \max_{0 < a_i \leq 1, 0 \leq \lambda_j} L(y, \lambda, a) \quad (4.8)$$

be a global maximizer of the likelihood with the constraint  $a_i \leq 1$ . If there exists a global maximizer without that constraint,

$$(a_u, \lambda_u) \in \arg \max_{0 < a_i, 0 \leq \lambda_j} L(y, \lambda, a) \quad (4.9)$$

then for some constant  $K > 0$ ,  $(a_u/K, K\lambda_u)$  is also a global constrained maximizer.

*Proof.* Define the maximum attenuation factor  $K = \max(a_u) = \max_{i \in 1..N} y_i/p_i < \infty$ . Adding a constraint (in this case  $a_i \leq 1$ ) can never increase the value of the maximum, and therefore

$$L(y, \lambda_c, a_c) \leq L(y, \lambda_u, a_u) = L(y, \lambda^*, a^*) \quad (4.10)$$

where we define  $a^* = a_u/K, \lambda^* = K\lambda_u$  and the last equality follows from the scale invariance. Thus  $L(y, \lambda^*, a^*) \geq L(y, \lambda_c, a_c)$  and by construction  $a_i^* \leq 1$ , so  $(a^*, \lambda^*)$  is also a global constrained maximizer of the likelihood.  $\square$

When applicable Lemma 1 means that maximum likelihood solutions can be obtained by ignoring the constraint  $a_i \leq 1$  and by scaling the solution a posteriori. The method derived in this paper is not applicable if  $L(y, \lambda, a)$  has no global constrained optimizer and it is unclear whether such a situation is possible.

#### 4.2.3 The reduced log-likelihood function $\tilde{L}$

Inserting the optimized attenuation factor (4.6) in the log-likelihood (4.3), and keeping only the terms that depend on  $\lambda$ , we are left with the problem of maximizing

$$L(y, \lambda, a^*) = \tilde{L}(y, \lambda) + \text{terms independent of } \lambda \quad (4.11)$$

where the *reduced log-likelihood* is defined as

$$\tilde{L}(y, \lambda) = \sum_{i=1}^N \left\{ -y_i \log(p_i) + \sum_{t=1}^T y_{i,t} \log(p_{i,t}) \right\} = \sum_{i=1}^N \sum_{t=1}^T y_{i,t} \log \frac{p_{i,t}}{p_i} \quad (4.12)$$

We assume in sections 4.2.3 and 4.2.4 that  $p_{i,t} > 0$  unless  $y_{i,t} = 0$ . When satisfied this condition implies also that  $p_i > 0$  unless  $y_i = 0$ . The definition of  $\tilde{L}(y, \lambda)$  when  $p_{i,t} = 0$  or  $p_i = 0$  will be discussed separately in section 4.2.5.

The gradient of the *reduced log-likelihood* (4.12) is

$$\frac{\partial \tilde{L}(y, \lambda)}{\partial \lambda_j} = \sum_{i=1}^N \left\{ -\frac{y_i c_{i,j}}{p_i} + \sum_{t=1}^T \frac{y_{i,t} c_{i,j,t}}{p_{i,t}} \right\} \quad j = 1, \dots, M \quad (4.13)$$

and the  $M \times M$  Hessian matrix is

$$H_{j,k} = \frac{\partial^2 \tilde{L}(y, \lambda)}{\partial \lambda_j \partial \lambda_k} = \sum_{i=1}^N \left\{ \frac{y_i c_{i,j} c_{i,k}}{p_i^2} - \sum_{t=1}^T \frac{y_{i,t} c_{i,j,t} c_{i,k,t}}{p_{i,t}^2} \right\} \quad j, k = 1, \dots, M \quad (4.14)$$

The Hessian is not necessarily non-positive definite and one cannot exclude the existence of local maxima and of saddle points (beyond the undetermined global factor due to the scale invariance of the likelihood). However we recall the following result [63]. The proof is repeated for completeness.

*Proposition 2.* If the data are consistent the reduced log-likelihood has no local maximum.

*Proof.* Consistent data (belonging to the range of the TOF-PET transform) can be written as

$$y_{i,t} = a_i^\dagger p_{i,t}^\dagger \text{ with } p_{i,t}^\dagger = \sum_{j=1}^M c_{i,j,t} \lambda_j^\dagger \quad i = 1, \dots, N \quad t = 1, \dots, T \quad (4.15)$$

and  $p_i^\dagger = \sum_t p_{i,t}^\dagger$ , for some non-negative  $\lambda_j^\dagger \geq 0$  and  $a_i^\dagger > 0$ . From (4.13) one sees that  $\lambda^\dagger$  is a stationary point of the reduced log-likelihood and one verifies by inserting (4.15) in (4.12) that

$$\tilde{L}(y, \lambda^\dagger) = \sum_{i=1}^N \left\{ -y_i \log y_i + \sum_{t=1}^T y_{i,t} \log y_{i,t} \right\} \quad (4.16)$$

In addition  $\lambda^\dagger$  is a global maximizer. This can be seen by considering an arbitrary non-negative  $\lambda$  and by subtracting (4.12) from (4.16),

$$\tilde{L}(y, \lambda^\dagger) - \tilde{L}(y, \lambda) = \sum_{i=1}^N \left\{ y_i \log \frac{p_i}{y_i} - \sum_{t=1}^T y_{i,t} \log \left( \frac{p_{i,t}}{y_{i,t}} \right) \right\} \quad (4.17)$$

By the concavity of the log function

$$\sum_t \frac{y_{i,t}}{y_i} \log \left( \frac{p_{i,t}}{y_{i,t}} \right) \leq \log \left( \sum_t \frac{y_{i,t}}{y_i} \frac{p_{i,t}}{y_{i,t}} \right) = \log \frac{p_i}{y_i} \quad (4.18)$$

---

4. TRANSMISSION-LESS ATTENUATION CORRECTION IN TIME-OF-FLIGHT PET:  
ANALYSIS OF A DISCRETE ITERATIVE ALGORITHM.

---

and using this inequality in (4.17) shows that  $\tilde{L}(y, \lambda^\dagger) \geq \tilde{L}(y, \lambda)$ .

Consider now an arbitrary non-negative  $\lambda$ . Note first that  $\lambda^t \cdot \nabla \tilde{L}(y, \lambda) = 0$  and calculate the scalar product

$$\begin{aligned} Z &= (\lambda^\dagger)^t \cdot \nabla \tilde{L}(y, \lambda) = \sum_{i=1}^N \left\{ -\frac{y_i p_i^\dagger}{p_i} + \sum_{t=1}^T \frac{y_{i,t} p_{i,t}^\dagger}{p_{i,t}} \right\} \\ &= \sum_{i=1}^N \frac{1}{a_i^\dagger} \left\{ -\frac{y_i^2}{p_i} + \sum_{t=1}^T \frac{y_{i,t}^2}{p_{i,t}} \right\} \geq 0 \end{aligned} \quad (4.19)$$

where we used the data consistency  $a^\dagger p^\dagger = y$  (equation (4.15)) and the inequality follows from the convexity of the function  $x^2$  because

$$\sum_{t=1}^T \frac{y_{i,t}^2}{p_{i,t}} = p_i \sum_{t=1}^T \frac{p_{i,t}}{p_i} \left( \frac{y_{i,t}}{p_{i,t}} \right)^2 \geq p_i \left( \sum_{t=1}^T \frac{p_{i,t}}{p_i} \frac{y_{i,t}}{p_{i,t}} \right)^2 = \frac{y_i^2}{p_i} \quad (4.20)$$

Note that both in (4.18) and (4.19) the equality holds if and only if for all lines of response  $i = 1, \dots, N$  the ratios  $p_{i,t}/y_{i,t}$  are independent of  $t$ . In that case  $Z = 0$  and  $\lambda$  is also a global maximum of the reduced likelihood, i.e.  $\tilde{L}(y, \lambda) = \tilde{L}(y, \lambda^\dagger)$ .

The proof of Proposition 2 proceeds by contradiction. Suppose  $\tilde{\lambda}$  is a local maximum of the reduced log-likelihood. Consider the restriction of  $\tilde{L}$  to the segment linking  $\lambda^\dagger$  and  $\tilde{\lambda}$ :

$$U(\alpha) = \tilde{L}(y, \lambda_\alpha = \alpha \lambda^\dagger + (1 - \alpha) \tilde{\lambda}) \quad 0 \leq \alpha \leq 1 \quad (4.21)$$

Since we assumed that  $U(\alpha)$  has a local maximum in  $\alpha = 0$  and is maximum in  $\alpha = 1$ , its derivative

$$U'(\alpha) = (\lambda^\dagger - \tilde{\lambda})^t \cdot \nabla \tilde{L}(y, \lambda_\alpha) \quad (4.22)$$

must take strictly negative values somewhere in the interval  $(0, 1)$ . But this is in contradiction with inequality (4.19) because for  $0 < \alpha < 1$ , the derivative can be rewritten as

$$\begin{aligned} U'(\alpha) &= \frac{1}{1 - \alpha} \left( (\lambda^\dagger)^t \cdot \nabla \tilde{L}(y, \lambda_\alpha) - (\lambda_\alpha)^t \cdot \nabla \tilde{L}(y, \lambda_\alpha) \right) \\ &= \frac{1}{1 - \alpha} (\lambda^\dagger)^t \cdot \nabla \tilde{L}(y, \lambda_\alpha) \geq 0 \end{aligned} \quad (4.23)$$

and this is non-negative by (4.19). Local maxima are therefore impossible when the data are consistent.  $\square$

#### 4.2.4 A surrogate approach and the MLACF algorithm

We consider some activity image  $\tilde{\lambda}$  and the corresponding unattenuated data expectations

$$\tilde{p}_{i,t} = \sum_{j=1}^M c_{i,j,t} \tilde{\lambda}_j \quad i = 1, \dots, N \quad t = 1, \dots, T \quad (4.24)$$

and  $\tilde{p}_i = \sum_t \tilde{p}_{i,t}$ . We assume in this section that all images are strictly positive,  $\lambda_j > 0, j = 1, \dots, M$ . As will be seen in section 4.2.5 (Lemma 3) this assumption holds for the iterated solutions defined by the algorithm derived below.

Aiming at the iterative optimization of the reduced likelihood by optimization transfer [111], we build a function  $\tilde{L}^{sur}(y, \lambda, \tilde{\lambda})$ , with the usual surrogate properties

$$\begin{aligned}\tilde{L}^{sur}(y, \tilde{\lambda}, \tilde{\lambda}) &= \tilde{L}(y, \tilde{\lambda}) \\ \tilde{L}^{sur}(y, \lambda, \tilde{\lambda}) &\leq \tilde{L}(y, \lambda).\end{aligned}\quad (4.25)$$

Such a surrogate function can be obtained by considering separately the two terms in (4.12). For the *first term* the rooftop theorem for the concave log function yields

$$\log p_i \leq \log \tilde{p}_i + (p_i - \tilde{p}_i) \left( \frac{d \log p_i}{dp_i} \right)_{p_i=\tilde{p}_i} = \log \tilde{p}_i + \frac{p_i - \tilde{p}_i}{\tilde{p}_i} \quad (4.26)$$

and therefore

$$-y_i \log(p_i) \geq -y_i \log \tilde{p}_i - \frac{y_i (p_i - \tilde{p}_i)}{\tilde{p}_i} \quad (4.27)$$

For the *second term* in (4.12) define the quantities

$$w_{i,j,t} = \frac{c_{i,j,t} \tilde{\lambda}_j}{\tilde{p}_{i,t}} \quad z_{i,j,t} = \frac{\lambda_j \tilde{p}_{i,t}}{\tilde{\lambda}_j} \quad (4.28)$$

which satisfy  $w_{i,j,t} \geq 0$ ,  $\sum_j w_{i,j,t} = 1$ , and  $\sum_j w_{i,j,t} z_{i,j,t} = p_{i,t}$ . Since the log is concave, one has then for each  $i, t$  that

$$\log p_{i,t} = \log \left( \sum_j w_{i,j,t} z_{i,j,t} \right) \geq \sum_{j=1}^M w_{i,j,t} \log z_{i,j,t} \quad (4.29)$$

Putting the two terms together and summing over the data bins yields

$$\tilde{L}^{sur}(y, \lambda, \tilde{\lambda}) = \sum_{i=1}^N \left\{ -y_i \log \tilde{p}_i - \frac{y_i (p_i - \tilde{p}_i)}{\tilde{p}_i} + \sum_{t=1}^T \sum_{j=1}^M \frac{y_{i,t} c_{i,j,t} \tilde{\lambda}_j}{\tilde{p}_{i,t}} \log \left( \frac{\lambda_j \tilde{p}_{i,t}}{\tilde{\lambda}_j} \right) \right\} \quad (4.30)$$

One easily checks using (4.27) and (4.29) that this function satisfies the two properties (4.25) and is therefore a valid surrogate for the reduced likelihood. In addition  $\tilde{L}^{sur}$  is separable (i.e. equal to a sum of terms, each of which depends on a single voxel  $\lambda_j$ ) and hence easy to maximize.

The gradient of the surrogate is

$$\nabla \tilde{L}_j^{sur} = \frac{\partial \tilde{L}^{sur}(y, \lambda, \tilde{\lambda})}{\partial \lambda_j} = \sum_{i=1}^N \left\{ -\frac{y_i c_{i,j}}{\tilde{p}_i} + \sum_{t=1}^T \frac{y_{i,t} c_{i,j,t} \tilde{\lambda}_j}{\tilde{p}_{i,t}} \frac{1}{\lambda_j} \right\} \quad (4.31)$$

The Hessian matrix is diagonal and negative semi-definite,

$$\frac{\partial^2 \tilde{L}^{sur}(y, \lambda, \tilde{\lambda})}{\partial \lambda_j^2} = -\frac{\tilde{\lambda}_j}{\lambda_j^2} \sum_{i=1}^N \sum_{t=1}^T \frac{y_{i,t} c_{i,j,t}}{\tilde{p}_{i,t}} \leq 0 \quad (4.32)$$

---

#### 4. TRANSMISSION-LESS ATTENUATION CORRECTION IN TIME-OF-FLIGHT PET: ANALYSIS OF A DISCRETE ITERATIVE ALGORITHM.

---

hence the surrogate is concave and has no local maxima.

Solving  $\nabla \tilde{L}^{sur} = 0$  we obtain an iterative update which maps the estimate  $\tilde{\lambda}$  on a new estimate  $\lambda$  [63]:

$$\lambda_j = \mathcal{T}(\tilde{\lambda})_j = \frac{\tilde{\lambda}_j}{\sum_{i=1}^N \frac{y_i c_{i,j}}{\tilde{p}_i}} \sum_{i=1}^N \sum_{t=1}^T \frac{y_{i,t} c_{i,j,t}}{\tilde{p}_{i,t}} \quad (4.33)$$

Applying this mapping iteratively with  $\tilde{\lambda} = \lambda^k$  and  $\lambda = \lambda^{k+1}$ , where  $k$  denotes the iteration number, defines the MLACF algorithm. Some remarks are in order:

- The algorithm is closely related to the usual maximum-likelihood-expectation-maximization (ML-EM) algorithm for emission tomography with known attenuation. The similarity is best appreciated by rewriting (4.33) in the same form as ML-EM with attenuation factors  $a_i^* = y_i/\tilde{p}_i$  defined according to (4.7):

$$\mathcal{T}(\tilde{\lambda})_j = \frac{\tilde{\lambda}_j}{\sum_{i,t} a_i^* c_{i,j,t}} \sum_{i,t} \frac{y_{i,t} c_{i,j,t}}{\tilde{p}_{i,t}} \quad (4.34)$$

- The curvature of the surrogate is high along axes  $j$  for which  $\lambda_j$  is small, resulting as with ML-EM in a slow convergence of the "cold" voxels.
- The algorithm is scale invariant: multiplying the initial estimate by a factor  $\alpha > 0$  produces the same sequence of iterates, all multiplied by  $\alpha$ . This is expected since the solution is determined only up to a factor. In practice, the activity image  $\lambda$  can be rescaled at each iteration, e.g. to guarantee that  $\max_i a_i^* = 1$  or that  $\|\lambda\| = 1$ . We chose the latter option and define the *normalized MLACF algorithm* with the mapping:

$$\mathcal{T}_N(\tilde{\lambda}) = \frac{1}{\|\mathcal{T}(\tilde{\lambda})\|} \mathcal{T}(\tilde{\lambda}) \quad (4.35)$$

with the  $L_2$  norm  $\|x\| = (\sum_j x_j^2)^{1/2}$ .

- In the non-TOF case, there is only a single time bin,  $T = 1$ . The mapping (4.33) reduces then to the  $M \times M$  identity  $\mathcal{T} = \mathbb{I}$ .

##### 4.2.5 Active data bins and the handling of zeroes

In the previous sections, the reduced log-likelihood (4.12), the surrogate (4.30), and the MLACF iteration (4.33) have been defined assuming that  $p_{i,t} > 0$  and  $p_i > 0$ , unless the corresponding data are also zero.

Define the set of active data bins for a given voxel as:

$$\tau_j = \{(i, t) \mid c_{i,j,t} y_{i,t} > 0\} \quad j = 1, \dots, M \quad (4.36)$$

and adopt an equivalent definition for the TOF-summed data,

$$\iota_j = \{i \mid c_{i,j} y_i > 0\} \quad j = 1, \dots, M \quad (4.37)$$

Note that  $\iota_j = \emptyset \Rightarrow \tau_j = \emptyset$ . If for some voxel  $\tau_j = \emptyset$ , then

$$\frac{\partial \tilde{L}(y, \lambda)}{\partial \lambda_j} = \sum_{i \in \iota_j} \left\{ -\frac{y_i c_{i,j}}{p_i} \right\} \leq 0 \quad (4.38)$$

and therefore any maximizer of the reduced log-likelihood satisfies  $\lambda_j = 0$  (because of the non-negativity constraint). If in addition  $\iota_j = \emptyset$  the reduced log-likelihood does not depend on the value of voxel  $j$ , the maximizer is undefined and we chose the logical (but arbitrary) estimate  $\lambda_j = 0$ . These inactive voxels with  $\tau_j = \emptyset$  can be set to zero and need not be further considered when maximizing  $\tilde{L}(y, \lambda)$ . We therefore assume from now on that  $\tau_j \neq \emptyset$  for  $j = 1, \dots, M$ . We will also assume that  $y_i \geq 1$  and  $y_{i,t} \geq 1$  for all non-zero data bins.

Having thus discarded the inactive voxels, one easily shows that the MLACF iterates are strictly positive:

*Lemma 3.* If  $\lambda_j^0 > 0, j = 1, \dots, M$ , the MLACF iterates defined by the sequence  $\lambda^{n+1} = \mathcal{T}_N(\lambda^n)$  are strictly positive, i.e.  $\lambda_j^n > 0, j = 1, \dots, M$ .

*Proof.* If  $\lambda_j^n > 0, j = 1, \dots, M$ , then  $p_{i,t}^n > 0$  for all  $(i, t)$ , and hence also  $p_i^n = \sum p_{i,t}^n > 0$ . Therefore the MLACF update  $\lambda^{n+1} = \mathcal{T}(\lambda^n)$  defined by (4.33) produces a positive image,  $(\mathcal{T}(\lambda^n))_j > 0, j = 1, \dots, M$ . Applying this recursively, and starting from a positive initial image estimate  $\lambda^0$  proves the lemma.  $\square$

The positivity property of Lemma 3 does not exclude that the MLACF iterates might converge to a limit point having some zero voxels,  $\lambda_j^n \rightarrow 0$ . One needs therefore to extent the definition of the reduced likelihood. If for some data bin  $(i, t)$ ,  $y_{i,t} > 0$  and  $p_i > 0$  but  $p_{i,t} = 0$ , it is natural to define  $\tilde{L}(y, \lambda) = -\infty$ , which is the limit of (4.12) when  $p_{i,t} \rightarrow 0$ . If in addition  $p_i = 0$ , the ratio  $p_{i,t}/p_i$  and the reduced log-likelihood are undetermined. In this latter case ( $p_i = 0$  and  $y_i > 0$  for some LOR  $i$ ), it is impossible (even by rescaling) to satisfy the constraint that  $a_i^* = y_i/p_i \leq 1$  (see equation (4.6)).

#### 4.2.6 Convergence of MLACF

The following proposition gives the main properties of the MLACF algorithm. The proof is given in appendix.

*Proposition 4.* Consider the sequence of *normalized* iterates  $\lambda^{n+1} = T_N(\lambda^n)$  with a positive initial image  $\lambda_j^0 > 0$ .

- The sequence of iterates is asymptotically regular,  $\|\lambda^{n+1} - \lambda^n\| \rightarrow 0$  as  $n \rightarrow \infty$ , and the reduced likelihood is non-decreasing,  $\tilde{L}(y, \lambda^{n+1}) \geq \tilde{L}(y, \lambda^n)$ .
- The sequence has a limit point  $\lambda^*$ , and  $\nabla_j \tilde{L}(y, \lambda^*) = 0$  for any voxel satisfying  $\lambda_j^* > 0$ .
- All limit points of the sequence  $\lambda^{n+1} = T_N(\lambda^n)$  have the same value of the reduced log-likelihood.

---

#### 4. TRANSMISSION-LESS ATTENUATION CORRECTION IN TIME-OF-FLIGHT PET: ANALYSIS OF A DISCRETE ITERATIVE ALGORITHM.

---

This result provides only a partial understanding of the convergence of MLACF. The limit points cannot be minima because  $\tilde{L}$  is non-decreasing, but they might be saddle points or local maxima because there is no guarantee that the Hessian (4.14) is concave. Proposition 4 guarantees convergence of MLACF only under the restrictive additional assumptions that a) the likelihood has a unique global maximum  $\lambda^\dagger$  such that  $\lambda_j^\dagger > 0$  for all active voxels ( $\tau_j \neq \emptyset$ ), and b) all limit points  $\lambda^*$  of the sequence of iterates are such that  $\lambda_j^* > 0$  for all active voxels.

### 4.3 Numerical results

#### 4.3.1 Simulation parameters

We digitized a 2D thorax phantom on a  $M = 64 \times 64$  image with pixel size 8.027 mm. Simulated TOF-PET data are generated by forward projecting this phantom with radial pixel size 8.027 mm, 64 angular samples on  $[0, \pi)$ , and  $T = 8$  times bins with sampling  $\Delta\tau = 64.0$  mm. The TOF profile was a Gaussian with a FWHM of 80 mm. The aim of this study is not to assess the practical value of MLACF but to get insight into its convergence and uniqueness properties, hence this coarse discretization was chosen to allow performing a very large number of iterations with various initial estimates  $\lambda^0$ . The activity and attenuation images are shown in Figure 4.1, the phantom support is an ellipse with axes 300 mm and 470 mm and the minimum attenuation factor  $a_i$  was 0.015. A vial with activity 0.5, diameter 40 mm, and water attenuation was added outside the phantom and used to scale the reconstructed activity image at the end of the reconstruction. Poisson noise was added to the data to generate three noisy data sets S1, S2 and S3 with respectively a total of 479705, 15990 and 3198 events, corresponding to respectively 300, 10, and 2 events in the maximum data bin  $\langle y_{i,t} \rangle$ . A large number of data bins are equal to zero in data set S3, allowing to challenge the algorithm's behaviour at the edge of the admissible domain. When generating the noisy data, a rescaling is applied after adding noise to ensure that  $\sum y_i$  is the same for the three data sets S1, S2 and S3, up to statistical fluctuations.

The MLACF iteration was run up to  $10^5$  iterations (without using data subsets and with a matched backprojector), starting with a uniform image estimate  $\lambda_j^0 = 1$  and with a set of 30 random initial images generated as  $\lambda_j^0 = 0.1 + 0.9R$  where  $R$  is a pseudo-random number with uniform distribution in  $(0, 1)$ . All calculations were done in double precision. Initially we replaced the ratios  $y_{i,t}/p_{i,t}$  and  $y_i/p_i$  in the numerator and denominator of the MLACF update (4.33) by zero when  $p_{i,t}$  (respectively  $p_i$ ) was smaller than some small  $\epsilon$ , however we found that this margin is not needed and it is not used in the results presented here.

#### 4.3.2 Convergence

Figure 4.2 shows the activity image reconstructed starting from a uniform initial image. Figure 4.3, 4.4 and 4.5 show the convergence of the reduced log-likelihood for the three noise levels. We verified that  $\tilde{L}(y, \lambda^n)$  monotonically increases for all

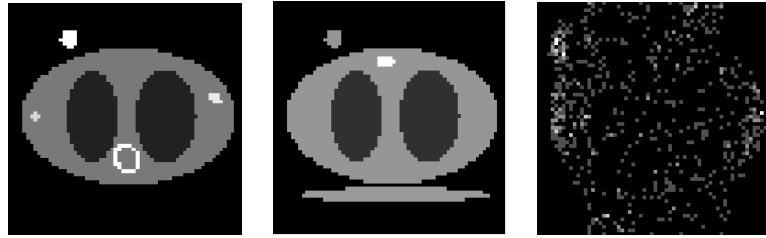


Figure 4.1: The simulated phantom. Emission (left): activity is 0.2 (background tissues), 1.7 ("heart"), 0.05 ("lungs"), 0.40 and 0.45 ("tumors"), and 0.5 (vial). Attenuation (middle): 0.00966/mm (background tissues and vial), 0.00266/mm ("lungs"), 0.0187/mm ("spine"), and 0.01/mm ("bed"). Right: sinogram of the central TOF bin of the noisiest data S3, illustrating the large number of bins ( $i, t$ ) with zero counts. The displayed sinogram only has five different grey levels corresponding to 0,1,2,3 and 4 events.

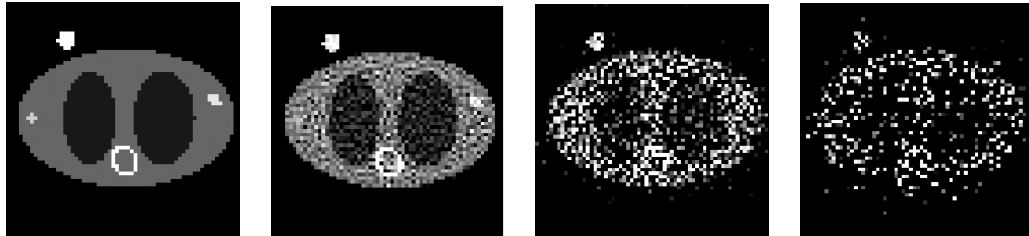


Figure 4.2: The activity image reconstructed from noise-free data and from the data sets S1, S2 and S3 (left to right). Grey scale (0, 0.5).

data sets, initializations, and iterations, even though the convergence becomes slower with increasing noise level. Figure 4.3 and 4.5 also show the difference between the reduced log-likelihood obtained with a uniform estimate and with one particular random initialization.

In some cases (Figure 4.4), the convergence is irregular, with long sequences of iterates without significant improvement of the cost function. The second set of points in Figure 4.4 is obtained applying exactly the same algorithm but to a different realization S2' of the noisy data, for the same maximum count as S2. This result shows that the irregular convergence observed with S2 is specific to a particular noise realization. Figure 4.6 compares for that data set S2 the solution during that convergence plateau and at the last iteration. The convergence of the iterates shown in Figure 4.7 appears compatible with the asymptotic regularity of the algorithm predicted by Proposition 4.

#### 4. TRANSMISSION-LESS ATTENUATION CORRECTION IN TIME-OF-FLIGHT PET: ANALYSIS OF A DISCRETE ITERATIVE ALGORITHM.

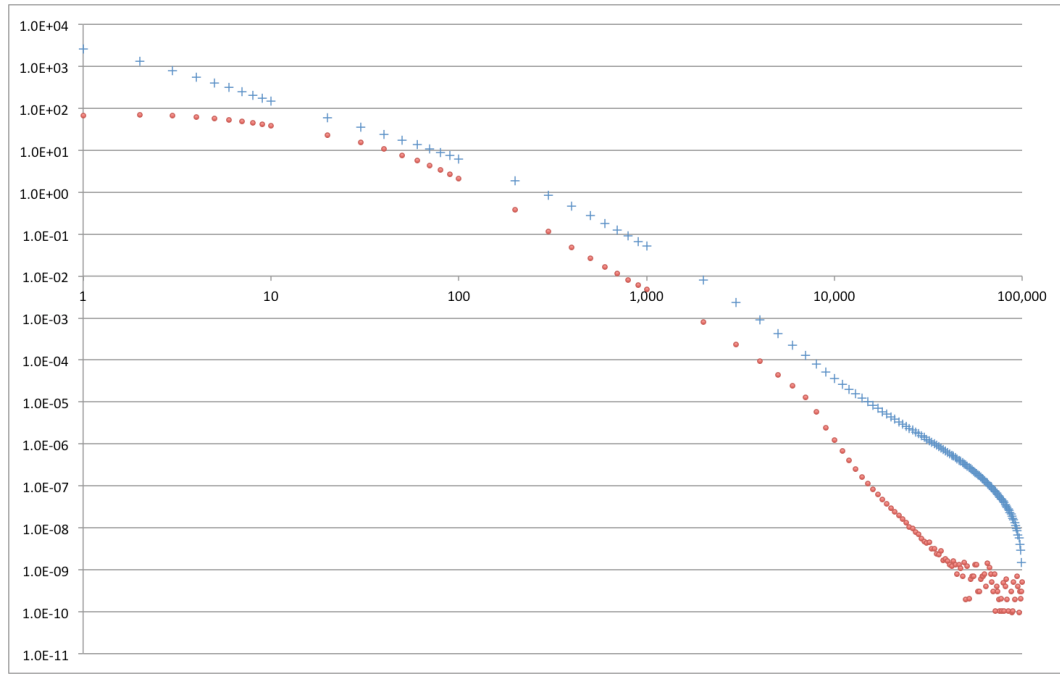


Figure 4.3: The reduced log-likelihood  $-\tilde{L}(y, \lambda^n) + \tilde{L}(y, \lambda^{100000})$  for the low noise data set S1 (blue +), and the difference  $|\tilde{L}(y, \lambda^n) - \tilde{L}(y, \lambda'^n)|$ , (red circles), versus the number of iterations  $n$ . The sequences  $\lambda^n$  and  $\lambda'^n$  are obtained respectively with a uniform and one of the random initial images.

##### 4.3.3 Uniqueness

Unless the data are consistent (see Proposition 2), we were not able to determine whether the reduced log-likelihood has a unique (up to the undetermined scale factor) global maximum. To get some insight into the possible existence of local maxima and of saddle points we compared the reconstructions obtained with the 31 initial activity images described in section 4.3.1. First we compare the final values of the reduced likelihood after  $10^5$  MLACF iterations. The ratio  $(\max(\tilde{L}(y, \lambda^{10^5})) - \min(\tilde{L}(y, \lambda^{10^5}))/|\text{mean}(\tilde{L}(y, \lambda^{10^5}))|$  is equal to  $5.7 \times 10^{-14}$ ,  $4.2 \times 10^{-9}$ , and  $4.4 \times 10^{-4}$  for the data sets S1, S2 and S3 respectively. Figure 4.8 shows a plot of the relative RMSE difference  $||\lambda - \lambda'||/||\lambda||$  between all pairs of images  $\lambda, \lambda'$  reconstructed for each data set using different initializations, with the values sorted by increasing magnitudes. The RMSE differences are small for S1 and do not show any particular structure, and the same behaviour is observed for S2 (not shown). For the noisiest data set S3, however, the RMSE are larger and the plot shows some structure. This structure might suggest convergence to different images, but might also be caused by the slow convergence or by numerical errors. For very noisy data sets the question of uniqueness remains open, though Figure 4.9 shows that the differences between reconstructions obtained with different initial images are visually small.

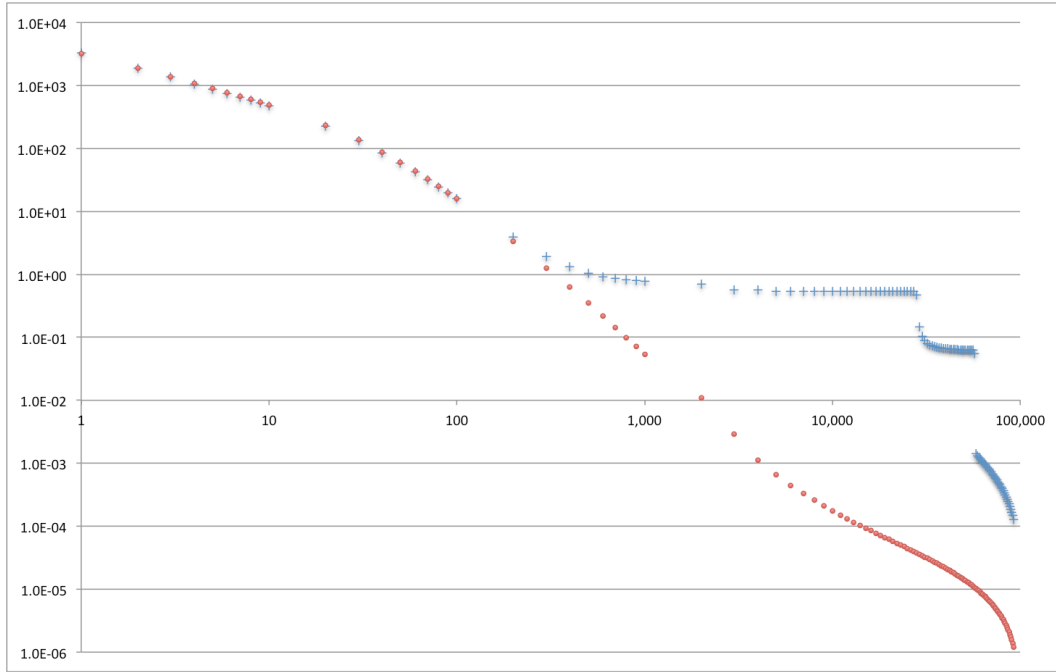


Figure 4.4: The reduced log-likelihood  $-\tilde{L}(y, \lambda^n) + \tilde{L}(y, \lambda^{100000})$  for the medium noise data set S2 (blue +), and for another data set S2' with the same total count, (red circles), versus the number of iterations  $n$ . The sequences  $\lambda^n$  are obtained with a uniform initial images.

#### 4.3.4 Comparison with OSEM

The MLACF algorithm estimates the activity image without using any information on the attenuation. To evaluate the influence this lack of information has on convergence, we reconstructed the same data using ML-EM, assuming that the exact value of the attenuation factors  $a_i$  is known:

$$\lambda_j^{n+1} = \frac{\lambda_j^n}{\sum_{i=1}^N a_i c_{i,j}} \sum_{i=1}^N \sum_{t=1}^T \frac{y_{i,t} c_{i,j,t}}{p_{i,t}^n} \quad (4.39)$$

The ML-EM implementation uses the same ingredients as MLACF (matched back-projector, double precision arithmetic). Figure 4.7 shows that ML-EM has a faster and more regular convergence, and the difference is more marked for the low count case. Since the goal of this work is to study convergence, the ML-EM and MLACF reconstructions have not been regularized. Nevertheless, Figure 4.10 shows that the unregularized reconstructed ML-EM and MLACF activity images have similar noise level and structure, though as expected the ML-EM reconstructions are better. This observation and the RMSE data in Table 1 suggest that the redundancy of the TOF data is sufficient to avoid dramatic image degradation by the absence of attenuation information.

4. TRANSMISSION-LESS ATTENUATION CORRECTION IN TIME-OF-FLIGHT PET:  
ANALYSIS OF A DISCRETE ITERATIVE ALGORITHM.

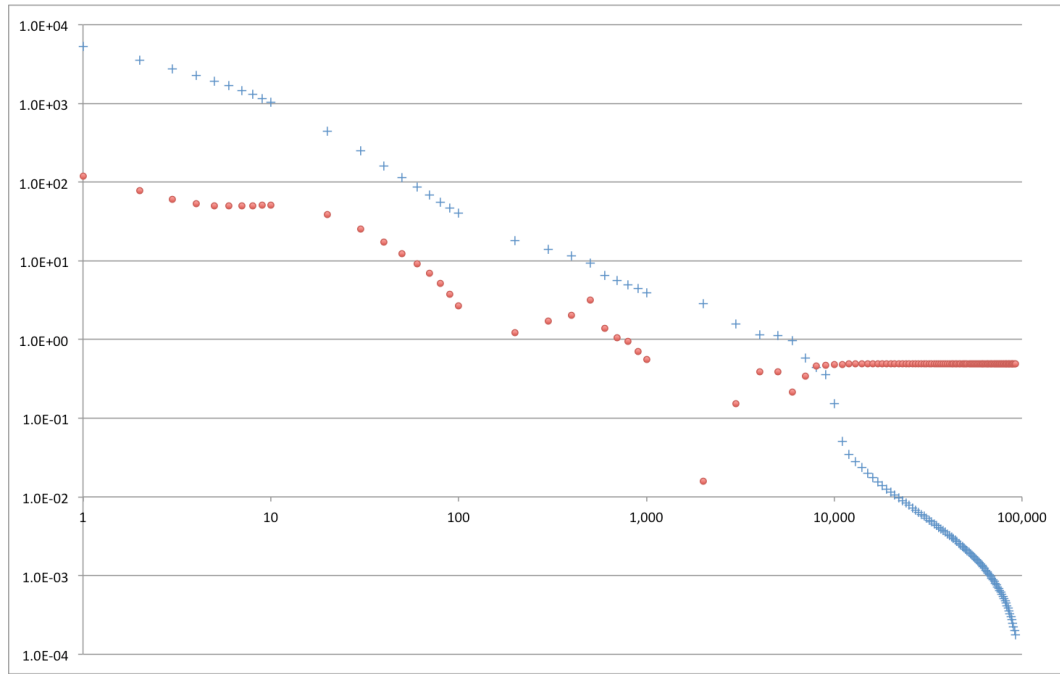


Figure 4.5: The reduced log-likelihood  $-\tilde{L}(y, \lambda^n) + \tilde{L}(y, \lambda^{100000})$  for the high noise data set S3 (blue +), and the difference  $|\tilde{L}(y, \lambda^n) - \tilde{L}(y, \lambda'^n)|$ , (red circles), versus the number of iterations  $n$ . The sequences  $\lambda^n$  and  $\lambda'^n$  are obtained respectively with a uniform and one of the random initial images.

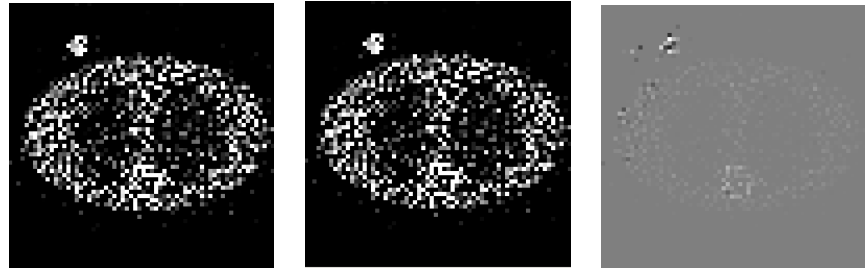


Figure 4.6: The activity image reconstructed from data set S2 with  $10^5$  (left) and 5000 (center) iterations, with grey scale (0, 0.5). The right image is the difference, grey scale  $(-0.015, +0.015)$ .

Figure 4.11 compares the log-likelihood (4.3) obtained with ML-EM and MLACF. The values for MLACF are calculated as  $L(y, \lambda, a^*(\lambda)) = \tilde{L}(y, \lambda) + \sum_i (-y_i + y_i \log(y_i))$ . The likelihood converges to a larger value with MLACF than with ML-EM since MLACF does not fix the attenuation factors a priori and therefore has more degrees of freedom available to maximize the likelihood. For the same reason the difference between MLACF and ML-EM increases as the number of counts decreases.

### 4.3. Numerical results

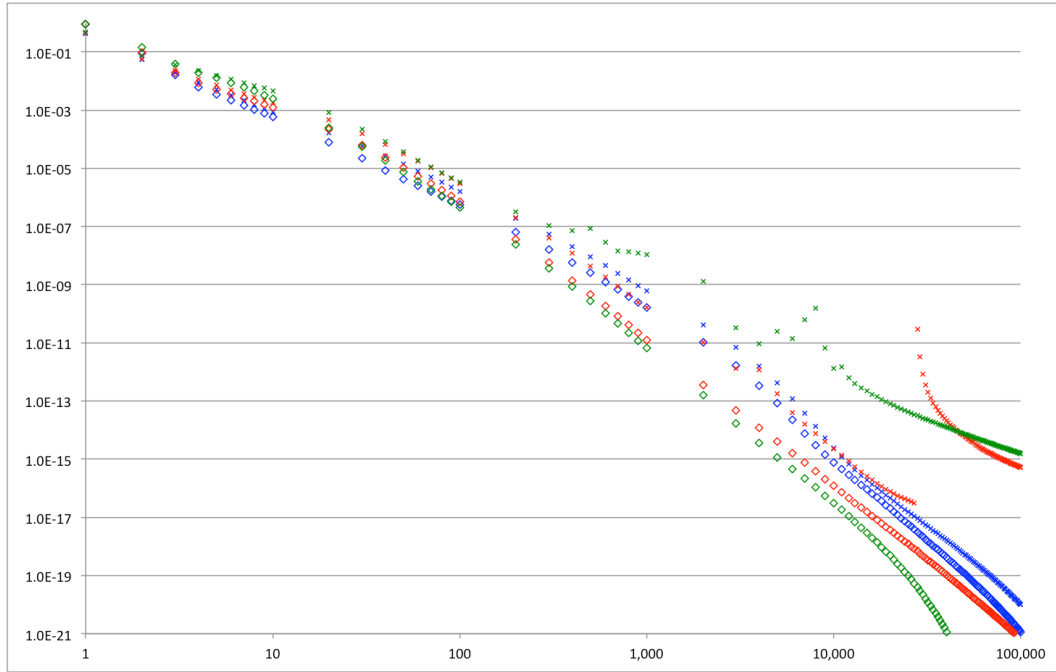


Figure 4.7: The value of  $\|\lambda^{n+1} - \lambda^n\|^2 / \|\lambda^n\|^2$  versus iteration number  $n$  for data set S1 (blue), S2 (red), and S3 (green). The sequences  $\lambda^n$  are obtained with the ML-EM algorithm with known attenuation factors  $a$  (diamonds) and with MLACF (x), both starting with a uniform initial image.

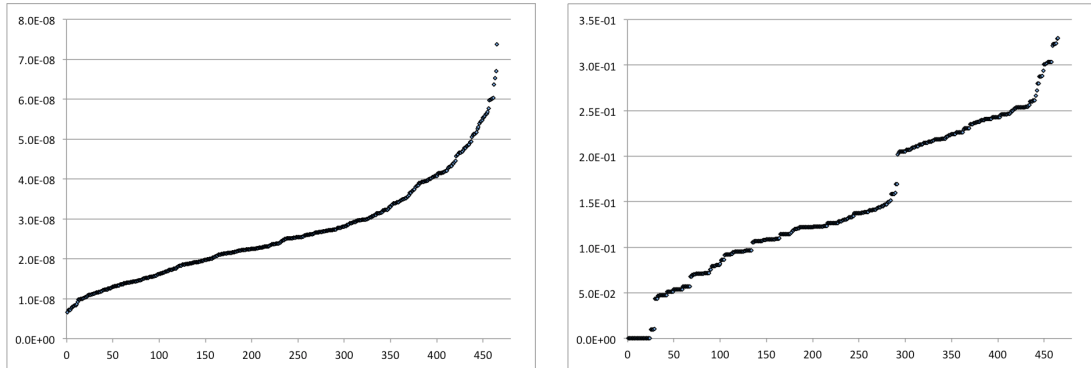


Figure 4.8: The relative RMSE difference between all pairs among 31 reconstructions from data set S1 (left) and among 31 reconstructions from data set S3 (right). The values are sorted by increasing magnitudes. All reconstructions use  $10^5$  MLACF iterations but starting from the different initial images described in section 4.3.1.

Finally, the three data sets have been reconstructed using 100000 iterations of ML-EM, with the same 31 initial images as used in section 4.3.3. In contrast with

#### 4. TRANSMISSION-LESS ATTENUATION CORRECTION IN TIME-OF-FLIGHT PET: ANALYSIS OF A DISCRETE ITERATIVE ALGORITHM.



Figure 4.9: The activity image reconstructed from the data set S3 with the two random initial images that resulted in the largest RMSE difference (0.33). Grey scale (0, 0.5). Right: Difference image, grey scale ( $-0.5, +0.5$ ).

Table 4.1: Relative RMSE differences between reconstructed and exact activity images (uniform initial image,  $10^5$  iterations).

	noise free	data S1 max. count 300	data S2 max. count 10	data S3 max. count 2
ML-EM vs. phantom	$8.53 \times 10^{-6}$	$2.48 \times 10^{-1}$	$9.24 \times 10^{-1}$	1.66
MLACF vs. phantom	$1.93 \times 10^{-5}$	$2.05 \times 10^{-1}$	1.16	1.54
MLACF vs. ML-EM	$1.64 \times 10^{-5}$	$1.94 \times 10^{-1}$	$6.42 \times 10^{-1}$	$8.58 \times 10^{-1}$

the similar comparison for MLACF in section 4.3.3, the relative RMSE differences between pairs of images reconstructed for each data set are all lower than  $10^{-10}$ , even for the noisiest case S3. This observation is expected since ML-EM is known to converge to the unique maximizer of the likelihood, but it suggests that the RMSE shown in Figure 4.8 can probably not be attributed to numerical errors.

## 4.4 Conclusion

Several groups have shown that time-of-flight PET allows to simultaneously estimate the activity and attenuation images. These results open new perspectives for various applications including for example stand-alone PET, PET-CT studies where patient motion prevents the direct utilization of the CT data for attenuation correction, PET-CT studies with a reduced CT field-of-view, and also potential applications in PET-MR.

The maximum likelihood method for this problem can use as unknown parameter either the attenuation image or the attenuation factors. Promising results have been obtained with the two approaches, but fundamental questions remain concerning the uniqueness of the maximum likelihood estimator and the convergence of the iterative algorithms. The difficulty with this non-linear inverse problem stems from the non-concavity of the likelihood, and we were only able to prove uniqueness of the maximum likelihood estimator when the data are consistent.

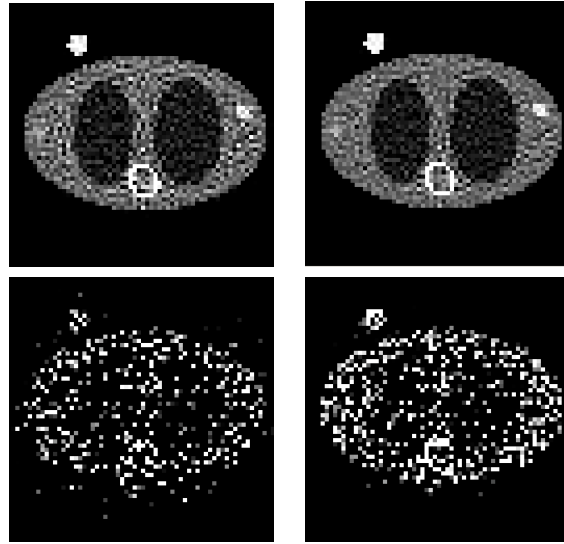


Figure 4.10: The activity image reconstructed from data set S1 (top row) and S3 (bottom row) with  $10^5$  iterations. Left: MLACF. Right: ML-EM with known attenuation. Grey scale (0, 0.5).

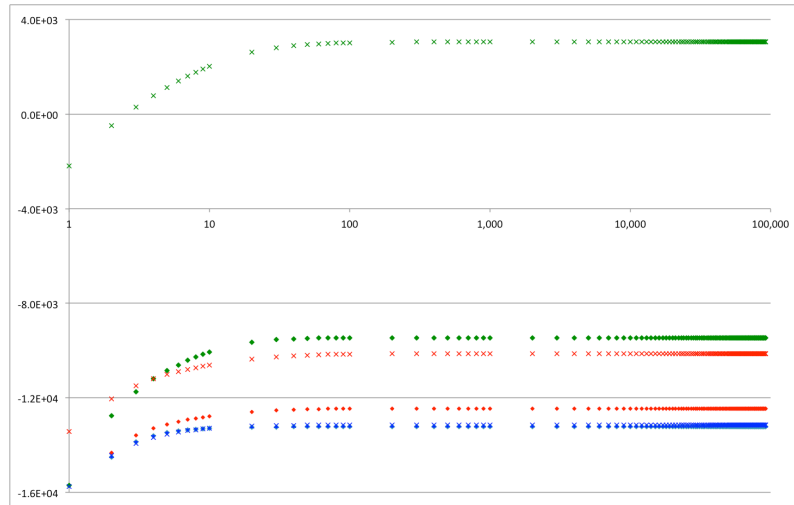


Figure 4.11: The log-likelihood  $L(y, a, \lambda^n)$  versus iteration number  $n$  for data set S1 (blue), S2 (red) and S3 (green). The sequences  $\lambda^n$  are obtained with the ML-EM algorithm (diamonds) with known attenuation factors  $a$ , and with MLACF ( $\times$ ), both starting with a uniform initial image.

This paper dealt with the second approach, which takes the attenuation factors and activity image as unknown parameters. We assumed that the scatter and random background is negligible or has been pre-corrected and showed that this

---

#### 4. TRANSMISSION-LESS ATTENUATION CORRECTION IN TIME-OF-FLIGHT PET: ANALYSIS OF A DISCRETE ITERATIVE ALGORITHM.

---

assumption allows eliminating the attenuation parameters. This led to an iterative algorithm, MLACF [63], which only updates the activity image. Attractive properties of MLACF include its simplicity and similarity with ML-EM, the monotonic increase of the likelihood, and the asymptotic regularity (the norm of the solution increments tends to zero). Convergence however could not be proven in general. We conducted simulation studies with the unregularized MLACF algorithm and with a number of iterations much larger than would be applied in practice. The results give reasonable confidence that MLACF converges in practice to a unique maximizer of the likelihood, except for extremely noisy data sets. Additional studies are warranted for that case.

### Acknowledgements

This work is supported by a grant of the Fonds voor Wetenschappelijk Onderzoek Vlaanderen (F.W.O.). The authors thank Girish Bal, Mike Casey, Maurizio Conti, Christian Michel, Vladimir Panin and Charles Watson (Siemens Healthcare, Molecular Imaging, Knoxville, TN) for useful discussions.

### 4.5 Appendix: convergence of the MLACF algorithm.

Let  $\lambda^n, n = 0, 1, 2, \dots$  be the sequence of iterates generated by a positive initial estimate  $(\lambda^0)_j > 0$  and by the update step  $\lambda^n = \mathcal{T}_N(\lambda^{n-1})$  defined by the normalized mapping (4.35). This appendix presents the proof of proposition 4. The general line of the analysis follows the scheme in [112].

The following positive quantities will be used:

$$\begin{aligned}\xi_j &= \min_{i \in \iota_j} c_{i,j} > 0 \quad , \quad \xi = \min_j \xi_j > 0 \\ \eta_j &= \min_{(i,t) \in \tau_j} c_{i,j,t} > 0 \quad , \quad \eta = \min_j \eta_j > 0 \\ \omega &= \max_i \sum_j c_{i,j} \quad , \quad \sigma = \max_{i,t} \sum_j c_{i,j,t} > 0\end{aligned}\tag{4.40}$$

*Lemma 5.* The sequence  $\tilde{L}(y, \lambda^n), n = 0, 1, 2, \dots$  is non-decreasing and converges.

*Proof.* The iterates are obtained by optimization transfer and the surrogate properties (4.25) guarantee by construction that the sequence  $\tilde{L}(y, \lambda^n), n = 0, 1, 2, \dots$  is non-decreasing. The positivity of the  $\lambda^n$  (Lemma 3) and of the system matrix elements  $c_{i,j,t}$  guarantee that  $p_{i,t}^n \leq p_i^n$ , and therefore

$$\tilde{L}(y, \lambda^n) = \sum_{i=1}^N \sum_{t=1}^T y_{i,t} \log \frac{p_{i,t}^n}{p_i^n} \leq 0\tag{4.41}$$

so that the sequence  $\tilde{L}(y, \lambda^n)$  is bounded above by 0. A non-decreasing upper bounded sequence converges.  $\square$

#### 4.5. Appendix: convergence of the MLACF algorithm.

---

*Lemma 6.* Let  $\tilde{\lambda} \in \text{IR}^M$  be any positive vector. The following inequality holds for the non-normalized mapping  $\mathcal{T}$  in (4.33):

$$\tilde{L}(y, \mathcal{T}(\tilde{\lambda})) - \tilde{L}(y, \tilde{\lambda}) \geq \frac{1}{2} \sum_j \left( \mathcal{T}(\tilde{\lambda}) - \tilde{\lambda} \right)_j^2 \frac{\tilde{\lambda}_j}{\tilde{\lambda}_j^2} \sum_{(i,t) \in \tau_j} \frac{y_{i,t} c_{i,j,t}}{\tilde{p}_{i,t}} \quad (4.42)$$

where  $\bar{\lambda} = \alpha \mathcal{T}(\tilde{\lambda}) + (1 - \alpha) \tilde{\lambda}$  for some  $0 \leq \alpha \leq 1$ .

*Proof.* For any positive  $x \in \text{IR}^M$  and a fixed  $\tilde{\lambda}$ , we can represent  $\tilde{L}^{sur}(y, x, \tilde{\lambda})$  by a Taylor expansion around its maximizer  $\lambda = \mathcal{T}(\tilde{\lambda})$ . Using the fact that  $\nabla_\lambda \tilde{L}^{sur}(y, \lambda, \tilde{\lambda}) = 0$ ,

$$\tilde{L}^{sur}(y, x, \tilde{\lambda}) = \tilde{L}^{sur}(y, \lambda, \tilde{\lambda}) + \frac{1}{2} (x - \lambda)^t \cdot \nabla^2 \tilde{L}^{sur}(y, \bar{\lambda}, \tilde{\lambda}) \cdot (x - \lambda) \quad (4.43)$$

where the Hessian is taken at some point  $\bar{\lambda}$  on the segment linking  $\lambda$  to  $x$ . Rewriting this equation at  $x = \tilde{\lambda}$ , using from (4.25) the surrogate properties  $\tilde{L}^{sur}(y, \tilde{\lambda}, \tilde{\lambda}) = \tilde{L}(y, \tilde{\lambda})$  (for the LHS) and  $\tilde{L}^{sur}(y, \lambda, \tilde{\lambda}) \leq \tilde{L}(y, \lambda)$  (for the RHS), one obtains

$$\tilde{L}(y, \tilde{\lambda}) \leq \tilde{L}(y, \lambda) + \frac{1}{2} (\tilde{\lambda} - \lambda)^t \cdot \nabla^2 \tilde{L}^{sur}(y, \bar{\lambda}, \tilde{\lambda}) \cdot (\tilde{\lambda} - \lambda) \quad (4.44)$$

Using the diagonal non-positive Hessian (4.32) concludes the proof.  $\square$

*Lemma 7.* Let  $\tilde{\lambda} \in \text{IR}^M$  be any positive vector with  $\|\tilde{\lambda}\| = 1$ .

$$\tilde{L}(y, \mathcal{T}(\tilde{\lambda})) - \tilde{L}(y, \tilde{\lambda}) \geq C \frac{\|\mathcal{T}(\tilde{\lambda}) - \tilde{\lambda}\|^2}{\max(1, \|\mathcal{T}(\tilde{\lambda})\|)} \quad (4.45)$$

where  $\mathcal{T}$  is the mapping (4.33) and  $C = (1/2) \min(\xi/\omega, \eta/\sigma) > 0$ .

*Proof.* Define  $\lambda = \mathcal{T}(\tilde{\lambda})$  and denote the curvature factor in (4.42) as

$$\rho_j = \frac{\tilde{\lambda}_j}{(\alpha \lambda_j + (1 - \alpha) \tilde{\lambda}_j)^2} \sum_{(i,t) \in \tau_j} \frac{y_{i,t} c_{i,j,t}}{\tilde{p}_{i,t}} \quad (4.46)$$

Using the MLACF update (4.33) one has the equivalent expression

$$\rho_j = \frac{\lambda_j}{(\alpha \lambda_j + (1 - \alpha) \tilde{\lambda}_j)^2} \sum_{i \in \beta_j} \frac{y_i c_{i,j}}{\tilde{p}_i} \quad (4.47)$$

To obtain a lower bound on  $\rho_j$  we consider separately the two cases  $\lambda_j \geq \tilde{\lambda}_j$  and  $\lambda_j < \tilde{\lambda}_j$ .

- If  $\lambda_j \geq \tilde{\lambda}_j$ , then  $\bar{\lambda}_j \leq \lambda_j$  because  $0 \leq \alpha \leq 1$ , and therefore, using (4.47),

$$\rho_j \geq \frac{1}{\lambda_j} \sum_{i \in \iota_j} \frac{y_i c_{i,j}}{\tilde{p}_i} \quad (4.48)$$

4. TRANSMISSION-LESS ATTENUATION CORRECTION IN TIME-OF-FLIGHT PET:  
ANALYSIS OF A DISCRETE ITERATIVE ALGORITHM.

---

Using  $\tilde{p}_i = \sum_k c_{i,k} \tilde{\lambda}_k \leq \omega \max_k \tilde{\lambda}_k$ , and noting that  $\tilde{\lambda}_k \leq \|\tilde{\lambda}\| = 1$ , and that  $y_i \geq 1$  for  $i \in \iota_j$ , one obtains

$$\rho_j \geq \frac{1}{\lambda_j} \frac{\xi_j}{\omega} \geq \frac{1}{\|\lambda\|} \frac{\xi}{\omega} \quad (4.49)$$

where we used  $\lambda_j \leq \|\lambda\|$ .

- If  $\lambda_j < \tilde{\lambda}_j$ , then  $\bar{\lambda}_j \leq \tilde{\lambda}_j$  and therefore, using (4.46),

$$\rho_j \geq \frac{1}{\tilde{\lambda}_j} \sum_{(i,t) \in \tau_j} \frac{y_{i,t} c_{i,j,t}}{\tilde{p}_{i,t}} \quad (4.50)$$

Using  $\tilde{p}_{i,t} = \sum_k c_{i,k,t} \tilde{\lambda}_k \leq \sigma \max_k \tilde{\lambda}_k$ , and noting that  $\tilde{\lambda}_k \leq \|\tilde{\lambda}\| = 1$ , and that  $y_{i,t} \geq 1$  for  $(i,t) \in \tau_j$ , one obtains

$$\rho_j \geq \frac{\eta_j}{\sigma} \geq \frac{\eta}{\sigma}. \quad (4.51)$$

Inserting the lower bounds (4.49) and (4.51) into (4.42) yields inequality (4.45).  $\square$ .

*Lemma 8.* Asymptotic regularity. Starting with any positive initial estimate  $\lambda_j^0 > 0$ , the sequence of *normalized* iterates  $\lambda^{n+1} = \mathcal{T}_{\mathcal{N}}(\lambda^n)$  is such that

$$\begin{aligned} \lim_{n \rightarrow \infty} \|\mathcal{T}(\lambda^n) - \lambda^n\| &= 0 \\ \lim_{n \rightarrow \infty} \|\mathcal{T}(\lambda^n)\| &= 1 \\ \lim_{n \rightarrow \infty} \|\mathcal{T}_{\mathcal{N}}(\lambda^n) - \lambda^n\| &= 0 \end{aligned} \quad (4.52)$$

*Proof.* Applying Lemma 7 with  $\tilde{\lambda} = \lambda^n$  yields

$$\frac{\|\mathcal{T}(\lambda^n) - \lambda^n\|^2}{\max(1, \|\mathcal{T}(\lambda^n)\|)} \leq e_n \quad (4.53)$$

with  $e_n = (1/C)(\tilde{L}(y, \mathcal{T}(\lambda^n)) - \tilde{L}(y, \lambda^n))$ . From Lemma 5, the sequence of reduced log-likelihoods converges (recall that the value of the reduced log-likelihood is not modified by the normalization), therefore  $\lim_{n \rightarrow \infty} e_n = 0$ . Defining  $z_n = \mathcal{T}(\lambda^n) - \lambda^n$  inequality (4.53) becomes

$$\|z_n\|^2 \leq e_n \max(1, \|\lambda^n + z_n\|) \leq e_n \max(1, 1 + \|z_n\|) \leq e_n (1 + \|z_n\|) \quad (4.54)$$

where we used  $\|\lambda^n\| = 1$  and the triangular inequality. Inequality (4.54) can be rewritten as

$$(\|z_n\| - e_n/2)^2 \leq e_n + e_n^2/4 \quad (4.55)$$

and finally

$$\|z_n\| \leq e_n/2 + \sqrt{e_n + e_n^2/4} \quad (4.56)$$

#### 4.5. Appendix: convergence of the MLACF algorithm.

---

The upper bound in the RHS tends to zero because  $e_n \rightarrow 0$ , hence  $\|z_n\| \rightarrow 0$ . This proves the first equation of the Lemma. The second equation of the Lemma follows because the iterates  $\lambda^n$  are normalized so that, again using the triangular inequality,

$$1 - \|\mathcal{T}(\lambda^n) - \lambda^n\| \leq \|\mathcal{T}(\lambda^n)\| \leq 1 + \|\mathcal{T}(\lambda^n) - \lambda^n\| \quad (4.57)$$

Finally,

$$\begin{aligned} \|\mathcal{T}_N(\lambda^n) - \lambda^n\| &= \left\| \frac{\mathcal{T}(\lambda^n)}{\|\mathcal{T}(\lambda^n)\|} - \lambda^n \right\| \leq \left\| \frac{\mathcal{T}(\lambda^n)}{\|\mathcal{T}(\lambda^n)\|} - \mathcal{T}(\lambda^n) \right\| + \|\mathcal{T}(\lambda^n) - \lambda^n\| \\ &\leq |(1 - \|\mathcal{T}(\lambda^n)\|)| + \|\mathcal{T}(\lambda^n) - \lambda^n\| \end{aligned} \quad (4.58)$$

We have already shown that the two terms in the RHS tend to zero, therefore the LHS tends to zero, which proves the last equation in (4.52).  $\square$

*Lemma 9.* If a positive sequence  $\lambda^n \in IR^M$  converges to some limit point  $\lambda^*$  such that  $\lambda_j^* > 0$ , then

$$\begin{aligned} \lim_{n \rightarrow \infty} \frac{y_i c_{i,j}}{p_i^n} &= \frac{y_i c_{i,j}}{p_i^*} \\ \lim_{n \rightarrow \infty} \frac{y_{i,t} c_{i,j,t}}{p_{i,t}^n} &= \frac{y_{i,t} c_{i,j,t}}{p_{i,t}^*} \end{aligned} \quad (4.59)$$

with  $p_i^n = \sum_k c_{i,k} \lambda_k^n$ ,  $p_i^* = \sum_k c_{i,k} \lambda_k^*$ ,  $p_{i,t}^n = \sum_k c_{i,k,t} \lambda_k^n$  and  $p_{i,t}^* = \sum_k c_{i,k,t} \lambda_k^*$ .

*Proof.* Take any LOR such that  $y_i c_{i,j} > 0$ . Consider the quantity

$$\Delta^n = \left| \frac{1}{\sum_k c_{i,k} \lambda_k^n} - \frac{1}{\sum_k c_{i,k} \lambda_k^*} \right| \leq \left| \frac{\sum_k c_{i,k} (\lambda_k^* - \lambda_k^n)}{(c_{i,j})^2 \lambda_j^n \lambda_j^*} \right| \quad (4.60)$$

Since  $\lambda_j^n \rightarrow \lambda_j^*$ , there is an integer  $N$  such that for each  $n > N$ ,  $\lambda_j^n > (1/2)\lambda_j^* > 0$ . Therefore,

$$\Delta^n \leq \left| 2 \frac{\sum_k c_{i,k} (\lambda_k^* - \lambda_k^n)}{(c_{i,j})^2 (\lambda_j^*)^2} \right| \quad (4.61)$$

The denominator is a positive number independent of  $n$ , and as  $\lambda^n \rightarrow \lambda^*$ , one concludes that  $\Delta^n \rightarrow 0$ . The first relation in (4.59) immediately follows. The proof of the second relation is similar.  $\square$

*Proposition 4.* Consider the sequence of *normalized* iterates  $\lambda^{n+1} = T_N(\lambda^n)$  with a positive initial image  $\lambda_j^0 > 0$ .

- The sequence of iterates is asymptotically regular,  $\|\lambda^{n+1} - \lambda^n\| \rightarrow 0$  as  $n \rightarrow \infty$ , and the reduced likelihood is non-decreasing,  $\tilde{L}(y, \lambda^{n+1}) \geq \tilde{L}(y, \lambda^n)$ ,
- The sequence of iterates has an limit point  $\lambda^*$ , and  $\nabla_j \tilde{L}(y, \lambda^*) = 0$  for any voxel satisfying  $\lambda_j^* > 0$ ,
- All limit points of the sequence  $\lambda^{n+1} = T_N(\lambda^n)$  have the same value of the reduced log-likelihood.

---

#### 4. TRANSMISSION-LESS ATTENUATION CORRECTION IN TIME-OF-FLIGHT PET: ANALYSIS OF A DISCRETE ITERATIVE ALGORITHM.

---

*Proof.* The asymptotic regularity and monotonicity are given by Lemmas 5 and 8. The  $\lambda^n$  are normalized, hence their sequence is bounded and contains a converging subsequence  $\lambda^{n(s)}$ ,  $s = 1, 2, \dots$ . Denote  $\lambda^*$  the limit of this subsequence.

We now consider some voxel  $j$  such that  $\lambda_j^* > 0$  and prove that  $\nabla_j \tilde{L}(y, \lambda^*) = 0$ . Recall that  $\lambda_j^{n(s)} > 0$  for all  $j$  by Lemma 3. Define

$$d_j^n = \sum_{i=1}^N \frac{y_i c_{i,j}}{p_i^n} \quad \text{and} \quad v_j^n = \sum_{i=1}^N \sum_{t=1}^T \frac{y_{i,t} c_{i,j,t}}{p_{i,t}^n} \quad (4.62)$$

and using (4.33) note that

$$\lambda_j^{n+1} = (T_N(\lambda^n))_j = \frac{1}{\|T(\lambda^n)\|} T(\lambda^n)_j = \frac{1}{\|T(\lambda^n)\|} \lambda_j^n \frac{v_j^n}{d_j^n} \quad (4.63)$$

Applying this and using (4.13),

$$\begin{aligned} \lambda_j^n \nabla_j \tilde{L}(y, \lambda^n) &= \lambda_j^n (-d_j^n + v_j^n) \\ &= (\lambda_j^{n+1} - \lambda_j^n) d_j^n + (1 - \frac{1}{\|T(\lambda^n)\|}) \lambda_j^n v_j^n \end{aligned} \quad (4.64)$$

On the other hand one has from (4.62) the identity

$$\sum_{j=1}^M \lambda_j^n d_j^n = \sum_{j=1}^M \lambda_j^n v_j^n = \sum_{i=1}^N y_i := Y. \quad (4.65)$$

Combined with the non-negativity of all quantities involved this implies that  $\lambda_j^n d_j^n \leq Y$  and  $\lambda_j^n v_j^n \leq Y$ .

Consider a voxel such that  $\lambda_j^* > 0$ . Since  $\lambda_j^{n(s)} \rightarrow \lambda_j^*$ , there is an iteration number  $S$  such that for  $s > S$ , the subsequence is sufficiently close to convergence, so that  $\lambda_j^{n(s)} > \lambda_j^*/2$ . Equation (4.64) leads then, for  $s > S$ , to

$$\begin{aligned} (\lambda_j^*/2) |\nabla_j \tilde{L}(y, \lambda^{n(s)})| &\leq \lambda_j^{n(s)} |\nabla_j \tilde{L}(y, \lambda^{n(s)})| \\ &\leq |\lambda_j^{n(s)+1} - \lambda_j^{n(s)}| \frac{Y}{(\lambda_j^*/2)} + |1 - \frac{1}{\|T(\lambda^{n(s)})\|}| Y \end{aligned} \quad (4.66)$$

The two terms in the RHS tend to zero because by Lemma 8 the sequence  $\lambda^n$  is asymptotically regular and  $\|T(\lambda^n)\| \rightarrow 1$ . Therefore  $\nabla_j \tilde{L}(y, \lambda^{n(s)}) \rightarrow 0$ . By Lemma 9, it follows that  $\nabla_j \tilde{L}(y, \lambda^*) = \lim_s \nabla_j \tilde{L}(y, \lambda^{n(s)}) = 0$ .

Finally, two limit points  $\lambda^*$  and  $\lambda^\dagger$  of the bounded sequence  $\lambda^n$  have the same value of the reduced log-likelihood: this is an immediate consequence of Lemma 5.  $\square$

### Acknowledgements

This work is supported by a grant of the Fonds voor Wetenschappelijk Onderzoek Vlaanderen (FWO), by a KU Leuven research grant (GOA/11/006) and by Siemens Healthcare. The authors thank Girish Bal, Mike Casey, Maurizio Conti, Christian Michel, Vladimir Panin and Charles Watson (Siemens Healthcare, Molecular Imaging, Knoxville, TN) for useful discussions.

## Chapter 5

# ML-reconstruction for TOF-PET with Simultaneous Estimation of the Attenuation Factors

A. Rezaei, M. Defrise, and J. Nuyts, “ML-Reconstruction for TOF-PET With Simultaneous Estimation of the Attenuation Factors”, *IEEE Transactions on Medical Imaging*, vol. 33, no. 7, pp. 1563–1572, Jul. 2014

### Abstract

In positron emission tomography (PET), attenuation correction is typically done based on information obtained from transmission tomography. Recent studies show that time-of-flight (TOF) PET emission data allow joint estimation of activity and attenuation images. Mathematical analysis revealed that the joint estimation problem is determined up to a scale factor. In this work, we propose a maximum likelihood reconstruction algorithm that jointly estimates the activity image together with the sinogram of the attenuation factors. The algorithm is evaluated with 2D and 3D simulations as well as clinical TOF-PET measurements of a patient scan and compared to reference reconstructions. The robustness of the algorithm to possible imperfect scanner calibration is demonstrated with reconstructions of the patient scan ignoring the varying detector sensitivities.

## 5.1 Introduction

A quantitative reconstruction of the tracer activity distribution in positron emission tomography (PET) requires correction of the emission data for the attenuation factors. In current PET/CT systems, attenuation correction is typically done by means of well-aligned CT images adjusted to the photon energy of 511 keV [2], [17]. However, because the PET and CT scans are acquired sequentially and because the acquisition durations are very different, the images are not perfectly matched, and PET attenuation correction artifacts are unavoidable [113]. These inaccurate tracer distribution values are the result of respiratory and/or patient motion during and between the two scans. Several research groups have tried to estimate the activity and attenuation images simultaneously from non time-of-flight (TOF) PET emission data, in an attempt to overcome this problem [25], [27], [28], [39], [41], [43], [45], [47], [48]. Despite some useful results the problem of joint estimation was found to be highly ill-posed. However, recent studies show that the data redundancy in TOF-PET data allows stable reconstruction of both attenuation and activity from TOF-PET emission data [56], [61], [63]. Moreover, mathematical analysis revealed that the TOF-PET data determine the attenuation correction factors uniquely except for a scale factor [58].

As well as correction for the attenuation factors, the PET data need to be corrected for the sensitivity differences between different lines-of-response (LORs). Commonly, these detector pair sensitivities are estimated by means of dedicated calibration scans, where the response of each LOR is measured for known activity phantoms [114], [115]. However, the detector pair sensitivities are prone to change from one scan to the other, thus potentially resulting in sub-optimal tracer distribution reconstructions [116]. In an attempt to overcome this issue, some researchers have proposed to jointly estimate tracer activity distributions together with detector pair sensitivities [117], [118]. These “self-normalizing” algorithms make an attempt to refine the PET detector pair sensitivities which were originally obtained from previous calibration scans.

In this paper, we propose a new maximum likelihood algorithm (called MLACF) that jointly estimates the image of the activity distribution and the sinogram with the attenuation factors. We also show that the algorithm is robust to errors in the detector pair sensitivities. This method avoids the reconstruction of the attenuation image, and thus requires some a-priori knowledge about the activity or the attenuation factors to be quantitatively accurate. In its most general form, the algorithm must keep an image of the tracer distribution and a sinogram of the attenuation factors in memory during reconstruction. However, if additive contributions (such as scatter and/or randoms) can be ignored, the algorithm does not even require the storage of the attenuation correction factors. It has been shown in the latter case that when the emission data are consistent, the log-likelihood can be expressed in a “reduced” form and that the solution space to this reduced log-likelihood is free of possible local maxima [63], [65]. Further properties and some convergence analysis of the scatter and randoms free case can be found in [64], [65].

The paper is organized as follows: in section II the algorithm is derived and a

theoretical analysis of its convergence is given. Section III describes 2D and 3D simulations so as to compare activity reconstructions of the newly proposed method to reference activity reconstructions of the well established MLEM and the MLAA (maximum likelihood activity and attenuation reconstruction [47], [61]) methods. The new algorithm does not impose the consistency of the attenuation sinogram, i.e. the estimated attenuation sinogram will not in general be equal to the projection of a non-negative attenuation image. Since this may result in increased noise, we analyze its noise properties in 2D simulations. The results of these simulations are shown and compared, together with results of a patient scans in section IV. We conclude the paper by discussing the results and drawing some conclusions in section V.

## 5.2 Methods

### 5.2.1 MLACF

In TOF-PET, the expected count  $\bar{y}_{it}$  for line-of-response (LOR)  $i$  and TOF-bin  $t$  can be expressed as

$$\bar{y}_{it} = a_i p_{it} + s_{it} \quad (5.1)$$

for,

$$a_i = e^{-\sum_{j=1}^J l_{ij} \mu_j}, \quad p_{it} = \sum_{j=1}^J c_{ijt} \lambda_j$$

where  $a_i$  is the attenuation factor of LOR  $i$ ,  $p_{it}$  is the (unattenuated) TOF projection of the activity image for LOR  $i$  and TOF-bin  $t$  and  $s_{it}$  is the expected additive contribution of scatter and/or randoms.  $\lambda_j$  and  $\mu_j$  are the activity and attenuation coefficient at voxel  $j$ ,  $c_{ijt}$  is the sensitivity of the measurement bin at  $(i, t)$  for activity in  $j$  in absence of attenuation and  $l_{ij}$  is the effective intersection length of LOR  $i$  with voxel  $j$ . We represent summation over the TOF-index (corresponding to the non-TOF values) by dropping the  $t$  index, e.g.  $c_{ij} = \sum_t c_{ijt}$ . The same convention is also used for the non-TOF measurements  $y_i$  and  $p_i$ .

The Poisson log-likelihood function for the emission measurements  $y_{it}$  is then expressed as

$$L(y, \lambda, a) = \sum_{it} y_{it} \log \bar{y}_{it}(\lambda, a) - \bar{y}_{it}(\lambda, a) \quad (5.2)$$

where we wish to estimate  $\lambda$  and  $a$  by maximizing (5.2). We propose an alternated optimization approach: first  $a$  is updated keeping  $\lambda$  fixed, and then  $\lambda$  is updated keeping  $a$  fixed. The monotonic iterative algorithm (referred to below as MLACF)

## 5. ML-RECONSTRUCTION FOR TOF-PET WITH SIMULTANEOUS ESTIMATION OF THE ATTENUATION FACTORS

---

which preserves the non-negativity of all variables is given by:

$$\begin{aligned} a_i^{k+1} &= a_i^k + \frac{a_i^k}{p_i^h} \frac{\partial L(y, \lambda^h, a)}{\partial a_i} \Big|_{a^k} \\ &= a_i^k \sum_t \frac{p_{it}^h}{p_i^h} \frac{y_{it}}{a_i^k p_{it}^h + s_{it}} \end{aligned} \quad (5.3)$$

$$\lambda_j^{h+1} = \frac{\lambda_j^h}{\sum_i c_{ij} a_i^{k+1}} \sum_{it} c_{ijt} a_i^{k+1} \frac{y_{it}}{\sum_\xi c_{i\xi t} a_i^{k+1} \lambda_\xi^h + s_{it}} \quad (5.4)$$

where the superscripts  $h$  and  $k$  represent the iteration, and the algorithm is initialized with  $a_i^0 > 0$  and  $\lambda_j^0 > 0$ . We used two iteration symbols, because the optimization could be done by alternately applying a few updates (3) followed by a few updates of (4). An ordered subsets version of the MLACF algorithm is obtained in the standard way, i.e. by restricting the summations over  $i$  in (4) to the LORs in the subset.

### 5.2.2 Convergence

The second step (5.4) is the standard TOF-MLEM algorithm, which is known to monotonically increase the likelihood [112]. In the following, we show that the first step (5.3) iteratively increases the likelihood as well. Moreover, we show that at fixed  $\lambda = \lambda^h$  (the superscripts of the activity estimate and its corresponding (non-)TOF projection will be dropped for convenience), with repeated application of (5.3) the attenuation factor estimate  $a$  converges to the constrained maximizer

$$a^* = \arg \max_{a \geq 0} L(y, \lambda, a) \quad (5.5)$$

The first and second derivatives of the log-likelihood (5.2) with respect to  $a_i$  (at fixed  $\lambda$ ) can be written as:

$$\frac{\partial L(y, \lambda, a)}{\partial a_i} = \sum_t p_{it} \frac{y_{it}}{\bar{y}_{it}} - p_i \quad (5.6)$$

$$\frac{\partial^2 L(y, \lambda, a)}{\partial a_i^2} = \sum_t -p_{it}^2 \frac{y_{it}}{\bar{y}_{it}^2} \leq 0 \quad (5.7)$$

If we consider only LORs  $i$  for which  $y_{it} > 0$  and  $p_{it} > 0$  for at least one TOF index  $t$  (an LOR with activity), the second derivative is strictly negative and the unconstrained maximizer

$$\tilde{a} = \arg \max_a L(y, \lambda, a) \quad (5.8)$$

is unique. This maximizer is a solution to  $\partial L(y, \lambda, a)/\partial a_i = 0$  and satisfies

$$1 = \sum_t \frac{p_{it}}{p_i} \frac{y_{it}}{\tilde{a}_i p_{it} + s_{it}} \quad (5.9)$$

However, the attenuation factors are constrained and limited to  $a_i \geq 0$ . We show that (5.3) converges to the constrained maximizer (5.5), which has the following property:

$$a_i^* = \begin{cases} \tilde{a}_i, & \tilde{a}_i \geq 0 \\ 0, & \tilde{a}_i < 0 \end{cases} \quad (5.10)$$

To prove this, we analyze each case separately.

$$\tilde{a}_i > 0$$

It follows immediately from (5.9) that in this case, a fixed point of (5.3) is also the constrained maximizer  $a^*$  of the log-likelihood (5.2), provided that the fixed point is strictly positive. Furthermore,

- If  $a_i^k < a_i^*$ , then  $a_i^k < a_i^{k+1} < a_i^*$ .

*proof:* When  $a_i^k < a_i^*$ , then  $\partial L/\partial a_i|_{a^k} > 0$ , because  $L$  is a concave function with a unique maximum. Inserting this in (5.3) one finds  $a_i^k < a_i^{k+1}$ . Furthermore, replacing  $a_i^k$  with  $a_i^*$  in (5.3) results in a larger increase of the numerator compared to the denominator (since  $s_{it} \geq 0$ , see section 5.2.3 for the case where  $s_i = 0$ ), and therefore  $a_i^{k+1} < a_i^*$ .

- If  $a_i^k > a_i^*$ , then  $a_i^k > a_i^{k+1} > a_i^*$ .

The proof is similar to the previous case except that in this case;  $\partial L/\partial a_i|_{a^k} < 0$ . Therefore, together with the previous case we see that starting from any strictly positive initial attenuation factor value  $a_i^0 > 0$  the log-likelihood is not decreasing.

- The algorithm asymptotically converges to the fixed point  $a_i^*$ , i.e.  $\lim_{k \rightarrow \infty} a_i^k = a_i^*$ .

*proof:* When  $\lambda$  is fixed,  $L$  is a concave function in  $a$  with a unique maximum. Combining (5.3) and (5.9) one obtains,

$$a_i^{k+1} - a_i^* = (a_i^k - a_i^*) \sum_t \frac{s_{it}}{(a_i^k p_{it} + s_{it})} \frac{p_{it}}{p_i} \frac{y_{it}}{(a_i^* p_{it} + s_{it})} \quad (5.11)$$

Using the fact that all quantities are non-negative and that an upper limit  $\alpha_i$  can be found for the fraction  $s_{it}/(a_i^k p_{it} + s_{it})$  for each of the cases mentioned above, we have

$$\begin{aligned} |a_i^{k+1} - a_i^*| &\leq |a_i^k - a_i^*| \alpha_i \sum_t \frac{p_{it}}{p_i} \frac{y_{it}}{(a_i^* p_{it} + s_{it})} \\ &= |a_i^k - a_i^*| \alpha_i \leq |a_i^0 - a_i^*| \alpha_i^{k+1} \end{aligned} \quad (5.12)$$

with,

$$\alpha_i = \begin{cases} \max_{t,p_{it}>0} \left( \frac{s_{it}}{a_i^0 p_{it} + s_{it}} \right), & a_i^0 < a_i^* \\ \max_{t,p_{it}>0} \left( \frac{s_{it}}{a_i^* p_{it} + s_{it}} \right), & a_i^0 \geq a_i^* \end{cases} \quad (5.13)$$

---

## 5. ML-RECONSTRUCTION FOR TOF-PET WITH SIMULTANEOUS ESTIMATION OF THE ATTENUATION FACTORS

---

where the restriction over the  $t$  range is due to the fact that terms with  $p_{it} = 0$  do not contribute to the sum. Using this restriction together with  $a_i^0 > 0$  and  $a_i^* = \tilde{a}_i > 0$ , one finds that  $\alpha_i < 1$ ,  $(\alpha_i)^k \rightarrow 0$  and therefore  $|a_i^k - a_i^*| \rightarrow 0$ . From this proof we expect a fast geometric convergence rate of order (scatter and randoms fraction) $^k$ .

$$\tilde{a}_i = 0$$

When started with  $a_i^0 > 0$ , the sequence  $a_i^k$  is bounded below by zero because (5.3) preserves non-negativity, and is non-increasing because the derivative of the log-likelihood is negative for  $a_i^k \geq \tilde{a}_i$ . Therefore, this sequence converges to some  $a_i^\dagger \geq 0$ . However, if  $a_i^\dagger > 0$ , then  $a_i^k \geq a_i^\dagger$  for all  $k$  and the upper limit  $\alpha_i$  on  $a_i^k$  in (5.13) can be replaced by

$$\alpha_i = \max_{t,p_{it}>0} \left( \frac{s_{it}}{a_i^\dagger p_{it} + s_{it}} \right) < 1 \quad (5.14)$$

and hence  $a_i^k \rightarrow 0$ , which is in contradiction with the assumption that  $a_i^\dagger > 0$ . Therefore,  $a_i^\dagger = 0 = a_i^*$ .

$$\tilde{a}_i < 0$$

Since at fixed  $\lambda$ ,  $L$  is a concave function with a unique maximum, it follows that:

$$\frac{\partial L(y, \lambda, a)}{\partial a_i} \Big|_{a_i=0} < 0 \Leftrightarrow \sum_t \frac{p_{it}}{p_i} \frac{y_{it}}{s_{it}} < 1 \quad (5.15)$$

which defines an upper limit to (5.3) such that:

$$a_i^{k+1} \leq a_i^k \left\{ \sum_t \frac{p_{it}}{p_i} \frac{y_{it}}{s_{it}} \right\} \quad (5.16)$$

The factor in the brackets is independent of  $k$  and is strictly smaller than 1, therefore  $a_i^k \rightarrow 0$ .

### 5.2.3 Special Case of Zero Scatter and Randoms

As suggested above, the first step of the algorithm, equation (5.3), converges in a single iteration when the additive contribution  $s_{it}$  vanishes. Setting  $s_{it} = 0$  in (5.3) and (5.4) results in the standard MLEM algorithm, except that in every iteration  $k + 1$  the attenuation factors  $a_i^{k+1}$  are replaced with  $y_i/p_i^h$ . In this case, there is no need for separate storage of the attenuation factor sinogram and the two step MLACF algorithm reduces to a single step MLEM-like algorithm:

$$\lambda_j^{h+1} = \frac{\lambda_j^h}{\sum_i \frac{y_i}{p_i^h} c_{ij}} \sum_{it} c_{ijt} \frac{y_{it}}{\sum_\xi c_{i\xi t} \lambda_\xi^h} \quad (5.17)$$

Furthermore, inserting the new attenuation update (5.3) in the log-likelihood (5.2), and keeping only the terms that depend on  $\lambda$ , one obtains the reduced log-likelihood function ( $\tilde{L}$ ):

$$\tilde{L}(y, \lambda) = \sum_i \sum_t y_{it} \log p_{it}(\lambda) - y_i \log p_i(\lambda). \quad (5.18)$$

Although we currently have no results for the general log-likelihood (5.2), it is shown that for the case of consistent data the reduced log-likelihood function (5.18) has no local maxima other than the global maximum [63], [65]. In [64], [65], an alternative derivation of the MLEM-like algorithm (5.17) from the reduced log-likelihood function (5.18) is given, and it is shown that the proposed algorithm monotonically increases the likelihood and is asymptotically regular, i.e. the difference between consecutive reconstruction updates converges to zero.

### 5.3 Experiment Design

The simulation parameters were chosen according to the Siemens Biograph mCT scanner specifications [92]. The 2D and 3D TOF-PET emission data consist of 200 radial bins of 0.4 cm width, 168 projection angles over 180 deg, and 13 TOF-bins of 312 ps width with an effective TOF resolution of 580 ps. In the 2D thorax simulations, the phantom was discretized in an image of  $600 \times 600$  pixels and each LOR is simulated as the average of three LORs to introduce a slight mismatch between the simulation and reconstruction projectors. The 3D simulation (and patient) TOF-PET data are organized as 5D sinograms [98], consisting of 200 radial bins, 168 azimuthal angles, 7 (9) co-polar angles with 81 (109) planes of 0.2 cm width, and 13 time bins.

To simulate a reasonable scatter (and randoms) contribution, the noiseless emission sinograms were smoothed in the radial, angular, axial and TOF directions with a Gaussian kernel of 12 cm, 0.43 rad, 12 cm and 9.4 cm FWHM, respectively. The 2D and 3D simulated scatter estimates are scaled to obtain a scatter-to-primary ratio of 50%, and are added to the emission sinograms prior to adding Poisson noise to the measurements. For scatter correction, the exact noise-free scatter profile was used.

The 2D measurements are reconstructed in a  $200 \times 200$  pixel grid with a pixel width of 0.4 cm and the reconstructed 3D activity and attenuation images had a  $200 \times 200 \times 81 (\times 109)$  voxel grid with a voxel width of 0.4 cm and 0.2 cm in the transaxial and axial directions, respectively. The algorithm was initialized with a uniform activity image and an attenuation factors sinogram of all ones. Activity figures are shown in a white-to-black color map whereas a black-to-white color map is used to show the attenuation images as well as the attenuation factors.

#### 5.3.1 2D Simulation

2D TOF-PET data were generated from the thorax phantom shown in figure 5.1. Activity reconstructions of the TOF-PET emission data are then generated with MLACF and compared to reconstructions of MLAA and MLEM with known attenuation. In MLAA [61], the activity and attenuation images are updated in an

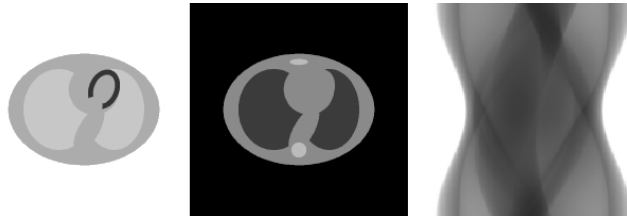


Figure 5.1: 2D activity (left) and attenuation images (center) of the thorax and the corresponding attenuation factors (right).

interleaved manner by keeping one of the images from the pair fixed while updating the other, and the non-negativity constraint is enforced on the attenuation image  $\mu$ .

### Reconstructions

MLACF, MLAA and MLEM reconstructions were analyzed for noise-free, moderate-noise and high-noise TOF-PET emission data. The moderate-noise and high-noise emission data have on average 31.9 and 6.4 maximum counts in the TOF sinogram, corresponding to 105.7 and 21.1 counts in their non-TOF sinograms, respectively. In the joint estimation methods (MLACF, MLAA), we assumed that the total amount of activity was known and the activity reconstructions were scaled during reconstructions accordingly. This (rather unrealistic) assumption is used because the TOF-PET data determine the activity and attenuation factors only up to a multiplicative constant.

In order to get more insight into the convergence properties of MLACF compared to MLAA and MLEM, the log-likelihood of equation (5.2) as well as the mean square difference (MSD) between the reconstructions and a converged reconstruction was computed within the support of the thorax phantom for each iteration of the three algorithms. In this study, no ordered subsets acceleration was applied, i.e. all projection angles were used in every iteration. The reconstruction of the 1000<sup>th</sup> iteration was considered as the converged reconstruction, and the two measures were computed as a function of the number of iterations.

### Noise Analysis

To analyze the noise properties of MLACF and MLAA, activity reconstructions were made (after 3 iterations of 42 subsets) with varying amounts of noise in the TOF-PET data. The lowest amount of noise in this study corresponds to the moderate-noise case described in the previous section. Five additional data sets were created, making a series of six data sets in all, where each data set has one-half the total counts of the previous data set in the series (so that the final image set has 1/32nd of the counts of the first data set). We assume that the noise-free activity reconstructions of MLACF and MLAA are good estimates for their respective mean activity reconstructions over multiple noise realizations. After subtracting the mean reconstruction from the noisy reconstructions, standard deviation and a noise correlation coefficient measure are

computed for each noise level. As reference we use MLEM activity reconstructions and compute the noise correlation coefficients as:

$$NCC = \frac{\sum_{j \in \Omega} (\mathcal{N}_j^n - \mathcal{N}_j^f)(\mathcal{R}_j^n - \mathcal{R}_j^f)}{\sqrt{\sum_{j \in \Omega} (\mathcal{N}_j^n - \mathcal{N}_j^f)^2 \sum_{j \in \Omega} (\mathcal{R}_j^n - \mathcal{R}_j^f)^2}} \quad (5.19)$$

where,  $\mathcal{N}$  is the MLACF or MLAA activity reconstruction,  $\mathcal{R}$  defines the reference MLEM activity reconstruction, superscripts  $n$  and  $f$  correspond to noisy and noise-free reconstructions, respectively,  $j$  is the pixel index, and  $\Omega$  determines the support of the activity image.

### Bias-Variance

With the same level of noise as in the high-noise level case, we study bias and variance of the MLACF activity reconstructions and compare the results to bias and variance curves of MLAA and MLEM emission reconstructions as a function of activity reconstruction updates. All three algorithms are initialized with the same initial activity image, i.e. uniform disk of activity. Just as before, the reconstructions are scaled in each update according to the total amount of activity in the reconstructed activity image. Bias and variance estimates are then computed in the support of the 2D thorax phantom for 150 iterations of the three algorithms. In this study, no ordered subsets acceleration was applied. As before, we assume that a noise-free reconstruction of the thorax phantom is a good estimate of the average of noisy reconstructions from multiple noise realizations. In each iteration, bias is computed as the average absolute pixel-by-pixel difference between the noise-free reconstruction and the activity phantom of figure 5.1. It is reported with the variance of activity reconstructions of 100 different TOF-PET noise realizations.

When going from 2D to 3D TOF-PET, the number of unknown attenuation factors (i.e. the size of the sinogram) increases dramatically, due to the inclusion of all the oblique lines. To keep the simulations simple and fast, we model a similar effect by a three-fold increase in the number of angles of the 2D bias-variance study. By doing so, the total counts in the sinogram increases three-fold, however the expected count per pixel remains the same. We compare the results of MLACF to those of the standard MLEM and MLAA algorithms. We expect that this overdetermined 2D bias-variance analysis will be predictive of the noise properties in the fully 3D case. The bias and variance measures are again computed within the support of the 2D phantom for 150 iterations, and the measures are computed from a noise-free activity reconstruction as well as activity reconstructions from 50 different noise realizations of the TOF-PET emission data.

#### 5.3.2 3D Simulation

Figure 5.2 shows the activity and attenuation images of the NCAT phantom used in our 3D simulation study. The NCAT phantom was forward projected with a 3D TOF-PET projector, scatter (with a scatter-to-primary ratio of 50%) was added

## 5. ML-RECONSTRUCTION FOR TOF-PET WITH SIMULTANEOUS ESTIMATION OF THE ATTENUATION FACTORS

---

to the noise-free emission data and Poisson noise was added to the measurements. The resulting TOF sinogram had a maximum count of 24, while its corresponding non-TOF sinogram had a maximum count of 56. The MLACF activity reconstruction was then compared to MLAA and MLEM activity reconstructions. As before, we assumed that the total amount of activity was known, hence the joint reconstructions were scaled accordingly.

### 5.3.3 Patient data

A clinical 4 minute TOF-PET thorax scan of a patient injected with 296 MBq of  $^{18}\text{F}$ -FDG is reconstructed with MLACF and compared to activity reconstructions of MLAA and MLEM. The emission data is acquired 80 minutes post-injection, and the scatter and randoms fraction of the TOF emission data are 19% and 45%, respectively.

### 5.3.4 Self-Normalizing Algorithm

2D detector sensitivities were simulated mimicking transaxial detector pair sensitivities of the Biograph mCT scanner. The sensitivity variations are dominated by the gaps between the detector blocks with streak artifacts similar to the ones produced by faulty detector blocks [98]. However, in addition to the latter effect, detector pair variabilities were also accounted for by assigning a random value generated from a uniform distribution in (0.95, 1.05) to LORs which were not affected by the “gap effect”. 2D TOF-PET measurements of the thorax phantom (figure 5.1) were simulated, taking into account these detector sensitivities. Activity images were then reconstructed with MLACF using two approaches. In the first one, the simulated detector pair sensitivities are taken into account by modeling them into the system matrix  $c_{ijt}$ . In the second approach, the sensitivities are ignored altogether, hence MLACF needs to estimate the product of the attenuation factors and the sensitivities. Activity reconstructions were also made ignoring the Biograph mCT scanner sensitivities for the 4 minute patient data.

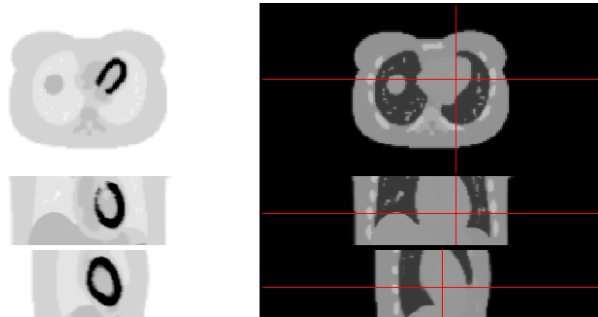


Figure 5.2: Transaxial (top), coronal (middle) and sagittal (bottom) views of the NCAT activity (left) and attenuation (right) images used in the 3D study.

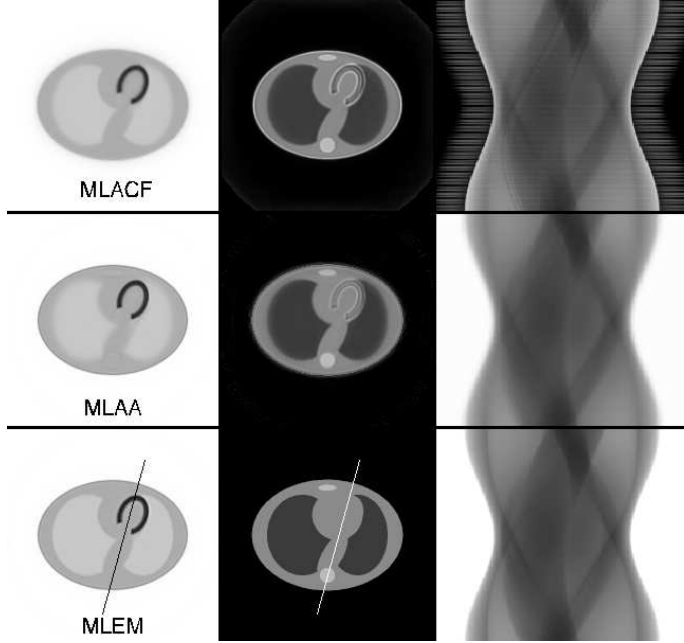


Figure 5.3: MLACF (top), MLAA (middle) and MLEM (bottom) reconstructions of the activity image (left), attenuation image (center) and attenuation factors (right) of the noise-free TOF-PET emission data. The true attenuation image and sinogram are shown for comparison in the third row.

## 5.4 Results

### 5.4.1 2D Simulation

#### Reconstructions

MLACF, MLAA and MLEM activity reconstructions from the noise-free data are shown in figure 5.3. The figure also shows the MLACF attenuation image computed by post-reconstruction of the attenuation factors, together with MLAA estimated attenuation factors obtained by projection of the attenuation reconstruction (they have been computed to enable comparison of the MLAA and MLACF results). MLACF reconstructions are after 3 iterations of 42 subsets where the attenuation factor estimate (equation (5.3)) is updated 3 times for each update of the activity (equation (5.4)). The MLACF attenuation image was reconstructed with 5 iterations of 42 subsets of the MLEM algorithm from the logarithm of the estimated attenuation factors assuming there was no attenuation along LORs without activity. The MLAA reconstructions are after 3 iterations of 42 subsets where the attenuation reconstruction is updated 3 times for each update of the activity [61]. MLEM reconstructions are after the same number of activity updates as MLACF and MLAA (3 iterations of 42 subsets). It should be mentioned that the ratio of three updates of the attenuation (sinogram in MLACF or image in MLAA) to one update of the activity image is empirical and was not rigorously optimized.

5. ML-RECONSTRUCTION FOR TOF-PET WITH SIMULTANEOUS ESTIMATION OF THE ATTENUATION FACTORS

---

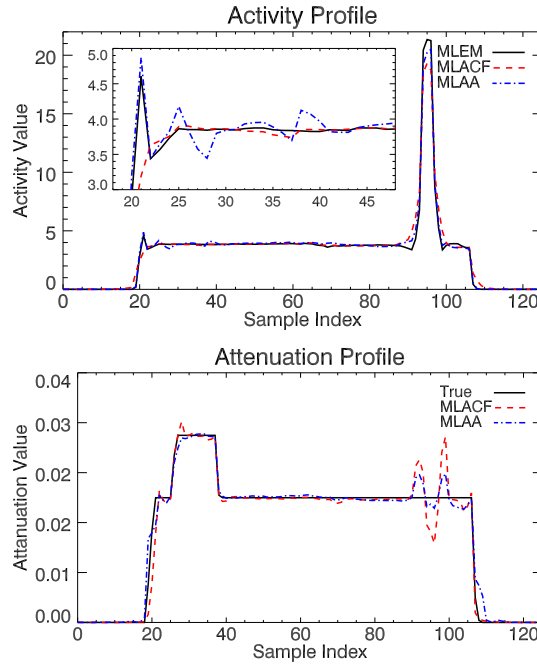


Figure 5.4: Activity (top) and attenuation (bottom) profiles through MLACF and MLAA reconstructions of noise-free data plotted against reference MLEM activity and the true attenuation profiles, respectively. The profiles correspond to the lines depicted in figure 5.3.

Figure 5.4 shows profiles through the reconstructed MLACF, MLAA and MLEM activity images together with the attenuation profiles of MLACF and MLAA attenuation reconstructions and the true attenuation images. The activity profile shows that MLACF suffers less from artifacts in regions with strong attenuation gradients than MLAA. However, the post-reconstructed attenuation profile of MLACF seems to be more sensitive in regions with a strong change of activity.

Figure 5.5 shows MLACF and MLAA reconstructions when the emission data are corrupted by Poisson noise. The displayed activity reconstructions of the high-noise case are scaled and shown in the same color map as the moderate-noise case. It is interesting to see that the attenuation factors of MLACF tend to be noisier than the attenuation estimates of MLAA. This is due to the fundamental difference between the two algorithms and is the result of the consistency of the attenuation factors in MLAA.

Figure 5.6 shows the log-likelihood (5.2) normalized to the upper-limit of (5.2) determined by the data, i.e.  $\sum_{it} y_{it} \ln y_{it} - y_{it}$ , as well as the MSD of the reconstructions normalized to have the same total amount of activity as the activity phantom for the noise-free and the high-noise TOF-PET emission simulations. It is interesting to see that for the joint estimation methods, the log-likelihood and MSD rank the convergence of the algorithms differently. We believe that convergence as measured by the MSD better reflects the clinically relevant behaviour of the algorithms. Figure

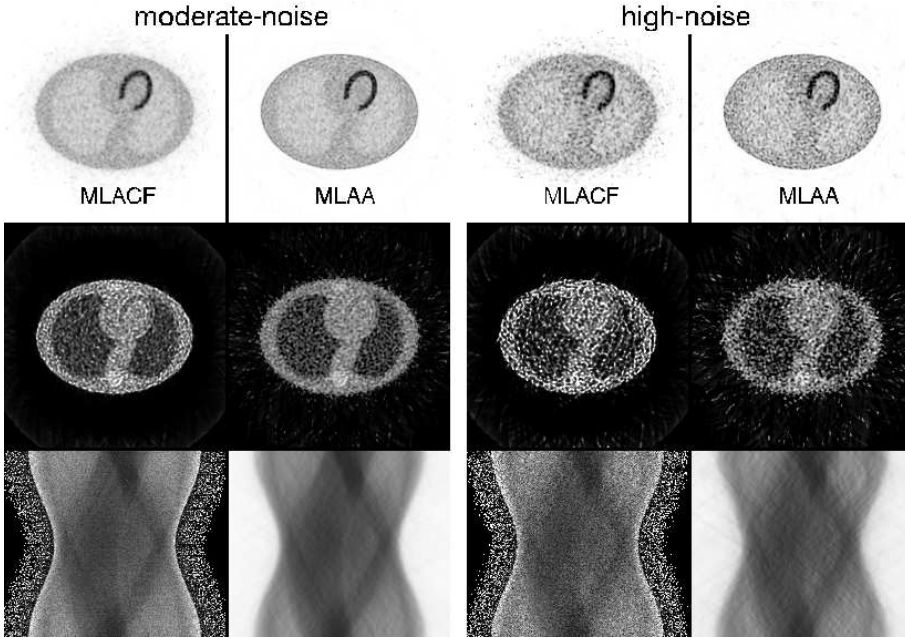


Figure 5.5: MLACF (columns 1,3) and MLAA (columns 2,4) reconstructions of the activity image (top), attenuation image (middle) and attenuation factors (bottom). The reconstructions are for moderate (columns 1,2) and high (column 3,4) Poisson noise in the TOF-PET emission data. The high-noise activity reconstructions are scaled to be shown in the same color map as moderate-noise activity reconstructions.

5.6 shows that the MLACF reconstructions are slower to converge compared to the MLAA and MLEM reconstructions. However it should be mentioned that while MLAA has a faster convergence rate, it is also computationally more demanding. It is also worth noting that because MLACF does not require consistency of the attenuation factors, it has more degrees of freedom to explain the TOF-PET emission data. Hence, it produces a higher likelihood in the case of noisy data, with the difference to reference MLAA and MLEM computed likelihoods increasing with increasing amount of noise in the TOF-PET emission data.

### Noise Analysis

Figure 5.7 shows the standard deviation of the two algorithms, which are comparable except for extreme-noise in the emission data. Figure 5.7 also shows the computed noise correlation coefficients of MLACF and MLAA with varying amounts of noise in the data. The noise of the MLAA activity reconstructions is highly correlated to the noise in the MLEM images in all cases. In contrast, the MLACF noise is less correlated to the MLEM noise, and the correlation decreases for increasing amounts of noise in the TOF-PET emission data.

## 5. ML-RECONSTRUCTION FOR TOF-PET WITH SIMULTANEOUS ESTIMATION OF THE ATTENUATION FACTORS

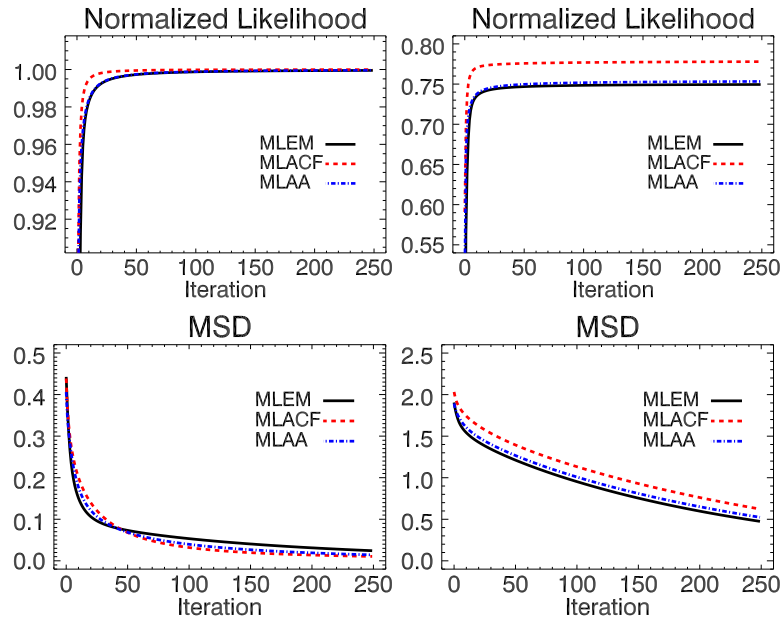


Figure 5.6: Log-likelihood of equation (5.2) (top) and the MSD measure (bottom) for MLACF, MLAA and MLEM reconstructions of the noise-free (left) and high-noise (right) TOF-PET emission data.

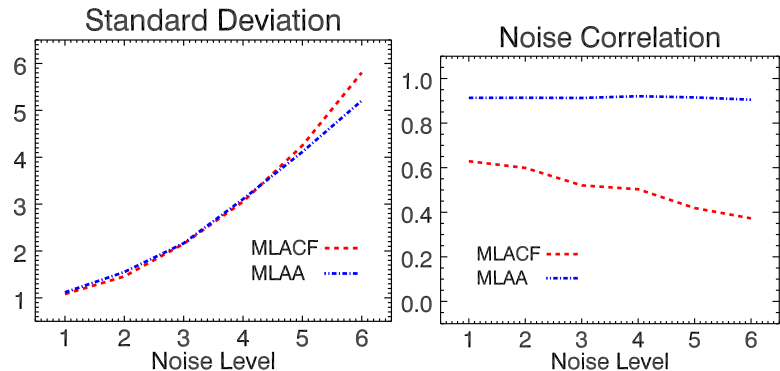


Figure 5.7: Standard deviation (left) of MLACF and MLAA activity reconstructions, and their noise correlation coefficient (right) with reference MLEM activity reconstructions computed using (5.19) for varying noise levels in the TOF-PET emission data.

### Bias-Variance

The bias-variance curves of the 2D activity reconstructions of MLACF, MLAA and MLEM can be seen in figure 5.8, where bias and variance are computed for each update of the activity reconstructions. The reconstructions are for a high level of noise in the TOF-PET emission data (corresponding to a maximum count of 6.4 in the TOF sinogram). The curves are computed for a total of 150 updates of the activity

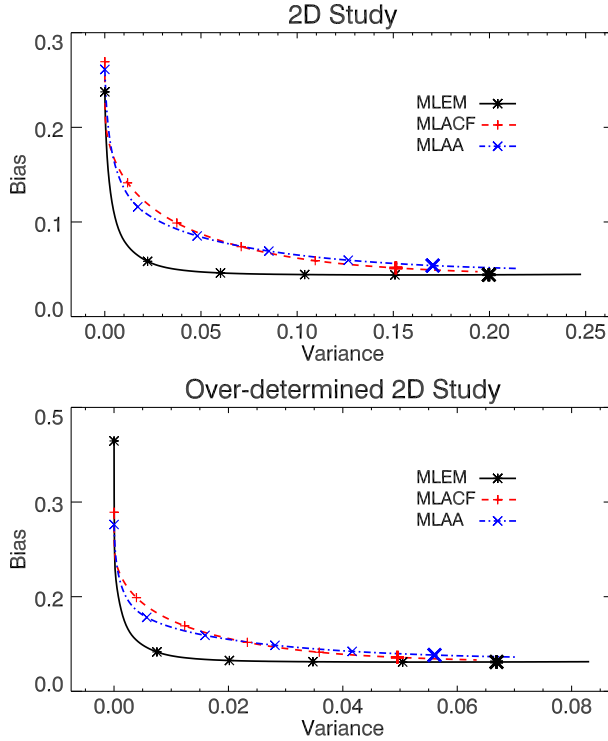


Figure 5.8: 2D (top) and overdetermined 2D (bottom) bias-variance curves for MLACF, MLAA and MLEM activity reconstructions from 100 and 50 noise realizations, respectively. The marked points on the curves are bias and variance values after 25 updates of the three algorithms. The bold symbols are bias and variance values for 126 (corresponding to 3 iterations of 42 subsets) reconstruction updates.

reconstructions with all the projections used to update the reconstructions (no ordered subsets acceleration). Although in early iterations MLAA is able to achieve lower bias for the same level of variance than MLACF, the MLACF reconstructions have lower bias closer to convergence. However, the difference between the two curves is small.

Figure 5.8 also shows the bias-variance curves of the overdetermined 2D activity reconstructions of MLACF, MLAA and MLEM. With the increased total sinogram count, the three algorithms produced images with decreased variance. As before, MLACF and MLAA had similar performance and were outperformed by MLEM, in particular at lower iterations. This suggests that the 3D activity reconstructions of MLACF will have similar bias and noise properties as activity reconstructions of MLAA.

#### 5.4.2 3D Simulation

Figure 5.9 shows MLACF, MLAA and MLEM activity reconstructions of the 3D NCAT phantom. The figure also shows the estimated MLACF, estimated (and

## 5. ML-RECONSTRUCTION FOR TOF-PET WITH SIMULTANEOUS ESTIMATION OF THE ATTENUATION FACTORS

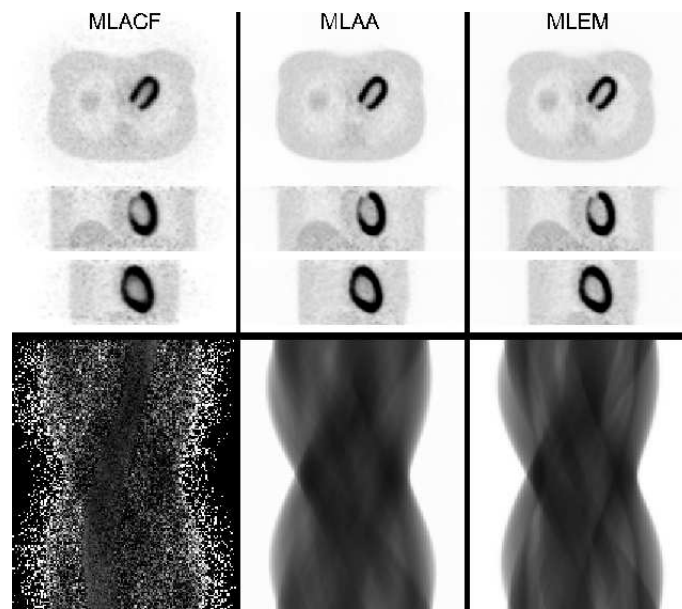


Figure 5.9: MLACF (left), MLAA (center) and MLEM (right) activity reconstructions (top) of the NCAT phantom post-smoothed with a Gaussian of 0.6 cm FWHM, together with the estimated MLACF, estimated MLAA and the true attenuation factors (bottom) for the transaxial slice of the 3D NCAT phantom.

projected) MLAA and the true attenuation factors of the transaxial slice of the NCAT phantom. The activity reconstructions of the three algorithms were generated after 3 iterations of 42 subsets, and displayed after post-smoothing the activity distributions with a Gaussian of 0.6 cm FWHM. The activity reconstructions of the three algorithms are comparable. However, the MLACF reconstruction is more noisy outside the support of the NCAT phantom. This is because only LORs that intersect the phantom support contain information about the attenuation factors. Because segmenting these LORs is not straightforward, we have not attempted to identify these LORs to impose an attenuation factor of 1. Consequently, these LORs are assigned arbitrary values, and because of this non-zero background attenuation, the reconstructed activity outside the object is increased as well.

### 5.4.3 Patient data

Figure 5.10 shows MLACF, MLAA and MLEM activity reconstructions of the 4 minute  $^{18}\text{F}$ -FDG patient data. The MLACF and MLAA reconstructions are scaled in each iteration to have the same amount of tracer activity as the MLEM reconstruction. The displayed activity reconstructions are smoothed with a Gaussian of 0.6 cm FWHM. Just as in the 3D simulation, the activity reconstructions are comparable, except for increased activity values outside the support of the patient. However, close inspection reveals that activity reconstructions of MLAA and MLACF suffer less from shadow-like artifacts [113] near the dome of the liver and the lateral

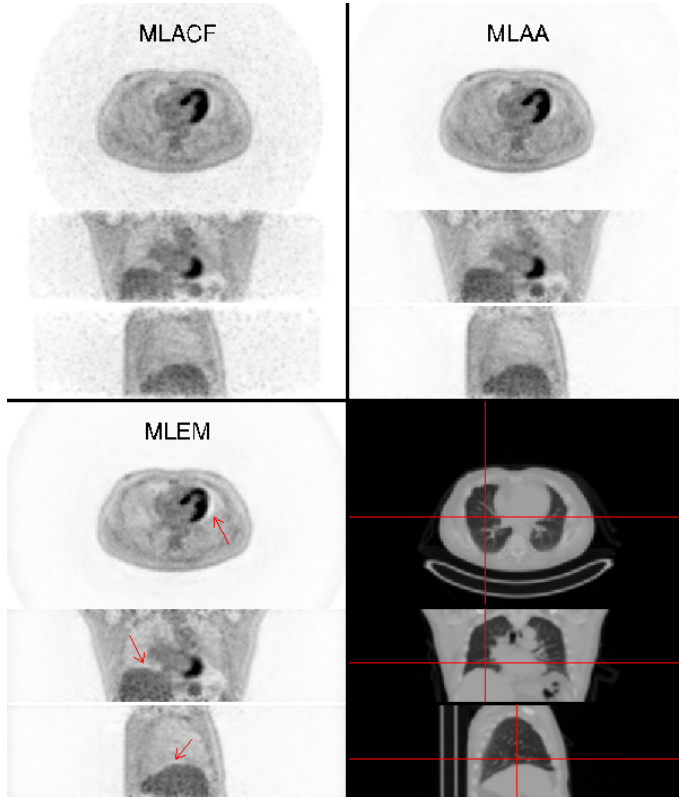


Figure 5.10: Transaxial, coronal and sagittal views of MLACF (top-left), MLAA (top-right) and MLEM (bottom-left) activity reconstructions of the 4 minute  $^{18}\text{F}$ -FDG patient data post-smoothed with a Gaussian of 0.6 cm FWHM. The MLEM activity reconstruction was obtained taking into account the CT-based attenuation image (bottom-right). The arrows indicate artifacts due to respiratory motion, which are more severe in the MLEM reconstructions.

wall of the heart (arrows in red) than the activity reconstruction of MLEM. This is indication to a geometric mismatch between PET emission data and CT-attenuation factors, which is expected since the CT was obtained in a breath-hold position.

#### 5.4.4 Self-Normalizing Algorithm

Figure 5.11 shows MLACF activity reconstructions of the 2D thorax phantom together with the estimated attenuation factors, with and without correction for detector pair sensitivities during reconstructions. Figure 5.12 shows MLACF activity reconstructions of the patient data with and without correction for detector pair sensitivities during reconstructions. For comparison MLEM reconstructions of the patient data are also shown when detector pair sensitivities are not taken into account. The activity images displayed are after smoothing the reconstructions with a Gaussian of 0.6 cm FWHM. Figure 5.13 shows the estimated attenuation factors of MLACF when detector pair sensitivities are ignored. For comparison the product

## 5. ML-RECONSTRUCTION FOR TOF-PET WITH SIMULTANEOUS ESTIMATION OF THE ATTENUATION FACTORS

---

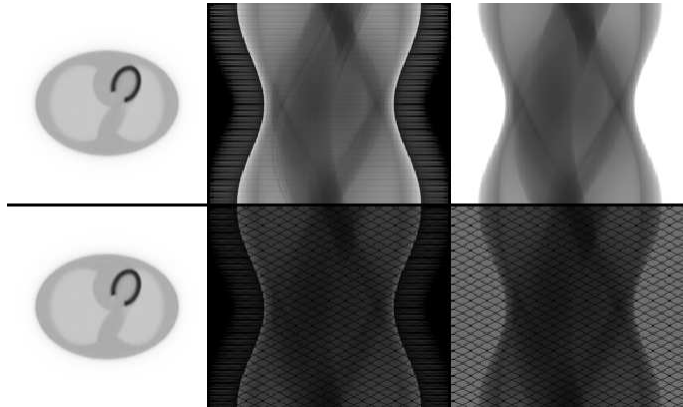


Figure 5.11: MLACF reconstructions of the activity image (left) and attenuation factors (center) when the detector pair sensitivities are taken into account (top) and when they are ignored (bottom). The true attenuation factors (top-right) and their multiplication with detector pair sensitivities (bottom-right) are shown for comparison.

of the CT-attenuation factors and detector sensitivities is also shown.

## 5.5 Discussion

Joint reconstruction of activity and attenuation has gained a lot of interest since it was shown and proven that TOF-PET data provide information about attenuation that was not previously available. In the same spirit, this paper proposes a maximum likelihood approach to jointly estimate the activity image together with the attenuation factors. Because the TOF-PET data determine the solution only up to a scale, some prior knowledge is required to obtain accurate quantification. Because MLAA estimates the attenuation image, it is straightforward to impose the known tissue attenuation value. Since MLACF does not estimate the attenuation image, one may have to find ways to obtain prior knowledge about the tracer distribution. In this study, we have simply assumed that the total amount of activity in the field of view was known. In practice, it may be difficult to obtain this kind of knowledge, unless one accepts to add objects with a known activity in the field of view. However, in some cases, it may be possible to obtain (partial) information about the attenuation factors to solve the scale problem. E.g., it may be possible to use the noisy transmission data provided by the Lu background radiation in LSO and LYSO scanners [119]. In [104], a modified version of the algorithm was proposed that made use of the partially known CT-attenuation factors.

In contrast to MLAA, this algorithm does not enforce consistency of the attenuation factors. As a consequence, MLACF activity reconstructions were expected to be noisier than their MLEM and MLAA counterparts. Although the noise structure in the activity reconstructions of MLACF and MLAA seems to be different, the noise realization study showed little difference between their bias-variance curves.

However, under extremely noisy conditions MLACF activity reconstructions seem to be influenced more by noise than MLAA reconstructions (figure 5.7, left panel). Compared to MLAA, MLACF requires fewer (back-) projections in every iteration of the algorithm. In the 3D simulations, the computation time of an MLAA iteration was roughly 2.5 times longer than that of an MLACF iteration.

Furthermore, the two joint estimation algorithms seem to respond differently to gradients in the attenuation image, where MLACF seems to have an advantage over MLAA (figure 4). A similar response was also observed in regions of the activity image with a high activity gradient, e.g. near the heart of the 2D thorax phantom (see the activity and attenuation profiles around sample index 90 in Figure 4). In the MLAA (and MLEM) reconstruction Gibbs over- and undershoots were observed in earlier iterations compared to MLACF reconstructions. We believe that in MLACF these high frequency elements are initially incorporated in the attenuation factors, where they cause the artifacts seen when this sinogram is reconstructed.

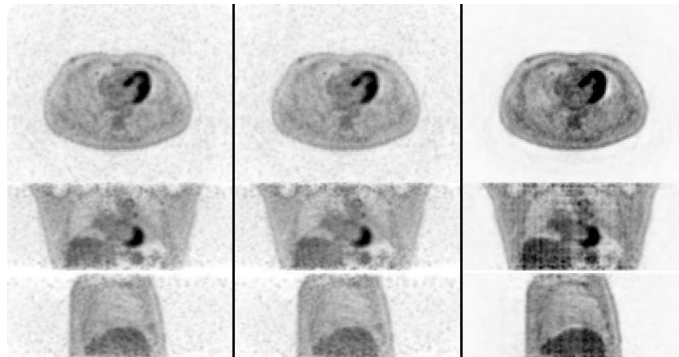


Figure 5.12: MLACF reconstructions of the tracer activity when the detector pair sensitivities are taken into account (same MLACF reconstruction as figure 5.10) (left). MLACF (center) and MLEM (right) activity reconstructions when detector pair sensitivities are ignored during reconstruction. The reconstructions are post-smoothed with a Gaussian of 0.6 cm FWHM.

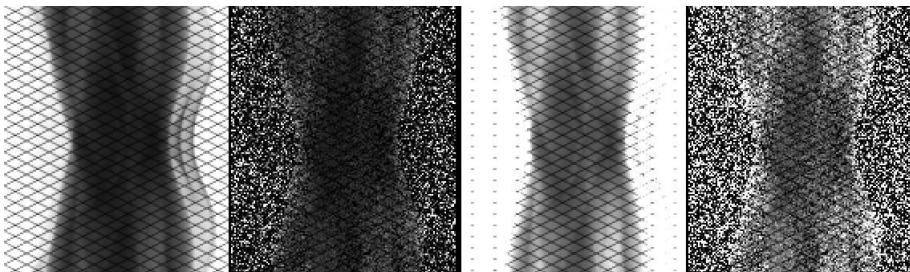


Figure 5.13: CT-attenuation factors multiplied by detector pair sensitivities shown together with the MLACF estimated attenuation factors ignoring detector pair sensitivities (left pair) for the transaxial slice of figure 5.12. The same attenuation factors are shown with a different gray level scale (right pair).

---

## 5. ML-RECONSTRUCTION FOR TOF-PET WITH SIMULTANEOUS ESTIMATION OF THE ATTENUATION FACTORS

---

Our current tests indicate that in the absence of noise the differences between the images of two algorithms tend to reduce at high iteration numbers, and the activity reconstructions become comparable. This suggests that they are mostly caused by different trajectories towards the solution, and much less by differences in the final solutions. The study of these effects are subject to future investigations.

Convergence of the attenuation estimate of MLACF (update expression (5.3)) is shown to be geometric with a ratio equal to the scatter fraction of the emission data. If the scatter and randoms contribution in the measurements can be ignored, the algorithm reduces to an MLEM-like algorithm with an immediate convergence of the attenuation factors. Properties and some convergence results for such an algorithm can be found in [63]–[65], where it is also proven that the log-likelihood is free of local maxima for consistent TOF emission measurements.

In the clinical system considered here, the scatter contribution is estimated from the CT-based attenuation coefficients [101]. We have used this scatter estimate in the MLACF reconstruction of the patient data. However, we believe that, if required, a scatter estimate independent of the CT could be obtained as well, from a first MLACF reconstruction where the scatter is ignored. From the estimated attenuation sinogram, an approximate attenuation map could be reconstructed, which could be used to estimate the scatter. With this estimate, MLACF could be applied again to obtain scatter corrected activity estimates. In [61], some evidence was given that this procedure would work for MLAA, which makes us believe that it could be applied to MLACF as well.

The proposed method proves to be very robust against variations in detector pair sensitivities. This was demonstrated with reconstructions where detector pair sensitivities were ignored for a 4 minute  $^{18}\text{F}$ -FDG scan of a patient thorax. Although MLACF obtained almost identical activity images when detector pair sensitivities were ignored or accounted for, we do not propose to ignore the sensitivities during reconstructions. When the sensitivities are estimated by means of dedicated high count calibration scans, the detector pair sensitivities are estimated with greater precision. Moreover, using the estimated sensitivities during MLACF reconstructions allows the reconstruction of the attenuation image if needed, which otherwise is not possible. But the results show that MLACF will automatically compensate for any residual calibration errors that might be present in the estimated sensitivities.

In the patient study, we observed shadow-like artifacts in MLEM reconstructions of the activity which were not present in the activity estimates of MLACF and MLAA. We believe that these artifacts are caused by motion between the CT and PET scans, and that these artifacts can be mitigated by algorithms which jointly estimate the activity and the attenuation.

## 5.6 Conclusion

This paper introduces a new algorithm in the framework of joint activity and attenuation reconstructions from TOF-PET data. The MLACF algorithm, which makes alternating updates of the activity and the attenuation factors, worked well

in our 2D and 3D simulations as well as in a patient scan. Although MLACF does not impose consistency to the estimated attenuation factors, the activity reconstructions possess similar noise characteristics as activity reconstructions of MLAA for considerable amounts of noise in the emission data. The method also proves to be a powerful tool in case of inaccurate estimates of detector pair sensitivities which otherwise can cause image degradation in the reconstructions.

## Acknowledgement

The authors would like to thank A. Bousse for his comments which helped improve the convergence analysis, and C. Michel, M. Casey, G. Bal, F. Kehren, M. Conti, C. Watson, V. Panin and J. Hamill from Siemens Healthcare, Molecular Imaging for help with the data processing and the very interesting discussions. The authors would also like to thank S. Stroobants, S. Staelens and M. Lambrechts of the Universiteit Antwerpen for providing the patient data.



## Chapter 6

# Simultaneous Reconstruction of the Activity Image and Registration of the CT Image in TOF-PET

A. Rezaei, C. Michel, M. E. Casey, and J. Nuyts, “Simultaneous Reconstruction of the Activity Image and Registration of the CT Image in TOF-PET”, *Physics in Medicine and Biology*, In-press, 2015

### Abstract

Previously, maximum-likelihood methods have been proposed to jointly estimate the activity image and the attenuation image or the attenuation sinogram from time-of-flight (TOF) positron emission tomography (PET) data. In this contribution, we propose a method that addresses the possible alignment problem of the TOF-PET emission data and the computed tomography (CT) attenuation data, by combining reconstruction and registration. The method, called MLRR, iteratively reconstructs the activity image while registering the available CT-based attenuation image, so that the pair of activity and attenuation images maximise the likelihood of the TOF emission sinogram. The algorithm is slow to converge, but some acceleration could be achieved by using Nesterov’s momentum method and by applying a multi-resolution scheme for the non-rigid displacement estimation. The latter also helps to avoid local optima, although convergence to the global optimum cannot be guaranteed. The results are evaluated on 2D and 3D simulations as well as a respiratory gated clinical scan. Our experiments indicate that the proposed method is able to correct for possible misalignment of the CT-based attenuation image, and is therefore a very promising approach to suppressing attenuation artefacts in clinical PET/CT. When applied to respiratory gated data of a patient scan, it produced deformations that are compatible with breathing motion and which reduced the well known attenuation artefact near the dome of the liver. Since the method makes use of the energy-converted CT attenuation image, the scale problem of joint reconstruction is automatically solved.

---

## 6. SIMULTANEOUS RECONSTRUCTION OF THE ACTIVITY IMAGE AND REGISTRATION OF THE CT IMAGE IN TOF-PET

---

### 6.1 Introduction

Positron emission tomography (PET) data are acquired over a relatively long time interval whereas computed tomography (CT) attenuation values are acquired almost instantaneously. In addition, in current PET/CT scanners, the CT and PET scans are acquired sequentially. Thus, artifacts due to patient and/or breathing motion are expected in emission reconstructions (in-scan motion) together with artifacts due to possible misalignment of PET and CT data (between-scan motion). Recent studies have shown that in time-of-flight (TOF) PET, joint and stable estimation of the activity and the attenuation is possible [56], [58], [61]. Given the availability of TOF-PET data, the activity image can be jointly estimated either with the attenuation image [56], [60], [61] or with the attenuation sinogram [65], [66], [104], [109]. Because TOF-PET determines the attenuation only up to a constant [58], some constraining is required for accurate quantitative reconstruction. The MLAA algorithm [61], [120] jointly estimates the two images, solving for the constant by imposing the known attenuation of tissue. Alternatively, Mehranian et al. [121] solved the scale problem by incorporating an intensity prior on the estimated attenuation values using a Gaussian mixture model of different tissue types. For MLACF [65], [66], which jointly estimates the activity image and the attenuation sinogram, this straightforward constraining method is not possible. However, Panin et al. [104] proposed a modified MLACF version to complete the attenuation factors obtained from CT, in which the constant is determined by the available CT-data.

Although the use of consistency conditions for the estimation of attenuation from non-TOF emission data [39], [41], [79] has had limited success in practice, they were found to be useful in determining the strength of regularisation parameters for maximum *a-posteriori* reconstruction of the attenuation image from transmission measurements [122]. Furthermore, studies have shown that the consistency conditions of the non-TOF emission data can also be used to estimate the attenuation image that has affected the measurements as an affine transform of a known attenuation image [24], [27]. This approach was used as a means to correct for attenuation in the case of between-scan motion [33], [36]. Although instability issues were reported with an affine motion model [33], the results seemed to be encouraging with a rigid motion model despite a slow convergence [36]. However, the problem of correcting for patient and/or breathing motion requires more complex transformation models. Since with the introduction of TOF, the PET emission data provide more information about the attenuation than before, it is expected that the TOF-PET data also provide a means to estimate more complex motion models, and could help mitigate the problems of in-scan and between-scan motion in TOF-PET.

In current TOF-PET/CT systems, the PET attenuation image is normally estimated by converting the CT-image values to the linear attenuation values for the 511 keV photons [123]. In this study, we use this CT-derived attenuation image in a joint estimation framework and align the attenuation image so that the pair of the activity image and the deformed CT-based attenuation image better explain the emission measurements. To do so, the estimation of the attenuation image of MLAA [61] is replaced with a transformation (rigid or non-rigid) estimation based on

minimising a sum of squared differences (SSD) term in the joint estimation framework. We show below that weighing the SSD term by the curvature of the emission log-likelihood ensures that a decrease of the SSD term will produce an increase of the quadratic surrogate function for the likelihood. The proposed algorithm is called MLRR (maximum likelihood reconstruction of activity and registration of attenuation), which aims at combining the high signal to noise ratio of the CT image with the optimal (i.e. the maximum likelihood) alignment produced by the joint estimation. Since the method makes use of CT-based attenuation images, no extra correction is required for the missing scale problem in the joint estimation method.

The paper is organised as follows; the MLRR algorithm is described in section 6.2. We will also look at options to improve its convergence, since the method was shown to have a slow convergence rate with a non-rigid motion model [67]. The design of the 2D and 3D simulation experiments are presented in section 6.3. The simulation results are shown together with the results of a respiratory gated clinical scan in section 6.4. In section 6.5, we conclude by discussing the results, drawing some conclusions and giving an outline of future research on the topic.

## 6.2 Method/Theory

Assuming Poisson statistics and ignoring constant terms, the log-likelihood function for TOF-PET emission data  $y$  can be expressed as:

$$L(\lambda, \mu, y) = \sum_{it} y_{it} \ln \bar{y}_{it} - \bar{y}_{it} \quad (6.1)$$

where  $\lambda$  and  $\mu$  represent the emission and attenuation parameters and  $\bar{y}_{it}$  is the expected emission sinogram value for line-of-response (LOR)  $i$  and TOF-bin  $t$ , which is computed as:

$$\bar{y}_{it} = b_{it}a_i + s_{it} = \sum_j c_{ijt}\lambda_j e^{-\sum_k l_{ik}\mu_k} + s_{it} \quad (6.2)$$

where  $b_{it}$  is the TOF-projection of the activity image along LOR  $i$  and in TOF-bin  $t$ ,  $a_i$  is the attenuation factor along the same LOR and  $s_{it}$  represents the contributions of scatter and/or randoms for the same data bin  $i, t$ . Furthermore,  $c_{ijt}$  represents the sensitivity of detector  $i$  and TOF-bin  $t$  to emissions coming from voxel  $j$ ,  $\lambda_j$  is the activity in voxel  $j$ ,  $l_{ij}$  is the effective intersection length between LOR  $i$  and voxel  $j$ ,  $\mu_j$  is the attenuation at voxel  $j$ . Note that summation over the TOF index ( $t$ ) yields the corresponding non-TOF values ( $\sum_t c_{ijt} = c_{ij}$  and  $\sum_t y_{it} = y_i$ ).

The MLRR algorithm treats the log-likelihood function as a function of the activity  $\lambda$  and the attenuation  $\mu[\Theta]$ , where  $\Theta = \{\Theta_p | p = 1 \dots P\}$  represents a set of deformation parameters, which deform the known attenuation image  $\mu^\dagger$  into the attenuation image  $\mu[\Theta]$ . The log-likelihood is maximised by estimating the activity values  $\lambda_j$  in every voxel  $j$  and the deformation parameters  $\Theta$ . Below, an iterative algorithm is derived which alternately updates the activity values while keeping the attenuation image fixed, and then updates the deformation parameters while keeping the activity values fixed.

## 6. SIMULTANEOUS RECONSTRUCTION OF THE ACTIVITY IMAGE AND REGISTRATION OF THE CT IMAGE IN TOF-PET

---

When the deformation, and therefore the attenuation, is fixed, the problem of updating the activity image is the same as in standard maximum likelihood expectation maximisation (MLEM) reconstruction. Hence, the activity is updated by applying an iteration of the MLEM algorithm or its accelerated version, ordered subsets expectation maximisation (OSEM). When the activity is fixed, the deformation of the attenuation map must be updated such as to increase the likelihood. This problem could be solved by deriving a dedicated gradient ascent algorithm for this subproblem. Instead, we propose to use a nested approach, which first computes a desired attenuation update using an established ML algorithm for transmission tomography (MLTR [124]) and then apply an established registration algorithm to find the (incremental) deformation that results in a good approximation of that desired update. In section 2.1 this method is derived, essentially by applying the chain rule to the gradient of the likelihood and introducing reasonable approximations. This leads to the algorithm (6.12) - (6.14). In section 2.2 an acceleration scheme based on Nesterov's momentum method is proposed. We consider both rigid and non-rigid deformations of the attenuation map. For rigid deformations, the second step of the nested approach (eq. (6.14)) is solved with a weighted least squares registration algorithm, as briefly discussed in section 2.3. Section 2.4 proposes a method for non-rigid deformations, where the deformation step is computed with a slightly modified version of the demons algorithm [125].

### 6.2.1 Attenuation Deformation Estimation

When the activity is fixed, the log-likelihood function becomes similar to that of standard transmission tomography, except that instead of updating the attenuation values, we wish to adjust the attenuation image by modifying the deformation parameters.

The proposed algorithm is based on the MLTR algorithm [124], a maximum likelihood reconstruction algorithm for transmission tomography. In every iteration MLTR makes a quadratic approximation to the Poisson likelihood function, which is then replaced by a separable quadratic surrogate function. The surrogate function has the following form:

$$S(\mu^{(n)} + \delta\mu, y) = L(\mu^{(n)}, y) + \sum_j \dot{L}_j^{(n)} \delta\mu_j + \sum_j \frac{1}{2} \ddot{L}_j^{(n)} (\delta\mu_j)^2 \quad (6.3)$$

where,

$$\dot{L}_j^{(n)} \triangleq \dot{L}_j \Big|_{\mu=\mu^{(n)}} = \frac{\partial L}{\partial \mu_j} \Big|_{\mu=\mu^{(n)}}, \quad \ddot{L}_j^{(n)} \triangleq \ddot{L}_j \Big|_{\mu=\mu^{(n)}} = \sum_k \frac{\partial^2 L}{\partial \mu_j \partial \mu_k} \Big|_{\mu=\mu^{(n)}}$$

where  $\mu^{(n)}$  represents the attenuation reconstruction at the current iteration  $n$  and  $\delta\mu$  is its update. Maximising (6.3) produces the MLTR update  $\delta\mu^{(n)}$ :

$$\mu_j^{(n+1)} = \mu_j^{(n)} + \delta\mu_j^{(n)} \quad (6.4)$$

$$\delta\mu_j^{(n)} = \arg \max_{\delta\mu} S(\mu^{(n)} + \delta\mu, y) = -\frac{\dot{L}_j^{(n)}}{\ddot{L}_j^{(n)}} \quad (6.5)$$

Details on the MLTR update for TOF-PET data are given in Appendix A. The update maximises the surrogate and guarantees that the value of the quadratic approximation to the likelihood increases. The likelihood is therefore expected to increase as well, but because of the approximation, monotonicity cannot be guaranteed. However, it should be mentioned that other transmission reconstruction algorithms exist, e.g. the separable paraboloidal surrogates (SPS) algorithm [126], with guaranteed monotonicity even with an additive randoms or scatter contribution in the emission data. In our experience the MLTR reconstruction algorithm works very well in practice and increases the likelihood monotonously.

The MLTR algorithm is now adapted to the new problem using an approach similar to that proposed by Wang and Qi [127] for direct reconstruction of kinetic parameters. For the problem at hand, the surrogate function (6.3) is rewritten as a function of the deformation parameters  $\Theta$ :

$$\tilde{S}(\mu[\Theta^{(n)}] + \delta\mu[\theta], y) = L(\mu[\Theta^{(n)}], y) + \sum_j \dot{L}_j^{(n)} \delta\mu_j[\theta] + \sum_j \frac{1}{2} \ddot{L}_j^{(n)} (\delta\mu_j[\theta])^2 \quad (6.6)$$

where  $\Theta^{(n)}$  is the deformation at the current iteration  $n$ ,  $\theta$  is an update to that deformation and  $\delta\mu[\theta] = \mu[\Theta^{(n)} + \theta] - \mu[\Theta^{(n)}]$ . The new value of  $\Theta$  is obtained as

$$\Theta^{(n+1)} = \Theta^{(n)} + \theta^{(n)} \quad (6.7)$$

$$\theta^{(n)} = \arg \max_{\theta} \tilde{S}(\mu[\Theta^{(n)}] + \delta\mu[\theta], y) \quad (6.8)$$

where we have slightly misused the '+' sign to denote the composition of the transformations. The update is obtained by setting the derivatives of (6.6) to zero, which yields:

$$\frac{\partial \tilde{S}}{\partial \theta_p} = \left( \sum_j \dot{L}_j^{(n)} + \ddot{L}_j^{(n)} \delta\mu_j[\theta] \right) \frac{\partial \delta\mu_j[\theta]}{\partial \theta_p} = 0, \quad p = 1, \dots, P \quad (6.9)$$

This maximisation is equivalent to the following least squares problem:

$$\theta^{(n)} = \arg \min_{\theta} \frac{1}{2} \sum_j \ddot{L}_j^{(n)} \left( \delta\mu_j[\theta] - \delta\mu_j^{(n)} \right)^2 \quad (6.10)$$

Finally, (6.10) can be regarded as an image registration problem using a weighted least squares criterion, since it can be rewritten as:

$$\theta^{(n)} = \arg \min_{\theta} \frac{1}{2} \sum_j \ddot{L}_j^{(n)} \left( (\mu_j[\Theta^{(n)}] + \delta\mu_j[\theta]) - (\mu_j[\Theta^{(n)}] + \delta\mu_j^{(n)}) \right)^2 \quad (6.11)$$

The two images that are registered are

- the static image  $\mu[\Theta^{(n)}] + \delta\mu^{(n)}$ , which is obtained by applying MLTR iteration (6.5) to the image obtained in the current iteration, and
- the image  $\mu[\Theta^{(n)}] + \delta\mu[\theta]$ , which is obtained by deforming the image at the current iteration according to the deformation parameters  $\theta$ .

## 6. SIMULTANEOUS RECONSTRUCTION OF THE ACTIVITY IMAGE AND REGISTRATION OF THE CT IMAGE IN TOF-PET

---

Consequently, the MLRR algorithm is obtained by iterating the following three steps procedure:

1. apply MLEM to update  $\lambda_j$ :

$$\lambda_j^{(n+1)} = \frac{\lambda_j^{(n)}}{\sum_i c_{ij} a_i} \sum_{it} c_{ijt} a_i \frac{y_{it}}{\sum_\xi c_{i\xi t} a_i \lambda_\xi^{(n)} + s_{it}} \quad (6.12)$$

2. apply the MLTR algorithm to obtain the intermediate reconstruction  $m^{(n)}$  (see Appendix A for expressions for  $\dot{L}_j$  and  $\ddot{L}_j$ ):

$$m_j^{(n)} = \mu_j[\Theta^{(n)}] + \delta\mu_j^{(n)} = \mu_j[\Theta^{(n)}] - \dot{L}_j^{(n)} / \ddot{L}_j^{(n)} \quad (6.13)$$

3. apply a weighted least squares registration to update the deformation:

$$\Theta^{(n+1)} = \Theta^{(n)} + \arg \min_{\theta} \frac{1}{2} \sum_j \ddot{L}_j^{(n)} \left( \mu_j[\Theta^{(n)}] + \delta\mu_j[\theta] - m_j^{(n)} \right)^2 \quad (6.14)$$

### 6.2.2 Acceleration

We have observed previously that the MLRR algorithm is slow to converge [67]. Here we introduce a term based on Nesterov's momentum [128], [129] that affects the estimation of the intermediate reconstruction  $m^{(n)}$ , and significantly improves the convergence speed of the algorithm. In this accelerated scheme, the second step of the algorithm (eq. (6.13)) is replaced by:

- 2.\* replace MLTR update  $m^{(n)}$  with the update  $m^{(n)*}$ , which is obtained with Nesterov's momentum method as follows:

$$\begin{aligned} m_j^{(n)*} &= \mu_j[\Theta^{(n)}] + \delta\mu_j^{(n)*} \\ &= \mu_j[\Theta^{(n)}] - \left. \frac{\dot{L}_j}{\ddot{L}_j} \right|_{\mu=\mu[\Theta^{(n)}]+\alpha^{(n)}\delta\mu_j^{(n-1)*}} + \alpha^{(n)} \delta\mu_j^{(n-1)*} \end{aligned} \quad (6.15)$$

where,  $\delta\mu^{(n)*}$  is the current accelerated MLTR attenuation update, and

$$\alpha^{(n)} = \frac{h^{(n-1)} - 1}{h^{(n)}}, \quad h^{(n)} = \frac{1 + \sqrt{1 + 4(h^{(n-1)})^2}}{2} \quad (6.16)$$

with  $h^{(0)} = 1$ .

The addition of a term based on previous MLTR reconstruction updates  $\delta\mu^{(n-1)*}$  provides some momentum for attenuation reconstruction, and consequently for the estimated motion parameters. The acceleration with Nesterov momentum is known to be non-monotonic even if the original optimiser is monotonic.

### 6.2.3 Special Case of Rigid Motion Estimation

To simultaneously reconstruct the activity image and rigidly align the attenuation map, the parameter set  $\Theta$  contains 6 rigid motion parameters (three translations and three rotation angles). They are determined by a rigid registration algorithm which minimises the sum of weighted squared differences (6.11), using a gradient descent algorithm and accelerated by incorporating the momentum produced by (6.15).

### 6.2.4 Special Case of Non-rigid Deformation Estimation

For the non-rigid case, the deformation parameters  $\Theta$  are replaced by a vector<sup>1</sup>  $\mathbf{D}_j = (D_j^x, D_j^y, D_j^z)$  of displacement fields for every voxel  $j$ . Minimising (6.10) by means of the demons registration algorithm [125], an incremental displacement  $\mathbf{d}$  update is computed as:

$$\mathbf{d}_j^{(n)} = \frac{(\nabla\mu[\mathbf{D}^{(n)}])_j \delta\mu_j^{(n)}}{\|(\nabla\mu[\mathbf{D}^{(n)}])_j\|^2 - \beta/\ddot{L}_j^{(n)}} \quad (6.17)$$

where  $(\nabla\mu[\mathbf{D}^{(n)}])_j$  is the gradient of the deformed attenuation image at voxel  $j$  with respect to the image coordinates  $(x, y, z)$ , and  $\beta/\ddot{L}_j^{(n)}$  helps to stabilise the incremental displacement estimate  $\mathbf{d}^{(n)}$  at low gradient values of the deformed attenuation image in which  $\beta$  is the strength of a penalty term. Details on the derivation of the incremental displacement update are given in Appendix B.

The displacement update (6.17) is essentially the constrained demons update [125], differing from it only by using a different form for the stabilisation term and by only using the gradient of the deformed CT image<sup>2</sup>. The original demons algorithm uses  $\|\delta\mu\|^2$  in the denominator which automatically limits the step size to a maximum of 0.5 pixels. As the iterations proceed and the maximum likelihood solution is approached, the values  $\delta\mu$  become small, hence a smaller maximum step size would be more desirable. The use of the stabilising term  $\beta/\ddot{L}_j^{(n)}$  further reduces the influence of the vanishing  $\delta\mu_j^{(n)}$  in later iterations. Unfortunately  $\ddot{L}_j^{(n)}$  is count-dependent. This count-dependency is accounted for by adjusting  $\beta$  such that the incremental displacement update of (6.17) gives a maximum change of 0.5 voxels in the early iterations of the MLRR algorithm. The value of  $\beta$  is then kept constant in subsequent iterations, ensuring that the displacement updates (6.17) will vanish with vanishing  $\delta\mu_j$ .

When using the acceleration provided by the momentum of the attenuation updates (using the accelerated estimate  $\delta\mu^{(n)*}$  defined in (6.15) instead of  $\delta\mu^{(n)}$ ), in order to limit the maximum incremental displacement in (6.17) to the defined maximum, the same acceleration scheme must also be applied to the stabilising term  $\beta/\ddot{L}^{(n)}$ . Since  $\beta$  is fixed and  $\ddot{L}^{(n)}$  changes little with iterations, we alternatively weight the strength of the regularisation term in each iteration by:

$$\gamma^{(n)} = 1 + \alpha^{(n)} \gamma^{(n-1)} \quad (6.18)$$

<sup>1</sup>A bold symbol indicates a three element vector throughout the text.

<sup>2</sup>The gradient of the moving image is used as opposed to the gradient of the fixed image [130].

## 6. SIMULTANEOUS RECONSTRUCTION OF THE ACTIVITY IMAGE AND REGISTRATION OF THE CT IMAGE IN TOF-PET

---

where,  $\gamma^{(0)} = 0$  and use  $\gamma^{(n)}\beta/\ddot{L}_j^{(n)}$  as the modified regularisation term in (6.17).

The task of image registration can also be accelerated by a multi-resolution registration scheme. A multi-resolution approach offers two advantages: not only it accelerates the registration process, it also reduces the risk of getting stuck at possible local maxima of the solution space. However, with a non-rigid motion model, convergence to the global solution is never guaranteed. In our implementation of the multi-resolution registration scheme, the incremental displacement update is estimated in multiple resolution levels in every iteration, where the pixel width in a coarser level was set to twice that of the finer resolution level. After updating the incremental displacement fields in each resolution level, the final incremental displacement field is computed as the composition of the multi-resolution incremental displacement fields (coarse-to-fine resolution levels), and is used to deform the CT attenuation image.

In addition to constraining the incremental displacement update to small displacement values by introducing a quadratic penalty term defined in (6.30), we also favour locally smooth displacement estimates  $\mathbf{d}_j$  by enforcing a fluid-like and a diffusion-like smoothing on the estimated displacement fields. These approaches have been previously shown to be very effective for optimisation with the demons [130]. When computing the non-rigid displacement fields at each resolution level, the additional regularisation was done by applying a Gaussian smoothing to the displacement fields, i.e.:

$$\mathbf{d}_j^{(n)} = \sum_{\xi} G_{j\xi}^F \mathbf{d}_{\xi}^{(n)} \quad (6.19)$$

$$\mathbf{D}_j^{(n+1)} = \sum_{\xi} G_{j\xi}^D (\mathbf{D}_{\xi}^{(n)} + \mathbf{d}_{\xi}^{(n)}) \quad (6.20)$$

where,  $G^F$  and  $G^D$  are the fluid-like and diffusion-like regularising Gaussian kernels [130], [131], respectively. Details about the parameter values used in the experiments are provided in the simulation designs of section 6.3.

When the activity is fixed and the log-likelihood is treated as a function of voxel attenuation values, the associated Hessian is negative semi-definite, and therefore, the only local maximum is the global one [132]. However, when the log-likelihood is treated as a function of a displacement field, the computation of the Hessian is challenging, and it seems very likely that there will be multiple local maxima. Therefore, starting the non-rigid motion estimation from a rigidly aligned attenuation map would be recommended.

### 6.3 Experiment Design

The Siemens Biograph mCT scanner specifications [92] (with a radial detector mashing of 2) were chosen in the simulations. In the 2D simulations, the TOF-PET data were organised in a 3D sinogram consisting of 200 radial bins of 0.4 cm width, 168 projection angles over 180 deg, and 13 TOF-bins of 312 ps width (which is sufficient to avoid aliasing artifacts in the reconstructions [3]) with an effective TOF

resolution of 580 ps. A small discrepancy between the simulation and reconstruction projectors was introduced by discretising the 2D thorax phantom in an over-sampled grid of  $600 \times 600$ , and the simulated LORs were subsequently under-sampled (mashed) as the average of three neighbouring LORs. Both activity and attenuation images were forward-projected using Joseph's method [133], where for each TOF-bin the activity image was weighted by the effective weights of the TOF-bin width and the TOF-resolution. Activity and attenuation images were then reconstructed in a  $200 \times 200$  pixel grid of 0.4 cm width.

In the fully 3D simulation, the TOF-PET emission data were organised in a 5D sinogram consisting of 200 radial bins of 0.4 cm width, 168 azimuthal angles, 9 co-polar angles with 109 planes of 0.2 cm width, and 13 TOF-bins of 312 ps width. A 3D implementation of the above forward-projection was used to obtain the 5D TOF-PET emission measurements. The resulting 3D activity and attenuation reconstructions had a  $200 \times 200 \times 109$  voxel grid with a voxel width of 0.4 cm and 0.2 cm in the transaxial and axial directions, respectively.

The above described MLRR images were compared to the reconstructions obtained with the MLAA algorithm [61], with the aim of revealing similarities and differences between the joint reconstructions. The goal was not to identify one as the preferred algorithm. The MLAA reconstructions were initialised with a uniform activity image and a uniform tissue attenuation image in the phantom/patient support. In order to eliminate any confounding effects of the scale factor in the reconstructions, the scale problem in MLAA was fixed by assuming knowledge of the total tracer activity. The MLRR algorithm is initialised with a uniform activity image, the misaligned CT-based attenuation image  $\mu^\dagger$  and the identity displacement field for a non-rigid motion model. Furthermore, the CT attenuation image used in the simulations had the same image resolution as the true phantoms that were used to create the PET emission data. In the patient data reconstructions, a Gaussian smoothing of 4 mm FWHM was applied to the CT image to correct for the difference in PET and CT system resolutions.

In the following, the activity and attenuation figures are displayed in inverse gray and gray colour maps, respectively.

### 6.3.1 2D Simulation

The MLRR and MLAA algorithms were compared in a 2D TOF-PET simulation of a 2D thorax phantom. Figure 6.1 shows the activity and attenuation images with three (tissue (blue), lung (green), and tumour (red)) contours of the regions of interest (ROIs) where the reconstructions are analysed in. The figure also shows the two mismatched CT attenuation images used in the study. The mismatch in the CT1 attenuation image is created by an increase of the size of the lungs, and a change in the size and location of the simulated tumour lesion. The CT2 attenuation image is obtained by a rigid transformation of the CT1 attenuation image, i.e. rotation of 30 deg, and a translation of 2.4 cm and 6.0 cm in the horizontal and vertical directions, respectively.

## 6. SIMULTANEOUS RECONSTRUCTION OF THE ACTIVITY IMAGE AND REGISTRATION OF THE CT IMAGE IN TOF-PET

---

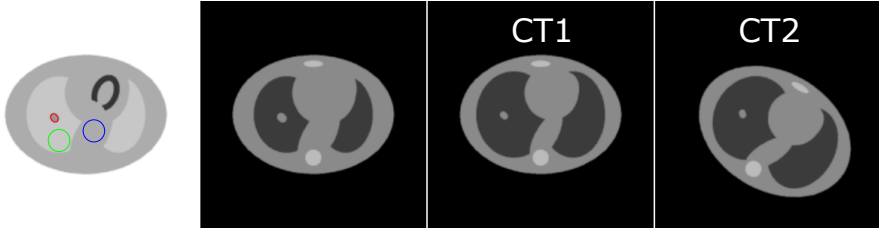


Figure 6.1: 2D activity (column 1) and attenuation (column 2) images of a simulated thorax phantom. The activity contours define tissue (blue), lung (green), and tumour (red) regions of interest (ROIs). The two mismatched CT attenuation images used in the 2D simulation study are shown in columns 3 and 4. CT1 (column 3) differs from the true attenuation by a non-rigid deformation of the attenuation image, CT2 (column 4) is obtained by a rigid transformation of the CT1 attenuation image.

### Reconstructions

MLAA and MLRR reconstructions are compared for noise-free TOF-PET data as well as moderate-noise and high-noise in the emission data. The moderate-noise TOF-PET data had an expected maximum count of 50.4 and 146.0 in the TOF-PET sinogram and its corresponding non-TOF sinogram data bins, for the high-noise data these count values were 12.6 and 36.5. In this study, the CT2 attenuation image was used as the mismatched attenuation image. For MLAA, we assumed that the total amount of activity was known and the MLAA activity reconstructions were scaled in each iteration accordingly.

The reconstructions are analysed after 5 iterations of 24 subsets of the MLRR algorithm, where the attenuation image is updated three times for each update of the activity image (i.e. after each MLEM sub-iteration, three MLTR sub-iterations are applied). The first iteration estimates the rigid transformation parameters, providing an initial alignment of the given CT attenuation image. The following 4 iterations assume a non-rigid deformation model, where the multi-resolution scheme is used to update the displacement parameters in two resolution levels in each iteration. A diffusion-like and fluid-like regularisation of the displacement field was obtained by smoothing the displacement field and its update with a Gaussian of 1.0 and 2.5 pixels FWHM, respectively. The same smoothing regularisation was applied for the noise-free and the noisy TOF-PET emission data sets. For the MLAA reconstructions, 3 iterations with 24 subsets were applied, again with 3 MLTR sub-iterations for each MLEM sub-iteration. For the MLEM reconstruction 3 iterations with 24 subsets were computed. In both MLAA and MLRR, the attenuation is updated more frequently than the activity because its convergence tends to be slower.

The emission data provide no attenuation information in LORs that do not intersect the activity distribution. In order to improve the attenuation reconstruction of MLAA, LOR-values outside the support of the activity distribution were given a small count in the “blank” (un-attenuated projection of the activity image) and measured sinograms, which encourages the MLTR algorithm to assign zero attenuation outside the activity distribution support. For MLRR, the displacement estimation

was restricted to the voxels within the support of the CT-based attenuation image.

### Bias-Variance

We analysed noise properties of the activity reconstructions of both MLRR and MLA. First a noise-free data set was computed (with the same expected maximum count as the high-noise data set of section 6.3.1), which was then used as the expectation for a pseudo-random Poisson noise generator to generate 100 independent noise realisations. In this study, the CT2 mismatched attenuation image was used, and the reconstruction parameters were set as previously described. The results are reported after 120 updates of MLRR and MLA activity reconstructions, where all projection angles were used in every update. For MLRR, a rigid motion model is used in the first 24 activity updates and a non-rigid motion model is used for the following 96 updates of the MLRR activity image. The joint activity reconstructions are compared to MLEM reconstructions with the attenuation sinograms of the true, CT1, and CT2 attenuation images. We assume that the noise-free reconstructions of the thorax phantom are a good estimate of the average of noisy reconstructions. Bias is computed as the average absolute pixel-by-pixel difference between the noise-free reconstruction and the activity phantom of figure 6.1, and variance is computed as the squared mean difference from the noise-free reconstructions. We report the estimated bias as well as the variance of activity reconstructions in the support of the 2D thorax phantom for 100 different TOF-PET noise realisations.

### Convergence Analysis

In order to get more insight into the convergence properties of MLRR, the log-likelihood of equation (6.1) as well as the root mean square error (RMSE) between the attenuation reconstructions and the true attenuation image were computed for each iteration of MLRR. The log-likelihood was normalised by its upper limit defined by the TOF emission data, i.e.  $\sum_{it} y_{it} \ln y_{it} - y_{it}$ . The influence of Nesterov's momentum acceleration as well as the multi-resolution displacement estimation scheme in MLRR are analysed in the noise-free and the moderate-noise TOF-PET emission data. A non-rigid motion model starting from the CT1 mismatched attenuation image was used in the analysis, and the likelihood and RMSE are plotted for 250 updates of the attenuation image. In this study, no ordered subsets acceleration was applied, i.e. all projection angles were used in every iteration.

### TOF-resolution

The effects of the TOF-resolution was studied by varying the simulated TOF Gaussian kernel ranging from 1.2 ns to 0.2 ns FWHM. In order to avoid aliasing artifacts, the emission data were projected in 40 TOF-bins of 100 ps width. Similar to section 6.3.1, the algorithm is initialised with the CT1 mismatched attenuation image, only a non-rigid motion model was considered and no ordered subsets were applied during reconstructions. We report on the likelihood and RMSE obtained after 250 updates of the attenuation image.

## 6. SIMULTANEOUS RECONSTRUCTION OF THE ACTIVITY IMAGE AND REGISTRATION OF THE CT IMAGE IN TOF-PET

### 6.3.2 3D Simulation

The XCAT phantom [134] was used to generate realistic respiratory motion. A maximum diaphragm motion of 2.0 cm and a maximum anterior-posterior motion of 1.2 cm was used to simulate the breathing cycle, which was gated into 8 (motion-free) frames. Figure 6.2 shows the activity and attenuation images of the XCAT phantom frame used in this study as well as the mismatched CT attenuation image which was chosen from a different frame in the respiratory cycle.

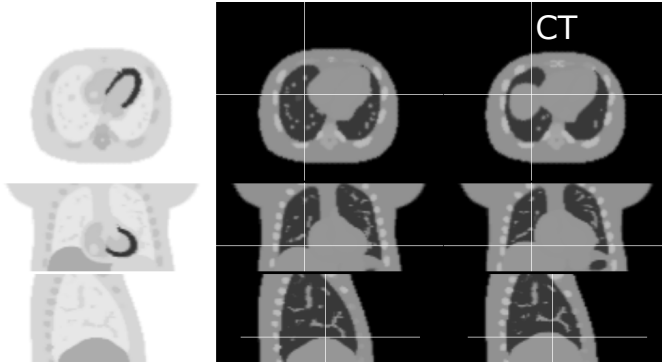


Figure 6.2: Transaxial, coronal and sagittal views through the true activity (left), true attenuation (centre), and the mismatched CT attenuation (right) images of the breathing XCAT phantom. The XCAT phantom was gated into 8 respiratory gates, the true activity and attenuation images, and the mismatched attenuation image correspond to frames 4 and 2, respectively.

The XCAT phantom was forward projected with the 3D TOF-PET projector, and Poisson noise was added to the measurements to simulate a 4 min  $^{18}\text{F}$ -FDG thorax scan. The average maximum count of the TOF sinogram and its corresponding non-TOF sinogram were 10.6 and 28.2, respectively, and the 5D sinogram had a total of 46 M events. MLRR and MLAA activity and attenuation reconstructions are then compared. Furthermore, the attenuation reconstruction of MLRR is compared to a demons [125] registration of the CT attenuation image and the reference true attenuation of figure 6.2. In the 3D simulation, the displacement estimate of MLRR was regularised by a diffusion-like smoothing of 1.0 voxel FWHM and a fluid-like smoothing of 2.5 voxels FWHM. The activity and attenuation reconstruction comparison of MLAA and MLRR are after 3 iterations of 24 subsets, and the demons registered attenuation image is obtained after the same number of registration updates in two resolution levels.

### 6.3.3 Patient Data

#### Reconstruction

A clinical 4 min TOF-PET thorax scan (Siemens Biograph mCT) of a patient injected with 296 MBq of  $^{18}\text{F}$ -FDG is reconstructed with MLRR and compared to activity reconstructions of MLEM. The emission data was acquired 80 minutes post-injection,

and had a measured true-to-prompt coincidence event ratio of 36%. The additive contribution of randoms as well as the single-scatter estimate [101] were corrected for during reconstructions. The displacement estimates were updated as in section 6.3.2.

### Gated Reconstructions

The amplitude-based data-driven gating of [135] is used to gate the 4 min  $^{18}\text{F}$ -FDG thorax scan of the patient into 3 respiratory gates. For each gate, we compare the MLEM activity reconstruction with the CT-based attenuation image to the activity reconstruction of MLRR, initialised with the same CT-based attenuation image.

## 6.4 Results

### 6.4.1 2D Simulation

#### Reconstructions

An MLEM activity reconstruction with the mismatched CT2 attenuation image is shown in figure 6.3 together with the joint activity and attenuation reconstructions of MLAA and MLRR for the noise-free TOF-PET emission data. Figure 6.3 also shows the attenuation estimates of MLRR (after 1 iteration of 24 subsets) assuming a rigid transformation model and the non-rigid attenuation estimate of MLRR (the following 4 iterations of 24 subsets). The MLRR attenuation estimate is comparable to the attenuation reconstruction of MLAA; however, it differs slightly near rapid directional changes of the attenuation gradient.

Figure 6.4 shows the MLRR and MLAA activity and attenuation reconstructions for the moderate-noise and the high-noise TOF-PET emission data. As in the noise-free case, the MLRR attenuation reconstructions are obtained after an initial rigid parameter estimation followed by a non-rigid displacement estimation. Since noise behaves differently in both algorithms, the attenuation reconstructions are visually different. In MLAA noise directly influences the voxel values whereas in MLRR noise propagates through the deformation into the position of the anatomical boundaries (i.e. gradients in the attenuation image), however, the resulting attenuation image is still piecewise smooth similar to the original CT-based attenuation image. Thus, implicitly applying a very strong noise suppression to the attenuation coefficients, except near anatomical boundaries.

At both noise levels, the activity reconstructions of MLAA and MLRR are very similar. To quantify the accuracy of the reconstructions, two error measures were used; 1- the mean absolute difference (MAD) and 2- the mean difference (MD) of the reconstructions. The error terms were computed as:

$$\text{MAD} = \frac{\sum_j |\text{ACT}_j - \text{GT}_j|}{\sum_j \text{GT}_j}, \quad \text{MD} = \frac{\sum_{j \in \text{ROI}} \text{ACT}_j - \sum_{j \in \text{ROI}} \text{GT}_j}{\sum_{j \in \text{ROI}} \text{GT}_j} \quad (6.21)$$

where GT is the ground truth activity distribution (figure 6.1) and ACT was set to the activity reconstruction of MLRR, MLAA and MLEM<sup>CT2</sup>, respectively. For

## 6. SIMULTANEOUS RECONSTRUCTION OF THE ACTIVITY IMAGE AND REGISTRATION OF THE CT IMAGE IN TOF-PET

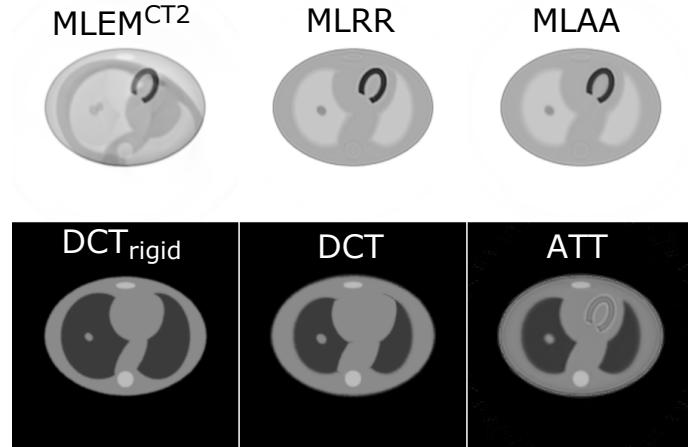


Figure 6.3: The top row shows the activity images produced by MLEM with the mismatched CT2 attenuation image, by MLRR and by MLAA. The bottom row shows the deformed CT (DCT) attenuation images of MLRR obtained after the initial rigid alignment (left) and the final non-rigid alignment (middle), and the MLAA estimated attenuation image (ATT) where remaining artefacts can be observed at the boundary of the high activity region of the heart (right). (The mismatched CT2 attenuation image is shown in fig 6.1.)

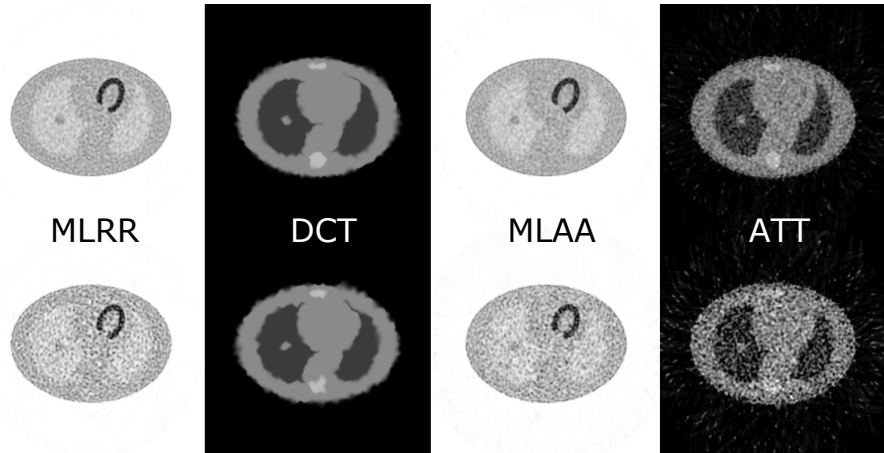


Figure 6.4: Activity (columns 1 and 3) and attenuation (columns 2 and 4) reconstructions of MLRR and MLAA for the moderate-noise (top) and high-noise (bottom) TOF-PET emission data.

the reconstructions of figure 6.4, the mean absolute difference of MLRR and MLAA were 28.9% and 26.5% for the moderate-noise activity reconstructions and 51.1% and 48.8% for the high-noise simulations, respectively. The same measure of error was 42.8% and 50.6% for the MLEM reconstruction with the mismatched CT attenuation image. Table 6.1 reports on the mean difference (MD) errors obtained in the ROIs defined in figure 6.1. Although the MLRR and MLAA produce similar error terms

in the defined ROIs, the results could still be affected by a difference in convergence of the two methods.

Table 6.1: Mean difference (MD) errors of different regions of interest (ROIs) for MLRR/MLAA activity reconstructions and the ground truth activity of figure 6.1.

	Tumor ROI		Tissue ROI		Lung ROI	
	MLRR	MLAA	MLRR	MLAA	MLRR	MLAA
noise-free (%)	7.0	2.9	2.6	0.6	1.9	-0.7
moderate-noise (%)	-4.0	-1.6	-6.9	-4.8	2.4	-3.9
high-noise (%)	-3.0	-10.1	-6.1	-7.5	-0.8	-0.3

### Bias-Variance

Figure 6.5a shows the bias and variance properties of MLRR and MLAA activity reconstructions compared to reference MLEM reconstructions with the true ( $\text{MLEM}^{\text{True}}$ ), CT1 ( $\text{MLEM}^{\text{CT1}}$ ), and CT2 ( $\text{MLEM}^{\text{CT2}}$ ) attenuation images. As expected, the misalignment of the CT can strongly influence bias in the emission reconstructions. Interestingly, after changing from a rigid motion model (prior to the kink in the curve) to a non-rigid motion model, bias and variance values for MLRR and MLAA are similar. Figure 6.5a suggests that similar bias should be expected by both MLRR and MLAA at a matched variance level. Furthermore, figure 6.5b shows the scatter plots of the MLRR/MLAA and the MLEM mean and variance activity reconstructions of the 100 noise realisations, where linear regression was applied to quantify image similarities. For both the mean and the variance images, slightly better similarity measures (slope  $q$ , coefficient of determination  $r^2$ ) were computed for MLRR than for MLAA compared to the reference MLEM mean and variance images.

### Convergence Analysis

Figure 6.6 shows the normalised likelihood (6.1) and the RMSE values for 250 updates of the MLRR algorithm where no subsets were used for the estimation of the MLTR attenuation update. The two measures are computed with no acceleration and a registration in only the finest resolution level (MLRR). The results are then compared to the results obtained by using Nesterov's momentum ( $\text{MLRR}^+$ ), registration in two resolution levels in each iteration ( $\text{MLRR}^{\text{MR}}$ ), and the combined acceleration and multi-resolution scheme ( $\text{MLRR}^{\text{MR}+}$ ). Although monotonicity of the likelihood cannot be guaranteed in MLRR, the likelihood has increased in each iteration in all simulated cases. In all simulations, the reconstructions accelerated by Nesterov's momentum achieve a higher likelihood and a lower RMSE than the non-accelerated MLRR reconstructions. Furthermore, the joint utilisation of Nesterov's momentum together with multi-resolution registration scheme provides an increased level of convergence with the least amount of error. It should also be mentioned that applying

## 6. SIMULTANEOUS RECONSTRUCTION OF THE ACTIVITY IMAGE AND REGISTRATION OF THE CT IMAGE IN TOF-PET

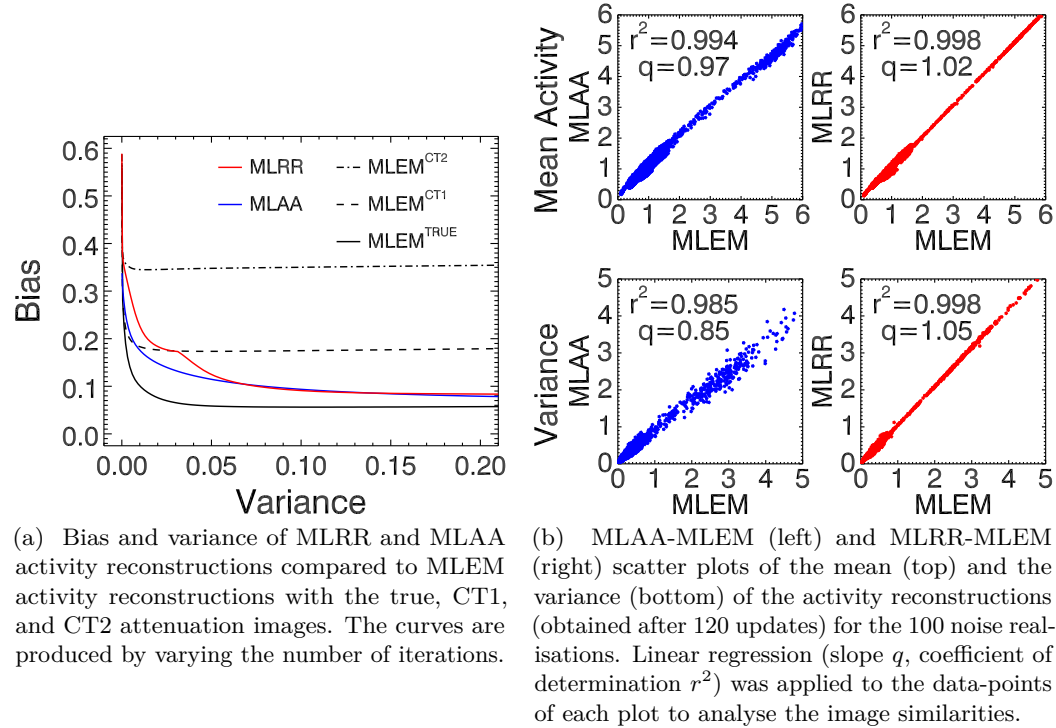


Figure 6.5: Results of the noise realisation study, (a): bias and variance curves, (b): MLRR and MLAA scatter plots.

ordered subsets lead to further acceleration of the algorithm; however, the decrease in the RMSE values was no longer monotonic.

### TOF-Resolution

Figure 6.7 shows the estimated likelihood and the RMSE of the reconstructed activity images compared to the ground truth activity image of figure 6.1. It can be observed that as the TOF-resolution improves so does the convergence of the MLRR algorithm. Analysing the RMSE for different sets of fluid-like and diffusion-like regularisation of the estimated displacements, we found that the fluid-like regularisation had a minimal effect on the RMSE values, whereas the diffusion-like regularisation could cause instabilities most likely occurring at discontinues of the gradient image of the attenuation.

#### 6.4.2 3D Simulation

Figure 6.8 shows the MLRR and MLAA activity reconstructions as well as the MLEM activity reconstructions with the true attenuation image ( $\text{MLEM}^{\text{True}}$ ) and the mismatched CT ( $\text{MLEM}^{\text{CT}}$ ) image which was chosen from a different respiratory frame. As expected, the MLEM reconstruction suffers from motion artifacts (most

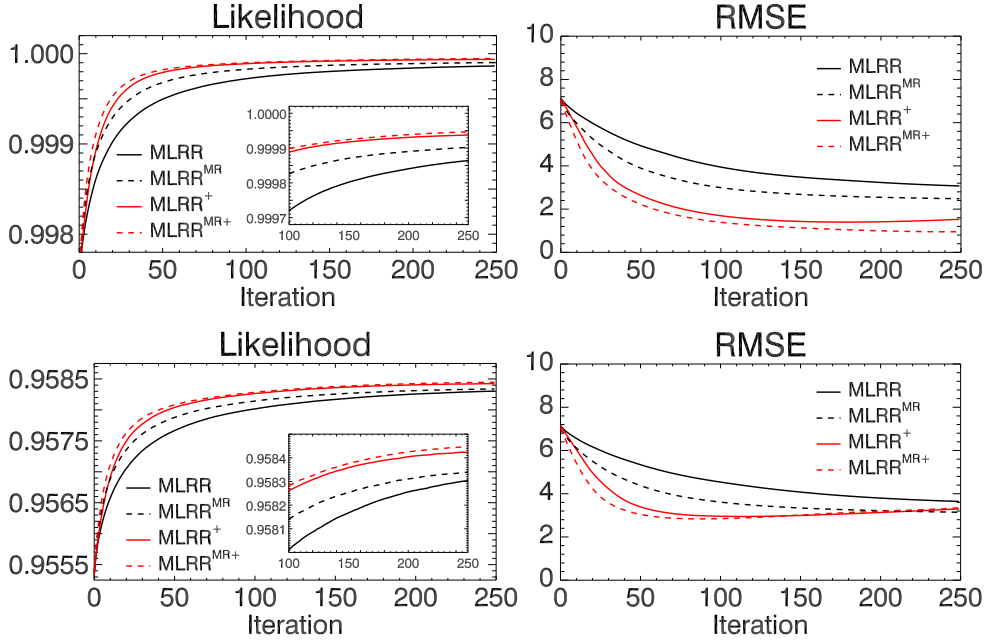


Figure 6.6: Normalised log-likelihood of (6.1) (left) together with the RMSE (right) of the attenuation estimates of MLRR for noise-free (top) and moderate-noise (bottom) TOF-PET emission data.

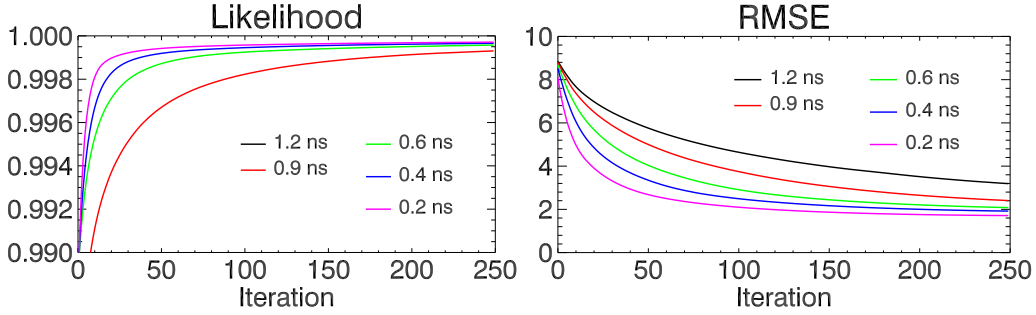


Figure 6.7: Normalised log-likelihood of (6.1) (left) together with the RMSE (right) of the activity reconstructions of MLRR for the noise-free TOF-PET emission data with a varying TOF Gaussian resolution of 1.2 ns to 0.2 ns FWHM.

pronounced near the dome of the liver), and the joint activity reconstructions of MLAA and MLRR are comparable to the MLEM reconstruction with the true attenuation image ( $\text{MLEM}^{\text{True}}$ ). The figure also shows the attenuation reconstruction of MLAA (ATT) and the attenuation estimate of MLRR (DCT) together with a registered demons attenuation image. Although the attenuation reconstruction of MLAA is sufficient for attenuation correction, the attenuation details are lost due to the amount of noise in the data. In contrast, the MLRR attenuation estimate has the benefit of producing an aligned attenuation estimate while roughly maintaining the resolution of the mismatched CT attenuation image. Visual inspection shows a

## 6. SIMULTANEOUS RECONSTRUCTION OF THE ACTIVITY IMAGE AND REGISTRATION OF THE CT IMAGE IN TOF-PET

good agreement between MLRR attenuation image and the true attenuation image.

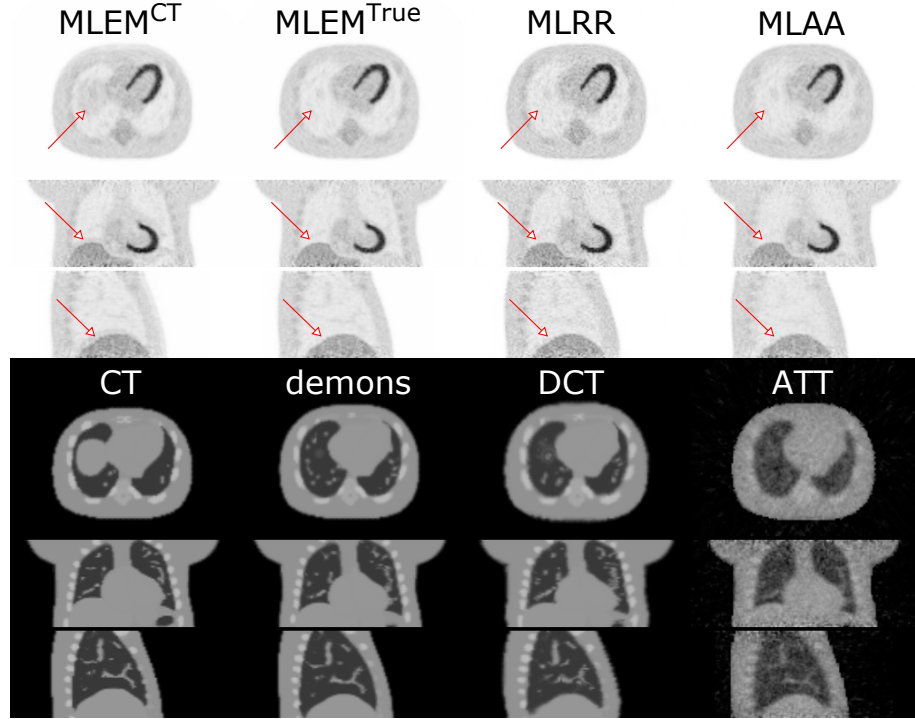


Figure 6.8: Activity (top) and attenuation (bottom) reconstructions of the XCAT phantom. The MLRR (column 3) and MLAA (column 4) activity reconstructions are compared to activity reconstructions of MLEM with the mismatched CT (column 1 - top) and the true attenuation image (column 2 - top). The CT (column 1 - bottom) and the registered demons (column 2 - bottom) attenuation images are shown as reference. For the true attenuation image, see figure 6.2 (centre column).

### 6.4.3 Patient Data

#### Reconstruction

Figure 6.9 shows the MLEM activity reconstruction together with the MLRR and MLAA activity and attenuation reconstructions of the 4 min  $^{18}\text{F}$ -FDG patient scan. The reconstructions are obtained after 3 iterations of 24 subsets, and the activity reconstructions are post-smoothed by a Gaussian of 0.4 cm FWHM. The shadow-like artifacts (more pronounced near the dome of the liver and the lateral wall of the heart) in the MLEM activity reconstruction suggest slight mismatch between the CT and the average attenuation image that has affected the TOF-PET emission data. The reconstructed attenuation image of MLRR (and MLAA) supports this claim, where the boundary of the liver is shifted upward and hence the activity reconstruction of MLRR (and MLAA) seems free of the shadow-like artifacts. It has been shown that TOF-PET is more robust than non-TOF PET to errors in the attenuation image [13].

Hence, to better reveal the presence of possible attenuation mismatches, non-TOF data were produced by summing all TOF-bins and reconstructed with non-TOF MLEM using the different attenuation maps. The comparison of these non-TOF MLEM images based on the CT, the deformed CT of MLRR (DCT) and the MLAA (ATT) attenuation images provide more evidence that the alignment of attenuation image has been improved by the joint estimation methods.

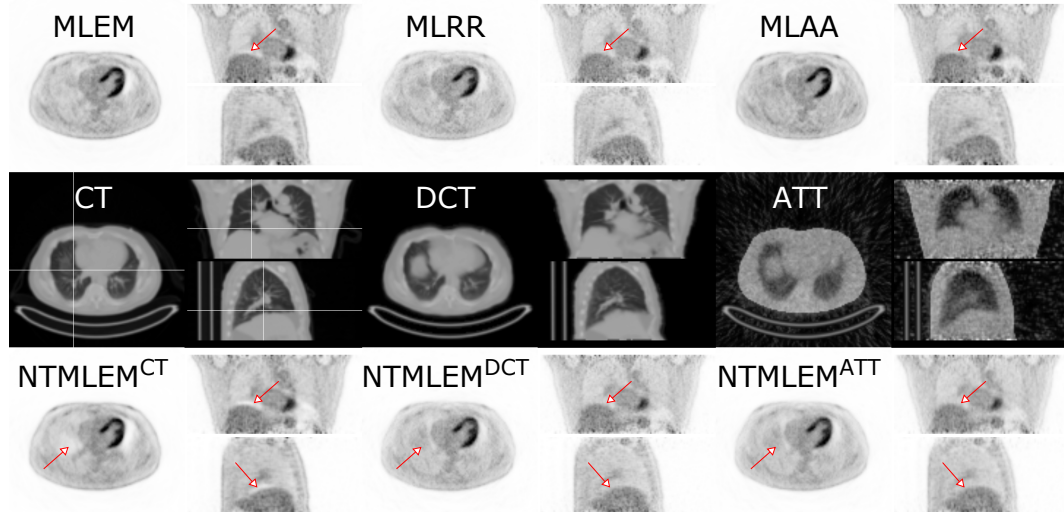


Figure 6.9: Transaxial, coronal and sagittal slices through the activity (top) reconstructions of MLEM (left), MLRR (centre) and MLAA (right) shown together with the CT-based attenuation (middle-left), the MLRR deformed-CT attenuation (middle-centre) and the MLAA attenuation (middle-right) reconstruction. The non-TOF (intensifying motion-induced artifacts) MLEM activity reconstructions (bottom) with the CT-based (left), MLRR deformed-CT (centre) and the MLAA (right) attenuations are shown for reference.

### Gated Reconstructions

Figure 6.10 shows the MLRR reconstruction of the same 4 min  $^{18}\text{F}$ -FDG patient scan when the emission data was gated into 3 respiratory gates. As before, the reconstructions are obtained after 3 iterations of 24 subsets and the activity reconstructions are post-smoothed by a 0.4 cm FWHM Gaussian kernel. It is interesting to see that the position of the lung-liver boundary differs for the attenuation reconstruction of each gate, and that the MLRR activity reconstructions seem to be free of the shadow-like artifacts observed in the MLEM activity reconstruction close to the boundary of the liver. Although the shadow-like artifacts near the lateral wall of the heart seem to be reduced in the MLRR activity reconstruction, there are some remaining artifacts which are observed in both MLRR and MLAA activity reconstructions which we attribute to the cardiac motion.

## 6. SIMULTANEOUS RECONSTRUCTION OF THE ACTIVITY IMAGE AND REGISTRATION OF THE CT IMAGE IN TOF-PET

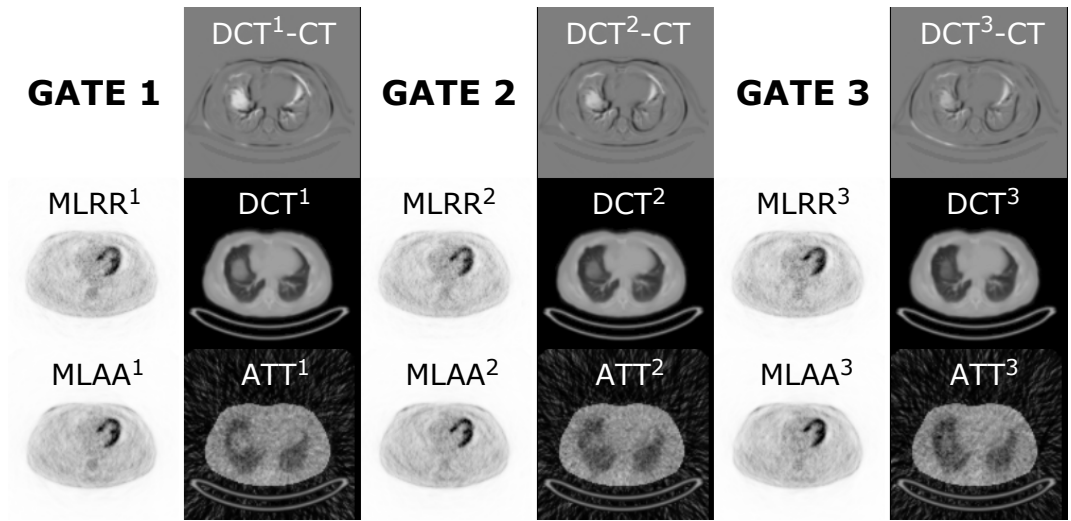


Figure 6.10: Results for the gated TOF-PET emission data. The superscripts denote the gate number. For each of the three gates, the following images are shown: MLRR activity and attenuation images (centre row), the MLAA activity and attenuation images (bottom row) and the difference between the MLRR attenuation image and the original CT-based attenuation (top right).

## 6.5 Discussion

Time-of-flight PET has attracted a lot of interest among researchers due to the desired properties of the emission reconstructions from TOF-PET data [13], e.g. faster convergence rate, improved contrast-to-noise ratio, robustness to possible inaccuracies in normalisation and attenuation factors, etc. More recently a systematic study on a population of clinical patient scans [136] has shown that TOF reconstructions substantially improve the quantitative accuracy of tracer distribution as a result of the TOF robustness to possible imperfections. Since it was shown that the TOF-PET emission data provide information about the attenuation that is not available in non-TOF data [13], [56], [58], the topic of joint activity and attenuation reconstruction from TOF-PET data has gained increased attention. In addition to the desired properties of TOF-PET reconstructions, the joint reconstruction methods provide a novel approach to activity and attenuation alignment in case of between-scan and in-scan motion.

Although methods have been proposed that make use of the invaluable CT [104] or MR [56], [109] data, the methods assume a perfect activity and attenuation alignment. In this contribution we use the available CT-based attenuation images and non-rigidly align them to the emission data. By doing so we obtain aligned attenuation images while approximately preserving the resolution and signal-to-noise ratio of the CT-images. Furthermore, since the CT-based attenuation images are pre-corrected for the appropriate photon energy of 511 keV, no extra handling of the data is required to correct for the unknown scale in the joint estimation problem [58].

The proposed MLRR algorithm builds on the MLAA algorithm by replacing the update of the attenuation image by estimating transformation parameters that produce the required attenuation update. For each MLAA sub-iteration (with a 1:3 activity to attenuation update ratio), a total of 16 (back/)projections are required which only 2 are TOF (back/)projections. For reference, each MLEM sub-iteration involves only 2 TOF and 1 non-TOF (back/)projection operations. In addition to the same number of (back/)projections as MLAA, MLRR requires 3 incremental (rigid/nonrigid) motion estimations per iteration. In our implementation of the algorithm, each iteration of the MLRR algorithm roughly takes twice as long as an MLAA iteration.

The method was accelerated by using Nesterov's momentum which makes use of the previous attenuation update as well as the current update of MLTR. Our use of the momentum method is empirical, since it was used here to accelerate the MLTR algorithm, ignoring the fact that MLTR was interleaved with updates of the deformation. Nevertheless, it was found to yield a very significant acceleration. The effects of using Nesterov's momentum as well as the multi-resolution approach were investigated by means of the log-likelihood function and the RMSE of the MLRR attenuation reconstructions (figure 6.6). The convergence analysis showed a monotonic increase/decrease in the log-likelihood/RMSE values in the simulations. However, we should note that Nesterov's acceleration method is known to be non-monotonic. We anticipate that with a better TOF-resolution, a similar improvement would be expected for MLRR reconstructions as with MLAA reconstructions reported in [61].

In our experience and in the case of a non-rigid motion model, we were able to achieve stable results provided that the incremental displacement updates were small and locally smooth. The use of a multi-resolution scheme further improves the stability of the non-rigid registration. Although the proposed non-rigid update of (6.17) is count dependent, it reduces the influence of the vanishing attenuation updates in later iterations. We found the update of (6.17) to be better suited than the original regularised demons update with a fixed maximum displacement update in each iteration [130]. We do not expect problems due to the count-dependency of (6.17) in clinical practice as the strength of the quadratic regularisation ( $\beta$ ) of the estimated displacement field could be computed from the initial iterations to give the desired maximum update of the displacement fields.

In this study, the Gaussian fluid-like and diffusion-like smoothing parameters were chosen empirically; however, similar to [137], a more extensive study is still required to optimise and to analyse the effect of the smoothing parameters on the estimated displacement field and on the quantitative accuracy of the reconstructed activity image. As illustrated in figure 6.4, noise on the emission data propagates into the MLRR attenuation map as uncertainties on the position of the contours in the deformed attenuation image. The results of the 2D noise analysis (figure 6.5) showed that noise propagation has no adverse effect on the noise in the reconstructed activity image. However, for some applications, e.g. when the deformed CT would also be used for defining regions of interest, it may be desirable that the deformation of the CT is as realistic as possible. For such applications a stronger constraining

## 6. SIMULTANEOUS RECONSTRUCTION OF THE ACTIVITY IMAGE AND REGISTRATION OF THE CT IMAGE IN TOF-PET

---

may be needed than the one we have applied in our experiments.

In the clinical patient scan, MLRR was able to produce an aligned attenuation image which effectively removed parts of the shadow-like artifacts observed in the MLEM activity reconstruction. The shadow-like artifacts which were observed above the dome of the liver were also absent in the MLRR activity reconstruction of the 3 respiratory gates; however, artifacts were still present near the lateral wall of the heart. We attribute this to the cardiac motion, present in each respiratory phase. MLRR produced a fairly large deformation near the lateral wall. We assume this deformation minimises the inconsistencies due to the cardiac motion. It is likely that these inconsistencies can not be eliminated entirely, since there is no stationary object that can explain the attenuation produced by an active and attenuating object which moved during the acquisition [70], [138]. Otherwise, the deformations produced by MLRR seem to be well in agreement with respiratory motion.

The registration step in the MLRR algorithm preserves the CT attenuation intensities, and is not mass preserving. The effects of utilising a mass preserving algorithm, and its comparison to the current intensity preserving algorithm remains to be studied. Furthermore, applying additional constraints on the estimated deformation field such as the ones which enforce local rigidity might provide a tool to better reflect internal motion. With the recent developments and interest in simultaneous PET/MR systems, adapting the method to also use the anatomical information gathered from the MR by combining MLRR (i.e. jointly estimating deformation and activity) with Salomon's approach [56] (i.e. jointly estimating a small number of attenuation values and activity) could be fruitful.

### 6.6 Conclusion

The MLRR algorithm was proposed to make use of the high quality CT image and to iteratively reconstruct the activity image while deforming the CT-based attenuation image. Our 2D and 3D simulations indicate that the method is able to produce aligned activity and attenuation reconstructions similar to MLAA, with two advantages: the missing scale problem is solved automatically by using CT-based attenuation coefficients, and the resulting attenuation image is “almost free of noise”. Furthermore, the improved alignment of CT and PET might also benefit the diagnostic value of the image pair, which remains to be investigated. However, some constraining of the estimated motion parameters is required to avoid inaccuracies observed mostly at high gradients of the attenuation image. The noise analysis showed that the corresponding activity reconstructions of MLRR were comparable to the ones produced by MLAA in terms of bias and variance. As expected, the activity reconstructions of the clinical scans produced by MLRR suffer less from motion-induced or mismatch artifacts than the reference MLEM activity reconstructions. In addition, the attenuation results of the gated patient data are in agreement with expected breathing motion.

## Acknowledgements

This research is supported by a research grant (GOA) from KU Leuven and FWO project G027514N, and by Siemens Healthcare, Anderlecht, Belgium. The authors would like to thank A. Ribbens from KU Leuven for insightful discussions, J. Jones from Siemens Healthcare, Molecular Imaging for data processing and providing the data-based gating software.

## 6.7 Appendix A

Given the time-of-flight PET emission data  $y_{it}$ , the variables  $\dot{L}$  and  $\ddot{L}$  in (6.5) can be computed from the Poisson log-likelihood (6.1) to give the MLTR attenuation update as:

$$\begin{aligned}\dot{L}_j &= \frac{\partial L}{\partial \mu_j} = \sum_{it} l_{ij} (\bar{y}_{it} - y_{it}) (1 - \frac{s_{it}}{\bar{y}_{it}}) \\ &= \sum_i l_{ij} \left( (\bar{y}_i - y_i) - \sum_t (\bar{y}_{it} - y_{it}) \frac{s_{it}}{\bar{y}_{it}} \right)\end{aligned}\quad (6.22)$$

$$\approx \sum_i l_{ij} (\bar{y}_i - y_i) (1 - \frac{s_i}{\bar{y}_i}) \quad (6.23)$$

$$\begin{aligned}\ddot{L}_j &= \sum_k \frac{\partial^2 L}{\partial \mu_j \partial \mu_k} = - \sum_k \sum_{it} l_{ij} l_{ik} (\bar{y}_{it} - s_{it}) (1 - \frac{y_{it} s_{it}}{\bar{y}_{it}^2}) \\ &\approx - \sum_i l_{ij} \left( (\bar{y}_i - s_i) - \sum_t (\bar{y}_{it} - s_{it}) \frac{s_{it}}{\bar{y}_{it}} \right) \sum_k l_{ik}\end{aligned}\quad (6.24)$$

$$\approx - \sum_i l_{ij} (\bar{y}_i - s_i) (1 - \frac{s_i}{\bar{y}_i}) \sum_k l_{ik} \quad (6.25)$$

where, approximation (6.24) is achieved by assuming that the fraction  $y_{it}/\bar{y}_{it} \approx 1$ , and since it is imposed in computing  $\dot{L}$  (the denominator of the MLTR attenuation update) it only influences the convergence speed of the algorithm. Approximations (6.23) and (6.25) are achieved by assuming that the fraction  $s_{it}/\bar{y}_{it}$  is roughly independent of the TOF-bin  $t$ , and can be replaced by the non-TOF fraction  $s_i/\bar{y}_i$ . This approximation eliminates the summation over the TOF index for both  $\dot{L}$  and  $\ddot{L}$ . Since our approximation is exact for  $s_{it} = 0$ , we can expect it to be a good approximation for small  $s_{it}$ . In cases where this is not so, the approximation does not affect the final solution (since in the noise-free case the problem of attenuation estimation has the same solution for non-TOF as well as for TOF emission data); however, it may adversely affect the noise propagation. The advantage of the approximation is that it reduces the computation time for the attenuation update.

Although the use of the TOF data has been suggested for the attenuation update in the joint estimation frame-work [110], in our experiments the TOF information was ignored to reduce the computation time. The combination of (6.23) and (6.25)

## 6. SIMULTANEOUS RECONSTRUCTION OF THE ACTIVITY IMAGE AND REGISTRATION OF THE CT IMAGE IN TOF-PET

---

which we used, is the standard non-TOF MLTR update with an additive contribution [124].

### 6.8 Appendix B

In this section, with some approximations we derive the displacement update (6.17) justifying the use of the demons algorithm [125] to update the deformation field. We parameterise the transformation by a displacement field, i.e. the deformation parameters  $\Theta$  now consist of a vector  $\mathbf{D}_j = (D_j^x, D_j^y, D_j^z)$  for every voxel  $j$ , and focus on the estimation of the displacement field that non-rigidly deforms  $\mu^\dagger$  to an attenuation image that agrees best with the TOF-PET emission data according to the Poisson likelihood. The derivative in (6.9), with respect to an incremental displacement field  $\mathbf{d}$  at voxel  $j$ , can now be approximated by:

$$\frac{\partial \delta \mu_k[\mathbf{d}]}{\partial \mathbf{d}_j} = \frac{\partial \mu_k[\mathbf{D}^{(n)} + \mathbf{d}]}{\partial \mathbf{d}_j} \approx (\nabla \mu[\mathbf{D}^{(n)}])_j \delta_{jk} \quad (6.26)$$

where  $(\nabla \mu[\mathbf{D}^{(n)}])_j$  is the gradient of the deformed attenuation image at voxel  $j$  with respect to the image coordinates  $(x, y, z)$ , and  $\delta_{jk}$  is the Kronecker delta. This approximation assumes that the value in a pixel is independent of the deformation in other pixels. In reality however, there will be some dependence on neighbouring voxels due to unavoidable interpolations.

Furthermore, using the first order Taylor series expansion of  $\mu_j[\mathbf{D}^{(n)} + \mathbf{d}]$  together with (6.26) we find<sup>3</sup>:

$$\delta \mu_j[\mathbf{d}] \approx (\nabla \mu[\mathbf{D}^{(n)}])_j \mathbf{d}_j \quad (6.27)$$

Inserting (6.26) and (6.27) in (6.9) we obtain:

$$\frac{\partial \tilde{S}}{\partial \mathbf{d}_j} = (\dot{L}_j^{(n)} + \ddot{L}_j^{(n)} (\nabla \mu[\mathbf{D}^{(n)}])_j \mathbf{d}_j) (\nabla \mu[\mathbf{D}^{(n)}])_j = 0 \quad (6.28)$$

The solution of (6.28) is not unique. By taking the minimum norm solution (the same choice was made in [125], [130]) an incremental displacement  $\mathbf{d}_j$  is estimated in the direction of  $(\nabla \mu[\mathbf{D}^{(n)}])_j$ , which reduces the problem to a set of 1D problems with solution

$$\mathbf{d}_j^{(n)} = -\frac{(\nabla \mu[\mathbf{D}^{(n)}])_j}{\|(\nabla \mu[\mathbf{D}^{(n)}])_j\|^2} \frac{\dot{L}_j^{(n)}}{\ddot{L}_j^{(n)}} = \frac{(\nabla \mu[\mathbf{D}^{(n)}])_j}{\|(\nabla \mu[\mathbf{D}^{(n)}])_j\|^2} \delta \mu_j^{(n)} \quad (6.29)$$

where  $\delta \mu^{(n)}$  is the attenuation update of MLTR (6.5). Equation (6.29) is the unconstrained optical flow equation commonly used in image registration methods.

Since the registration problem is highly under-determined, it is often necessary to regularise the estimated displacement fields. This is typically achieved by adding

---

<sup>3</sup>In this context all vector multiplications are inner products.

a penalty term that favours smaller values of displacements  $\mathbf{d}_j$ . Adding a quadratic penalty term to the surrogate function (6.9), we have:

$$\tilde{S}_{reg}(\mu[\mathbf{D} + \mathbf{d}], y) = \tilde{S}(\mu[\mathbf{D} + \mathbf{d}], y) - \sum_j \frac{1}{2} \beta \|\mathbf{d}_j\|^2 \quad (6.30)$$

where  $\beta$  determines the strength of the penalty term. With the same approximations, the incremental displacement update is then given in (6.17), where  $\beta/\ddot{L}_j^{(n)}$  helps to stabilise the incremental displacement estimate  $\mathbf{d}^{(n)}$  at low gradient values of the deformed attenuation image.



## Chapter 7

# Joint reconstruction of activity and attenuation in Time-of-Flight PET: A Quantitative Analysis

A. Rezaei, C. Deroose, T. Koesters, K. Salvo, M. Defrise, F. Boada, and J. Nuyts,  
“Joint Reconstruction of Activity and Attenuation in Time of Flight PET: A Quantitative Analysis”, *Journal of Nuclear Medicine*, In-preparation,

## 7. JOINT RECONSTRUCTION OF ACTIVITY AND ATTENUATION IN TIME-OF-FLIGHT PET: A QUANTITATIVE ANALYSIS

---

### Abstract

Joint activity and attenuation reconstruction methods from time of flight (TOF) positron emission tomography (PET) data provide an effective solution to attenuation correction when no (or incomplete/inaccurate) information of the attenuation is available. One of the main contributors to limiting their use in clinical practice is the lack of validations of these methods on a relatively large patient database. In this contribution, we aim at validating the activity reconstructions of the maximum likelihood activity and attenuation reconstruction (MLAA) algorithm on a whole body patient data set. By avoiding the scale problem (for now) of MLAA algorithm, we present a quantitative comparison of the joint reconstructions to the current clinical gold-standard maximum likelihood expectation maximization (MLEM) reconstruction with CT-based attenuation correction. **Methods:** The whole body TOF-PET emission data of each patient data set is processed as a whole to reconstruct an activity volume covering all the acquired bed positions, which helps to reduce the problem of a scale per bed position to a global scale for the entire activity volume. Three reconstruction algorithms are used: MLEM, MLAA and the maximum likelihood activity reconstruction and attenuation registration (MLRR). The reconstruction results are then analyzed with different scatter estimates: the single scatter simulation (SSS) estimate, the tail-fitted SSS (TF-SSS) estimate and a maximum likelihood scaling of the SSS (ML-SSS) estimate to the emission data. The results are then compared in different regions of interest. **Results:** We find that an inaccurate scatter estimate can produce significant bias in the reconstructions, which can be different for different reconstruction algorithms, complicating the validation of MLAA versus MLEM. Using a Monte-Carlo simulation of the NEMA IEC phantom, we find that a global under-estimation of 17.3% of the tracer activity was reduced to 0.9% when using the ML-SSS scatter estimate. Furthermore, the use of the ML-SSS scatter estimate showed improvements in occasionally observed artifacts in clinical scans and improved agreement between the images reconstructed using the different algorithms. The joint reconstructions provide better quantification in case of PET and CT misalignments caused by patient motion. We also find that misalignments between the PET and the CT could cause inaccuracies in the shape of the single scatter estimate, and hence deteriorate the quantitative accuracy of the reconstructions. **Conclusion:** Joint activity and attenuation estimation methods provide a useful means to estimate the tracer distribution in cases where CT-based attenuation images are not available or are subject to misalignments. With an accurate estimate of the scatter contribution in the emission measurements, the joint TOF-PET reconstructions are within clinical acceptable accuracies.

### 7.1 Introduction

Since it was shown that the time of flight (TOF) positron emission tomography (PET) data provide information about the attenuating medium of the emission data [56], [58], a number of algorithms have been developed that exploit the added

information available with TOF. The majority of the newly developed methods aim at simultaneously reconstructing an activity and an attenuation image from the TOF-PET emission data [61], [121], [139]. Furthermore, a number of methods have been proposed which avoid the reconstruction of the attenuation medium and attempt to estimate the attenuation correction values which more directly influence the TOF emission measurements [65], [66], [109].

It is known that information available by TOF emission data does not allow a quantitative assessment of the reconstructed distribution of activity, as TOF-PET data determine the activity distribution up to a constant scale [58]. This limiting factor might be the main reason why the use of joint estimation methods has not yet been introduced in clinical practice. Recently, methods have been proposed that take advantage of available computed tomography (CT) images of the patient [68], [104], which is commonly available in the state-of-the-art TOF-PET/CT systems. Where the method introduced in [139] aims at completing the sinogram of the attenuation correction factors for planes for which no CT measurements are available, the method introduced in [68] aims at deforming the CT-based attenuation image to correct for any possible mismatch between the CT and PET acquisitions. As a result of using the energy-adjusted CT images in the joint reconstruction framework, the scale problem is automatically overcome. Apart from these methods which use the added information of the CT, other scale correction techniques for joint activity and attenuation reconstructions exist in the literature which include: methods that use tissue prior maps and utilize (during reconstruction) an intensity prior on expected tissue values being reconstructed [121], methods which attempt to solve the problem by adding transmission sources in the scanner [104], [140] or by using the LSO background radiation source as the transmission source [119], and methods which ambitiously try to determine the scale from the scattered events in the emission data [141].

Another limiting factor for the use of joint reconstruction methods in clinical practice is the lack of a comprehensive validation of these methods on a large patient database. Although studies have been performed on a number of patient data sets, the studies have been mainly restricted to 3D simulations often even ignoring some of the data corrections routinely done in clinical practice (e.g. scatter/randoms corrections). An initial study was done in [138] where after taking the scale problem into account, the results of the joint estimation method were found to be similar to the gold-standard without the effects of motion. It was found in [120], [121], [142] that the joint reconstruction results outperform methods which utilize an MR-based attenuation correction scheme for attenuation correction of the TOF-PET emission data. The studies demonstrated that the joint reconstruction methods were able to remove some MR-related artifacts which otherwise propagate into the emission reconstruction. In a more recent study [143], the joint estimation methods were analyzed in a retrospective cardiac study on a relatively bigger patient data base. As expected it was found that the joint reconstruction method proposed was able to remove possible PET/CT mismatch and furthermore demonstrated that the activity reconstructions could potentially be influenced by the presence of CT mismatch in the scatter estimation procedure.

## 7. JOINT RECONSTRUCTION OF ACTIVITY AND ATTENUATION IN TIME-OF-FLIGHT PET: A QUANTITATIVE ANALYSIS

---

In this study we perform a quantitative analysis of the joint reconstructed activity images comparing them to the current clinical gold-standard (i.e. MLEM with a CT-based attenuation correction of the emission data), on a set of whole body patient scans. Because the joint estimation methods have more degrees of freedom to explain the same TOF-PET emission data than our gold-standard MLEM reconstruction, we try to identify and avoid possible sources of errors that might influence this comparison. The paper is organized as follows, in section 7.2 we describe the reconstruction and image analysis parameters. Using a Monte-Carlo simulation of a NEMA-like phantom we analyze the effects of an inaccurate scatter scale on the emission reconstructions. In addition to this, the effects of a mismatched CT attenuation image directly on the reconstructions and indirectly through the scatter shape is also analyzed by means of activity reconstructions of different organs. The results are presented in section 7.3 and discussed in section 7.4.

### 7.2 Materials and Methods

#### 7.2.1 Data Acquisition and Processing

A total of 23 whole body  $^{18}\text{F}$ -FDG patient scans were acquired using the Siemens Biograph mCT scanner [92]. On average each patient was injected with 550 MBq of the  $^{18}\text{F}$ -FDG tracer and scanned approximately one hour post-injection. The emission data were acquired in 5-8 different bed positions, each scanned for 120 s per bed position. The data were collected in 5D sinograms in the native Siemens format consisting of 400 radial bins of 2.005 mm width, 168 azimuth angles over 180 degrees, 621 planes of 2.027 mm width (with the first 109 planes being the direct planes (segment 0) and the rest the oblique planes (segments  $\pm 1, \pm 2, \pm 3, \pm 4$ )), and 13 TOF-bins of 312 ps width. The e7tools provided by Siemens were used to process the raw data and to generate the expected scatter and randoms contribution of the emission measurements.

#### 7.2.2 Reconstructions

Similar to [144] a virtual scanner was designed allowing to simultaneously reconstruct the TOF-PET emission data acquired over all the bed positions. Prior to reconstruction, the data were mashed in the radial direction with a mashing factor of 2, and the activity and attenuation images were consequently reconstructed in a  $200 \times 200$  voxel grid of 0.40724 cm width transaxially and up to 543 planes of 0.2007 cm width axially. The TOF resolution of the scanner was modelled as a Gaussian with 580 ps FWHM.

In this study, three algorithms were used to analyze the tracer distribution uptake; 1) maximum likelihood expectation maximization (MLEM) which makes use of the available CT-based attenuation correction values, 2) maximum likelihood activity and attenuation (MLAA) which reconstructs an activity image together with an attenuation image directly from the emission data [61], and 3) maximum likelihood activity reconstruction and attenuation registration (MLRR) which aims

## 7.2. Materials and Methods

---

to reconstruct an activity image while deforming an available CT-based attenuation image (DCT) such that the pair of images best fit the measurements [68].

In the case of MLAA, the activity and attenuation reconstructions are obtained after 5 iterations of 24 subsets where the attenuation image was updated three times for each update of the activity reconstruction. The algorithm was initialized with uniform activity in the field of view (FOV) and uniform tissue attenuation ( $0.095 \text{ cm}^{-1}$ ) in the patient support determined from CT. In order to eliminate any confounding effects of the scale factor in the reconstructions, the scale problem in MLAA was fixed by imposing the total tracer activity of the MLEM reconstruction within the support of the CT-based attenuation image. The MLRR reconstructions are obtained after 3 iteration of 24 subsets, with a 3:1 attenuation deformation to activity update ratio in each subset. A uniform activity image inside the FOV is used to initialize the algorithm together with the zero vector displacement field. The displacement field is only updated inside the patient support and is regularized by a fluid-like and diffusion-like regularization. Because the convergence of MLRR, MLAA and MLEM may be different, “standard” activity images are produced by standard MLEM reconstructions (3 iterations of 24 subsets) using the MLRR and MLAA estimated and the CT-based attenuation sinograms <sup>1</sup>. In all cases the final activity reconstruction was post-smoothed with a Gaussian of 6 mm FWHM. The list of reconstruction acronyms can be found in table 7.1.

Table 7.1: List of reconstruction acronyms. X represents MLEM, MLAA or MLRR activity reconstructions.

$X^{\text{GT}}$	ground truth (GT) activity reconstruction
$X^{\text{TF}}$	activity reconstructions using the tail-fitted (TF) SSS estimate
$X^{\text{ML}}$	activity reconstructions using the maximum-likelihood (ML) SSS estimate

### 7.2.3 Image Analysis

The activity reconstructions are then compared and evaluated in different regions. A separate mask is generated by segmenting the bladder, liver, heart, a lumbar vertebra and some tumor/inflammatory lesions with high local tracer uptake in our patient database. These organ masks were generated by thresholding the MLAA reconstructed activity image with an ML scaling of the SSS estimate of the scatter ( $\text{MLAA}^{\text{ML}}$ ). For the delineation of the lumbar vertebra, the CT-based attenuation image was also used. The bladder and the lumbar vertebrae regions (REG1) were chosen to report on the behaviour of the algorithms in regions with no significant patient motion. The liver region (REG2) was chosen as its activity is typically used as reference, and is occasionally subject to between-scan motion. The heart region as well as the tumor/inflammatory lesions (REG3) are the clinically relevant regions in patient studies, which are typically subject to significant in-scan patient motion

<sup>1</sup>In the following we will still refer to the MLEM with MLAA and MLRR generated attenuation sinograms as MLAA and MLRR activity reconstructions, respectively.

## 7. JOINT RECONSTRUCTION OF ACTIVITY AND ATTENUATION IN TIME-OF-FLIGHT PET: A QUANTITATIVE ANALYSIS

---

In our REG1 comparative analysis of the activity distributions, we compare the MLEM and MLAA reconstructions considering three scenarios: reconstructions with the single scatter simulation (SSS) estimate, the tail-fitted SSS (TF-SSS) estimate, and an ML-scaled SSS scatter (ML-SSS) estimate (details provided in section 7.2.4). It should be noted that TF-SSS is the Siemens standard estimate of the expected scatter, and the SSS is the same except that the scatter scale factors of the direct planes are forced to 1 (avoiding the scatter tail-fitting). For the following two studies (i.e. analysis of REG2 and REG3), in addition to a comparison of the MLEM and MLAA results we also compare the MLRR and MLAA reconstructions aiming at removing possible errors due to the CT attenuation mismatch. In addition to this, by using the DCT attenuation reconstruction of MLRR to estimate the SSS estimate we try to remove remaining errors due to the possible CT/PET mismatch in the scatter estimate. The reported results of REG2 and REG3 are all for reconstructions with the ML-SSS estimate. The list of image analysis acronyms are presented in table 7.2.

Table 7.2: List acronyms used for image analysis.

EMAA	comparison of MLEM and MLAA activity reconstructions
RRAA (CT)	comparison of MLRR and MLAA activity reconstructions obtained with the CT-based ML-SSS estimate
RRAA (DCT)	comparison of MLRR and MLAA activity reconstructions obtained after recomputing the ML-SSS estimate using the DCT attenuation of MLRR

### 7.2.4 ML Scatter Scaling

The SSS estimate produced with e7tools provides an estimate of the expected scatter only in direct planes. It is assumed that the scatter estimates of the direct planes provide an adequate estimate of the scatter in the oblique planes. Given the SSS scatter estimate of the direct planes  $s^\dagger$ , the expected scatter is estimated for all sinogram planes as:

$$s_{i_p t} = \mathcal{X}^T (\alpha_d s_{i_d t}^\dagger) \quad (7.1)$$

where  $s_{i_p t}$  is the 4D sinogram of the expected scatter for LOR  $i_p$  and TOF-bin  $t$ , where  $p \in [1, 621]$  denotes the 4D sinogram plane index. The 4D expected scatter sinogram is computed by expanding  $s_{i_d t}^\dagger$  at the direct LOR  $i_d$  and TOF-bin  $t$ , where  $d \in [1, 109]$  denotes the direct planes of the rebinned sinogram plane index<sup>2</sup>,  $\mathcal{X}$  is the single slice rebinning operator and  $T$  denotes a matrix transpose.  $\alpha_d$  is the scaling factor for the direct plane  $d$  that we have introduced, and is set to 1 for the SSS estimate.

---

<sup>2</sup> In the case of multiple bed acquisitions the range of the direct plane index is increased by the number of direct planes covered by the 4D acquisitions of all bed positions.

Assuming Poisson statistics on the emission data  $y_{i_p t}$ , one can iteratively estimate the scatter scaling values as in [69] by:

$$\alpha_d^{(n+1)} = \frac{\alpha_d^{(n)}}{\sum_{i_d t} \mathcal{X}(s_{i_p t})} \sum_{i_d t} \mathcal{X}(s_{i_p t} \frac{y_{i_p t}}{\bar{y}_{i_p t}}) \quad (7.2)$$

where  $(n)$  is the iteration and  $\bar{y}$  is the expected emission counts. The  $\alpha_d$  scales are computed for all the direct planes  $d$  (as also done by TF-SSS) simultaneously with the standard MLEM reconstruction of the emission data by sequentially updating the ML scatter scales and then the activity distribution (and therefore  $\bar{y}$ ).

### 7.2.5 Monte Carlo Simulation Study

A Monte Carlo simulation study was conducted on a NEMA-like phantom with the Siemens Biograph mCT scanner specifications to analyze the ML scaling of [69] and to get more insight into differences between the activity reconstructions of MLEM and MLAA. The emission data was processed by the Siemens tools, which provides the TF-SSS estimate. In this simulation, no randoms events were modelled. Since the simulation provides the actual single and multiple scatter estimates within the data, a least-squares fit of the TF-SSS to the true scatter estimates will be considered as the ground truth for the ML scatter scaling described in section 7.2.4. The ML scatter scaling was initially done with no radial mashing of the emission data. A radial mashing of 2 and 4 was used to analyze the accuracy of the ML scatter scales estimate which were later compared to the ground truth (GT) fit of the scatter scales. The GT scatter estimate was computed with a least squares (LS) fit as follows:

$$\alpha_d^{GT} = \frac{\sum_{i_d t} \mathcal{X}((s_{i_p t}^{SGL} + s_{i_p t}^{MLT}) * s_{i_p t})}{\sum_{i_d t} \mathcal{X}(s_{i_p t}^2)} \quad (7.3)$$

where  $s^{SGL}$  and  $s^{MLT}$  are the single and multiple scatter estimates in the emission data.

The ML scatter scales are computed jointly with an MLEM reconstruction of the activity using 3 iteration of 24 subsets. Following the estimation of the ML scatter scales, two sets of MLEM and MLAA activity distributions are reconstructed with the TF-SSS and the ML-SSS estimates, respectively. The reference activity image (that the reconstructions were compared to) was obtained by applying MLEM and MLAA to the true prompts (non scattered and non random events) in the emission data.

## 7.3 Results

### 7.3.1 Monte Carlo Simulation Study

Figure 7.1 shows the final scatter scales estimated after 72 updates, as well as the progression of the scales of 5 direct plane with each update. Since the GT-SSS

## 7. JOINT RECONSTRUCTION OF ACTIVITY AND ATTENUATION IN TIME-OF-FLIGHT PET: A QUANTITATIVE ANALYSIS

and the ML-SSS were computed using the (already scaled) TF-SSS, the GT-scale factors in figure 7.1 reveals that the tail fitting of the SSS estimate has overestimated the scatter in the emission data by roughly a factor of 2. As reported in [145], the ML-procedure tends to produce a more accurate estimate of the scatter scale (and hence a better ML-SSS) when the emission data are mashed and subsequently reconstructed in a coarser (transaxial) voxel grid. It seems that only after 25 updates a plateau is reached for the ML scales of the different planes. When computing the ML scatter scales for the patient data base, a plateau is reached after more updates of the ML scatter scales which could in part be explained by a lower scatter fraction of the patient emission data compared to the scatter fraction of the emission data in this study.

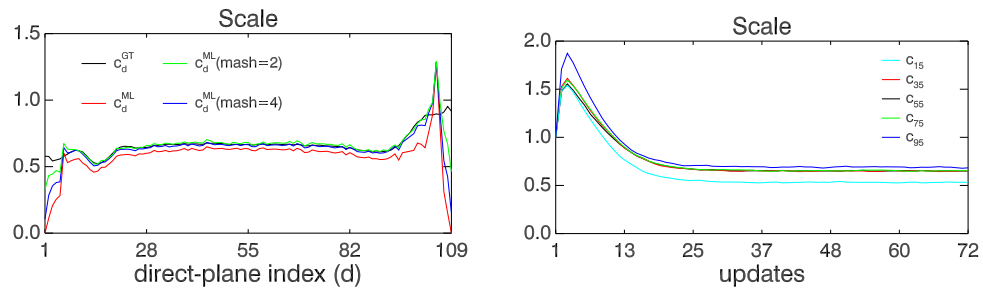


Figure 7.1: Left: ML scatter scale estimates compared to the ground truth LS scale estimate (black curve) for the direct planes. Right: The progression of the ML scatter scale estimates (the case of a radial mashing of 2) with the number of updates for selected direct planes indexes.

Figure 7.2 shows the reference MLAA and MLEM reconstructions (obtained by reconstructing only the true prompts in the TOF-PET emission data) as well as the difference of the two reconstructed activity images. There seems to be no evident sign of cross-talk in the MLAA reconstructions, however, the difference image reveals some differences between MLAA and MLEM activity reconstructions.

The top two rows of figure 7.3 show the difference images of the MLEM<sup>X</sup> and MLAA<sup>X</sup> activity reconstructions where X = GT determines the reference reconstruction and, X = TF or ML determine the reconstructions using the TF-SSS or the ML-SSS estimates of the scatter, respectively. Because the TF-SSS estimate over-estimates the scatter within the emission data (as shown in figure 7.1), the total activity of the MLEM reconstruction was under-estimated by 17.3%. In contrast, when the ML-SSS estimate was used for scatter correction, the total activity of the MLEM reconstruction was slightly over-estimated by 0.9%. In order to better reflect any possible structure present in the difference images, the reconstructions of figure 7.3 were scaled to have the same total activity as the reference MLEM activity reconstruction prior to the comparison.

A comparison of the difference image of reconstructions with the TF-SSS estimate (figure 7.3 - left column) and the difference images of reconstruction with the ML-SSS estimate (figure 7.3 - right column), reveals a slightly different structure. Although the activity reconstructions with the ML-SSS estimate have produced a

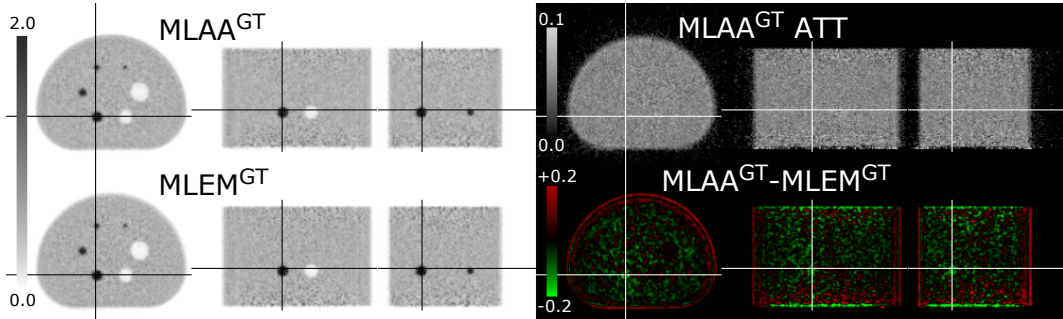


Figure 7.2: Reference activity (top-left) and attenuation (top-right) reconstructions of MLAA shown together with the reference MLEM activity reconstruction (bottom-left) and the difference of the two activity reconstructions (bottom-right). The reference reconstructions are obtained after subtracting the true single and multiple scatters from the measured emission data.

slightly different noise profile in the image, they seem to be free of a systematic difference. For the  $\text{MLAA}^{\text{TF}} - \text{MLEM}^{\text{TF}}$  difference image, the intensity differences in the center are positive whereas those at the edges are negative. In contrast, the  $\text{MLAA}^{\text{ML}} - \text{MLEM}^{\text{ML}}$  difference image contains mostly zero mean noise. The absolute voxel-by-voxel difference of MLAA and MLEM reconstructions normalized by the total activity counts in the MLEM reconstruction was computed for the TF-SSS and the ML-SSS expected scatter estimates as 10.5% and 7.8%, respectively. As reference, the same measure was computed to be 7.8% for the ground truth reconstructions of figure 7.2.

Moreover, it is interesting to see that the MLAA activity reconstructions seem to be more robust to the inconsistencies in the TF-SSS estimate values than MLEM activity reconstructions. This is best seen in the difference images near plane 14, indicated with an arrow in figure 3. Near plane 14, the TF-SSS scatter estimate was more overestimated than in the other planes, as revealed by the dip of the GT-scale in figure 7.1. This caused an increased bias in the  $\text{MLEM}^{\text{TF}}$  image (arrow in figure 7.3), but not in the  $\text{MLAA}^{\text{TF}}$  image. Since MLEM and MLAA have different degrees of freedom during reconstruction, it could be expected that they respond differently to possible inconsistencies in the shape and magnitude of the scatter estimate.

### 7.3.2 Patient Data

When computing the ML scatter scaling values for the patient data, a radial mashing factor of 4 was used during reconstructions. Furthermore, the ML scaling was applied to the SSS estimate (rather than the TF-SSS estimate, in the case of the Monte Carlo study). Consequently, SSS has a scale of 1 everywhere. Although the results vary for different data sets, TF-SSS tends to produce scale factors larger than 1, whereas ML-SSS typically produces scale factors less than 1. This agrees with the Monte Carlo simulation experiment, hence indicates that the ML-SSS scales are probably more accurate. It might be interesting to note that in 2 of the datasets the TF-SSS

## 7. JOINT RECONSTRUCTION OF ACTIVITY AND ATTENUATION IN TIME-OF-FLIGHT PET: A QUANTITATIVE ANALYSIS

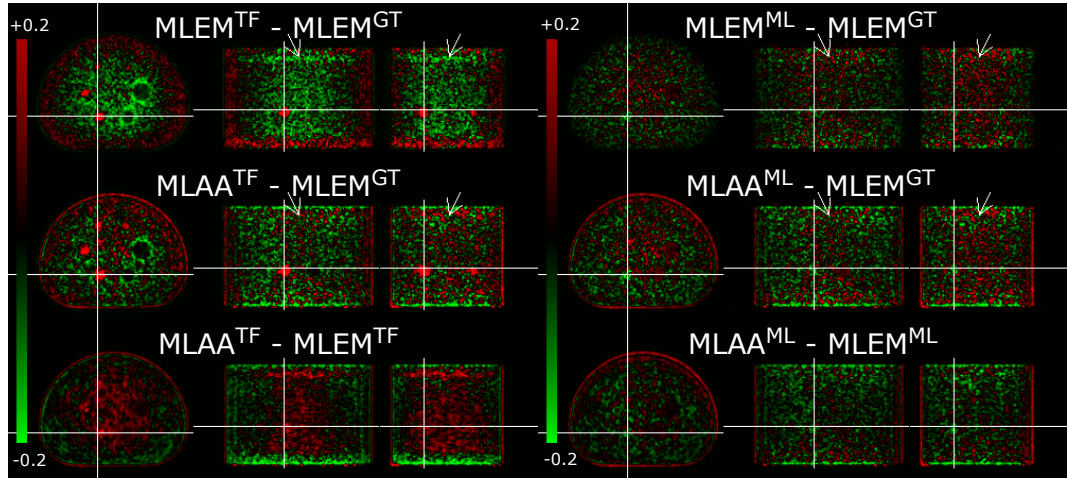


Figure 7.3: Difference images of MLEM (top row) and MLAA (center row) activity reconstructions with the TF-SSS (left column) and ML-SSS (right column) scatter estimates used for scatter correction to the reference MLEM activity reconstruction. The difference between the two activity reconstruction of MLEM and MLAA are also shown in the bottom row for the two scatter estimates, which to some extent reflects the same error structure of the MLEM and MLAA reconstructions. The difference images are obtained after normalizing both reconstructions to the same total intensity.

estimate grossly over-estimated the scatter contribution, resulting in severe artifacts in the emission reconstructions. Figure 7.4 reveals typical artifacts observed in the activity reconstructions when the scatter contribution is overestimated. Although the inaccuracies affect the entire reconstruction, the effects are most pronounced in and near hot structures, such as the bladder and the heart.

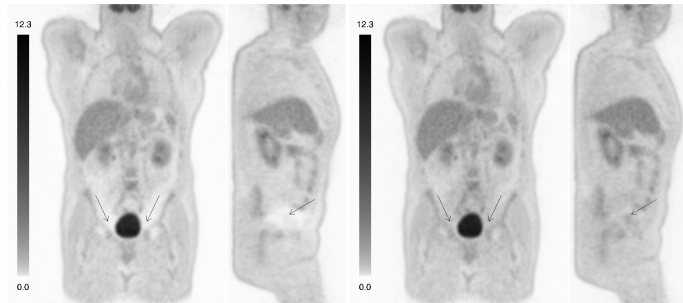


Figure 7.4: MLEM activity reconstructions of a patient using the TF-SSS (left) and the ML-SSS (right) estimates, which reveal some indirect evidence of possible inaccuracies in the TF-SSS estimate. The MLEM activity reconstruction of the SSS estimate (not shown here) is also visually similar to the TF-SSS reconstruction (left).

The Monte Carlo simulation indicated that with a better scatter estimate, the MLEM and MLAA activity images become more similar. Therefore, we computed

the difference between these two reconstructions on a pixel by pixel basis (recall that in this chapter the MLAA image is actually a standard MLEM image computed using the MLAA attenuation map). A VOI around the bladder was defined and the mean difference divided by the mean MLEM activity in this VOI was computed. Figure 5 shows the results for each of the three scatter scaling methods. On average, the MLEM and MLAA reconstructions with the SSS, TF-SSS and ML-SSS estimates resulted in a relative difference of 12.4%, 17.6% and 7.2%, respectively. In the vertebrae region, the average differences were 15.0%, 16.2% and 16.9% for the SSS, TF-SSS and ML-SSS estimates, respectively, with the MLAA estimate being lower than the MLEM estimate. The differences observed in the vertebrae region are more significant than the differences observed in the bladder region. This could in part be explained by the vicinity of the segmented regions to bone attenuation which either are not fully resolved in the MLAA attenuation reconstructions or slightly overestimated in the CT-based attenuation image. In hope to get more insight, a new set of MLAA activity images were reconstructed. This time MLAA was initialized with the DCT-based attenuation images of MLRR, and the ML-SSS estimate was used during reconstruction. After comparison to the MLEM and MLAA reconstructions, a difference of 15.4% and 1.5% was observed between the reconstructions, respectively. We find that even when initialized with an aligned CT-based attenuation image, MLAA produces slightly different values than the MLEM reconstruction, suggesting issues not associated with the convergence of MLAA. The segmented bladder volume and its contrast compared to the liver as well as the errors on the segmented vertebrae region and their contrast to the liver can be found in the appendix.

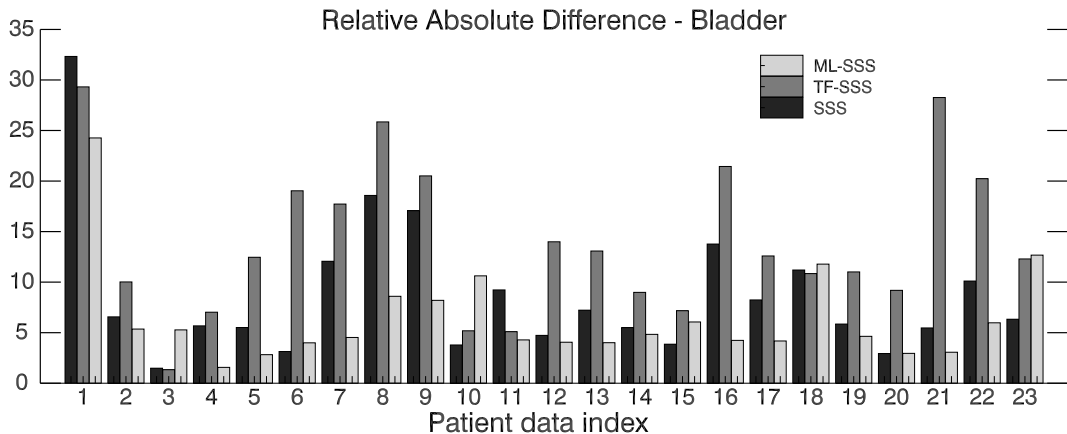


Figure 7.5: Mean activity differences of MLEM and MLAA reconstructions in a bladder region. The results are obtained after using different expected scatter estimates during reconstruction, i.e. SSS, TF-SSS, and ML-SSS.

In standard practice a volume of interest well within the liver region is segmented to quantify the activity concentration in the liver. However, the CT data are often acquired and reconstructed in a breathing phase that differs significantly from the average breathing pose in the PET scan. This would result in significant artifacts in the activity reconstructions of the PET emission data. Figure 7.6 shows such

## 7. JOINT RECONSTRUCTION OF ACTIVITY AND ATTENUATION IN TIME-OF-FLIGHT PET: A QUANTITATIVE ANALYSIS

a case where the CT and PET data are acquired at two different phases of the breathing cycle. Although the MLEM reconstruction is greatly affected by the between-scan mismatch, the MLAA reconstruction is able to provide accurate values in the motion-affected area. In spite of such extensive internal motion, the MLRR reconstruction was also able to produce a motion corrected reconstruction using a deformed CT attenuation image.

An initial naive segmentation of the liver region (which included most of the liver and therefore possible motion affected areas) was used to compare the reconstruction results. The subsequent comparison of the activity reconstructions resulted in a difference of 16.4% and 9.1% between the MLAA and MLEM activity reconstructions and between the activity reconstructions of MLAA and MLRR, respectively. Further improving the segmented liver region by avoiding the superior parts of the liver that could be affected by motion, an average difference of 7.5% was computed for the MLEM and MLAA reconstructions over all our patient database. Correcting for the attenuation mismatch by means of the MLRR algorithm, the average difference was computed as 7.4% between MLRR and MLAA. When the deformed MLRR attenuation image (DCT) was used in the scatter generation procedure, the average error was further reduced to 6.4%. The effect of the scatter shape on the activity reconstruction has also been reported in [143]. A bar plot of the quantification results of the liver can be found in the appendix.

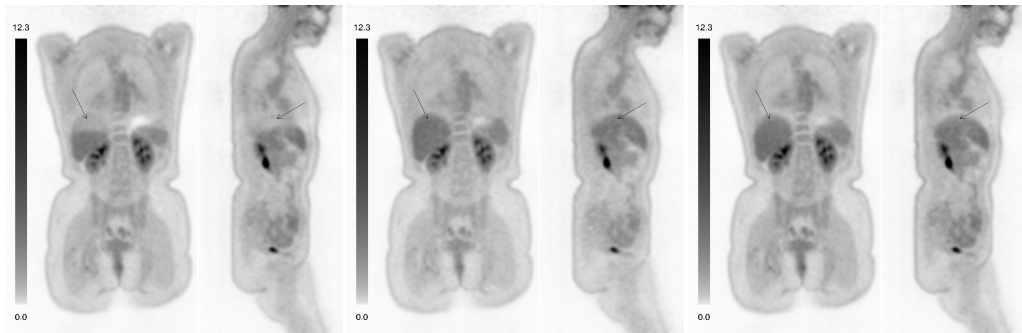


Figure 7.6: MLEM (left), MLAA (center) and MLRR (right) activity reconstructions of a patient where the CT and PET data were acquired at different phases of the breathing cycle. The reconstructions are all obtained using the ML-SSS estimate of the scatter.

Figure 7.7 shows the results on the relative differences of the “standard” MLEM/MLRR and MLAA activity reconstructions in the heart region. Initially the MLAA activity images are compared to the MLEM activity reconstructions corrected for attenuation with the CT-based attenuation factors. This resulted in an average relative difference of 8.0% in the reconstructions (“EMAA” in Figure 7.7). As before, the CT-attenuation image was deformed to account for any possible mismatch between the PET and the CT by applying MLRR to estimate the motion (producing the deformed CT (DCT) attenuation image), the mean relative error was reduced to an average of 6.5% (“RRAA (CT)” in Figure 7.7). As opposed to the liver region

where the segmented region was chosen outside the motion-affected region, it was impossible to segment such a volume of interest to analyze the heart in. Moreover, when the deformed CT (DCT) attenuation image was used to compute the ML-SSS estimate, the mean errors were further reduced to 5.0% (“RRAA (DCT)” in Figure 7.7). Interestingly, the largest mismatch between the DCT and the CT attenuation images (results not shown) were observed for patient index numbers 8, 5 and 21 where a similar trend is also observed in figure 7.7.

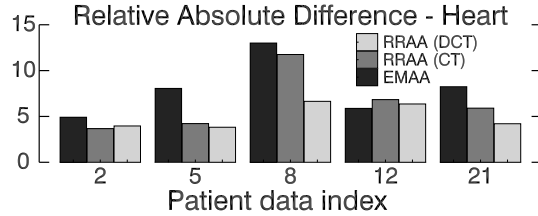


Figure 7.7: Mean activity differences of MLEM/MLRR and MLAA reconstructions in a heart region. In all cases the results are for reconstruction with the ML-SSS estimate. Please refer to the text for the explanation of the labels: RRAA (DCT), RRAA (CT) and EMAA.

A total of 58 lesions with a high local activity uptake were segmented which included tumors of different organs and inflammatory lesions with abnormal high activity. It should be noted that only 15 of the 23 patient scans (65%) were used in this study, as there were no such lesions found in the other 8 whole body images. Also, a maximum number of 5 lesions were selected for each patient. When possible lesions were selected from different organs and larger lesions were selected to avoid problems related to partial volume effects. The average pixel-by-pixel difference between MLEM and MLAA (EMAA), MLRR and MLAA with the CT-based ML-SSS estimate (RRAA (CT)), and MLRR and MLAA with the deformed CT-based ML-SSS estimate (RRAA (DCT)) was respectively 8.8%, 8.7% and 9.4%. The quantification results of the tumor/inflammatory lesions and a histogram of the contrast of these high activity lesions to the liver can be found in the appendix.

The segmented lesions were manually classified based on their location into lesions which could potentially be affected by motion and lesions which were probably not affected by motion. Lesions located in the mediastinum and the ones within or in close proximity of the lungs were regarded as motion-affected lesion. Furthermore the errors were computed in the segmented volume of interest as opposed to the pixel-by-pixel basis. Table 7.3 reports the results for these two clusters of lesions as well as the overall differences in all the segmented regions. Comparing the EMAA and RRAA (CT) results, we observe that the activity difference of the lesions not being affected by motion remain more or less unchanged, however a slight improvement is observed for the motion affected lesions. The overall differences observed in the tumor region seems to be small and could possibly be explained by a slightly different noise profile in the reconstructions.

## 7. JOINT RECONSTRUCTION OF ACTIVITY AND ATTENUATION IN TIME-OF-FLIGHT PET: A QUANTITATIVE ANALYSIS

---

Table 7.3: Absolute ROI error between MLEM/MLRR and MLAA for the tumor/inflammatory lesions with high local tracer uptake.

	EMAA	RRAA (CT)	RRAA (DCT)
all	7.5%	7.0%	7.5%
non motion-affected	7.6%	7.4%	8.3%
motion-affected	7.4%	6.4%	6.3%

## 7.4 Discussion

In this study we have tried to validate the joint activity and attenuation reconstructions of MLAA/MLRR to the current clinical gold-standard which is the activity reconstruction of MLEM with a correction of the attenuation using at CT attenuation image adjusted to the 511 keV photon energy of PET. These three methods have different degrees of freedom for the reconstruction of the tracer activity from the TOF-PET emission data. Consequently, each of these algorithms may respond differently to inconsistencies in the data. Hence, any inaccuracy in the corrections applied either before or during image reconstruction could alter the results of our comparison. To this end, we have highlighted in this study 3 of the most prominent issues that could potentially influence the estimated tracer activity uptake. We observe that in case of a CT and PET mismatch the attenuation values that are computed from the adjusted CT image could directly and indirectly (through the scatter shape) influence the quantification results. In addition to this, we find that the current method that tries to model the effects of multiple scatter by scaling the SSS estimate of the single scatters can also cause variations in our reconstructions. We find that when these effects are well taken care of, the differences between the three methods reduce to about 7% or less, which is an acceptable error margin in clinical analysis.

The Monte-Carlo simulation results of the NEMA-like phantom demonstrate how inaccuracy in modelling the multiple scatter in the scatter simulation, can produce both a global and a local effect on the reconstruction of the tracer distribution. The MLEM reconstructions with the TF-SSS estimate under-estimated the total amount of tracer distribution by a factor of 17%, and caused some local inaccuracies in the tracer distribution reconstruction. When the ML scatter scaling method of [69], [145] was used to modify the TF-SSS, that error was reduced to less than 1%. In addition, the comparison with the gold-standard MLEM reconstruction showed no significant sign of the local inaccuracies previously observed. Interestingly, we observed that in case of an inaccurate scatter estimate (i.e. TF-SSS estimate) the MLAA activity reconstruction provides a slightly more accurate result compared to the MLEM activity reconstruction.

In the patient data analysis, we found that the typical artifacts caused by an inaccurate scatter estimate were removed after using the ML scatter scales to correct the emission data with, and in some patients dramatically improved the comparisons in the bladder compared to using the TF-SSS estimate. We did not observe an

improvement when analyzing the tracer distribution values at the segmented vertebrae in our patient database, the results were inconclusive and require a more thorough analysis of regions in the vicinity of bony structures.

The results on the liver region confirmed that when the reference volume of interest region is selected well outside the motion-affected region, any possible mismatch would not directly influence the quantification. However, in both the liver and the heart studies we found that a mismatch did indirectly influence the reconstructions as the mismatched CT-based attenuation image is used to generate the scatter estimate. Most importantly, we found the average differences on the focal high uptake regions were relatively small.

In this study we have focused on the differences observed between MLEM/MLRR and MLAA reconstructions. However, as mentioned earlier to avoid problems related to the scale in joint reconstructions, the total tracer activity of MLEM (in the tissue region) was used to correct the MLAA activity reconstruction. In cases where the CT-based attenuation image is available, MLRR could provide a better alternative (in particular in the case of between-scan or in-scan motion) to the clinical gold-standard MLEM reconstructions. Table 7.4 shows the average ROI-based differences between the MLRR and MLEM activity reconstructions for the different regions analyzed in our study. Compared to the results shown for MLAA, the errors between MLEM and MLRR activity images are less and well below clinically accepted values. As expected, higher differences are observed in the liver (naive segmentation) and the heart regions which are subject to between-scan and in-scan motions. We believe that in these regions MLRR is more accurate than MLEM.

Table 7.4: Average ROI differences between MLRR and MLEM for all the segmented regions.

	bladder	liver (naive segmentation)	liver	heart	vertebrae	tumor
ML-SSS (CT)	3.2%	8.4%	3.4%	4.2%	3.5%	3.4%

## 7.5 Conclusion

In an attempt to validate the joint activity and attenuation reconstructions from TOF-PET emission data, reconstructions of whole body scans of a patient data base were quantitatively analyzed and compared to the current clinical gold-standard. Our initial analysis revealed differences which were reduced after some of the contributing factors were identified and appropriately corrected for. We find that an inaccurate scaling of the single scatter estimates or patient mismatch (directly or indirectly through the scatter estimation) are enough to produce significant differences between the activity reconstructions. Our study demonstrates that in the presence of inaccuracies in the scatter estimate (Monte-Carlo study) or patient motion (patient study) and provided that an accurate estimate of the scale is available, the joint activity and attenuation reconstructions from TOF-PET provide a more accurate

## 7. JOINT RECONSTRUCTION OF ACTIVITY AND ATTENUATION IN TIME-OF-FLIGHT PET: A QUANTITATIVE ANALYSIS

reconstruction of the tracer distribution compared to the current gold-standard. The problem of obtaining an accurate scale of the joint reconstruction would be eliminated in cases where CT-based attenuation information is available. A more systematic investigation of MLRR and MLEM activity reconstructions remains subject of future studies.

### 7.6 Acknowledgments

This research is supported by a research grant (GOA) from KU Leuven, FWO project G027514N. The authors would like to thank Vladimir Panin, Michael E. Casey and Charles Watson for providing the Monte-Carlo simulation data and Kathleen Vunckx for insightful discussions.

### 7.7 Appendix

This appendix shows some additional results. Figure 7.8 shows the bladder to liver contrast ratios as well as the volume of the segmented bladder region. Figure 7.9 shows the quantification results on the segmented lumbar vertebrae region in addition to the average vertebrae to liver contrast values. Figure 7.10 shows the relative differences observed in the liver region when comparing MLEM and MLAA (EMAA), MLRR and MLAA with the CT-based ML-SSS estimate (RRAA (CT)) and finally MLRR and MLAA with the DCT-based ML-SSS estimate (RRAA (DCT)). These results are for the smaller liver region, which does not include the portion close to the lung and thus are possibly not affected by breathing motion. Figure 7.11 shows the quantification results on the segmented tumors/inflammatory regions with a high activity uptake together with a histogram of the segmented lesion based on their lesion to liver contrast ratios.

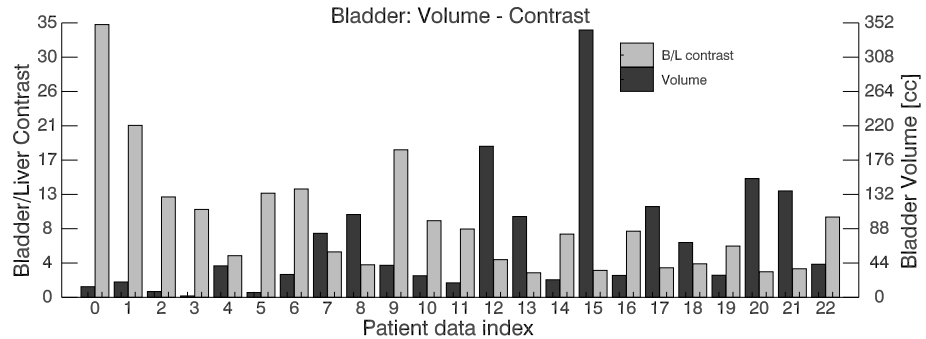


Figure 7.8: Bladder to liver contrast and the bladder volume. The bladder to liver contrast is computed as the average activity inside the bladder to the average activity inside the liver from MLEM reconstructions with the SSS expected scatter estimate.

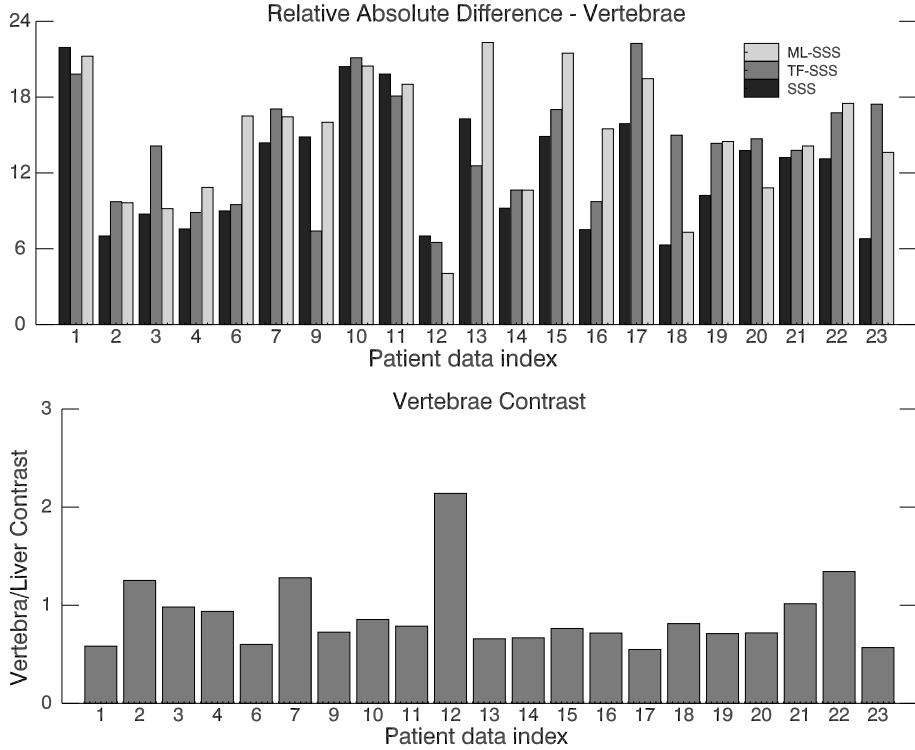


Figure 7.9: Mean ROI activity differences of MLEM and MLAA reconstructions in a lumbar vertebra (top), and the vertebrae to liver contrast (bottom) estimated as the average vertebrae activity to the average liver activity from MLEM activity reconstructions with the SSS expected scatter estimate. The results are reported for reconstruction with the SSS, TF-SSS and ML-SSS estimates. Patient indexes 5 and 8 have been excluded as they had an abnormal activity uptake in their vertebra possibly as a result of therapy.

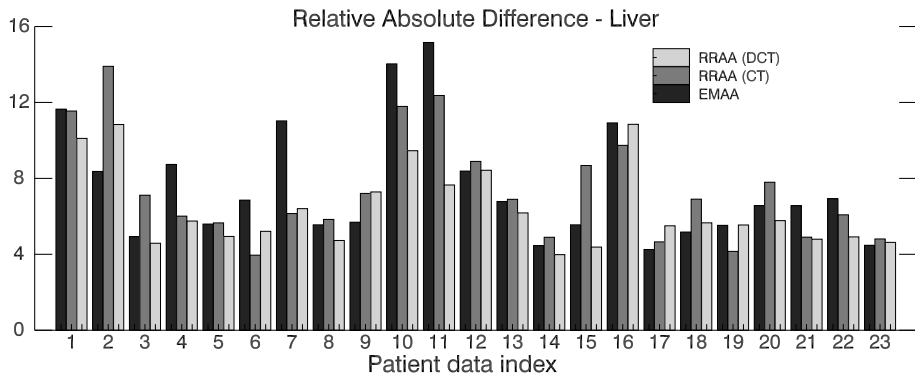


Figure 7.10: Mean activity differences of MLEM/MLRR and MLAA reconstructions in the liver region. In all cases the results are for reconstruction with the ML-SSS estimate. Please refer to the text for the explanation of the labels: RRAA (DCT), RRAA (CT) and EMAA.

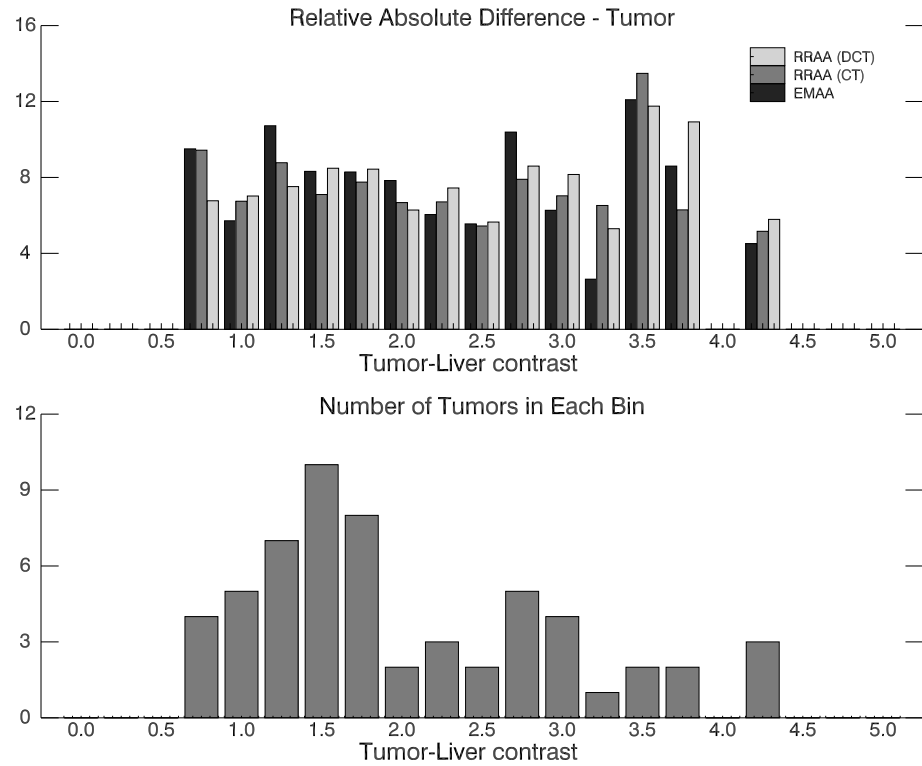


Figure 7.11: Mean ROI activity differences of MLEM/MLRR and MLAA reconstructions of the segmented tumors (top), and a histogram of the tumors classified by their tumor to liver contrast (bottom). In all cases the results are for reconstruction with the ML-SSS estimate. Please refer to the text for the explanation of the labels: RRAA (DCT), RRAA (CT) and EMAA.

## Chapter 8

# Reconstruction of a Motion and Attenuation Corrected Activity Distribution in Gated TOF-PET

A. Rezaei, M. Defrise, and J. Nuyts, “Reconstruction of a Motion and Attenuation Corrected Activity Distribution in Gated TOF-PET”, in *2014 IEEE Nuclear Science Symposium and Medical Imaging Conference (2014 NSS/MIC)*, 2014

## Abstract

In this work, we demonstrate a framework in which the respiratory gated TOF-PET emission data are used to reconstruct a single activity image (which is corrected for attenuation), together with motion parameters that deform the activity reconstruction (of the reference frame) to each of the frames. We compare the reconstructions to independent and registered (post-reconstruction) MLACF reconstructions of each frame. We propose a joint estimation method that avoids selecting a reference frame and provides low bias and variance compared to methods that select a reference frame from among the gated frames. Reconstruction results are also shown for the 3D breathing XCAT phantom.

## 8.1 Introduction

Various methods have been proposed that deal with gated PET emission data. Commonly the gated PET data are reconstructed independently (in each frame) and are registered (post-reconstruction) and then averaged to obtain a motion-free activity image [146]. More recently, methods have been proposed that take advantage of the emission data from all frames and combine the two reconstruction and registration steps [147]. In the latter approach, the method estimates one activity image together with multiple transformation parameters that deform the reconstructed activity image (in the reference frame) to the desired frames. Although promising results were reported, more studies are warranted on the topic, e.g. to investigate the selection of the reference frame and its effect on the final activity image and motion parameter estimates.

Furthermore, attenuation correction in gated PET studies has always been a challenge, since in principle each frame should be attenuation corrected based on an attenuation map that has been aligned to the particular breathing phase associated with that frame. This alignment problem has often been ignored to reduce the complexity. Since the TOF-PET data determine the attenuation factors sinogram up to a scale [58], the availability of time-of-flight (TOF) PET data provides a means to overcome this longstanding problem. In this contribution we use the newly developed algorithm MLACF [65], [66], which estimates an activity image and a sinogram of the attenuation factors from the gated TOF-PET emission data.

## 8.2 Methods

The proposed method jointly estimates an activity image together with transformation parameters that deform the activity image to a corresponding frame of the gated TOF-PET data. By using a modified version (for gated TOF-PET data) of the MLACF algorithm, we obtain an activity image which is corrected for attenuation, and with a similar approach to that in [67] we estimate the transformation parameters of either a rigid or non-rigid motion model, which deforms the activity of the reference frame to each of the frames. The activity and motion estimates are then updated sequentially. We refer to this approach as the fully 4-D (F4D) framework, where the activity image can be reconstructed in either a virtual reference frame (VRF) or a specific reference frame (SRF), depicted in figure 8.1. In both cases the activity image and the motion parameters are initialized by a uniform disk of activity and the identity motion parameter for each frame, respectively. With a non-rigid motion model, the computation of a displacement field, and its inverse are required to deform the activity reconstruction of the reference frame to each of the frames and back.

Since there are no constraints on the reference frame in the VRF case, it is likely that the activity image is reconstructed at a displacement approximately equal to the mean of the frame positions (which we call the ‘average position frame’). In contrast, a feature of the SRF case is that it requires one less displacement and its inverse to be estimated. In the following, we investigate the reconstruction results of the

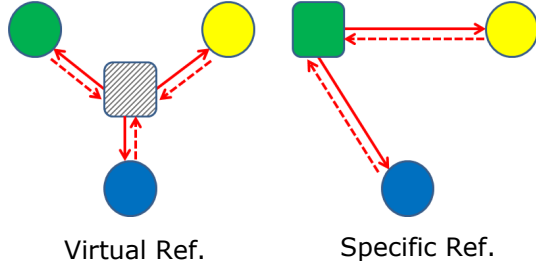


Figure 8.1: Depiction of the joint estimation framework where the single activity reconstruction is obtained in a virtual (left) or a specific (right) reference frame relative to the gated PET data. The colors represent the different phases of the gated motion. The squares represent the frame that the activity reconstruction will be reconstructed in, the solid arrows are the displacements that are to be estimated, and the dotted arrows are the inverse displacements that are computed from their corresponding displacement estimates.

joint activity and motion estimation method and compare the results to independent and registered MLACF reconstructions of each frame. We then briefly look into the effects of the choice of the reference frame on the estimated activity reconstructions.

## 8.3 Simulation Design

The simulation specifications were adjusted according to the Siemens Biograph mCT scanner specifications. In the 2D simulations, the TOF-PET emission data consist of 200 radial bins of 0.4 cm width, 168 projection angles over 180 deg, and 13 TOF-bins of 312 ps width with an effective TOF resolution of 580 ps. An oversampling of 3 was also used during simulations to introduce a slight mismatch (between the projector used during the reconstructions and the one used to simulate the acquisition process), and the reconstructed image had  $200 \times 200$  pixels of 0.4 cm width. In the 3D simulation, the TOF-PET data are organized as 5D sinograms, consisting of 200 radial bins, 168 azimuthal angles, 9 co-polar angles, 109 planes, and 13 TOF-bins. The reconstructed image had a  $200 \times 200 \times 109$  volume grid with a voxel width of 0.4 cm and 0.2 cm in the transaxial and axial directions, respectively.

### 8.3.1 2D Thorax Phantom

Figure 8.2 shows the 2D activity and attenuation images of 3 simulated frames. An increase in the size of the lungs and a displacement of the tumor lesion were used to simulate non-rigid deformations between the 3 frames. TOF-PET emission data were obtained for each frame assuming a scan duration ratio of 0.31, 0.46 and 0.23 for each frame, respectively.

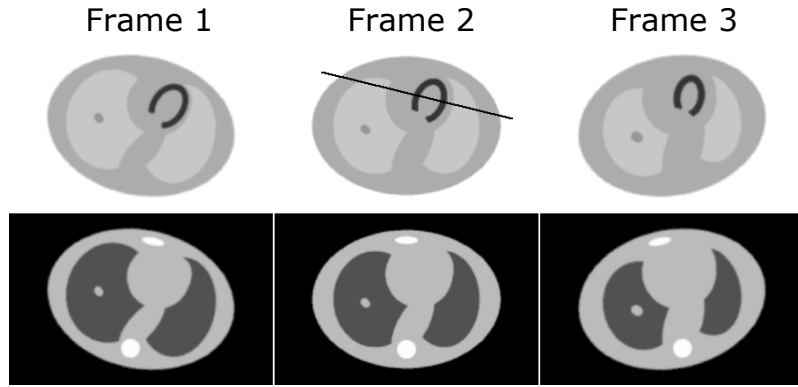


Figure 8.2: Activity (top) and attenuation (bottom) images of the 2D thorax phantom deformed into 3 frames. The line in Frame 2 serves as the ground truth profile through the thorax phantom which the different reconstructions will be compared to in figure 8.4.

### Reconstructions

After adding Poisson noise to the emission data, a single activity image was reconstructed together with 3 sinograms of the attenuation factors in each frame and 3/2 displacement estimates for the VRF/SRF joint estimation cases. We assumed that the total amount of activity in all frames was available, and the MLACF scale problem [58] was solved accordingly. The reconstruction update steps are as follows:

- after deforming the activity reconstruction to frame  $f$  using its frame displacement estimate  $\mathbf{D}^f$ , the attenuation factors  $a^f$  are computed together with the gradient image of the emission likelihood  $\dot{L}^f$  and the sensitivity image  $S^f$  for all frames.
- the update of the activity reconstruction is computed as ratio of the deformed gradient and sensitivity images, i.e.  $\Delta = \sum_f \dot{L}[\mathbf{D}^T]^f / \sum_f S[\mathbf{D}^T]^f$ , where  $T$  denotes matrix transpose.
- the displacement estimate of each frame is updated using the demons registration algorithm and the driving image equal to  $\Delta - \Delta^f$ , where  $\Delta^f = \dot{L}^f / S^f$  is the activity update of each frame, which otherwise would have been used in updating the activity reconstruction of the frame.

The results are then compared to independent and registered MLACF activity reconstructions of each frame which we refer to as the FR-IR (frame-wise reconstruction and intra-frame registration) approach. The registration algorithm in the FR-IR approach was the same as the one used in the F4D framework. The demons [125], [130] registration algorithm was used in two resolution levels in each iteration, and the displacements were computed using a symmetric demons update rule for the FR-IR approach. This was to take full advantage of the independent reconstructions of each frame. The independent MLACF reconstructions are obtained after 5 iterations of

24 subsets, and the joint reconstructions are after 10 iterations of 24 subsets where the first iteration assumes a rigid motion model.

### Noise Propagation

The effect of the reference frame selection on bias and variance values of the reconstructed activity image (when deformed to each frame) is analyzed for 100 different noise realizations. Bias in each frame is computed as the average absolute pixel by pixel difference of the true activity images of each frame and the average (over the noise realizations) of joint activity reconstructions deformed to each frame. Variance is reported as the mean (over all pixels) of the pixel variance of the joint activity reconstructions deformed to each frame. The results are reported together with the results of independent and registered MLACF reconstruction of each frame.

#### 8.3.2 3D Breathing XCAT Phantom

The XCAT phantom was used to generate realistic respiratory motion. A maximum diaphragm motion of 2.0 cm and a maximum anterior-posterior motion of 1.2 cm were used to simulate the breathing cycle, which was gated into 8 (motion-free) frames of 1.25 min durations each. After adding Poisson noise to the emission measurements, a single activity image was reconstructed in a virtual reference frame, together with a set of 8 attenuation factor sinograms and 8 displacement fields. The joint reconstructions are obtained after 6 iterations of 24 subsets, assuming a rigid motion model for the first iteration and a non-rigid motion model for the following 5 iterations. The independent MLACF reconstruction of the frames are after 3 iterations of 24 subsets and the registered activity images are obtained after the same number of updates of the demons registration algorithm as the joint reconstruction method.

## 8.4 Results

### 8.4.1 2D Thorax Phantom

#### Reconstructions

Figure 8.3 shows independent MLACF and the post-reconstruction registered activity reconstructions of each frame together with the VRF joint reconstruction of the F4D framework after the single activity image was deformed to each frame. Since the scan duration of each frame was different, the independent activity reconstructions have a different noise response. The FR-IR activity images of each frame show a similar noise response between frames, however when comparing to the VRF reconstructions, we notice further improvements in the reconstructions of the F4D joint estimation method. Figure 8.4 shows a profile through the reconstructed activity images of frame 2, where the F4D method achieves a slightly better quantitative accuracy in the high activity regions of the phantom.

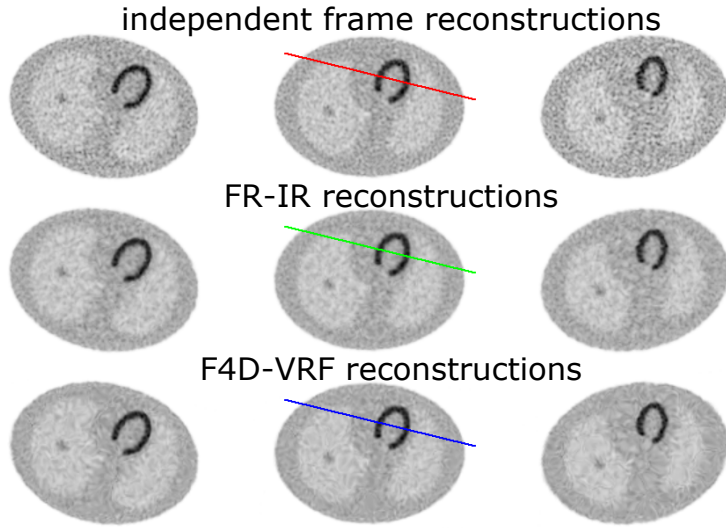


Figure 8.3: Independent MLACF activity reconstructions of each frame (top), frame-wise reconstructions and intra-frame registered (FR-IR) activity reconstructions (center), and the deformed activity reconstruction of the virtual reference frame (VRF) joint estimation method (bottom).

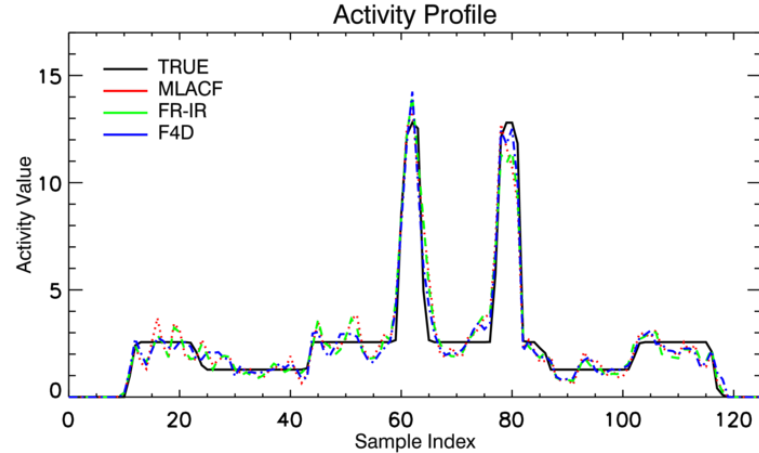


Figure 8.4: A profile through the activity reconstructions of figure 8.3.

### Noise Propagation

Table 8.1 reports bias and variance of the independent MLACF activity reconstructions of each frame together with the registered activity images (FR-IR), and the VRF/SRF joint estimation activity reconstruction ( $SRF-i$ ,  $i = 1, 2, 3$ , where  $i$  determines the reference frame) of the F4D approach, after the activity reconstruction is deformed to each frame. Table 8.1 shows that the selection of the reference frame influences bias and variance in the reconstructions. Interestingly, in the SFR cases the highest variance is seen in the reference frame. We believe this to be due to the

asymmetric updating of the activity reconstruction from all the different frames. The emission update and the activity reconstruction of all frames except the reference frame need to be deformed to and back from the reference frame, having a low-pass filtering effect on the transformed image volume. Moreover, it shows that the virtual reference frame reconstructions achieve low bias and variance compared to the specific reference frame reconstructions.

#### 8.4.2 3D Breathing XCAT Phantom

Figure 8.5 shows the true activity image of frame 5 together with the independent activity reconstruction of the frame (MLACF), the post-reconstruction registered image of the frame (FR-IR), and the activity reconstruction of the F4D joint estimation method with a virtual reference frame (F4D-VRF). It is interesting to see that the activity reconstruction of the joint estimation provides a more accurate reconstruction compared to the post-reconstruction registered activity image.

### 8.5 Conclusion

This work investigates the effect of the choice of the reference frame in joint activity and motion estimation methods, and its influence on the final activity reconstruction. The newly proposed MLACF algorithm is modified to deal with gated TOF-PET emission data and is used for the estimation of attenuation corrected activity images. The noise simulation suggests that when the reference frame is chosen close to the ‘average position frame’, reconstructions have the smallest error. The 2D/3D simulations show a qualitative improvement in the activity reconstructions compared to post-reconstruction registered activity images.

Table 8.1: Bias and variance of the independent MLACF, post-reconstruction registered, and the VRF/SRF joint estimated activity images of each frame

	Frame 1	Frame 2	Frame 3
scan duration ratio	31%	46%	23%
MLACF	0.189 (1.539)	0.195 (1.061)	0.220 (2.296)
FR-IR	0.180 (0.689)	0.204 (0.634)	0.218 (0.784)
F4D-VRF	0.167 (0.589)	0.191 (0.575)	0.191 (0.627)
F4D-SRF-1	0.168 (0.910)	0.193 (0.681)	0.183 (0.732)
F4D-SRF-2	0.180 (0.738)	0.193 (1.001)	0.176 (0.784)
F4D-SRF-3	0.183 (0.627)	0.203 (0.623)	0.265 (0.838)

8. RECONSTRUCTION OF A MOTION AND ATTENUATION CORRECTED ACTIVITY DISTRIBUTION IN GATED TOF-PET

---

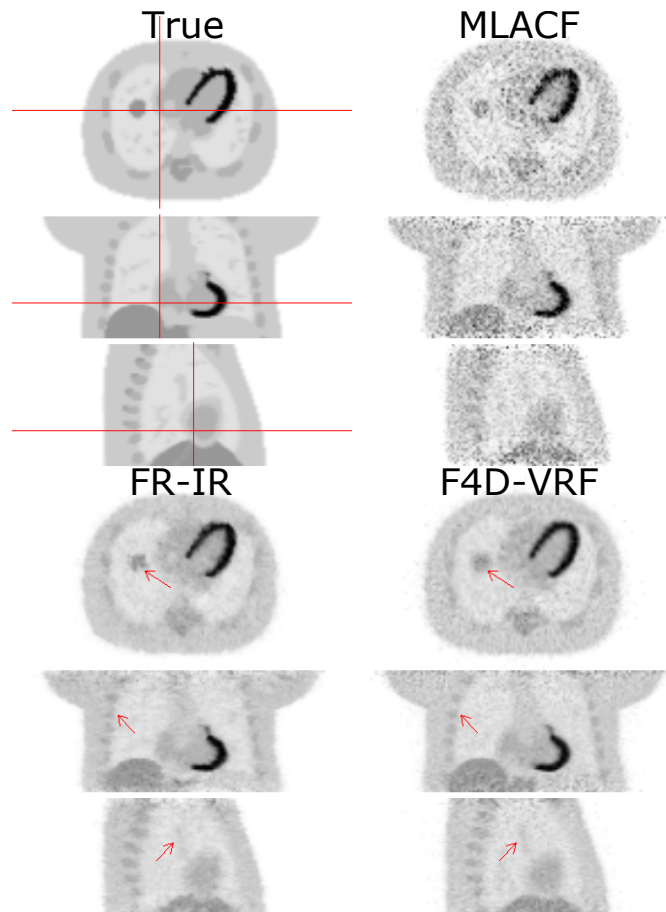


Figure 8.5: The true activity image of frame 5 (top-left) and its independent MLACF activity reconstruction (top-right) shown together with the post-reconstruction registered activity (bottom-left) and the deformed activity reconstruction of the F4D-VRF joint estimation method (bottom-right).

# Chapter 9

## Discussion

Since it was shown that the time of flight (TOF) positron emission tomography (PET) data provide information about the attenuation of the emission data [58], a number of newly developed algorithms have been proposed to exploit the added information available with TOF. It is understood however, that the TOF-PET emission data alone do not allow a quantitative assessment of the reconstructed distribution of activity, as TOF-PET data only determine the activity distribution up to a constant scale [58]. This limiting factor might be one of the main reasons why the use of joint estimation methods has not yet been introduced in clinical practice.

Applying the TOF consistency conditions to the TOF-PET emission data, estimates for gradients of the attenuation sinogram can be computed. In 2D TOF-PET, this procedure generates estimates for the derivatives with respect to the radial and angular coordinates [58]. In 3D TOF-PET, estimates for the derivatives with respect to the planar and tilt coordinates can also be obtained from the emission data [60]. Although the attenuation derivatives can be accurately estimated in the convex support of the activity, when approaching the support boundary these estimates become less reliable. An attenuation sinogram could subsequently be estimated by an integration of its gradients, and reconstructed if required. Alternatively, since the radial derivative of a sinogram is sufficient for its reconstruction, the radial derivative could be backprojected and the integration could be applied in the reconstruction space as proposed in [148]. In [109] with a slightly different approach, a maximum a posteriori (MAP) algorithm is proposed by applying the discretized TOF consistency condition to the TOF-PET emission data, and using the conjugate gradient (CG) optimization method instead of Landweber algorithm.

The majority of the newly developed methods aim at simultaneously reconstructing an activity and an attenuation image from the TOF-PET emission data [61], [110], [120], [121], [142], [143], [149], [150] by maximizing the Poisson log-likelihood function as originally suggested in [47]. However, recently methods have also been presented that use the alternative quadratic formulation of the problem [151], [152] and try to minimize the quadratic emission cost function together with an additional L<sub>1</sub>-norm constraint on the reconstructions minimizing the total voxel-by-voxel variance of the reconstructions.

## 9. DISCUSSION

---

As discussed in detail in chapter 3, the MLAA algorithm uses an alternated update scheme for activity and attenuation reconstructions. When the attenuation image is kept fixed, the activity update is computed by maximizing the TOF log-likelihood function, and the attenuation update is obtained by maximizing the non-TOF log-likelihood function (which can also be obtained by introducing approximations to the TOF log-likelihood function, chapter 6 - appendix A). In our implementation we have adopted the non-TOF version of the attenuation update, as it requires fewer TOF projections per iteration which in our implementation was very time-demanding, and the joint reconstructions with and without this approximation did not show obvious differences. However, a detailed analysis could help to justify the approximation similar to the studies which investigate the effects of the intensity prior strength [121], attenuation-to-activity update ratio schemes [153], and different initializations [154], [155] in the joint activity and attenuation reconstructions.

The most straightforward way to deal with the missing scale in quantitative joint estimation of the tracer distribution is to apply an intensity prior on the estimated attenuation coefficients favoring expected tissue attenuation. However, since the emission data provide less information outside the support of the activity, special handling of the attenuation values might be necessary. For example, in case of no attenuation outside the support of the activity, extra constraints might be required to ensure that the estimated attenuation values outside the support are (very close to) zero in the background. The use of MR prior maps has been shown to improve and provide added stability to the reconstructions [121], [150]. Since TOF allows for simultaneous emission and transmission imaging [140], the use of transmission data could provide an alternative to solving the scale as suggested in [139], [156]. Furthermore, since the scintillators emit  $\gamma$ -ray photons in coincidence with beta emission (at a lower energy level), this background radiation source can be used as an alternative to transmission sources inside the scanner [119], [157], [158]. In addition, scale correction techniques have been proposed which ambitiously try to determine the scale from the scattered events in the emission data [141].

A number of methods have been proposed which avoid the reconstruction of the attenuation medium and attempt to estimate the attenuation correction factors (ACFs) which more directly influence the TOF-PET emission measurements [65], [66], [159], [160]. The case of no additive scatter and/or randoms contributions was discussed in detail in chapter 4 where an immediate update for the ACFs was derived at each iteration of the MLACF algorithm. With the additive contribution of scatter and/or randoms, the update of the attenuation correction factors differs slightly when using the TOF log-likelihood function (chapter 5) or the non-TOF log-likelihood function [159] for the subproblem of estimating the attenuation correction factors when the activity is known. In the former case, the ACF update is no longer immediate and with an increasing amount of the additive contribution in the TOF-PET emission data, more ACF iterations are required at each MLACF iteration. Using the non-TOF log-likelihood function for the ACF estimation subproblem however, an immediate ACF update can be derived which in preliminary experiments seemed to produce more accurate estimates with high amount of noise present in the TOF-PET emission data. When a weighted (by the reciprocal of the unattenuated

---

emission measurements) quadratic formulation of the ACF estimation subproblem is used [104], the same update for the attenuation correction factors as the non-TOF log-likelihood function is derived. A more comprehensive study on the different flavours of the ACF estimate in MLACF is warranted for future studies.

For MLACF, solving the scale problem of joint reconstruction is more challenging and the straightforward constraining method of imposing the known attenuation of tissue is not possible. The scale problem could be solved by using information of a known activity source, e.g a vial of activity in the scanner. However as MLACF is much less time-demanding than MLAA, a more practical approach to solve the scale problem is to reconstruct the estimated attenuation correction factors post-estimation and imposing the attenuation constraining as previously mentioned. In cases where attenuation correction factors obtained from CT are available in some planes, the scale problem is automatically fixed by imposing this prior information during reconstruction [104].

The majority of algorithms that have been developed for joint reconstruction of activity and attenuation require an initial histogramming of the listmode data into a sinogram. In an attempt to directly use the listmode data in the joint reconstruction framework, methods have been proposed that combine listmode reconstruction algorithms for activity and attenuation in TOF-PET [161], [162]. Likewise, a listmode reconstruction algorithm was proposed for SPECT imaging [163]. In [162], the MLACF algorithm was also extended to incorporate the listmode TOF-PET emission data during reconstructions. It was demonstrated that although with listmode emission data the attenuation correction factors could no longer be estimated, their backprojection (also referred to as the "sensitivity image") can. Since this backprojection provides enough information for attenuation correction, it was possible to derive and validate a listmode version of MLACF. This proved to be an important feature of the algorithm for motion-corrected activity reconstructions of listmode data. The joint reconstruction of the activity and sensitivity images from TOF-PET data has also been demonstrated in [164].

We have demonstrated in chapter 5 that the joint reconstructions of MLACF are robust to inaccuracies in the estimated detector-pair sensitivities. We showed that MLACF was able to produce activity reconstructions free of artifacts, even when the necessary corrections for the detector-pair sensitivities were avoided. Although the activity reconstruction seemed to be unaffected by it, the estimated attenuation correction factors were highly affected as in this case the algorithm estimated the product of the attenuation correction factors and the detector-pair sensitivities. As a result, a post-reconstruction of the estimated ACFs without correction for the detector-pair sensitivities would no longer be free of artifact. The detector-pair sensitivity values are computed regularly from phantom measurements in clinical practice, however they could vary from time to time, in particular with the new detector technologies which are more sensitive to changes in the detector temperature. As demonstrated in [165], [166], in cases where the CT-based attenuation image is available and is thought to be well aligned to the emission data, the TOF-PET data could be used to estimate or refine the crystal efficiencies of the TOF-PET scanner instead of the attenuation correction factors.

## 9. DISCUSSION

---

Since the commercially available PET systems are commonly accompanied by CT or MR systems, the joint reconstruction methods need to be tailored to take advantage of the added anatomical information. In chapter 6 a method was proposed that uses the CT-based attenuation image to correct for any possible mismatch between the CT and PET acquisitions. The method is essentially very similar to MLAA, however instead of applying an attenuation update to the attenuation reconstruction, MLRR deforms the CT-based attenuation image. By using the energy adjusted CT-based attenuation image, no additional constraints are required to ensure a quantitative reconstruction of the tracer distribution.

The alignment of a template attenuation image dates back to the pioneering work of [27], and since then many methods have been proposed. Among those are the more recent works [167]–[170] which use a spline model to represent a deformation grid that also helps the motion estimation problem by significantly reducing the number of motion parameters being estimated as opposed to the MLRR method introduced in chapter 6 and in [68]. The proposed methods seem to perform well for a non-rigid motion estimation even without the benefits of the added TOF information.

The recent success of joint reconstructions with TOF-PET emission data has also inspired a renewed look at joint reconstruction in non-TOF. In [171], [172] an expectation maximization (EM) algorithm is proposed for the joint reconstruction of activity and attenuation. Similar to the work of Lange *et al.* [173], the joint estimation problem is formulated by the use of complete data variables and the proposed EM algorithm is obtained. Furthermore, the original non-TOF MLAA algorithm [47] has been modified by the incorporation of MR-derived prior information [174]–[176] to avoid the cross-talk problem in joint activity and attenuation problem. This has led to improvements in the quantification of activity reconstructions in PET/MR brain studies. The gains achieved by adding transmission sources in non-TOF PET systems and the improvements obtained by utilizing the added transmission information in the joint reconstruction problem has also been investigated in [177]. In [178] a joint (rigid/affine) motion estimation and a region-of-interest (ROI) activity reconstruction framework was proposed and studied in a pre-clinical setting where even the state-of-the-art systems are not able to provide useful TOF information.

Furthermore, with the increasing interest in dedicated breast PET scanners, the methods which model the attenuation as a uniform elliptical attenuating medium have been used to correct for the relatively uniform attenuation of the breast tissue [179]. As the added information gain introduced by TOF is limited or negligible for smaller objects, these methods still rely on estimating the attenuation from the Helgason-Ludwig consistency conditions.

Accurate attenuation correction in gated PET studies has always been a challenge, and is often ignored, resulting in some degradation of the final images. The availability of time of flight PET data however, provides a means to overcome this longstanding problem. The gated emission data are traditionally reconstructed in a series of independent frames and subsequently registered to a reference frame. We have demonstrated that the joint activity and attenuation reconstruction in addition to alleviating the attenuation correction problem of the gated emission data could help to improve the subsequent registration problem [67]. A more comprehensive

---

approach to reconstruction of gated emission data is the fully 4D reconstruction framework, where the motion estimation step is incorporated in the reconstruction framework. In chapter 8, a modified version of the MLACF reconstruction algorithm was presented for gated TOF-PET emission data. As expected the reconstructions of the fully 4D reconstructions provide a more accurate reconstruction of the tracer activity compared to independent reconstructions of gated emission data. We have found that the reference gate selection does influence the reconstruction and better results were obtained when the tracer activity image was reconstructed in a virtual reference frame. With a similar approach to [180], promising results have been also reported in [181] for gated TOF-PET data in a fully 4D reconstruction framework. The two joint reconstruction methods, MLAA and MLACF, have also been utilized in dynamic whole body parametric imaging and shown to improve the quantitative results [18], [182].

An important hurdle for the introduction of joint reconstruction methods in clinical practice is the lack of a comprehensive validation of these methods on a big patient database. An initial study was done in [138] where after taking the scale problem into account, the results of the joint estimation method were found to be similar to the gold-standard without the effects of motion. Furthermore, it was found that the joint reconstruction methods are able to outperform methods which utilize MR-based attenuation correction schemes with TOF-PET emission data [120], [121], [142] as well as non-TOF emission data [183]. In a more recent study [143], the joint estimation methods were analyzed in a retrospective cardiac study on a fairly large patient data base. As expected it was found that the joint reconstruction methods were able to remove any possible PET/CT mismatch and also demonstrated that the activity reconstructions could potentially be influenced by the presence of CT mismatch in the scatter estimation procedure.

In the quantitative study presented in chapter 7 an attempt was made to quantitatively analyze the joint reconstructed activity images, comparing them to the current clinical gold-standard (i.e. MLEM with a CT-based attenuation correction of the emission data), on a set of whole body patient scans. We concluded that the activity reconstructions of MLAA were within the clinically accepted range when accurate corrections for patient motion and the expected scatter estimate were applied. Using a Monte-Carlo simulation of a NEMA-like phantom we found that an inaccurate scatter estimate could produce artifacts as well as introducing significant bias in the activity reconstructions. Furthermore, we find that the joint reconstructions were more robust to these inaccuracies, and when comparing the reconstructions to the standard MLEM reconstruction, more differences are observed with an increasing deviation of the scatter estimate used during reconstruction from the true scatter estimate. These observed differences could be partly explained by the fact that joint estimation has more degrees of freedom than that of the standard MLEM reconstruction.

A recent review of joint estimation methods can also be found in [184].

## 9. DISCUSSION

---

### 9.1 Future Perspectives

An important achievement in the problem of joint estimation is the realization that time of flight PET emission data uniquely determine the attenuation sinogram up to a constant. In recent years, many different methods have been proposed which use the added information of TOF PET data for attenuation correction of the PET emission data. Although clinical studies could greatly benefit from the immediate alignment provided by the joint reconstruction methods, the fact that a quantitative tracer distribution can only be obtained when some prior information is used, has limited their use in clinical practice.

We showed in chapter 7 that an accurate tracer distribution could be obtained once a good estimate of the scale is at hand. Although different scale correction techniques are possible, a reliable correction for the scale could be achieved by incorporating an expected tissue intensity prior. In our quantitative study we have chosen to bypass the scale correction required in joint reconstruction, to avoid interference of the scale problem with other problems such as motion and scatter correction. An additional study validating solutions to the scale problem will be necessary to facilitate the introduction of these methods in clinical practice. We believe that when an attenuation image is at hand, techniques that combine reconstruction of activity image and registration of the attenuation image will be among the most obvious choices in practice. In hybrid PET/MR systems this might not be possible, but since current state-of-the-art systems also provide TOF information a combination of region-of-interest attenuation reconstruction as proposed by Salomon *et al.* [56] together with attenuation registration as in MLRR might be an ideal method for attenuation correction.

The current TOF-resolution of state-of-the-art scanners seems to be good enough for attenuation correction of the thorax region. Although promising results have been reported in joint reconstructions of non-TOF brain studies (with a much smaller activity extent), heavy constraining was deemed necessary. Furthermore, it has been shown that TOF-PET data can significantly reduce the required constraining of the joint reconstructions in TOF-PET brain studies. However without any constraints, the joint reconstructions are not artifact-free. It is still not clear what the adequate TOF-resolution is for artifact-free reconstructions of activity and attenuation in TOF-PET brain studies with very little to no constraining of the reconstructions.

In gated studies where obtaining the attenuation of each gated frame is often problematic, joint reconstruction methods provide an elegant solution. Our proposed method, discussed in 8, avoids and postpones the attenuation reconstruction of the TOF-PET gated data. With a similar idea in mind, a recent work demonstrated how an available CT-based attenuation image (which is not guaranteed to be in any of the gated frames) can be used in this gated framework [169]. In this work, the extra cost of not having the CT-based attenuation image in any of the gated frames is that the estimation of an additional deformation for the attenuation is required. A similarly intriguing approach would be to reconstruct a single activity and attenuation image pair with deformations that transform the pair to each of the gated frames.

# Bibliography

- [1] M. N. Wernick and J. N. Aarsvold, Eds., *Emission Tomography*. Elsevier, 2004.
- [2] H. Zaidi, M 'hamed Bentourkia, A. O. Boudraa, M. Braun, a. B. Brill, E. C. Frey, G. Germano, B. H. Hasegawa, B. F. Hutton, K. F. Koral, D. a Mankoff, M. Muzy, J. Nuyts, O. G. Rousset, P. Slomka, M. G. Stabin, B. M. W. Tsui, and K. Van Laere, *Quantitative Analysis in Nuclear Medicine Imaging*. 2006.
- [3] M. Defrise, V. Y. Panin, C. Michel, and M. E. Casey, "Continuous and discrete data rebinning in time-of-flight PET.", *IEEE Trans. Med. Imaging*, vol. 27, no. 9, pp. 1310–22, Sep. 2008.
- [4] T. Tomitani, "Image Reconstruction and Noise Evaluation in Photon Time-of-Flight Assisted Positron Emission Tomography", *IEEE Trans. Nucl. Sci.*, vol. 28, pp. 4581–4589, 1981.
- [5] D. L. Snyder, "Some Noise Comparisons of Data-Collection Arrays for Emission Tomography-Systems Having Time-of-Flight Measurements", *IEEE Trans. Nucl. Sci.*, vol. 29, no. 1, pp. 1029–1033, 1982.
- [6] D. L. Snyder and D. G. Politte, "Image Reconstruction from List-Mode Data in an Emission Tomography System Having Time-of-Flight Measurements", *IEEE Trans. Nucl. Sci.*, vol. 30, no. 3, pp. 1843–1849, 1983.
- [7] W.-H. Wong, N. A. Mullani, E. A. Philippe, R Hartz, and K. L. Gould, "Image improvement and design optimization of the time-of-flight PET", *J. Nucl. Med.*, vol. 24, no. 1, pp. 52–60, 1983.
- [8] D. G. Politte, "Image Improvements in Positron-Emission Tomography Due to Measuring Differential Time-of-Flight and Using Maximum-Likelihood Estimation", *IEEE Trans. Nucl. Sci.*, vol. 37, no. 2, 1990.
- [9] T. K. Lewellen, "Time-of-flight PET", *Semin. Nucl. Med.*, vol. 28, no. 3, pp. 268–275, 1998.
- [10] W. Moses, "Time of flight in pet revisited", *IEEE Trans. Nucl. Sci.*, vol. 50, no. 5, pp. 1325–1330, Oct. 2003.

## BIBLIOGRAPHY

---

- [11] W. Wang, Z. Hu, E. E. Gaultieri, M. J. Parma, E. S. Walsh, D. Sebok, Y. L. Hsieh, C. H. Tung, X. Song, J. J. Griesmer, J. A. Kolthammer, L. M. Popescu, M. Werner, J. S. Karp, and D. Gagnon, “Systematic and Distributed Time-of-Flight List Mode PET Reconstruction”, in *2006 IEEE Nucl. Sci. Symp. Conf. Rec.*, Ieee, 2006, pp. 1715–1722.
- [12] K. Vunckx, L. Zhou, S. Matej, M. Defrise, and J. Nuyts, “Fisher information-based evaluation of image quality for time-of-flight PET.”, *IEEE Trans. Med. Imaging*, vol. 29, no. 2, pp. 311–21, Mar. 2010.
- [13] M. Conti, “Why is TOF PET reconstruction a more robust method in the presence of inconsistent data?”, *Phys. Med. Biol.*, vol. 56, no. 1, pp. 155–68, Jan. 2011.
- [14] C. Burger, G. Goerres, S. Schoenes, A. Buck, A. Lonn, and G. von Schulthess, “PET attenuation coefficients from CT images: Experimental evaluation of the transformation of CT into PET 511-keV attenuation coefficients”, en, *European Journal of Nuclear Medicine and Molecular Imaging*, vol. 29, no. 7, pp. 922–927, Apr. 2002.
- [15] G. Glatting, M. Wuchenauer, and S. N. Reske, “Simultaneous iterative reconstruction for emission and attenuation images in positron emission tomography.”, *Med. Phys.*, vol. 27, no. 9, pp. 2065–71, 2000.
- [16] D. W. Townsend, “Combined PET / CT : The historical perspective”, *Semin. Ultrasound, CT, MRI*, vol. 29, no. 4, pp. 232–235, 2009.
- [17] P. E. Kinahan, D. W. Townsend, T. Beyer, and D. Sashin, “Attenuation correction for a combined 3D PET/CT scanner”, *Med. Phys.*, vol. 25, no. 10, p. 2046, 1998.
- [18] V. Y. Panin, H Bal, M Defrise, M. E. Casey, and A Rahmim, “Whole Body Parametric Imaging on Clinical Scanner: Direct 4D Reconstruction with Simultaneous Attenuation Estimation and Time- Dependent Normalization”, in *2015 IEEE Nucl. Sci. Symp. Med. Imaging Conf. (2015 NSS/MIC)*, 2015.
- [19] M. Hofmann, B. Pichler, B. Schölkopf, and T. Beyer, “Towards quantitative PET/MRI: A review of MR-based attenuation correction techniques”, *Eur. J. Nucl. Med. Mol. Imaging*, vol. 36, pp. 93–104, 2009.
- [20] V. Keereman, P. Mollet, Y. Berker, V. Schulz, and S. Vandenberghe, “Challenges and current methods for attenuation correction in PET/MR.”, *MAGMA*, vol. 26, no. 1, pp. 81–98, Feb. 2013.
- [21] G. Delso, F. Wiesinger, L. I. Sacolick, S. S. Kaushik, D. D. Shanbhag, M. Hüllner, and P. Veit-Haibach, “Clinical Evaluation of Zero-Echo-Time MR Imaging for the Segmentation of the Skull”, en, *Journal of Nuclear Medicine*, vol. 56, no. 3, pp. 417–422, Mar. 2015.
- [22] Y Shao, S. R. Cherry, K Farahani, K Meadors, S Siegel, R. W. Silverman, and P. K. Marsden, “Simultaneous PET and MR imaging.”, *Phys. Med. Biol.*, vol. 42, no. 10, pp. 1965–1970, 1997.

- 
- [23] C. Catana, Y. Wu, M. S. Judenhofer, J. Qi, B. J. Pichler, and S. R. Cherry, “Simultaneous acquisition of multislice PET and MR images: Initial results with a MR-compatible PET scanner.”, *J. Nucl. Med.*, vol. 47, no. 12, pp. 1968–1976, 2006.
  - [24] A. Welch, C. Campbell, R. Clackdoyle, F. Natterer, M. Hudson, A. Bromiley, P. Mikecz, F. Chillcot, M. Dodd, P. Hopwood, S. Craib, G. T. Gullberg, and P. Sharp, “Attenuation correction in PET using consistency information”, *IEEE Trans. Nucl. Sci.*, vol. 45, no. 6, pp. 3134–3141, 1998.
  - [25] A. R. De Pierro and F. Crepaldi, “Activity and attenuation recovery from activity dataonly in emission computed tomography”, *Comput. Appl. Math.*, vol. 25, no. 2-3, pp. 205–227, 2006.
  - [26] F. Natterer, *The Mathematics of Computerized Tomography*. Society for Industrial and Applied Mathematics, Jan. 2001.
  - [27] ———, “Determination of tissue attenuation in emission tomography of optically dense media”, *Inverse Probl.*, vol. 9, no. 6, pp. 731–736, Dec. 1993.
  - [28] A. Welch, R. Clack, F. Natterer, and G. T. Gullberg, “Toward accurate attenuation correction in SPECT without transmission measurements.”, *IEEE Trans. Med. Imaging*, vol. 16, no. 5, pp. 532–41, Oct. 1997.
  - [29] I. Laurette, R. Clackdoyle, A. Welch, F. Natterer, and G. Gullberg, “Comparison of three applications of ConTraSPECT”, *IEEE Trans. Nucl. Sci.*, vol. 46, no. 6, pp. 2146–2153, 1999.
  - [30] R. Faghihi and L. Desbat, “Experiments on the DCC for SPECT and CT scanner data registration”, *2001 IEEE Nucl. Sci. Symp. Conf. Rec. (Cat. No.01CH37310)*, vol. 3, pp. 1437–1440, 2002.
  - [31] A. Marques da Silva and C. Robilotta, “Attenuation Correction in Cardiac SPECT Using Consistency Conditions”, in *3rd IEEE Int. Symp. Biomed. Imaging Macro to Nano, 2006.*, IEEE, 2006, pp. 271–274.
  - [32] C. Mennessier, F. Noo, R. Clackdoyle, G. Bal, and L. Desbat, “Attenuation correction in SPECT using consistency conditions for the exponential ray transform.”, *Phys. Med. Biol.*, vol. 44, no. 10, pp. 2483–510, 1999.
  - [33] A. Bromiley, A. Welch, F. Chilcott, S. Waikar, S. McCallum, M. Dodd, S. Craib, L. Schweiger, and P. Sharp, “Attenuation correction in PET using consistency conditions and a three-dimensional template”, *IEEE Trans. Nucl. Sci.*, vol. 48, no. 4, pp. 1371–1377, 2001.
  - [34] F. Chatelain, L. Desbat, J. Moreira, C. Amblard, and V. Breton, “SPECT/CT registration with the DCC and MC simulations for SPECT imaging”, in *IEEE SYMP. Conf. Nucl. Sci. 2004.*, vol. 6, IEEE, 2004, pp. 3551–3554.
  - [35] A. Alessio, J. Caldwell, G. Chen, K. Branch, and P. Kinahan, “Attenuation-Emission Alignment in Cardiac PET/CT with Consistency Conditions”, in *2006 IEEE Nucl. Sci. Symp. Conf. Rec.*, IEEE, 2006, pp. 3288–3291.

## BIBLIOGRAPHY

---

- [36] A. M. Alessio, P. E. Kinahan, K. M. Champliey, and J. H. Caldwell, “Attenuation-emission alignment in cardiac PET/CT based on consistency conditions”, *Med. Phys.*, vol. 37, no. 3, p. 1191, 2010.
- [37] K. Kacperski, “Attenuation correction in SPECT without attenuation map”, *2011 IEEE Nucl. Sci. Symp. Conf. Rec.*, no. 4, pp. 3820–3822, 2011.
- [38] A. V. Bronnikov, “Numerical solution of the identification problem for the attenuated Radon transform”, *Inverse Probl.*, vol. 5, pp. 1315–1324, 1999.
- [39] A. V. Bronnikov, “Reconstruction of attenuation map using discrete consistency conditions.”, *IEEE Trans. Med. Imaging*, vol. 19, no. 5, pp. 451–62, May 2000.
- [40] V. Dicken, “A new approach towards simultaneous activity and attenuation reconstruction in emission tomography”, *Inverse Probl.*, vol. 15, no. 4, pp. 931–960, Aug. 1999.
- [41] H. Kudo and H. Nakamura, “A new approach to SPECT attenuation correction without transmission measurements”, in *2000 IEEE Nucl. Sci. Symp. Conf. Rec.*, vol. 2, IEEE, 2001, pp. 13/58–13/62.
- [42] Y. Yan and G. L. Zeng, “Attenuation map estimation with SPECT emission data only.”, *Int J Imaging Syst Technol*, vol. 19, no. 3, p. 271, 2009.
- [43] Y. Censor, D. E. Gustafson, A. Lent, and H. Tuy, “A New Approach to the Emission Computerized Tomography Problem: Simultaneous Calculation of Attenuation and Activity Coefficients”, *IEEE Trans. Nucl. Sci.*, vol. 26, no. 2, pp. 2775–2779, Apr. 1979.
- [44] S. Manglos and T. Young, “Constrained IntraSPECT reconstruction from SPECT projections”, in *1993 IEEE Conf. Rec. Nucl. Sci. Symp. Med. Imaging Conf.*, vol. 00, IEEE, 1993, pp. 1605–1609.
- [45] V. Y. Panin, G. L. Zeng, and G. T. Gullberg, “A method of attenuation map and emission activity reconstruction from emission data”, *IEEE Trans. Nucl. Sci.*, vol. 48, no. 1, pp. 131–138, 2001.
- [46] D. Gourion, D. Noll, P. Gantet, A. Celler, and J.-P. Esquerre, “Attenuation correction using SPECT emission data only”, in *2001 IEEE Nucl. Sci. Symp. Conf. Rec. (Cat. No.01CH37310)*, vol. 3, IEEE, 2002, pp. 1522–1526.
- [47] J. Nuyts, P. Dupont, S Stroobants, R Benninck, L Mortelmans, and P. Suetens, “Simultaneous maximum a posteriori reconstruction of attenuation and activity distributions from emission sinograms.”, *IEEE Trans. Med. Imaging*, vol. 18, no. 5, pp. 393–403, May 1999.
- [48] A. Krol, J. E. Bowsher, S. H. Manglos, D. H. Feiglin, M. P. Tornai, and F. D. Thomas, “An EM algorithm for estimating SPECT emission and transmission parameters from emissions data only.”, *IEEE Trans. Med. Imaging*, vol. 20, no. 3, pp. 218–32, Mar. 2001.

- 
- [49] M. Landmann, S. N. Reske, and G. Glatting, “Simultaneous iterative reconstruction of emission and attenuation images in positron emission tomography from emission data only”, *Med. Phys.*, vol. 29, no. 9, p. 1962, 2002.
  - [50] F. Natterer, “Numerical methods in tomography”, *Acta Numerica*, vol. 8, pp. 107–141, Jan. 1999.
  - [51] V. Panin, G. Zeng, and G. Gullberg, “A method of attenuation map and emission activity reconstructions from emission data”, in *1999 IEEE Nucl. Sci. Symp. Conf. Rec. 1999 Nucl. Sci. Symp. Med. Imaging Conf. (Cat. No.99CH37019)*, vol. 3, IEEE, 1999, pp. 1250–1254.
  - [52] A. De Pierro and F. Crepaldi, “Simultaneous activity attenuation reconstruction in positron emission tomography via maximum likelihood and iterative methods”, in *IEEE INT. Conf. Image Process. 2005*, IEEE, 2005, pp. III–624.
  - [53] F. Crepaldi and A. R. De Pierro, “Activity and Attenuation Reconstruction for Positron Emission Tomography Using Emission Data Only Via Maximum Likelihood and Iterative Data Refinement”, *IEEE Trans. Nucl. Sci.*, vol. 54, no. 1, pp. 100–106, 2007.
  - [54] A. Salomon, A. Goedicke, and T. Aach, “Attenuation Corrected Cardiac SPECT Imaging Using Simultaneous Reconstruction and a Priori Information”, *IEEE Trans. Nucl. Sci.*, vol. 58, no. 2, pp. 527–536, 2011.
  - [55] A. Salomon, V. Schulz, B. Schweizer, A. Goedicke, and T. Aach, “Simultaneous Reconstruction of Activity and Attenuation in Multi-Modal ToF-PET”, in *2009 Fully Three-Dimensional Image Reconstr. Radiol. Nucl. Med. Proc.*, 2009, pp. 339–342.
  - [56] A. Salomon, A. Goedicke, B. Schweizer, T. Aach, and V. Schulz, “Simultaneous reconstruction of activity and attenuation for PET/MR.”, *IEEE Trans. Med. Imaging*, vol. 30, no. 3, pp. 804–13, Mar. 2011.
  - [57] A. Rezaei, J. Nuyts, M. Defrise, G. Bal, C. Michel, M. Conti, and C. Watson, “Simultaneous reconstruction of activity and attenuation in Time-of-Flight PET”, in *2011 IEEE Nucl. Sci. Symp. Med. Imaging Conf. (2011 NSS/MIC)*, vol. 31, IEEE, Oct. 2011, pp. 2375–2382.
  - [58] M. Defrise, A. Rezaei, and J. Nuyts, “Time-of-flight PET data determine the attenuation sinogram up to a constant.”, *Phys. Med. Biol.*, vol. 57, no. 4, pp. 885–99, Feb. 2012.
  - [59] V. Y. Panin, M. Defrise, and M. E. Casey, “Restoration of fine azimuthal sampling of measured TOF projection data”, in *IEEE NUCL. Sci. Symp. Med. Imaging Conf.*, IEEE, Oct. 2010, pp. 3079–3084.
  - [60] A. Rezaei, J. Nuyts, and M. Defrise, “Analytic reconstruction of the attenuation from 3D time-of-flight PET data”, in *2012 IEEE Nucl. Sci. Symp. Med. Imaging Conf. Rec. (2012 NSS/MIC)*, IEEE, Oct. 2012, pp. 2330–2333.

## BIBLIOGRAPHY

---

- [61] A. Rezaei, M. Defrise, G. Bal, C. Michel, M. Conti, C. Watson, and J. Nuyts, “Simultaneous reconstruction of activity and attenuation in time-of-flight PET.”, *IEEE Trans. Med. Imaging*, vol. 31, no. 12, pp. 2224–33, Dec. 2012.
- [62] J. Nuyts, G. Bal, F. Kehren, M. Fenchel, C. Michel, and C. Watson, “Completion of a truncated attenuation image from the attenuated PET emission data.”, *IEEE Trans. Med. Imaging*, vol. 32, no. 2, pp. 237–46, Mar. 2013.
- [63] J. Nuyts, A. Rezaei, and M. Defrise, “ML-reconstruction for TOF-PET with simultaneous estimation of the attenuation factors”, in *2012 IEEE Nucl. Sci. Symp. Med. Imaging Conf. Rec. (2012 NSS/MIC)*, IEEE, Oct. 2012, pp. 2147–2149.
- [64] M. Defrise, A. Rezaei, and J. Nuyts, “Simultaneous reconstruction of attenuation and activity in TOF-PET : Analysis of the convergence of the MLACF algorithm .”, in *2013 Fully Three-Dimensional Image Reconstr. Radiol. Nucl. Med. Proc.*, 2013, pp. 67–70.
- [65] ———, “Transmission-less attenuation correction in time-of-flight PET: Analysis of a discrete iterative algorithm.”, *Phys. Med. Biol.*, vol. 59, no. 4, pp. 1073–95, Feb. 2014.
- [66] A. Rezaei, M. Defrise, and J. Nuyts, “ML-reconstruction for TOF-PET with simultaneous estimation of the attenuation factors.”, *IEEE Trans. Med. Imaging*, vol. 33, no. 7, pp. 1563–72, Jul. 2014.
- [67] A. Rezaei and J. Nuyts, “Simultaneous reconstruction of the activity image and registration of the CT image in TOF-PET”, in *2013 IEEE Nucl. Sci. Symp. Med. Imaging Conf. Rec. (2013 NSS/MIC)*, IEEE, Oct. 2013, pp. 1–3.
- [68] A. Rezaei, C. Michel, M. E. Casey, and J. Nuyts, “Simultaneous reconstruction of the activity image and registration of the CT image in TOF-PET”, *Phys. Med. Biol.*, vol. 61, no. 4, pp. 1852–1874, Feb. 2016.
- [69] M. Defrise, K. Salvo, A. Rezaei, J. Nuyts, V. Y. Panin, and M. E. Casey, “ML estimation of the scatter scaling in TOF PET”, in *2014 IEEE Nucl. Sci. Symp. Med. Imaging Conf. (2014 NSS/MIC)*, Nov. 2014.
- [70] A. Rezaei, J. Nuyts, and M. Defrise, “The Effect of Motion on Joint Estimates of Activity and Attenuation from Time-of-Flight PET Data”, in *2013 Fully Three-Dimensional Image Reconstr. Radiol. Nucl. Med. Proc.*, 2013, pp. 297–300.
- [71] J. Carney, T. Beyer, D. Brasse, J. Yap, and D. Townsend, “CT-based attenuation correction for PET/CT scanners in the presence of contrast agent”, in *2002 IEEE Nuclear Science Symposium Conference Record*, vol. 3, IEEE, 2003, pp. 1443–1446.
- [72] E. Schreibmann, J. a Nye, D. M. Schuster, D. R. Martin, J. Votaw, and T. Fox, “MR-based attenuation correction for hybrid PET-MR brain imaging systems using deformable image registration.”, *Medical physics*, vol. 37, no. 5, pp. 2101–2109, 2010.

- 
- [73] V. Keereman, Y. Fierens, T. Broux, Y. De Deene, M. Lonneux, and S. Vandenbergh, “MRI-based attenuation correction for PET/MRI using ultrashort echo time sequences.”, *Journal of nuclear medicine : Official publication, Society of Nuclear Medicine*, vol. 51, no. 5, pp. 812–818, 2010.
  - [74] M. Hofmann, I. Bezrukov, F. Mantlik, P. Aschoff, F. Steinke, T. Beyer, B. J. Pichler, and B. Schölkopf, “MRI-Based Attenuation Correction for Whole-Body PET/MRI: Quantitative Evaluation of Segmentation- and Atlas-Based Methods.”, *Journal of nuclear medicine : Official publication, Society of Nuclear Medicine*, vol. 52, no. 9, pp. 1392–1399, 2011.
  - [75] J. Nuyts, P. Dupont, S. Stroobants, A. Maes, L. Mortelmans, and P. Suetens, “Evaluation of maximum-likelihood based attenuation correction in positron emission tomography”, *IEEE Transactions on Nuclear Science*, vol. 46, no. 4, pp. 1136–1141, 1999.
  - [76] F. Natterer, *Attenuation correction in emission tomography*, 21-23. Sabatier, Academic Press, 1987.
  - [77] H. Erdogan and J. A. Fessler, “Joint estimation of attenuation and emission images from PET scans”, *Nuclear Science Symposium*, 1999.
  - [78] N. Clinthorne, J. Fessler, G. Hutchins, and W. Rogers, “Joint maximum likelihood estimation of emission and attenuation densities in PET”, in *Conference Record of the 1991 IEEE Nuclear Science Symposium and Medical Imaging Conference*, IEEE, pp. 1927–1932.
  - [79] F. Natterer and H. Herzog, “Attenuation correction in positron emission tomography”, *Math. Methods Appl. Sci.*, vol. 15, no. 5, pp. 321–330, Jul. 1992.
  - [80] C. Bai, P. E. Kinahan, D. Brasse, C. Comtat, D. W. Townsend, C. C. Meltzer, V. Villemagne, M. Charron, and M. Defrise, “An analytic study of the effects of attenuation on tumor detection in whole-body PET oncology imaging.”, *Journal of nuclear medicine : Official publication, Society of Nuclear Medicine*, vol. 44, no. 11, pp. 1855–1861, 2003.
  - [81] T. Turkington and J. Wilson, “Attenuation artifacts and time-of-flight PET”, in *2009 IEEE Nucl. Sci. Symp. Conf. Rec.*, Ieee, Oct. 2009, pp. 2997–2999.
  - [82] A. Salomon, V. Schulz, R. Brinks, B. Schweizer, A. Goedicke, and T. Aach, “Iterative generation of attenuation maps in TOF-PET/MR using consistency conditions”, in *Journal of nuclear medicine meeting abstract*, 2009, p. 2013.
  - [83] P. Mollet, V. Keereman, and S. Vandenbergh, “Experimental evaluation of simultaneous emission and transmission imaging using TOF information”, in *2011 IEEE Nucl. Sci. Symp. Med. Imaging Conf. Rec.*, Ieee, Oct. 2011, pp. 2976–2980.
  - [84] S. Ettl, J. Kaminski, M. C. Knauer, and G. Häusler, “Shape reconstruction from gradient data”, *Applied Optics*, vol. 47, no. 12, p. 2091, Apr. 2008.
  - [85] C. L. Byrne, *Applied iterative methods*. Ak Peters/CRC Press, 2007.

- [86] R. Gray, “On the asymptotic eigenvalue distribution of Toeplitz matrices”, *IEEE Transactions on Information Theory*, vol. 18, no. 6, pp. 725–730, Nov. 1972.
- [87] M. Defrise, P. E. Kinahan, and C. Michel, *Positron Emission Tomography*, D. L. Bailey, D. W. Townsend, P. E. Valk, and M. N. Maisey, Eds. London: Springer-Verlag, 2005.
- [88] C. M. Laymon and J. E. Bowsher, “A log likelihood based method for recovery of localized defects in PET attenuation-correction images”, in *2004 IEEE Nucl. Sci. Symp. Conf. Rec.*, vol. 5, IEEE, 2004, pp. 2710–2714.
- [89] J. Nuyts, C. Michel, M. Fenchel, G. Bal, and C. Watson, “Completion of a truncated attenuation image from the attenuated PET emission data”, in *2010 IEEE Nucl. Sci. Symp. Med. Imaging Conf.*, vol. 32, IEEE, Oct. 2010, pp. 2123–2127.
- [90] M. Conti, B. Bendriem, M. E. Casey, M. Chen, F. Kehren, C. Michel, and V. Y. Panin, “First experimental results of time-of-flight reconstruction on an LSO PET scanner.”, *Phys. Med. Biol.*, vol. 50, no. 19, pp. 4507–26, Oct. 2005.
- [91] S. Surti, A. Kuhn, M. E. Werner, A. E. Perkins, J. A. Kolthammer, and J. S. Karp, “Performance of Philips Gemini TF PET/CT scanner with special consideration for its time-of-flight imaging capabilities.”, *J. Nucl. Med.*, vol. 48, no. 3, pp. 471–80, Mar. 2007.
- [92] B. W. Jakoby, Y. Bercier, M. Conti, M. E. Casey, B. Bendriem, and D. W. Townsend, “Physical and clinical performance of the mCT time-of-flight PET/CT scanner.”, *Phys. Med. Biol.*, vol. 56, no. 8, pp. 2375–89, Apr. 2011.
- [93] L a Shepp and Y Vardi, “Maximum likelihood reconstruction for emission tomography.”, *IEEE Trans. Med. Imaging*, vol. 1, no. 2, pp. 113–22, Jan. 1982.
- [94] J. A. Fessler, E. P. Ficaro, N. H. Clinthorne, and K. Lange, “Grouped-coordinate ascent algorithms for penalized-likelihood transmission image reconstruction.”, *IEEE Trans. Med. Imaging*, vol. 16, no. 2, pp. 166–75, Apr. 1997.
- [95] J. Nuyts, B. D. Man, P. Dupont, M. Defrise, P. Suetens, and L. Mortelmans, “Iterative reconstruction for helical CT: A simulation study”, *Phys. Med. Biol.*, vol. 43, no. 4, pp. 729–737, Apr. 1998.
- [96] J. A. Fessler and W. L. Rogers, “Spatial resolution properties of penalized-likelihood image reconstruction: Space-invariant tomographs.”, *IEEE Trans. Image Process.*, vol. 5, no. 9, pp. 1346–58, Jan. 1996.
- [97] Q. Li, E. Asma, J. Qi, J. R. Bading, and R. M. Leahy, “Accurate estimation of the Fisher information matrix for the PET image reconstruction problem.”, *IEEE Trans. Med. Imaging*, vol. 23, no. 9, pp. 1057–64, Sep. 2004.
- [98] F. H. Fahey, “Data acquisition in PET imaging.”, *J. Nucl. Med. Technol.*, vol. 30, no. 2, pp. 39–49, Jun. 2002.

- 
- [99] J. Nuyts, D. Beque, P. Dupont, and L. Mortelmanns, “A concave prior penalizing relative differences for maximum-a-posteriori reconstruction in emission tomography”, *IEEE Trans. Nucl. Sci.*, vol. 49, no. 1, pp. 56–60, Feb. 2002.
  - [100] *NEMA IEC Body Phantom Set*, [http://www.spect.com/pub/NEMA\\_IEC\\_Body\\_Phantom\\_Set.pdf](http://www.spect.com/pub/NEMA_IEC_Body_Phantom_Set.pdf).
  - [101] C. Watson, “Extension of Single Scatter Simulation to Scatter Correction of Time-of-Flight PET”, *IEEE Trans. Nucl. Sci.*, vol. 54, no. 5, pp. 1679–1686, Oct. 2007.
  - [102] S. R. Meikle and R. D. Badawi, “Quantitative Techniques in PET”, in *Positron Emission Tomography*, London: Springer-Verlag, 2003, pp. 93–126.
  - [103] T. Xia, A. M. Alessio, B. De Man, R. Manjeshwar, E. Asma, and P. E. Kinahan, “Ultra-low dose CT attenuation correction for PET/CT.”, *Phys. Med. Biol.*, vol. 57, no. 2, pp. 309–28, Jan. 2012.
  - [104] V. Y. Panin, M. Defrise, J. Nuyts, A. Rezaei, and M. E. Casey, “Reconstruction of uniform sensitivity emission image with partially known axial attenuation information in PET-CT scanners”, in *2012 IEEE Nucl. Sci. Symp. Med. Imaging Conf. Rec. (2012 NSS/MIC)*, IEEE, Oct. 2012, pp. 2166–2173.
  - [105] A. Martinez-Möller, M. Souvatzoglou, G. Delso, R. a Bundschuh, C. Chef'd'hotel, S. I. Ziegler, N. Navab, M. Schwaiger, and S. G. Nekolla, “Tissue classification as a potential approach for attenuation correction in whole-body PET/MRI: Evaluation with PET/CT data.”, *Journal of nuclear medicine : Official publication, Society of Nuclear Medicine*, vol. 50, no. 4, pp. 520–526, 2009.
  - [106] V. Bettinardi, L. Presotto, E. Rapisarda, M. Picchio, L. Gianolli, and M. C. Gilardi, “Physical Performance of the new hybrid PETCT Discovery-690”, *Medical Physics*, vol. 38, no. 10, p. 5394, 2011.
  - [107] S. Vandenberghe, M. E. Daube-Witherspoon, R. M. Lewitt, and J. S. Karp, “Fast reconstruction of 3D time-of-flight PET data by axial rebinning and transverse mashing.”, *Physics in medicine and biology*, vol. 51, no. 6, pp. 1603–1621, 2006.
  - [108] S. Cho, S. Ahn, Q. Li, and R. M. Leahy, “Exact and approximate Fourier rebidding of PET data from time-of-flight to non time-of-flight.”, *Physics in medicine and biology*, vol. 54, no. 3, pp. 467–484, 2009.
  - [109] H. Li, G. El Fakhri, and Q. Li, “Direct MAP Estimation of Attenuation Sinogram using TOF PET Data and Anatomical Information”, in *2013 Fully Three-Dimensional Image Reconstr. Radiol. Nucl. Med. Proc.*, vol. 3, 2013, pp. 405–408.
  - [110] S. Ahn, H. Qian, and R. M. Manjeshwar, “Convergent iterative algorithms for joint reconstruction of activity and attenuation from time-of-flight PET data”, in *2012 IEEE Nucl. Sci. Symp. Med. Imaging Conf. Rec.*, IEEE, Oct. 2012, pp. 3695–3700.

## BIBLIOGRAPHY

---

- [111] K. Lange, D. Hunter, and I Yang, “Optimization transfer using surrogate objective functions”, *Journal of Computational and Graphical Statistics*, vol. 9, no. 1, pp. 1–20, 2000.
- [112] A. R. De Pierro, “A modified expectation maximization algorithm for penalized likelihood estimation in emission tomography.”, *IEEE Trans. Med. Imaging*, vol. 14, no. 1, pp. 132–7, Jan. 1995.
- [113] M. M. Osman, C. Cohade, Y. Nakamoto, and R. L. Wahl, “Respiratory motion artifacts on PET emission images obtained using CT attenuation correction on PET-CT.”, *Eur. J. Nucl. Med. Mol. Imaging*, vol. 30, no. 4, pp. 603–6, Apr. 2003.
- [114] M. Defrise, D. W. Townsend, D. Bailey, A Geissbuhler, C. Michel, and T Jones, “A normalization technique for 3D PET data.”, *Phys. Med. Biol.*, vol. 36, no. 7, pp. 939–52, Jul. 1991.
- [115] P. E. Kinahan, D. W. Townsend, D. Bailey, D. Sashin, F. Jadali, and M. Mintun, “Efficiency normalization techniques for 3D PET data”, in *1995 IEEE Nucl. Sci. Symp. Med. Imaging Conf. Rec.*, vol. 2, Ieee, 1995, pp. 1021–1025.
- [116] M. L. Camborde, A. Rhamim, D. Newport, S. Siegel, K. Buckley, E. Vandervoort, T. Ruth, and V. Sossi, “Effect of normalization method on image uniformity and binding potential estimates on microPET”, in *2004 IEEE Nucl. Sci. Symp. Conf. Rec.*, vol. 6, IEEE, 2004, pp. 3467–3471.
- [117] R. Badawi and P. Marsden, “Self-normalization of emission data in 3D PET”, *IEEE Trans. Nucl. Sci.*, vol. 46, no. 3, pp. 709–712, Jun. 1999.
- [118] A. Salomon, B. Goldschmidt, R. Botnar, F. Kiessling, and V. Schulz, “A self-normalization reconstruction technique for PET scans using the positron emission data.”, *IEEE Trans. Med. Imaging*, vol. 31, no. 12, pp. 2234–40, Dec. 2012.
- [119] H. Rothfuss, V. Panin, I. Hong, A. Moor, J. Young, J. Hamill, C. Michel, and M. Casey, “LSO background radiation as a transmission source using time of flight information”, *IEEE Nucl. Sci. Symp. Conf. Rec.*, vol. 5483, 2013.
- [120] R. Boellaard, M. B. M. Hofman, O. S. Hoekstra, and A. A. Lammertsma, “Accurate PET/MR quantification using time of flight MLAA image reconstruction”, *Mol. Imaging Biol.*, vol. 16, no. 4, pp. 469–477, 2014.
- [121] A. Mehranian and H. Zaidi, “Joint Estimation of Activity and Attenuation in Whole-Body TOF PET/MRI Using Constrained Gaussian Mixture Models”, *IEEE Trans. Med. Imaging*, vol. 34, no. 9, pp. 1808–1821, Sep. 2015.
- [122] V. Y. Panin, F. Kehren, J. J. Hamill, and C. Michel, “Application of discrete data consistency conditions for selecting regularization parameters in PET attenuation map reconstruction”, *Phys. Med. Biol.*, vol. 49, no. 11, pp. 2425–2436, Jun. 2004.

- [123] P. E. Kinahan, B. H. Hasegawa, and T. Beyer, “X-ray-based attenuation correction for positron emission tomography/computed tomography scanners.”, *Semin. Nucl. Med.*, vol. 33, no. 3, pp. 166–79, Jul. 2003.
- [124] K. Van Slambrouck and J. Nuyts, “Reconstruction Scheme for Accelerated Maximum Likelihood Reconstruction: The Patchwork Structure”, *IEEE Trans. Nucl. Sci.*, vol. 61, no. 1, pp. 173–181, Feb. 2014.
- [125] J. P. Thirion, “Image matching as a diffusion process: An analogy with Maxwell’s demons”, *Med. Image Anal.*, vol. 2, no. 3, pp. 243–260, Sep. 1998.
- [126] H. Erdogan and J. A. Fessler, “Ordered subsets algorithms for transmission tomography”, en, *Physics in Medicine and Biology*, vol. 44, no. 11, p. 2835, 1999.
- [127] G. Wang and J. Qi, “Generalized algorithms for direct reconstruction of parametric images from dynamic PET data.”, *IEEE Trans. Med. Imaging*, vol. 28, no. 11, pp. 1717–26, Nov. 2009.
- [128] D. Kim, S. Ramani, and J. A. Fessler, “Combining Ordered Subsets and Momentum for Accelerated X-Ray CT Image Reconstruction”, *IEEE Trans. Med. Imaging*, vol. 34, no. 1, pp. 167–178, Jan. 2015.
- [129] Y. Nesterov, “A method of solving a convex programming problem with convergence rate  $O(1/k^2)$ ”, *Sov. Math. Dokl.*, vol. 27, no. 2, pp. 372–376, 1983.
- [130] T. Vercauteren, X. Pennec, A. Perchant, and N. Ayache, “Diffeomorphic demons: Efficient non-parametric image registration.”, *Neuroimage*, vol. 45, no. 1 Suppl, S61–72, Mar. 2009.
- [131] P. Cachier and N. Ayache, “Isotropic Energies, Filters and Splines for Vector Field Regularization”, *J. Math. Imaging Vis.*, vol. 20, no. 3, pp. 251–265, May 2004.
- [132] K. Lange and J. A. Fessler, “Globally convergent algorithms for maximum a posteriori transmission tomography.”, *IEEE Trans. Image Process.*, vol. 4, no. 10, pp. 1430–8, Jan. 1995.
- [133] P. M. Joseph, “An Improved Algorithm for Reprojecting Rays through Pixel Images.”, *IEEE Trans. Med. Imaging*, vol. 1, no. 3, pp. 192–196, 1982.
- [134] W. P. Segars, G. Sturgeon, S. Mendonca, J. Grimes, and B. M. W. Tsui, “4D XCAT phantom for multimodality imaging research”, *Med. Phys.*, vol. 37, no. 9, p. 4902, 2010.
- [135] W. van Elmpt, J. J. Hamill, J. Jones, D. De Ruysscher, P. Lambin, and M. Ollers, “Optimal gating compared to 3D and 4D PET reconstruction for characterization of lung tumours.”, *Eur. J. Nucl. Med. Mol. Imaging*, vol. 38, no. 5, pp. 843–55, May 2011.
- [136] A. Mehranian and H. Zaidi, “Impact of Time-of-Flight PET on Quantification Errors in MR Imaging-Based Attenuation Correction”, *J. Nucl. Med.*, vol. 56, pp. 635–641, 2015.

## BIBLIOGRAPHY

---

- [137] B. T. T. Yeo, M. R. Sabuncu, R. Desikan, B. Fischl, and P. Golland, “Effects of registration regularization and atlas sharpness on segmentation accuracy”, *Med. Image Anal.*, vol. 12, no. 5, pp. 603–615, 2008.
- [138] J. J. Hamill and V. Y. Panin, “TOF-MLAA for attenuation correction in thoracic PET/CT”, in *2012 IEEE Nucl. Sci. Symp. Med. Imaging Conf. Rec.*, IEEE, Oct. 2012, pp. 4040–4047.
- [139] V. Y. Panin, M. Aykac, and M. E. Casey, “Simultaneous reconstruction of emission activity and attenuation coefficient distribution from TOF data, acquired with rotating external line source”, in *2011 IEEE Nucl. Sci. Symp. Conf. Rec.*, vol. 3649, IEEE, Oct. 2011, pp. 4329–4336.
- [140] P. Mollet, V. Keereman, E. Clementel, and S. Vandenbergh, “Simultaneous MR-compatible emission and transmission imaging for PET using time-of-flight information”, *IEEE Trans. Med. Imaging*, vol. 31, no. 9, pp. 1734–1742, 2012.
- [141] Y. Berker, F. Kiessling, and V. Schulz, “Scattered PET data for attenuation-map reconstruction in PET/MRI.”, *Med. Phys.*, vol. 41, no. 10, p. 102502, Oct. 2014.
- [142] A. Lougovski, G. Schramm, J. Maus, F. Hofheinz, and J. van den Ho, “Preliminary evaluation of the MLAA algorithm with the Philips Ingenuity PET/MR”, *EJNMMI Phys.*, vol. 1, no. Suppl 1, A33, 2014.
- [143] L. Presotto, E. Busnardo, D. Perani, L. Gianolli, M. C. Gilardi, and V. Bettinardi, “Simultaneous reconstruction of attenuation and activity in cardiac PET can remove CT misalignment artifacts”, *J. Nucl. Cardiol.*, 2015.
- [144] S. Stute and C. Comtat, “Could Simultaneous Reconstruction of Multiple Bed Positions Have Benefits in Whole-Body PET ?”, in *2014 IEEE Nucl. Sci. Symp. Med. Imaging Conf. (2014 NSS/MIC)*, 2014.
- [145] K. Salvo, V. Y. Panin, H. Rothfuss, and M. Defrise, “ML estimation of the scatter scaling in TOF PET”, in *2015 Fully Three-Dimensional Image Reconstruction in Radiology and Nuclear Medicine Proceedings*, 2015.
- [146] M. Dawood, F. Buther, X. Jiang, and K. P. Schaefers, “Respiratory motion correction in 3-D PET data with advanced optical flow algorithms.”, *IEEE Trans. Med. Imaging*, vol. 27, no. 8, pp. 1164–75, Aug. 2008.
- [147] M. Blume, A. Martinez-Möller, A. Keil, N. Navab, and M. Rafecas, “Joint reconstruction of image and motion in gated positron emission tomography.”, *IEEE Trans. Med. Imaging*, vol. 29, no. 11, pp. 1892–906, Nov. 2010.
- [148] Q. Yang, W. Cong, and G. Wang, “Attenuation map reconstruction from TOF PET data”, p. 10, Dec. 2013.
- [149] A. Mehranian and H. Zaidi, “Joint estimation of activity and attenuation in PET/MR using MR- constrained Gaussian priors”, in *2014 IEEE Nucl. Sci. Symp. Med. Imaging Conf. (2014 NSS/MIC) IEEE Nucl. Sci. Symp. Conf. Rec.*, 2014.

- 
- [150] S. Ahn, L. Cheng, D. Shanbhag, F. Wiesinger, and R. Manjeshwar, “Joint Reconstruction of Activity and Attenuation Using MR-Based Priors: Application to Clinical TOF PET/MR”, in *2015 IEEE Nucl. Sci. Symp. Med. Imaging Conf. (2015 NSS/MIC)*, 2015.
  - [151] X. Pan, B. Chen, Z. Zhang, S. Rose, and E. Y. Sidky, “Optimization-Based Simultaneous Determination of Emission Activity and Photon Attenuation in PET”, in *2015 Fully Three-Dimensional Image Reconstr. Radiol. Nucl. Med. Proc.*, 2015.
  - [152] Y. Hsu, P.-H. Hsu, and C.-Y. Chou, “Attenuation and activity distributions in flat-panel TOF-PET estimated by the alternating-direction method of multipliers”, in *2015 IEEE Nucl. Sci. Symp. Med. Imaging Conf. (2015 NSS/MIC)*, vol. 106, 2015.
  - [153] L. Presotto, V. Bettinardi, L. Gianolli, and D. Perani, “Alternating Strategies and Ordered Subset Acceleration Schemes for Maximum Likelihood Activity and Attenuation Reconstruction in”, in *2015 IEEE Nucl. Sci. Symp. Med. Imaging Conf. (2015 NSS/MIC)*, 2015, pp. 2–5.
  - [154] J.-c. K. Cheng, A. Salomon, M. Yaqub, and R. Boellaard, “Effects of Boundary Conditions in TOF-MLAA Reconstruction for PET / MR”, in *2015 IEEE Nucl. Sci. Symp. Med. Imaging Conf. (2015 NSS/MIC)*, 2015.
  - [155] ——, “Evaluation of a More Optimal Initial Attenuation Image Estimate in TOF-MLAA for PET / MR”, in *2015 IEEE Nucl. Sci. Symp. Med. Imaging Conf. (2015 NSS/MIC)*, 2015.
  - [156] V. Y. Panin, M Aykac, and M. E. Casey, “Simultaneous reconstruction of emission activity and attenuation coefficient distribution from TOF data, acquired with external transmission source”, *Phys. Med. Biol.*, vol. 58, no. 11, pp. 3649–3669, Jun. 2013.
  - [157] H. Rothfuss, V. Panin, A. Moor, J. Young, I. Hong, C. Michel, J. Hamill, and M. Casey, “LSO background radiation as a transmission source using time of flight.”, *Phys. Med. Biol.*, vol. 59, no. 18, pp. 5483–5500, Aug. 2014.
  - [158] T. Kaltsas, L. Caldeira, J. Scheins, L. Tellmann, E. R. Kops, N. J. Shah, and C. Lerche, “Reconstruction of attenuation maps for a PET / MR scanner based on the LSO background activity”, in *2015 IEEE Nucl. Sci. Symp. Med. Imaging Conf. (2015 NSS/MIC)*, 2015.
  - [159] V. Y. Panin, H Bal, M Defrise, C Hayden, and M. E. Casey, “Transmissionless brain TOF PET imaging using MLACF”, in *2013 IEEE Nucl. Sci. Symp. Med. Imaging Conf. (2013 NSS/MIC)*, IEEE, Oct. 2013, pp. 1–7.
  - [160] A. Sitek, “Image Reconstruction Using Multinomial Statistics: Application to Attenuation Correction for Time-of-Flight Positron Emission Tomography (TOF-PET)”, in *2013 IEEE Nucl. Sci. Symp. Med. Imaging Conf. (2013 NSS/MIC)*, 2013, Talk: M04–4.

## BIBLIOGRAPHY

---

- [161] P. Mollet and S. Vandenberghe, “Comparison of transmission- and emission-based attenuation correction for TOF-PET / MRI”, in *2014 IEEE Nucl. Sci. Symp. Med. Imaging Conf. (2014 NSS/MIC)*, 2014, pp. 1–5.
- [162] A. Rezaei, M. Bickell, R. Fulton, and J. Nuyts, “Joint Activity and Attenuation Reconstruction of Listmode TOF-PET data”, in *2015 IEEE Nucl. Sci. Symp. Med. Imaging Conf. (2015 NSS/MIC)*, 2015.
- [163] A. K. Jha, E. Clarkson, M. A. Kupinski, and H. H. Barrett, “Joint reconstruction of activity and attenuation map using LM SPECT emission data”, in *SPIE PROC. Vol. 8668 Med. Imaging 2013 Phys. Med. Imaging*, R. M. Nishikawa and B. R. Whiting, Eds., vol. 8668, Mar. 2013, 86681W.
- [164] J. L. Herraiz and A Sitek, “Sensitivity estimation in time-of-flight list-mode positron emission tomography”, *Med. Phys.*, vol. 42, no. 11, pp. 6690–6702, Nov. 2015.
- [165] M. E. Werner and J. S. Karp, “Detector Efficiency Calibration from Clinical Listmode TOF PET Data”, in *2014 IEEE Nucl. Sci. Symp. Med. Imaging Conf. (2014 NSS/MIC)*, 2014, talk: M14–2.
- [166] V. Y. Panin, “Simultaneous Activity and Crystal Efficiencies Reconstruction : TOF Patient-Based Detector Quality Control”, in *2014 IEEE Nucl. Sci. Symp. Med. Imaging Conf. (2014 NSS/MIC) IEEE Nucl. Sci. Symp. Conf. Rec.*, 2014.
- [167] S. Barendt and J. Modersitzki, “A variational model for SPECT reconstruction with a nonlinearly transformed attenuation prototype”, *Int. J. Comput. Math.*, vol. 90, no. 1, pp. 82–91, 2013.
- [168] A. Bousse, O. Bertolli, D. Atkinson, S. Arridge, S. Ourselin, B. F. Hutton, and K. Thielemans, “Direct Joint Motion EstimationImage Reconstruction in Attenuation-Corrected Gated PETCT Using a Single CT”, in *2015 Fully Three-Dimensional Image Reconstr. Radiol. Nucl. Med. Proc.*, 2015.
- [169] A. Bousse, O. Bertolli, D. Atkinson, S. Arridge, S. Ourselin, B. Hutton, and K. Thielemans, “Maximum-Likelihood Joint Image Reconstruction/Motion Estimation in Attenuation-Corrected Respiratory Gated PET/CT using a Single Attenuation Map”, *IEEE Trans. Med. Imaging*, vol. 35, no. 1, pp. 1–1, 2015.
- [170] A. Bousse, O. Bertolli, D. Atkinson, S. Arridge, S. Ourselin, B. F. Hutton, and K. Thielemans, “Maximum-likelihood joint image reconstruction and motion estimation with misaligned attenuation in TOF-PET/CT”, *Phys. Med. Biol.*, vol. 61, no. 3, p. L11, 2016.
- [171] A. Mihlin and C. S. Levin, “An MLEM method for joint tissue activity distribution and photon attenuation map reconstruction in PET”, in *2013 IEEE Nucl. Sci. Symp. Med. Imaging Conf. (2013 NSS/MIC)*, IEEE, Oct. 2013, pp. 1–3.

- 
- [172] ——, “An Ordered Subset Expectation Maximization Method for Joint Estimation of Emission Activity Distribution and Photon Attenuation Map in PET”, in *2015 IEEE Nucl. Sci. Symp. Med. Imaging Conf. (2015 NSS/MIC)*, 2015, pp. 1–3.
  - [173] K. Lange and R. Carson, “EM reconstruction algorithms for emission and transmission tomography.”, eng, *J. Comput. Assist. Tomogr.*, vol. 8, no. 2, pp. 306–316, Apr. 1984.
  - [174] T. Heusser, C. M. Rank, T. Beyer, and M. Kachelriess, “MR-consistent Simultaneous Reconstruction of Attenuation and Activity for non-TOF PETMR a Simulation Study”, in *2015 Fully Three-Dimensional Image Reconstr. Radiol. Nucl. Med. Proc.*, 2015.
  - [175] T. Heußer, C. M. Rank, M. T. Freitag, A. Dimitrakopoulou-Strauss, H. P. Schlemmer, T. Beyer, and M. Kachelrieß, “MR-Consistent Simultaneous Reconstruction of Attenuation and Activity for Non-TOF PET/MR”, *IEEE Transactions on Nuclear Science*, vol. PP, no. 99, pp. 1–1, 2016.
  - [176] D. Benoit, C. Ladefoged, A. Rezaei, S. Keller, F. Andersen, L. Hojgaard, A. Hansen, S. Holm, and J. Nuyts, “PET/MR: Improvement of the UTE mu-maps using modified MLAA”, in *EJNMMI PHYS.*, vol. 2, Springer Open Ltd, 2015, A58.
  - [177] C. C. Watson, V. Y. Panin, S. H. Keller, S. Holm, and J. Nuyts, “A Sparse Transmission Method for PET Attenuation Correction in the Head”, in *2014 IEEE Nucl. Sci. Symp. Med. Imaging Conf. (2014 NSS/MIC) IEEE Nucl. Sci. Symp. Conf. Rec.*, 2014.
  - [178] J. Nuyts and A. Rezaei, “Joint region-of-interest activity and alignment estimation in emission tomography”, in *2014 IEEE Nucl. Sci. Symp. Med. Imaging Conf. (2014 NSS/MIC)*, 2014, In-press.
  - [179] W. L. Long, C. Pei, W. Li-Wei, Y. Ming-Kai, Z. Xiao-Lin, L. Shuang-Quan, Z. Yu-Bao, S. Bao-Ci, and Wei, “Attenuation correction for dedicated breast PET using only emission data based on consistency conditions”, *Chinese Phys. C*, vol. 37, no. 1, p. 18201, 2013.
  - [180] A. Rezaei, M. Defrise, and J. Nuyts, “Reconstruction of a Motion and Attenuation Corrected Activity Distribution in Gated TOF-PET”, in *2014 IEEE Nucl. Sci. Symp. Med. Imaging Conf. (2014 NSS/MIC)*, Nov. 2014.
  - [181] H. Li, G. El Fakhri, A. A. Joshi, and Q. Li, “An ADMM Reconstruction Algorithm for Joint Registration and Attenuation Correction in Transmission-Less Gated TOF PET”, in *2014 IEEE Nucl. Sci. Symp. Med. Imaging Conf. (2014 NSS/MIC)*, 2014, talk: M22–1.
  - [182] V. Y. Panin, H Bal, and M. Defrise, “TOF ML-ACF Reconstruction of Dynamic Data”, in *2015 Fully Three-Dimensional Image Reconstr. Radiol. Nucl. Med. Proc.*, 2015.

## BIBLIOGRAPHY

---

- [183] D. Benoit, C. Ladefoged, A. Rezaei, S. H. Keller, F. Andersen, L. Hojgaard, A. Hansen, S. Holm, and J. Nuyts, “Optimized MLAA for quantitative non-TOF PET/MR of the brain”, *IEEE Trans Med Imag*, In-review, 2016.
- [184] Y. Berker and Y. Li, “Attenuation correction in emission tomography using the emission data — A review”, *Med. Phys.*, vol. 807, 2016.





## List of Publications - Journals

- [1] **A. Rezaei**, M. Bickell, R. Fulton, and J. Nuyts. "Joint Activity and Attenuation Reconstruction of Listmode TOF-PET data." In: (), In-preperation.
- [2] **A. Rezaei**, M. Defrise, and J. Nuyts. "Reconstruction of a Motion and Attenuation Corrected Activity Distribution in Gated TOF-PET." In: (), In-preperation.
- [3] **A. Rezaei**, C. Deroose, T. Koesters, K. Salvo, M. Defrise, F. Boada, and J. Nuyts. "Joint Reconstruction of Activity and Attenuation in Time of Flight PET: A Quantitative Analysis." In: *J. Nucl. Med.* (), In-preperation.
- [4] D. Benoit, C. Ladefoged, **A. Rezaei**, S. H. Keller, F. Andersen, L. Hojgaard, A. Hansen, S. Holm, and J. Nuyts. "Optimized MLAA for quantitative non-TOF PET/MR of the brain." In: *IEEE Trans Med Imag* (2016), In-review.
- [5] **A. Rezaei**, C. Michel, M. E. Casey, and J. Nuyts. "Simultaneous reconstruction of the activity image and registration of the CT image in TOF-PET." In: *Phys. Med. Biol.* 61.4 (Feb. 2016), pp. 1852–1874.
- [6] **A. Rezaei**, M. Defrise, and J. Nuyts. "ML-reconstruction for TOF-PET with simultaneous estimation of the attenuation factors." In: *IEEE Trans. Med. Imaging* 33.7 (July 2014), pp. 1563–72.
- [7] M. Defrise, **A. Rezaei**, and J. Nuyts. "Transmission-less attenuation correction in time-of-flight PET: analysis of a discrete iterative algorithm." In: *Phys. Med. Biol.* 59.4 (Feb. 2014), pp. 1073–95.
- [8] M. M. Cona, Y. Feng, Y. Li, F. Chen, K. Vunckx, L. Zhou, K. Van Slambrouck, **A. Rezaei**, O. Gheysens, J. Nuyts, A. Verbruggen, R. Oyen, and Y. Ni. "Comparative study of iodine-123-labeled hypericin and (99m)Tc-labeled hexakis [2-methoxy isobutyl isonitrile] in a rabbit model of myocardial infarction." In: *J. Cardiovasc. Pharmacol.* 62.3 (Sept. 2013), pp. 304–11.
- [9] **A. Rezaei**, M. Defrise, G. Bal, C. Michel, M. Conti, C. Watson, and J. Nuyts. "Simultaneous reconstruction of activity and attenuation in time-of-flight PET." In: *IEEE Trans. Med. Imaging* 31.12 (Dec. 2012), pp. 2224–33.
- [10] M. Defrise, **A. Rezaei**, and J. Nuyts. "Time-of-flight PET data determine the attenuation sinogram up to a constant." In: *Phys. Med. Biol.* 57.4 (Feb. 2012), pp. 885–99.

## List of Publications - Conference Proceedings

- [11] K. Vunckx, **A. Rezaei**, C. Liu, and C. Chan. "Investigation of Using Anatomical Knowledge in PET Imaging of Sub-Centimeter Lung Nodules." In: *2015 IEEE Nucl. Sci. Symp. Med. Imaging Conf. (2015 NSS/MIC)*. 2015.
- [12] M. G. Bickell, J.-H. Kim, **A. Rezaei**, J. Nuyts, and R. Fulton. "Rigid motion correction of PET and CT for PET/CT brain imaging." In: *2015 IEEE Nucl. Sci. Symp. Med. Imaging Conf. (2015 NSS/MIC)*. 2015, pp. 7–9.
- [13] **A. Rezaei**, M. Bickell, R. Fulton, and J. Nuyts. "Joint Activity and Attenuation Reconstruction of Listmode TOF-PET data." In: *2015 IEEE Nucl. Sci. Symp. Med. Imaging Conf. (2015 NSS/MIC)*. 2015.
- [14] D. Benoit, C. Ladefoged, **A. Rezaei**, S. Keller, F. Andersen, L. Hojgaard, A. Hansen, S. Holm, and J. Nuyts. "PET/MR: improvement of the UTE mu-maps using modified MLAA." In: *EJNMMI Phys.* Vol. 2. Springer Open Ltd, 2015, A58.

- [15] J. Nuyts and **A. Rezaei**. “Joint region-of-interest activity and alignment estimation in emission tomography.” In: *2014 IEEE Nucl. Sci. Symp. Med. Imaging Conf. (2014 NSS/MIC)*. 2014, In-press.
- [16] M. Defrise, K. Salvo, **A. Rezaei**, J. Nuyts, V. Y. Panin, and M. E. Casey. “ML estimation of the scatter scaling in TOF PET.” In: *2014 IEEE Nucl. Sci. Symp. Med. Imaging Conf. (2014 NSS/MIC)*. Nov. 2014.
- [17] **A. Rezaei**, M. Defrise, and J. Nuyts. “Reconstruction of a Motion and Attenuation Corrected Activity Distribution in Gated TOF-PET.” In: *2014 IEEE Nucl. Sci. Symp. Med. Imaging Conf. (2014 NSS/MIC)*. Nov. 2014.
- [18] **A. Rezaei** and J. Nuyts. “Simultaneous reconstruction of the activity image and registration of the CT image in TOF-PET.” In: *2013 IEEE Nucl. Sci. Symp. Med. Imaging Conf. Rec. (2013 NSS/MIC)*. IEEE, Oct. 2013, pp. 1–3.
- [19] **A. Rezaei** and J. Nuyts. “Joint registration of attenuation and activity images in gated TOF-PET.” In: *2013 IEEE Nucl. Sci. Symp. Med. Imaging Conf. (2013 NSS/MIC)*. IEEE, Oct. 2013, pp. 1–4.
- [20] **A. Rezaei**, J. Nuyts, and M. Defrise. “The Effect of Motion on Joint Estimates of Activity and Attenuation from Time-of-Flight PET Data.” In: *2013 Fully Three-Dimensional Image Reconstr. Radiol. Nucl. Med. Proc.* 2013, pp. 297–300.
- [21] M. Defrise, **A. Rezaei**, and J. Nuyts. “Simultaneous reconstruction of attenuation and activity in TOF-PET : analysis of the convergence of the MLACF algorithm .” In: *2013 Fully Three-Dimensional Image Reconstr. Radiol. Nucl. Med. Proc.* 2013, pp. 67–70.
- [22] J. Nuyts, **A. Rezaei**, and M. Defrise. “ML-reconstruction for TOF-PET with simultaneous estimation of the attenuation factors.” In: *2012 IEEE Nucl. Sci. Symp. Med. Imaging Conf. Rec. (2012 NSS/MIC)*. IEEE, Oct. 2012, pp. 2147–2149.
- [23] **A. Rezaei**, J. Nuyts, and M. Defrise. “Analytic reconstruction of the attenuation from 3D time-of-flight PET data.” In: *2012 IEEE Nucl. Sci. Symp. Med. Imaging Conf. Rec. (2012 NSS/MIC)*. IEEE, Oct. 2012, pp. 2330–2333.
- [24] V. Y. Panin, M. Defrise, J. Nuyts, **A. Rezaei**, and M. E. Casey. “Reconstruction of uniform sensitivity emission image with partially known axial attenuation information in PET-CT scanners.” In: *2012 IEEE Nucl. Sci. Symp. Med. Imaging Conf. Rec. (2012 NSS/MIC)*. IEEE, Oct. 2012, pp. 2166–2173.
- [25] **A. Rezaei**, J. Nuyts, M. Defrise, G. Bal, C. Michel, M. Conti, and C. Watson. “Simultaneous reconstruction of activity and attenuation in Time-of-Flight PET.” In: *2011 IEEE Nucl. Sci. Symp. Med. Imaging Conf. (2011 NSS/MIC)*. Vol. 31. IEEE, Oct. 2011, pp. 2375–2382.

# Ahmadreza REZAEI

**DOB:** 07-April-1983  
**Nationality:** Iranian  
**Address:** Celestijnenlaan 81/04  
3001 Heverlee, Belgium.  
**W** (+32) 163 49080  
**M** (+32) 489 685982  
**E** ahmadreza.rezaei@gmail.com

## Education

### Ph.D. candidate in Biomedical Sciences, KU Leuven, Belgium.

- Starting date: Apr-2012
- Research topic: "Statistical Methods for Attenuation Correction in Positron Emission Tomography (PET)".
- The research is supported by a research grant (GOA) from KU Leuven, Fonds Wetenschappelijk Onderzoek (FWO), and by Siemens Healthcare, Anderlecht, Belgium.

### Pre-doctoral training in Biomedical Sciences, KU Leuven, Belgium.

- Date of graduation: May-2012
- Thesis in medical image reconstruction, entitled: "Joint activity and attenuation estimation from emission data in time-of-flight PET".
- Graduated with honors (cum laude).

### M.Sc. in Biomedical Engineering, Amirkabir University of Technology, Iran.

- Date of graduation: May-2008
- Dissertation in digital image processing, entitled: "Stereo Sign Language Recognition".
- The work was performed under the support of Iran's Telecommunication Research Center (ITRC).

### B.Sc in Biomedical Engineering, Amirkabir University of Technology, Iran.

- Date of graduation: Sep-2005
- Project in robotics, entitled: "Design & hardware implementation of the electronic components of a Robot Snake".
- The project was performed with collaboration with the Mechanical Department.

## Selected Publication List

- [1] **A. Rezaei**, C. Michel, M. E. Casey, and J. Nuyts. "Simultaneous reconstruction of the activity image and registration of the CT image in TOF-PET." In: *Phys. Med. Biol.* 61.4 (Feb. 2016), pp. 1852–1874.
- [2] **A. Rezaei**, M. Defrise, and J. Nuyts. "ML-reconstruction for TOF-PET with simultaneous estimation of the attenuation factors." In: *IEEE Trans. Med. Imaging* 33.7 (July 2014), pp. 1563–72.
- [3] M. Defrise, **A. Rezaei**, and J. Nuyts. "Transmission-less attenuation correction in time-of-flight PET: analysis of a discrete iterative algorithm." In: *Phys. Med. Biol.* 59.4 (Feb. 2014), pp. 1073–95.
- [4] **A. Rezaei**, M. Defrise, G. Bal, C. Michel, M. Conti, C. Watson, and J. Nuyts. "Simultaneous reconstruction of activity and attenuation in time-of-flight PET." In: *IEEE Trans. Med. Imaging* 31.12 (Dec. 2012), pp. 2224–33.

- [5] M. Defrise, **A. Rezaei**, and J. Nuyts. “Time-of-flight PET data determine the attenuation sinogram up to a constant.” In: *Phys. Med. Biol.* 57.4 (Feb. 2012), pp. 885–99.

## Professional Experience

### Algorithm Developer 2008-2010

Worked as a computer vision and image processing expert at BeenaVision Co., where we used machine vision technology to designing train monitoring algorithms for the railroad industry (<http://www.beenavision.com>).

### Engineering Personnel 2006-2007

Worked as an engineering personnel of one of the biggest manufacturer and distributors of medical laboratory equipments and diagnostic products in Iran (Ari-aPharMed Co. & Tahghigh Gostar Co).

### Internship 2004

Trainee at Milad Hospital, Tehran, Iran.

### Executive Committee Member 2004

Executive committee member of the 11<sup>th</sup> Iranian Conference on Biomedical Engineering.

## Related Skills

**Hardware:** Z80 micro-processor, Intel 8085 micro-processor, AVR series micro-controllers.

**Computer:** Assembly, C/C++, Visual C, MATLAB, LabView, IDL.

**Language:** Farsi (mother tongue), English (Internet Based TOEFL (IBT) score: 100/120).

## Hobbies

Playing tar (traditional persian lute), jogging and playing football



